Structural and Functional Role of the Extracellular Loops and C-terminal Domain of the Voltage-gated Sodium Ion Channel

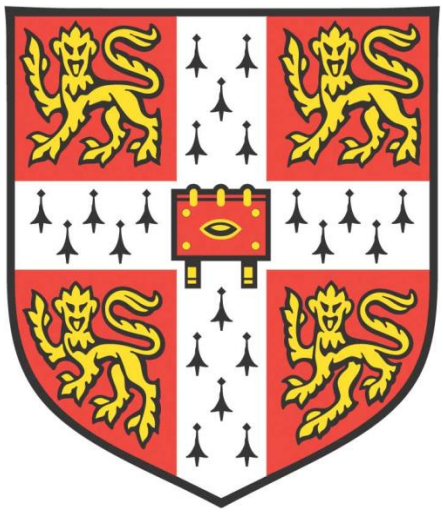

Zaki Farhad Habib

Department of Physiology, Development and Neuroscience

University of Cambridge

Girton College

This thesis is submitted for the degree of

Doctor of Philosophy

April 2022

Declaration

This thesis is the result of my own work and includes nothing which is the outcome of work done in collaboration except as declared in the acknowledgement and specified in the text. It is not substantially the same as any work that has already been submitted before for any degree or other qualification except as declared in the acknowledgement and specified in the text. It does not exceed the prescribed word limit for the Biological Sciences Degree Committee.

Zaki Farhad Habib

April 2022

Abstract

Voltage-gated sodium ion channels (Na_v) are central to action potential initiation through regulating the entry of sodium ions (Na^+) into excitable cells including cardiomyocytes and neurones. The α-subunit of Na_v consists of four homologous domains (DI-DIV), each consisting of six transmembrane helices (S1-S6). Helices S5-S6 of each domain forms the lining of the central pore through which sodium ions (Na^+) enters the cell upon channel activation. Helices S1-S4 of each domain form the voltage sensor which becomes displaced in response to changes in intracellular potential. Additionally, Na_v channels include an extracellular turret region, whose role in channel function is poorly understood. The C-terminal domain (CTD) of Na_v, connected to the DIV-S6, interacts with various other proteins including calmodulin (CaM) and fibroblast growth factor (FGF13) and mediates various regulatory roles. The subtype $Na_v1.5$ is primarily expressed in the heart where it initiates the cardiac action potential whereas $Na_v1.7$ is found in the peripheral nervous system where it is associated with nociception.

Various Na_v associated pathologies have been associated with mutations in the extracellular turret region; however, their molecular mechanism is not well understood. In the $Na_v1.5$ structure determined by cryogenic electron microscopy (cryoEM), the wild-type residues that correspond to some of these mutants form a complex salt bridge at the interface between the DII and DIII turret loops. Furthermore, adjacent aromatic residues could potentially form cation-π interactions with the complex salt bridge. This region was examined using site-directed mutagenesis, electrophysiology and *in silico* modelling, confirming functional roles for the inter-domain salt-bridges and the aromatic residues. Evidence that disruption of these contacts perturbs the geometry of the DEKA selectivity ring and both the outer and inner pore vestibules that are crucial for sodium ion permeability were provided. These findings provide insights into a class of pathological mutations occurring not only in $Na_v1.5$ but also in other sodium channel isoforms.

Further experiments performed preliminary studies that focussed on the CTD of $Na_v1.5$ and $Na_v1.7$, seeking to better understand the role of its regulation by Ca^{2+} and CaM, using various techniques such as ELISA, isothermal titration calorimetry (ITC) and Bio-Layer interferometry (BLI). The CTDs and CaM recombinant proteins were cloned using the Gateway cloning method, expressed in BL21 (DE3) cells using auto-induction, and purified via affinity chromatography and size exclusion chromatography. Also, attempts were made to determine the yet unresolved structure of $Na_v1.7$ using x-ray crystallography. Finally, using an in-house phage display library of single chain fragment variable (scFv) antibodies, specific binders to the CTD of $Na_v1.5$ and $Na_v1.7$, were found and purified. These scFvs could have gating effects on their Na_v channel targets, which might prove therapeutically applicable.

Acknowledgments

Alhamdulillah! This PhD would not have been possible without the help and support from many individuals. Firstly, I would like to whole-heartedly thank my supervisors, Prof. Christopher Huang and Dr. Tony Jackson, for their support during this project. From day 1 of my arrival in Cambridge, Chris, with his ever cheerful and warm welcome, made me feel at home. Without the encouragement, advice, and inspiration from Chris, especially with the electrophysiology work and administrative tasks, it would have been near impossible for me to navigate my way through this PhD journey. Tony, likewise, has been instrumental at guiding me through my molecular biology work. His timely inputs and advice helped mould my project to what it is now. I am also very thankful to Prof. Ming Lei (University of Oxford), for providing me with a great reference and introducing me to Chris, which eventually lead me to applying for this PhD position. Ming also provided me with some essential plasmids which I used in this project.

I am also very grateful to Dr. Samantha Salvage for training and assisting me with the whole-cell patch clamp, site-directed mutagenesis, confocal microscopy, and Western Blotting. She was always available for a quick consult and readily provided help whenever I needed it. Similarly, Dr. Johanna Rees helped a lot with any query I had regarding any molecular biology work. I would also like to thank Dr. Samir Hamaia, for introducing me to the world of single chain antibody phage display. With his ever-infectious enthusiasm, wit and warmth, Samir has single-handedly re-directed my research interest, for which I am ever grateful. I am also thankful to all the members of Chris and Tony's lab, who provided me with help from time to time, including Manas Kohli, Roshni Mistry and Hengrui Liu. I am particularly, very thankful to Manas Kohli for finding interest in my project and performing the MD simulation work along with Dr. Taufiq Rahman. In Dr. Taufiq, not only did I find a great research collaborator, but also an affectionate mentor, who, whenever I required, provided me with his time and advice. During my project I have also collaborated with Prof. Sir Tom Blundell and Dr. S. M. Arif, who helped me immensely with my x-ray crystallography work. I am also thankful to Dr. Katherine Stott, who, with utmost care, assisted and trained me with the protein-protein interaction studies (ITC, BLI).

I am also grateful to the members of the Prof. Guy Brown and Prof. Sarah Lummis's lab, who from time to time helped me with reagents and useful tips. It was wonderful sharing lab space with them.

I would also like to acknowledge Islamic Development Bank (IsDB) and Cambridge Trust for funding this studentship and the research bench fees. I have also received great support, for which I am very grateful, from my college tutor, Dr. Hilary Marlow and department advisor, Dr. Hugh Matthews. I would also like to thank Aileen Briggs, for assistance with all the administrative work.

Finally, I would also like to thank my friends here at Cambridge, who made staying away from home, a lot more bearable. Last but not the least, I would like to thank my incredible family for their unconditional love and support; in particular my parents and sister for never losing faith in me to complete my PhD and always pushing me to aim for the best; also my loving wife, Shafia, for being there beside me through all the ups and downs and providing me with a shoulder to lean on during my darkest hours and gifting me with a beautiful baby boy, Safeer, who filled both our hearts with boundless love and joy.

Publications

1. Salvage SC, **Habib ZF**, Matthews HR, Jackson AP, Huang CLH. Ca2+-dependent modulation of voltage-gated myocyte sodium channels. *Biochem Soc Trans*. October 2021; 10.1042/BST20200604.

2. **Habib ZF**, Kohli M, Salvage SC, Rahman T, Huang CL-H, Jackson AP. Pathological turret mutations in the cardiac sodium channel cause long-range pore disruption. *bioRxiv*. January 2021; 2021.01.15.426807.

3. Salvage SC, Zhu W, **Habib ZF**, Hwang SS, Irons JR, Huang CLH, Silva JR, Jackson AP. Gating control of the cardiac sodium channel Nav1.5 by its β3-subunit involves distinct roles for a transmembrane glutamic acid and the extracellular domain. *J Biol Chem*. December 2019; 294(51):19752-19763.

Abbreviations

BLI	Bio-layer interferometry
ßME	ß-mercaptoethanol
BrS	Brugada syndrome
BSA	Bovine serum albumin
Ca^{2+}	Calcium ion
CaM	Calmodulin
Ca_V	Voltage-gated calcium ion channel
CHO	Chinese hamster ovary cells
CNS	Central nervous system
CryoEM	Cryogenic electron microscopy
CTD	C-terminal domain
DEKA	Aspartic acid, glutamic acid, lysine, and alanine residues forming the selectivity ring of Na_V
DMEM	Dulbecco's modified Eagle's medium
DNA	Deoxyribonucleic acid
DS	Dravet syndrome
DTT	Dithiothreitol
ECG	Electrocardiogram
EDTA	Ethylenedinitrilotetraacetic acid
EGFP	Enhanced green fluorescent protein
EGTA	Ethylene glycol tetraacetic acid
EIEE	Early infantile epileptic encephalopathy
ELISA	Enzyme-linked immunosorbent assay
FGF13	Fibroblast growth factor 13
GEFS+	Generalized epilepsy with febrile seizures plus
HEK293	Human embryonic kidney 293 cells
$hNa_V1.5$	Human voltage-gated sodium ion channel protein type 5 α subunit
HwTX	Huwentoxin

IC_{50}	Half maximal inhibitory concentration
ICEGTC	Intractable childhood epilepsy with generalized tonic-clonic seizures
IFM	Isoleucine, phenylalanine, and methionine motif, part of the inactivation gate of Na_v
I_{Na}	Sodium current
iPSC-CM	Induced pluripotent stem cell derived cardiomyocytes
ITC	Isothermal titration calorimetry
I_{to}	Transient outward potassium current
K^+	Potassium ion
K_v	Voltage-gated potassium ion channel
LB	Luria Broth
LQT3	Long QT syndrome type 3
mAb	Monoclonal antibody
MD	Molecular dynamics
Na^+	Sodium ion
Na_v	Voltage-gated sodium ion channel protein α subunit
PCR	Polymerase chain reaction
PEI	Polyethylenimine
P-loops	Pore loops
ProTX	Protoxin
rNa_v1.5	Rat voltage-gated sodium ion channel protein type 5 α subunit
rpm	Rotation per minute
rtp	Room temperature and pressure
RVOT	Right ventricular outflow tract
RyR	Ryanodine receptor
scFv	Single chain fragment variable antibody
SCN3B	Gene encoding human ß-subunit of Na_v1.5 protein
SCN5A	Gene encoding human Na_v1.5 protein
Scn5a	Gene encoding mice Na_v1.5 protein
SIDS	Sudden infant death syndrome

SND	Sinus node dysfunction
SSS	Sick sinus syndrome
STX	Saxitoxin
TTX	Tetrodotoxin
$V_{1/2}$	Voltage of half-maximal activation or inactivation
WT	Wild-type

List of Figures

List of Tables

Table of Contents

Chapter 1

Introduction

1. General Introduction

Voltage-gated sodium ion channels (Na_v) are central to action potential initiation through regulating entry of sodium ions (Na^+) into excitable cells to cause cell membrane depolarization, which increases the membrane potential to up to +30 mV from the resting potential of about -40 to -90 mV. The membrane potential at which the action potential is initiated is called the threshold. Depolarization is followed by the repolarization phase caused by the efflux of potassium ions (K^+) which brings the potential back to the resting potential. Hodgkin and Huxley were the first to record and analyse the depolarizing Na^+ currents in giant squid axon membranes under voltage clamp. Subsequent biochemical studies have isolated the underlying principal α subunit (~260 kDa) of the Na_v channel protein with the aid of photoreactive α-scorpion toxin labeling[1,2]. Na_v channels are found in all higher animals including mammals, birds, reptiles, fish, and amphibians. The human Na_v channel (hNa_v) α subunit exists as a variety of isoforms of which $hNa_v1.1$, $hNa_v1.2$, $hNa_v1.3$ and $hNa_v1.6$ are expressed predominantly in human central nervous system, $hNa_v1.4$ and $hNa_v1.7$ in the peripheral nervous system, $hNa_v1.4$ and $hNa_v1.5$ in skeletal muscle, $hNa_v1.5$ in the heart and $hNa_v1.8$ and $hNa_v1.9$ in dorsal root ganglia [3-6]. Na_v2, another class of voltage-gated Na^+ ion channels with possible role in management of salt intake are also found in mammals [7-9]. The amino acid sequence homology between the Na_v1 and Na_v2 are less than 50%.

1.1 Na_v evolutionary history

Na_v is the most recently evolved ion channel within a superfamily of ion channels, which includes voltage-gated calcium channels (Ca_v), voltage-gated potassium channels (K_v), Trp-related channels and cyclic-nucleotide-gated channels (CNG)[10]. One theory arising from phylogenic analysis suggests that Na_v evolved from four homologous domain consisting of Ca_v which in turned evolved from single domain tetrameric K_v within two rounds of gene duplication and many single base mutations. Appearance of Na_v can be traced back to the same time metazoans, including cnidarians, evolved to have specialized neurons with exclusive Na^+ dependent action potentials[11]. Another theory asserts that Na_v and Ca_v arose from a prokaryotic single domain voltage dependent Na^+ channel, NaChBac, as found in Bacillus halodurans. This channel shows selectivity for Na^+ ions, but due to its similarity to Ca_v channel

especially in the pore region (with four glutamates forming a symmetric selectivity filter), it can be blocked by calcium channel blockers[12]. NaChBac however lacks an inactivation gate and hence has much slower rate of inactivation compared to Na_v. Similarities in gene sequence, selectivity to Na^+ ion, gating properties, and pharmacology between Na^+ ion channels found in invertebrates (like flies and jellyfish) and vertebrates (like humans) suggest that the first functioning Na_v was formed before the divergence of vertebrates and invertebrates. A third theory suggests that both four domain (Na_v and Ca_v) and one domain (K_v) six transmembrane channels arose from CNGs. The pore region of CNGs is very similar to the K_v channel while its one domain resembles the voltage sensing S4 helix found in all three voltage gated channels. CNGs allow both monovalent and divalent cations to pass through their pores, making them strong contenders to be precursors for both Na_v and Ca_v channels[13].

Employing a maximum parsimony assumption to generate a phylogenic tree of Na_v isoforms, groups them into distinct clusters defined by sequence homology, tetrodotoxin sensitivity and gene location. For instance, the tetrodotoxin (TTX) sensitive (nM concentration) group of Na_v which are mainly expressed in neurons, consisting of $Na_v1.1$, $Na_v1.2$, $Na_v1.3$ and $Na_v1.7$ all have their genes located on human chromosome 2q23–24. In contrast, the TTX resistant (μM concentration) isoforms which are mainly expressed in the heart and dorsal root ganglion, consisting of $Na_v1.5$, $Na_v1.8$ and $Na_v1.9$, although sharing amino acid sequence homology of more than 74% with TTX sensitive isoforms, have their genes located on human chromosome 3p21–24. $Na_v1.4$ (skeletal muscle) and $Na_v1.6$ (CNS), share 84% identical amino acid sequence with the TTX sensitive Na_v isoforms even though their distant location on human chromosome, 17q23–25 and 12q13 respectively, suggest distant evolutionary relationships[14,15]. Interestingly, resistance to TTX is conferred upon Na_v isoforms due to one single amino change in pore region of domain I, from phenylalanine to cysteine in $Na_v1.5$ and from phenylalanine to serine in $Na_v1.8$ and $Na_v1.9$[16].

1.2 Available structures of the Na_v, including the CTD

Until atomic resolution structures of mammalian Na_v channels became available, crystal structures of Na_v from other species served as useful guides to the relationships between channel function and structure. These include Na_v from the

bacterium Arcobacter butzleri[17], marine alphaproteobacterium HIMB11412 and marine bacterium Magnetococcus sp.[18]. These prokaryotic Na_v channels similarly form four tetramers, but these are identical subunits in contrast to the homologous but non-identical eukaryotic Na_v tetramers[19]. However, although these prokaryotic channels are popular models for studying molecular mechanisms of gating behaviour, such extrapolations need to consider the separate phylogenetic origins of the eukaryotic and prokaryotic Na^+ selective ion channel families[20]. Moreover, eukaryotic Na_v channels show both fast and slow inactivation, whereas the prokaryotic Na_v show a single inactivation process that resembles slow inactivation in eukaryotic Na_v[12,21,22]. More recently published near-atomic resolution eukaryotic Na_v structures from American cockroach (Periplaneta americana)[23] and electric eel (Electrophorus electricus)[24] provide models which more accurately mimic mammalian Na_v channel physiology and allow more reliable 3D modelling studies of Na_v.

The first human Na_v channel structure to be solved was that of $Na_v1.4$ in complex with the ß1 subunit[25]. Currently, cryoEM structures of $Na_v1.5$ and $Na_v1.7$ are also available which makes it possible to study structure guided hypothesis[26–28].

1.3 Na_v channel structure and gating mechanism

The principal α subunits of human voltage-gated sodium ion channels contain four homologous domains (DI-IV). Each domain contains six transmembrane alpha-helices each connected by extracellular or intracellular loops of varying lengths (Figure 1.1). Helices S5 and S6 from each domain are symmetrically arranged forming the pore at the centre. The extracellular pore-loops that connect the S5 and S6 helices within each domain, defined as pore-loops (P-loop), extend over the pore forming a turret-like structure and play a role in ion selectivity and permeation [29]. This turret region is glycosylated and contains highly conserved cysteines taking part in disulphide bonds[23]. P-loops (P1 and P2) of each domain re-entering membrane segments (membrane descending P1 and membrane ascending P2) assemble into an inverted and truncated cone-like structure. At its narrowest point lie the highly conserved residues forming an asymmetric high field strength site: Asp (DI); Glu (DII); Lys (DIII) and Ala (DIV) (Fig.1B). These form the DEKA selectivity ring, whose sequence and geometry are critical for selective Na^+ ion permeability and preventing permeation of other positive charges like potassium and calcium[30].

Helices S1-4 of each domain form the voltage-sensors and lie on the channel periphery (Figure 1.1, Figure 1.2). One face of the S4 of all the domains contain 4 to 8 repeats of positively charged amino acid residues (arginine or lysine), neutralized by ionic bonding with negatively charged residues on the S1-3 helices. These become displaced in the extracellular direction, by around 10 Å with a 30° rotation and tilt, in response to membrane depolarization[31]. In the resting state, these positive charges are displaced inwards, towards the intracellular membrane face, by the relative negative potential of the cytoplasm. Membrane depolarization results in a positive shift in the cytoplasmic potential, driving a movement of the positive charges in the opposite direction. This initiates a conformational change that widens the pore 'activation gate' on the intracellular face permitting transmembrane Na^+ ion entry into the cell [32]. This sliding helix or screw-helical model is backed by fluorescent labelling experiments and mutagenesis studies on prokaryotic Na_V channels[33–36]. Moreover, comparison between the 0 mV inactivated states of the recently determined cryo-EM structures of human Na_V and the resting state structure of Na_VAB, provides further support to the sliding helix model as positions of the S4 helix can be accurately ascertained and compared[28,37]. It has been additionally suggested that the inner region of the S4 helix can stretch by adopting high energy 3_{10} helix due to depolarization, providing the energy needed for the conformation change required to open the pore[31,38,39]. This has also been confirmed by a mesoscale simulation which determined the functional consequences of the sliding S4 helix[40].

The DI-DIII voltage sensors respond relatively rapidly to membrane depolarization and initiate channel activation whereas the voltage sensors of DIV respond more slowly and initiate the movement of the intracellular region connecting DIII-S6 to DIV-S1 (consisting of the highly conserved Ile/Phe/Met (IFM) motif) which acts as an inactivation gate, blocks the pore and initiates the early inactivation phase of the action potential [37,41]. As the resting potential is restored, all four S4 helices return to their original positions and the inactivated channel is reset into the closed, resting state, where it can again respond to further depolarization signals after a refractory period[38].

Slow inactivation of Na_V reduces the inward Na^+ current in response to prolonged depolarization (seconds to minutes). It is distinct from fast inactivation which occurs due to the DIII-DIV linker blocking the pore. Removal of the DIII-DIV linker or mutating the IFM motif to QQQ residues abolishes fast inactivation. However, the slow

inactivation phenomenon persists and indeed becomes more marked. It has been suggested that slow inactivation occurs as the pore collapses in on itself as the S4 helix of the voltage sensors keep getting pushed outwards due to prolonged depolarization. Recovery from this state takes much longer than the corresponding recovery from fast inactivation[42].

1.4 Post-translational modifications of Na_v channels

Na_v channel α-subunits have multiple glycosylation sites, the majority of which are sialic acids[43]. These large carbohydrates impart local negative charge which influences the overall channel gating. Thus, when neuramidase or recombinant deletion of likely glycosylation sites is used to remove sialic acid from the surface of the rat Na_v channel, it produces a 10 mV depolarizing shift in the steady-state voltage dependence of activation[44]. Interestingly, shifts in channel activation and inactivation properties were observed in $Na_v1.4$, but not $Na_v1.5$ channels, when these were expressed in cells which lack sialylation capability[43]. It has also been reported that $Na_v1.9$ is more glycosylated in neonatal than in adult DRG neurons [45]. ß-subunits also contain up to four N-linked glycosylation sites on their respective extracellular Ig domains. This has been demonstrated in the solved ß3 crystal structure[46]. ß-subunits also show phosphorylation to extents that vary with their cardiomyocyte localization. Phosphorylated ß1 localizes at the intercalated discs with connexin-43, N-caderin and $Na_v1.5$ whereas non-phosphorylated is localized with ankyrinB in the T-tubules[47].

1.5 Na_v channel auxiliary subunits

Na_v channels are also associated with auxiliary ß subunits, which are of four types ß1-4, and interact closely with the α subunit in some tissues [14]. ß subunits each consist of a single extracellular immunoglobulin (Ig) domain, and a single transmembrane alpha-helix (Figure 1.2). They modulate gating kinetics, voltage sensitivity and membrane trafficking of the Na_v channel α subunits, although the α subunit alone can fully function as an ion channel without the co-expression of the ß subunits [48]. Generally, ß subunits augment the overall activity of the Na_v channel by increasing rates of activation, inactivation and recovery from inactivation [49]. Ig domains of ß2 and ß4 subunits are similar in structure and sequence and bind with the α subunit through covalent interactions (disulphide bond) on the DII S5-S6 extracellular loop region [50,51]. The ß1 subunit is reported to bind non-covalently to

DI and DIV S5-S6 loop of α subunit; however the, ß3 binding site is yet to be resolved [52]. Some reports suggest that ß3 can form trimers and link multiple α subunits to form much larger oligomers [46]. α- α subunit dimer formation in absence of ß subunits has also been observed, however, it has been postulated that ß subunits would induce larger oligomerization [53].

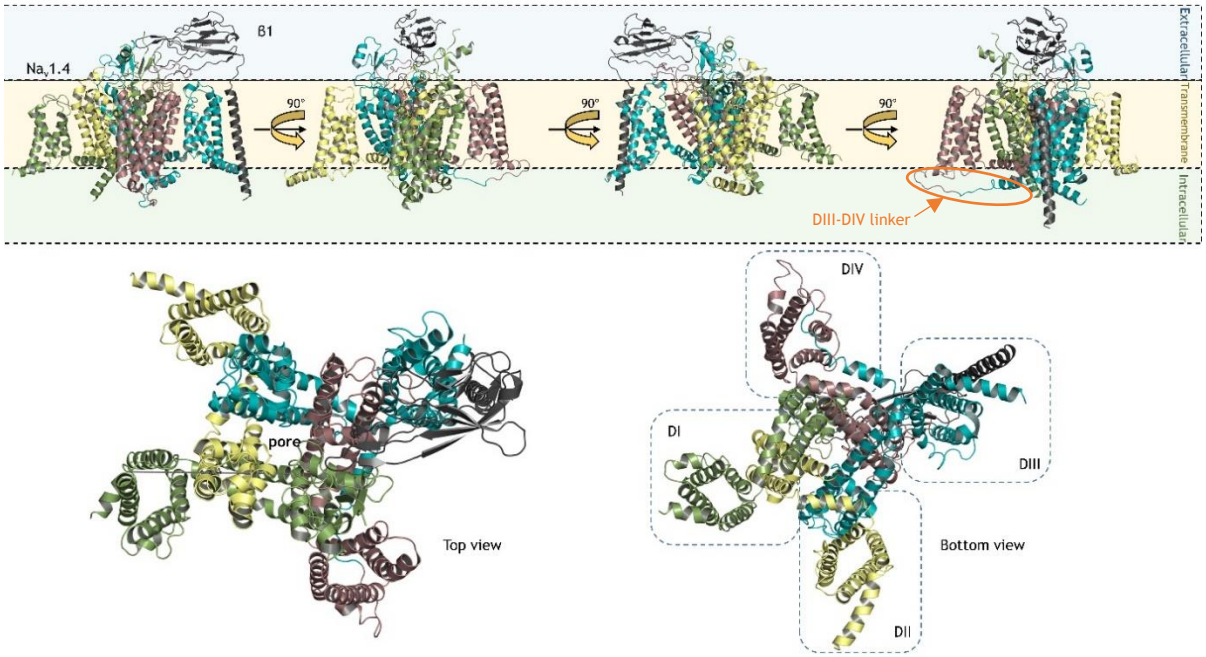

Figure 1.1. A cartoon representation of the crystal structure of human voltage-gated sodium channel (Na$_v$1.4) and associated ß1 subunit (PDB ID: 6agf).

(A) Topology of Na$_v$ and ß1 from the side. **(B)** Top and bottom view of the same channel showing the central ion-selective pore and four domains, each coloured differently, that surround it.

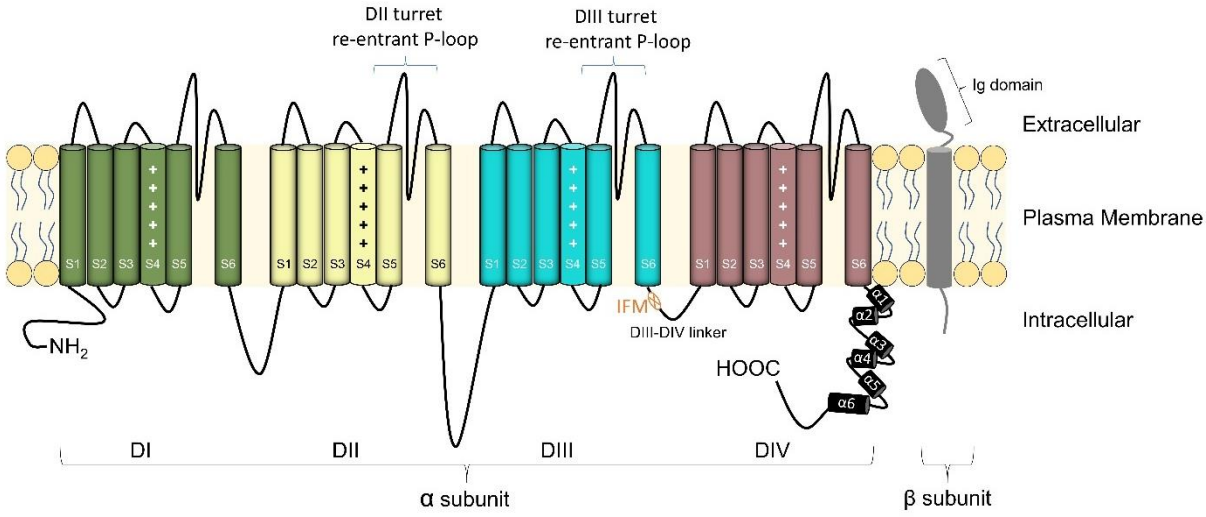

Figure 1.2 Schematic representation of the voltage gated Na$_v$ channel and ß subunit.

DI-DIV demonstrate the four homologous domains of the α-subunit, colour-coded to match Figure 1.1. The helices S5 and S6 line the pore of the channel, and the S4 helices function as the voltage sensor with the run of positive charges. The DIII-DIV linker and the inactivation gate (IFM motif) is also indicated. The C-terminal domain with six α-helices at the start are labelled accordingly. The ß-subunit and its extracellular Ig-domain connected by a flexible linker is also portrayed.

1.6 Channelopathies

As discussed above, voltage gated Na^+ ion channels occur extensively in the human body. In this section their most common associated channelopathies will be briefly discussed. Focus will also be given to the disease-related mutations in the extracellular turret region and the c-terminal domain region. It must be noted that a more recent recommendation by the American College of Medical Genetics and Genomics and the Association for Molecular Pathology to classify genetic mutations as 'pathogenic', 'likely pathogenic', 'uncertain significance', 'likely benign', and 'benign', has not been adopted here. This classification of variants is based on population data, computational and predictive data, functional data, segregation data, de novo data, and allelic data[54]. Although this represents a more robust standard of classification, for the purposes of purely functional analysis on some variants in this study, the older classification can still be used as a reference.

$Na_v1.1$

Mutations in the SCN1A gene encoding $Na_v1.1$ are associated with various pathologies including generalized epilepsy with febrile seizures plus (GEFS+), Dravet syndrome (DS), intractable childhood epilepsy with generalized tonic-clonic seizures (ICEGTC), familial hemiplegic migraine and familial febrile seizures. Mutations leading to DS are reported much more frequently in the literature compared to the others (Table 1.1, Table 1.2).

Dravet Syndrome (DS)

Dravet syndrome, previously known as severe myoclonic epilepsy of infancy, causes a severe form of childhood epilepsy. It is characterized by prolonged intractable seizures (up to or longer than 30 minutes) usually resistant to anti-epileptic medications and leading to premature death. One in 40,000 children are affected by this syndrome before reaching the age of 7 years, although in most cases it appears at some point during the first year of life[55,56]. Over the course of the disease, ataxia, gradual cognitive impairment accompanied by autistic traits and hyperactivity develop[57,58]. *De novo,* heterozygous, autosomal dominant, loss of function mutations in the SCN1A gene, which encodes for the $Na_v1.1$ channel, are implicated in more than 90% of DS cases[59,60]. Homozygous recessive mutations in SCN1B, which encodes for the ß1 subunit, can also cause DS, for example R125C, which is shown to

significantly reduce $Na_v1.1$ channel localization in plasma membrane[61]. Also, mutations in SCN2A gene, which encodes for $Na_v1.2$, for example R1312T causes DS[62]. Mutations in other genes with clinical features resembling DS have also been widely reported, which include KCNA2 (voltage gated potassium channel $K_v1.2$), HCN1 (potassium/sodium hyperpolarization-activated cyclic nucleotide-gated channel 1), CHD2 (chromodomain helicase DNA-binding protein 2), STXBP1 (syntaxin-binding protein 1), GABRG2 (γ2 subunit of $GABA_A$), PCDH19 (protocadherin-19), SCN8A ($Na_v1.6$) and SCN9A ($Na_v1.7$)[63-70]. In a study conducted by Ohmori, 24 of the 29 patients with mutations causing DS were mutations also found in Generalized Epilepsy with Febrile Seizure plus (GEFS+)[71]. Interestingly, animal models of DS show a very similar phenotype to humans with DS, like severe ataxia, spontaneous seizures, hyperactivity, and cognitive impairment. Both Scn1a -/- and Scn1a +/- mice showed normal gating behaviours in Na_vs in hippocampal neurons but exhibited reduced current density in inhibitory GABAergic interneurons. In another report, Scn1a +/- mice seizures developed were caused by increase in body temperature[72,73].

$Na_v1.2$

Mutations in the turret region of $Na_v1.2$ have been reported in cases of benign familial infantile seizure and developmental and epileptic encephalopathy (Table 1.1, Table 1.2). G211D and N212D mutations have been observed to eventually progress to West syndrome characterized by severe hypotonia. Patients with the K908E mutations had difficult to treat seizure for the first 3-12 months of life and when studied under whole cell patch clamp (mutant channel transfected in tsA201 cell), it showed 1.8-fold increase in current density with no change in other steady-state parameters.

In the CTD, R1882Q is implicated in early infantile epileptic encephalopathy (EIEE) caused by increased neuronal activity because of increase in peak Na^+ current density.

$Na_v1.3$

No known mutations in the extracellular turret region linked to any diseased phenotype is reported in literature. In CTD two mutations are reported, K1799Q and G1862C, causing early infantile epileptic encephalopathy and cryptogenic partial epilepsy respectively (Table 1.2).

$Na_v1.4$

Turret mutations in $Na_v1.4$ can cause periodic paralysis presenting as skeletal muscle stiffness in response to changes in temperature (L1433R and L1436P) and the opposite effect of myasthenic syndrome of a failure of skeletal muscle contraction (V1442E). The V1442E-$Na_v1.4$ that causes the myasthenic syndrome, its corresponding amino acid mutation in V1630L-$Na_v1.1$ and V1630M-$Na_v1.1$ are linked to Dravet syndrome. Moreover, a deletion of the corresponding residue in delF1617-$Na_v1.5$ is strangely implicated in both Brugada syndrome and Long QT syndrome. The pronounced effect due to this mutation could be due to its location right above the voltage sensing S4 helix of DIV. When transfected in HEK293 cells and studied on voltage clamp, V1442E showed significantly faster inactivation which is close to resting potential, and increased use-dependent inactivation on high-frequency stimulation.

Q1633E-$Na_v1.4$ and its corresponding Q1801E-$Na_v1.6$ cause myotonia and EIEE respectively. Q1633E produces a slower rate of current decay while F705I which causes paramyotonia congenita of von Eulenburg produces significant slowing down of fast inactivation.

$Na_v1.5$

Mutations in SCN5A which encodes for $Na_v1.5$ are generally associated with cardiac pathologies like progressive familial heart block 1A, Long QT syndrome type 3 (LQT3), Brugada syndrome 1 (BrS), Sick sinus syndrome 1 (SSS), familial paroxysmal ventricular fibrillation 1, sudden infant death syndrome (SIDS), atrial standstill 1, dilated cardiomyopathy 1E and familial atrial fibrillation 10 (Table 1.1, Table 1.2).

Brugada syndrome (BrS)

BrS is an inherited disease with autosomal dominant traits causing loss of function of the $Na_v1.5$ channel. Clinically, BrS is associated with ventricular tachyarrhythmias that may lead to syncope, cardiac arrest and sudden cardiac death[74]. Three different Electrocardiograms (ECG) patterns can be observed in BrS patients. Type 1 shows a persistent coved-type ST segment elevation with a high J point and an inverted T wave[75,76]. These high J points are also associated with early repolarization and is the result of a transmural voltage gradient in the epicardium created by the transient

outward potassium current (I_{to}). This gradient is the largest in the right ventricular outflow tract (RVOT), which explains why BrS is a right ventricular disease. Interestingly RVOT shows reduced gap junction and Na_v expression, which most likely contributes to the gradient difference[77,78]. In type 2 the amplitude of the ST segment elevation is ≥2 mm and shaped like a saddle-back whereas in type 3 the shape can be either coved or saddle-back but the amplitude is < 2mm. Minor conduction delay is observed at all cardiac levels for all types indicated by PR prolongation and QRS complex broadening, especially observed in one-fifth of all mutations that cause BrS and are involved in the loss of function of Na_v[79,80]. For the diagnosis of BrS, observance of a type 1 ECG is mandatory. Alternatively, if type 2 or 3 ECG pattern is observed, the patient can be challenged with Na_v channel blockers which, if BrS is indeed present, will convert the ECG pattern to type 1[81,82]. Na_v channel blockers generally always worsen the BrS. For instance lidocaine induced BrS was reported in a patient with V232I and L1308F mutations in the SCN5A gene[83]. However, quinidine is reported to have beneficial effects on BrS patients in addition to some inotropic drugs, cilostazol and milrinone[82,84]. BrS patients with type 1 ECG and if deemed highly susceptible to malignant arrhythmias can benefit from implantable cardioverter-defibrillator and/or epicardial ablation of the RVOT consisting of the arrhythmogenic substrate[85].

Mutations causing BrS mostly occur in the transmembrane region of $Na_v1.5$ although mutations in the ß3 subunit (L10P) have also been implicated in BrS, possibly by interfering with $Na_v1.5$ expression and plasma membrane trafficking thereby decreasing cardiac Na_v channel current [86]. BrS-related mutations are also associated with familial atrial fibrillation, confirming its overall importance in $Na_v1.5$ physiology and function [87].

Although more than 90% of the genetic mutations found in BrS patients are in the SCN5A gene, other genes which are susceptible to mutations leading to BrS include GPD1L (glycerol-3-phosphate dehydrogenase 1-like), CACNB2 (calcium channel, voltage-dependent, beta-2 subunit), CACNA1C (calcium channel, voltage-dependent, l type, alpha-1c subunit), SCN1B and SCN3B (Na_v channel ß-subunit 1 and 3), KCNE2, KCNE3 and KCNE4 (potassium channel, voltage-gated, isk-related subfamily, member 2, 3 and 4), and IRX5 (iroquois homeobox protein 5). More recent genome-wide association analyses shows a strong polygenic effect of single nucleotide polymorphism heritability and also identified a predominance of cardiac

transcription factors loci in BrS patients, suggesting that dysregulation of transcription is a key feature in the pathogenesis of BrS. A new molecular mechanism which involves effect on trafficking of Na_v due to defective binding to microtubule plus-end binding protein EB2, has also been uncovered[88].

Heterozygous knockout mice, Scn5a+/−, have been used to model BrS. These knockout mice showed approximately 50% reduction in Na_v channel expression, re-entrant arrhythmias such as tachycardia and conduction block although the QT interval remained indistinguishable from WT. So, Scn5a+/− mice could not be considered solely to represent BrS but rather a mix of cardiac pathologies. The abnormal conduction, ventricular arrhythmias and ST segment elevation observed in these mice were also shown to worsen with the use of flecainide[89,90]. More studies on the Scn5a+/− mice heart revealed that mRNA and Na_v channel protein expression were significantly lower in these mice compared to WT in addition to increase in fibrotic tissue[91]. An attempt to study homozygous knockout mice, Scn5a-/-, has been unsuccessful since it proved to be lethal to embryonic development due to major abnormalities in structure of the heart.

BrS disproportionately affects males, with females being nearly 10 times less likely to be symptomatic despite possessing the same underlying mutations as males causing BrS. Canine models of BrS pins this down to lower density of I_{to}, a small transient outward potassium current, in females compared to males[92,93].

Expression systems, like HEK293 cells (human embryonic kidney), CHO cells (Chinese hamster ovary) and tsA201 (SV transformed), transfected with plasmids containing genes which express BrS mutations identified in the clinical literature has also been extensively used to characterize and explain BrS. As expected, all studies report a loss of function of the Na_v channels consisting of BrS causing mutations, either due to reduction in number of Na_v channels in the cell surface membrane which reduces current density, positive shifts in activation and/or negative shifts in inactivation.

More recently, induced pluripotent stem cell derived cardiomyocytes (iPSC-CM) have been used to study BrS. This system has the advantage of considering the effects of $Na_v1.5$ regulatory proteins on gating parameters which HEK293 and tSA201 cells lack. Also, CRISPR/Cas9 mediated genome editing can be employed to study effects of BrS causing mutants. The disadvantage however is that iPSC derived cardiomyocytes display an immature phenotype, representative more of the fetal than the adult

cardiomyocytes. Literature consists of several use of this technology to characterize BrS mutants which confirm results obtained from other model systems[94–97].

The mutations in the turret region are variously associated with both the loss of function Brugada Syndrome (BrS) and gain of function Long QT syndrome (LQT3) in addition to progressive familial heart block and atrial fibrillation. In this study we investigated the following mutations R878C, R878H, D1430N and E1441Q, all of which were naturally found in patients with BrS[80,98]. Under voltage clamp, all these mutated channels showed no activity. In the case of D1430N it was confirmed not to be a trafficking defect as channel activity was still not observed by treatment with mexiletine or lidocaine at low temperature. Moreover, all these mutants were studied with immunostaining which showed membrane localization comparable to that of WT. A lot of the mutants which cause BrS are found to be due to decrease in the number of channels available on the surface hence decreasing/abolishing Na^+ current density, exemplified by D1690N and G1743R[99,100]. Sometimes trafficking defects are also accompanied by changes in activation and inactivation properties as in the case with G1748D[99].

In the case of LQT3, most of the mutations studied cause gain of function by positive shifts in $V_{1/2}$ of steady state activation and inactivation for example E1295K[101].

Interestingly, some mutations for e.g., at C-terminal domain Y1795, if mutated to cysteine causes LQT3 and atrial fibrillation with slowed onset of inactivation and increased sustained current; whereas mutations to histidine causes BrS with accelerated onset of inactivation and reduced peak current[102]. There have also been cases of the same mutant being ascribed to both BrS and LQT3 like T1779M and E1784K[80,103]. Some mutations on the CTD can also inhibit interaction with FGF12,13 and/or 14 like H1849R which slower steady state inactivation, prolonging action potential duration and showing LQT3 phenotype[104]. R1232W causes both BrS and progressive familial heart block[80,105,106]. The mutation G298S in addition to causing heart block is also associated with irritable bowel syndrome and is shown to cause delay in activation kinetics with an overall reduction in current density[107,108].

$Na_v1.6$

Mutations in the turret regions caused severe developmental delays even though patients responded well to treatment (Table 1.1). The P1719R-$Na_v1.6$ mutation

which causes familial myoclonus behaves very similar to the turret mutations on $Na_v1.5$ studied in our project, which primarily showed reduction in peak current density and relatively less significant effect on gating parameters[109]. A missense mutation in the same proline residue in $Na_v1.1$, P1739L, is implicated in generalized epilepsy with febrile seizures[110].

Moreover, I1605R-$Na_v1.6$ and its corresponding mutation in $Na_v1.4$ (L1436P) are both implicated in disease phenotypes namely epileptic encephalopathy and paramyotonia respectively. The patient with the I1605R had refractory epilepsy but remained seizure-free on Carbamazepine for 17 years[70].

Similarly equivalent mutations of N215R-$Na_v1.6$ and V216D-$Na_v1.6$ in $Na_v1.2$ (N212D and V213D respectively) cause developmental and epileptic encephalopathy in all the cases. It appears that in these two positions in domain I, replacement of the amino acid residue with any charged residues causes diseased phenotypes. Both the patients with N215R and V216D although having seizures very early on in their life, eventually became seizure free within 6 years of age[70,111].

In addition, in the CTD mutations in $Na_v1.6$ mostly trigger gain of function by increased channel activity and impaired channel inactivation (Table 1.2). Also, corresponding mutations N1768D-$Na_v1.6$ and N1788K-$Na_v1.1$ both are found in EIEE patients[112].

$Na_v1.7$

Congenital insensitivity to pain is the only disease associated with turret mutations in $Na_v1.7$ (Table 1.1). R907Q is the same arginine residue mutation as R878C in $Na_v1.5$, which also shows no current on voltage clamp[113]. Also, the corresponding arginine residue in $Na_v1.1$ mutation R931C causes Dravet Syndrome[71]. However, the channel localization of R878C-$Na_v1.5$ remains unaffected. Another interesting observation is that insensitivity to pain traditionally has been observed on truncated proteins which most likely lead to no $Na_v1.7$ protein production. The only two mutations found as an exception to this rule are those mentioned in Table 1.1 and both occur in the extracellular turret region near the pore but not in more critical places like the voltage sensing domains, activation gate or the pore itself. Both the

R907Q and del1382-1385 mutations cause a significant reduction in quantity of channel available on membrane compared to WT and voltage clamp with mutant transfected HEK293 cells, show no channel activity[113].

$Na_v1.8$

No mutations associated with disease are found in literature.

$Na_v1.9$

Although implicated in neuropathy and episodic pain syndrome no mutations in the extracellular turret region or the CTD associated with disease are found in literature.

Table 1.1. Mutations in the extracellular turret region related to diseased phenotypes in all the Na_v subtypes

Disease	Mutation (Domain)	References
$Na_v1.1$		
Generalized epilepsy with febrile seizures	Y790C (DII)	114
	N935H (DII)	115
	M960T (DII)	110
	K1249N (DIII)	116
	T1250M (DIII)	116
	L1309F (DIII)	117
	N1414D (DIII)	110
	P1739L (DIV)	110
	D1742G (DIV)	118
Dravet syndrome (severe myoclonic epilepsy of infancy)	C277R (DI)	119
	W280C W280R (DI)	120-123
	P281A P281L P281S (DI)	119,123
	E289V (DI)	124
	T297I (DI)	121
	R322I (DI)	119,125
	S340F (DI)	119
	A342V (DI)	110
	G343D (DI)	110,119,126
	C345R (DI)	119
	C351W (DI)	110
	G355D (DI)	119
	R356G (DI)	125
	N357I (DI)	119

	P358T (DI)	125
	N359S (DI)	110,127
	T363P T363R (DI)	110,123
	D366E (DI)	128
	R393C R393H R393S (DII)	59,110,123-125,129-131
	del854-855	110
	C927F (DII)	119
	R931C (DII)	71,119
	W932C (DII)	110
	H933P (DII)	110
	M934I (DII)	119,123,132
	C959R (DII)	59,129
	M960V (DII)	126
	E1238D (DIII)	110,133-135
	D1239G D1239Y (DIII)	119
	R1245Q (DIII)	122
	N1367K (DIII)	119,136
	A1370P (DIII)	110
	N1378H N1378T (DIII)	110
	F1385V (DIII)	123
	V1390M (DIII)	71,130,134
	N1391S (DIII)	119
	H1393P (DIII)	137
	T1394I (DIII)	110
	C1396G C1396Y (DIII)	133,134,138
	N1414Y (DIII)	125
	D1416G (DIII)	119
	N1417S (DIII)	110
	V1418G (DIII)	123
	A1441P (DIII)	134
	Q1450K Q1450R (DIII)	71,110,138
	P1451L P1451S (DIII)	110,122
	Y1453C (DIII)	123
	E1454K (DIII)	110
	E1561K (DIV)	119
	V1630L V1630M (DIV)	123,125,139
	G1688W (DIV)	110
	F1692S (DIV)	123,132

	Y1694C (DIV)	123,132
	F1707V (DIV)	134
	C1741R (DIV)	123
	G1749E (DIV)	59
	C1756G (DIV)	140,141
	G1762E (DIV)	122
Intractable childhood epilepsy with generalized tonic-clonic seizures	H290R (DI)	123
	N359S (DI)	110,127
	R393H (DI)	59,110,123-125,129-131
	C1376R (DIII)	123
	P1632S (DIV)	126,142
	T1709I (DIV)	126,142
Familial febrile seizures 3A	E1308D (DIII)	110,116,119,143
$Na_V1.2$		
Benign familial infantile seizures	K908E (DII)	144
Developmental and epileptic encephalopathy	G211D (DI)	135
	N212D (DI)	145
	V213D (DI)	145
	K905N (DII)	127,146
	T1623N (DIV)	145
$Na_V1.4$		
Paramyotonia congenita of von Eulenburg	L1433R (DIV)	147
	L1436P (DIV)	148
Congenital myasthenic syndrome	V1442E (DIV)	149
$Na_V1.5$		
Brugada Syndrome (BrS)	L212Q (DI)	80
	L276Q (DI)	80
	H278D (DI)	80
	R282C R282H (DI)	80,103
	A286S (DI)	80
	N291S (DI)	80
	V294M (DI)	103
	L299M (DI)	80
	V300I (DI)	80
	L315P (DI)	80
	G319S (DI)	103
	T320N (DI)	80
	L325R (DI)	80
	P336L (DI)	80,150
	G351D G351V (DI)	80,151
	T353I (DI)	152
	D356N (DI)	80,153

	G386E G386R (DI)	80
	E746K (DII)	80
	E867Q (DII)	80
	R878C R878H (DII)	80,154
	S910L (DII)	80,103
	C915R (DII)	80
	L917R (DII)	80
	E1225K (DIII)	79,80
	Y1228H (DIII)	80
	R1232Q R1232W (DIII)	80,106
	K1236N (DIII)	103
	F1293S (DIII)	80,103
	G1358W (DIII)	80
	K1359N (DIII)	80
	F1360C (DIII)	80
	C1363Y (DIII)	80
	S1382I (DIII)	79,80
	V1405L V1405M (DIII)	79,80
	A1428V (DIII)	80
	D1430N (DIII)	98
	R1432S (DIII)	80
	G1433V (DIII)	80
	P1438L (DIII)	80
	E1441Q (DIII)	80
	E1548K (DIV)	80
	Q1613 (DIV)	80
	delF1617 (DIV)	155
	T1620M (DIV)	80,105,156,157
	A1680T (DIV)	80
	D1690N (DIV)	99
	N1722D (DIV)	80
	C1728R C1728W (DIV)	80
	G1740R (DIV)	80,103,106
	G1743E G1743R (DIV)	79,80,100,106,158
	G1748D (DIV)	99
Long QT syndrome Type 3 (LQT3)	L212P (DI)	159
	N275K (DI)	159
	G289S (DI)	159
	R340W (DI)	159
	E1225K (DIII)	160
	E1231K (DIII)	160

	E1295K (DIII)	[101]
	R1432S (DIII)	[159]
	S1609W (DIV)	[161]
	delF1617 (DIV)	[159]
	T1723N (DIV)	[159]
	R1739W (DIV)	[159]
Progressive familial heart block	G298S (DI)	[107,108]
	R1232W (DIII)	[80,105]
Atrial fibrillation	S216L (DI)	[80,162]
$Na_v1.6$		
Developmental and epileptic encephalopathy	N215R (DI)	[70]
	V216D (DI)	[111]
	I1605R (DIV)	[70]
Familial myoclonus	P1719R (DIV)	[109]
$Na_v1.7$		
Congenital indifference to pain	R907Q (DII)	[113]
	del1381-1385 (DII)	[113]

Table 1.2 Mutations in the c-terminal domain region related to diseased phenotypes in all the Na_v subtypes

Disease	Mutation in c-terminal domain	References
$Na_v1.1$		
Dravet syndrome	E1787K	[110,125]
	N1788K	[119]
	A1792T	[123]
	del1807-1810	[126]
	F1808I	[119]
	W1812G	[126]
	W1812S	[119]
	del1813-1815	[119]
	F1831S	[126]
	A1832P	[110]
	L1835F	[119]
	M1852K	[110]
	P1855L	[110]
	G1880E	[110]
	E1881D	[163]
	T1909I	[71,129]
	del1909	[110]
	I1922T	[134]
	R1927IIQ	[110]

Generalized Epilepsy with Febrile Seizures plus 2	E1795K	[164]
	M1852T	[114,165]
	V1857L	[166]
	D1866Y	[167]
	I1867T	[110,168]
Intractable childhood epilepsy with generalized tonic-clonic seizures	F1808L	[126,142]
	R1861W	[123]
$Na_v1.2$		
Developmental and Epileptic Encephalopathy 11	L1829F	[169]
	H1853R	[170]
	R1882L	[171]
	R1882Q	[127,146,169,172,173]
Idiopathic generalized epilepsy	R1918H	[174]
$Na_v1.3$		
Developmental and Epileptic Encephalopathy 62	K1799Q	[175]
Cryptogenic partial epilepsy	G1862C	[176]
$Na_v1.4$		
Hyperkalaemic periodic paralysis	M1592V	[177]
Normokalaemic periodic paralysis	M1592V	[178]
Potassium aggravated Myotonia	Q1633E	[179]
Paramyotonia congenita of von Eulenburg	F1705I	[180]
$Na_v1.5$		
Brugada Syndrome	T1779M	[80]
	E1784K	[80,103]
	L1786EfsX2	[80]
	1795insD	[80,181]
	Y1795H	[102]
	F1808IfsX3	[80]
	S1812X	[80]
	L1825P	[182]
	E1823HfsX10	[80]
	Q1832E	[80,183]
	C1850S	[184]
	R1860KfsX13	[80]
	V1861I	[80]
	K1872N	[80,183]
	S1904L	[80,183]
	A1924T	[80,183,185]
	G1935S	[80,183]
	E1938K	[80,183]
	V1951L	[103]

	I1968S	186
	F2004L	183,187
	F2004V	80,183
Long QT 3 syndrome	T1779M	159,160
	E1784K	159,160,188,189
	D1790G	190,191
	Y1795C	102,159,160,192
	1795insD	80,181
	D1819N	161
	L1825P	182,193
	R1826H	159,194
	D1839G	159,195
	H1849R	104
	R1897W	159
	E1901Q	159
	S1904L	196
	Q1909R	160
	R1913H	191
	A1949S	160
	V1951L	162
	R1958Q	159,160
	Y1977N	159
	F2004L	162,187
	F2004V	80,159
	P2006A	197
	R2012C	159
Atrial fibrillation	R1826C	162
	V1951L	162
	V1951M	162
	N1986K	198
	F2004L	162
Sick Sinus Syndrome	D1792N	199
$Na_v1.6$		
Developmental and Epileptic Encephalopathy 13	N1768D	112
	Q1801E	70
	L1865P	169
	R1872L	200
	R1872Q	70,200
	R1872W	70,111,172,200,201
	N1877S	172,201,202
Benign familial infantile seizures 5	N1877S	172,201,202
$Na_v1.7$		
Congenital indifference to pain	W1786R	182

1.7 Non-canonical roles of Na_v

Studying the role of Na_v in non-excitable cells revealed that they are sometimes abnormally expressed especially in certain types of cancer where they promote cancer cell migration and invasion, which could be reversed by TTX[203,204]. For instance, $Na_v1.6$ mRNA levels are 40-fold higher in cervical cancer than in non-cancerous tissue samples[205]. Similarly, the neonatal D1:S3 splice variant of $Na_v1.5$ is found to be upregulated in human breast cancer cells with roles in advancing metastasis most likely via the CD44-src-cortactin signalling pathway[206]. The increase in the invasiveness of cancer is promoted by the activity of Na^+/H^+ exchanger, as the increased Na^+ current carried by overexpressed $Na_v1.5$ induces the efflux of more H^+, increasing the acidity of the surrounding and thus activating pH-dependent cysteine cathepsins which cause extracellular matrix degradation[207,208]. Phenytoin has been shown to reduce tumour growth and propagation in breast cancer, as it reduced the Na^+ current[209]. Same reduction in growth and metastasis has been observed with downregulation of $Na_v1.5$ using lentiviral shRNA in tumour[210]. More targeted blocking of neonatal $Na_v1.5$ by the use of a polyclonal antibody, NESOpAb, has shown similar benefits with the added advantage of not affecting adult $Na_v1.5$ function[211]. Similar upregulation of the ß1-subunit was also found in breast cancer tumours which promoted vascularization, growth and metastasis and reduced apoptosis[212].

$Na_v1.5$ is absent in normal colonic tissue but has been detected in colon cancer[213]. Furthermore, $Na_v1.1$, $Na_v1.2$, $Na_v1.3$, $Na_v1.4$, $Na_v1.5$ and $Na_v1.7$ mRNA expression levels were found to be significantly higher in ovarian cancer cells, with the levels of $Na_v1.2$, $Na_v1.4$, $Na_v1.5$ and $Na_v1.7$ particularly increasing with the increase in level of metastaticity[214].

$Na_v1.5$ has also been found to be expressed intracellularly in human monocyte-derived macrophages and regulate endosomal acidification by depleting endosomal Na^+ hence causing inflow of H^+ and decreasing pH inside the late endosome[215]. This could also potentially affect phagocytosis. It is however unclear how activation of these Na_vs are achieved through depolarization. The resting lysosomal membrane potential is reported to be between -20 to -40 mV[216]. $Na_v1.5$ and $Na_v1.8$ were also implicated in increased expression of a regulatory protein involved in DNA repair and phosphatase activity[217].

One of the earliest pieces of evidence of Na_v being present in non-excitable cells were confirmed by patch clamping Schwann cells from rabbit and astrocytes from rat. Depolarization presented with the typical fast activation and inactivation traces which could be blocked with TTX and STX[218,219]. Later studies also found presence of $Na_v1.2$, $Na_v1.3$, $Na_v1.5$ and $Na_v1.6$ in astrocytes[220].
$Na_v1.4$ and $Na_v1.7$ has also been detected in human erythroid progenitor cells (precursors to red blood cells), with yet to be identified role[221].

1.8 Na_v as a target of drugs and toxins

Numerous drugs which impart their action by modulating the Na_v currently exist for example as antiarrhythmics, anticonvulsants and local anaesthetics. Na_v are also a natural target of many toxins found in nature. The guanidium toxins, tetrodotoxin (TTX) and saxitoxin (STX) physically block the Na_v pore preventing passage of Na^+ ions whereas batrachotoxins and veratridine can activate the Na_v channels or prevent inactivation by binding to a site between DI-S6 and DIV-S6. Peptide toxins like proToxin (ProTX), huwentoxin (HwTX) has been isolated from the venoms of scorpions and spiders[222]. HwTX-IV selectively targets the DII voltage sensor of $Na_v1.7$ at IC50 of 26nM but has an IC50>10 μM for $Na_v1.5$[223]. Scorpion α-toxins (α-ScTxs) can also act as activators of Na_v by binding to DIV S3-S4 extracellular loop and preventing the movement of the voltage sensing S4 helix, hence inhibiting fast inactivation. ß-scorpion toxins (ß-ScTxs) and μO-conotoxins block the voltage sensing domain of DII and cause a hyperpolarizing shift in the steady state activation of Na_v thereby making it harder for Na_v to start firing. Brevetoxins (PbTx) and ciguatoxins (CTX) can cause hyperactivity of Na_v channels by binding between DI-S6 and DIV-S5. Local anaesthesia causing agents like lidocaine are known to bind to the S6 helix of either DI, DIII and DIV and block Na^+ conduction.

TTX, isolated from pufferfish, is still used to classify Na_v channels based on their sensitivity to TTX, for instance TTX-resistant (IC_{50} >30 nM) $Na_v1.5$, $Na_v1.8$, and $Na_v1.9$ and TTX-sensitive (IC50<30 nM) $Na_v1.1$, $Na_v1.2$, $Na_v1.3$, $Na_v1.4$, $Na_v1.6$, and $Na_v1.7$. TTX played a role in the determination of the selectivity filter of Na_v and the binding

site of the pore blockers of Na_v [224,225]. There are many instances where toxins were used as guides to find therapeutic agents, a recent example ziconotide for the treatment of chronic pain. Various methods like generation of phage display antibody libraries, peptide libraries, directed evolution and chemical modifications have been used in attempts to engineer proteins to have specificity and potency in targeting particular subtype of Na_v channels. For example, native tarantula ceratotoxin-1 which recognizes and binds to different Na_v channels was engineered through directed evolution and mutagenesis to only target $Na_v1.7$[226].

Furthermore, the exceptionally high specificity and potency of monoclonal antibodies (mAb), to target Na_v channels have been in long established use. This involved raising antibodies against peptides from different loop regions of Na_v channel's voltage sensor or pore loops[227]. SVmAb1 is one such example, which targets the same region as HwTx-IV, the second extracellular loop of DII S3-S4 voltage sensor. This mAb was found to impart its anti-neuropathic and anti-inflammatory pain effects on mice models by inhibiting $Na_v1.7$ channel activation by stabilizing the closed state. Although such reports were later found to be non-reproducible by another group, it only points to the challenge of finding mAb targets to Na_v channels[228]. More recently, camelid antibodies (nanobodies) and Phage display of scFv (single chain variable fragment) antibodies are also being utilized to tackle this problem. Moreover, knocking down Na_v channel protein expression by use of shRNAs are also being investigated, although this approach lacks suitable drug delivery methods currently[229–231].

.

1.9 The Na_V C-terminal domain

The globular C-terminal domain (CTD) is connected to the DIV S6 helix via a flexible and disordered linker and carries out many regulatory functions of the Na_Vs (Figure 1.3)[232,233]. Five α-helical regions of the CTD match the consensus sequence for an EF-like hand (EFL) (Figure 1.4)[234,235]. The fifth α-helical region acts as a binding site for the fibroblast growth factor homologous factor (FHF). The sixth α-helical region (IQ motif) is followed by a disordered region (structurally uncharacterized) consisting of regions involved in cytoskeletal binding and ubiquitination, including a Nedd4-like binding domain, PY motif domain and a syntrophin-anchoring PDZ binding motif[236,237].

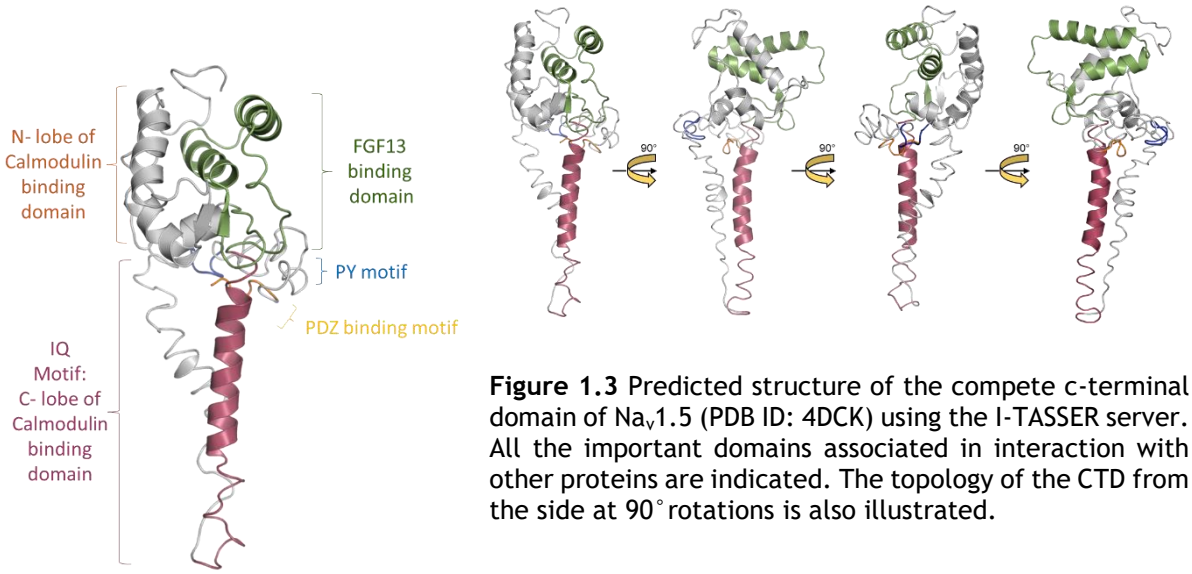

Figure 1.3 Predicted structure of the compete c-terminal domain of $Na_V1.5$ (PDB ID: 4DCK) using the I-TASSER server. All the important domains associated in interaction with other proteins are indicated. The topology of the CTD from the side at 90° rotations is also illustrated.

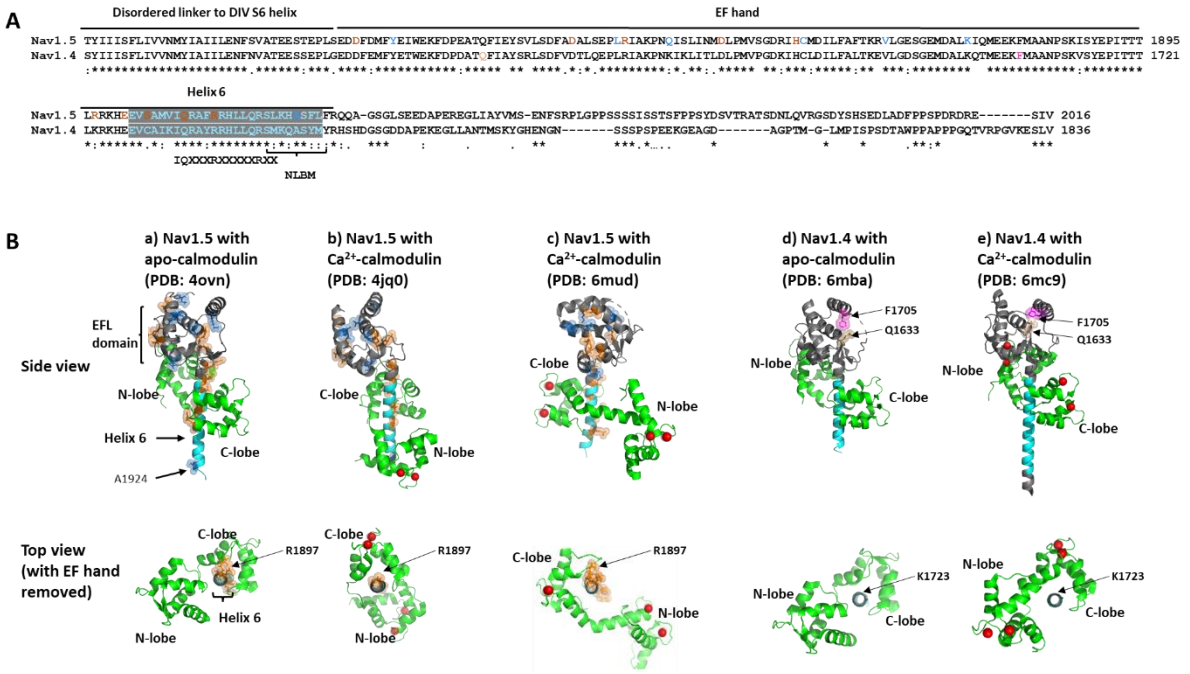

Figure 1.4 The $Na_v1.4$ and $Na_v1.5$ channel C-terminal domain. A. Clustal omega sequence alignment of $Na_v1.5$ and $Na_v1.4$ CTDs. Identical residues are indicated by (*), conservative changes by (:) and semi-conservative changes by (.). Locations of the linker region, EF hand and helix 6 highlighted. The extended region of helix 6 containing sequences implicated in apo- or Ca^{2+}-calmodulin binding coloured cyan. Within this region, the consensus IQ-motif is indicated. In the $Na_v1.5$ sequence, examples of LQT3 and BrS-associated residues coloured orange and sky blue, respectively. In the $Na_v1.4$ sequence, myotonia and PMC-associated residues coloured tan and purple, respectively. **B.** Comparative structures of CTDs from Nav1.5 (a–c) and $Na_v1.4$ (d,e) with apo-calmodulin (a,d) or Ca2+-calmodulin (b,c,e), in side view and top view. To emphasize the variety of ways in which calmodulin can bind to helix 6, the EF hands have been removed from the top views and the orientation of each helix 6 structure has been arbitrarily standardized, with $Na_v1.5$ residue R1897 and its $Na_v1.4$ equivalent K1723 placed at 12 o'clock. In the $Na_v1.5$ structures, LQT3 and BrS-associated residues highlighted as spheres and coloured orange and sky blue, respectively. In the $Na_v1.4$ structures, myotonia and PMC-associated residues highlighted as spheres and coloured tan and purple, respectively. Ca^{2+} ions shown as red balls.

1.10 Ca^{2+}-dependent modulation of voltage-gated myocyte sodium channels

Activation of Na_V channel leads to release of Ca^{2+} from the sarcoplasmic reticular (SR) stores via the ryanodine receptor (RyR), which increases the intracellular Ca^{2+} levels from ~100 nM to 10 µM, thereby initiating contraction of the myocytes. EF-hand like regions of C-terminal domain of Na_Vs have been reported to bind Ca^{2+} directly or via its association with calmodulin (CaM)[236,238]. Calmodulin itself has four EF-hands, two on each of the N- and C- lobes, which can bind Ca^{2+} (Ca^{2+}-CaM) with high affinity (nM to low µM range) and undergo structural changes in presence of Ca^{2+} i.e. Ca^{2+}-CaM (open and semi-open states) and absence of Ca^{2+} i.e. apo-calmodulin (apo-CaM) (closed and semi-open states)[239-241]. At its open and semi-open states a hydrophobic pocket opens up which can bind distinct α-helical motifs[239-241].

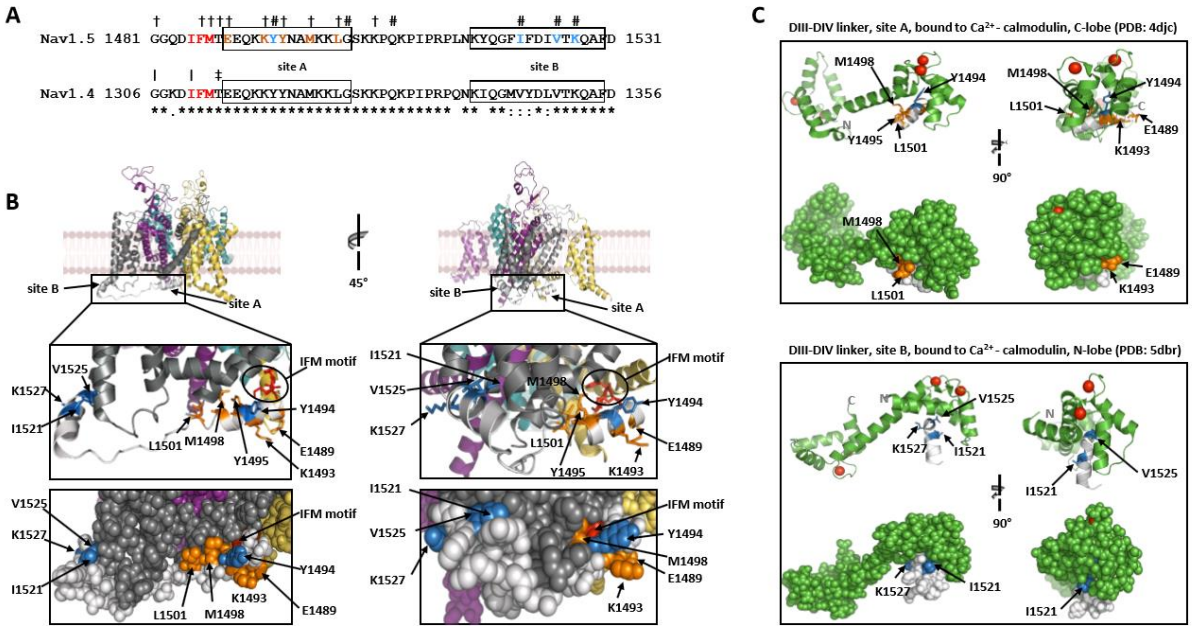

Figure 1.5. The intracellular DIII-DIV linker interaction with Calmodulin.

(A) Sequences of DIII-DIV linkers from $Na_V1.5$ and $Na_V1.4$ aligned using Clustal Omega. Identical residues indicated by (*), conservative changes by (:) and semi-conservative changes by (.) underneath the sequence alignments. IFM motifs of the inactivation gate are indicated in red. Site A and site B helices, inside respective boxes, are indicated. In the $Na_V1.5$ sequence, examples of residues whose mutations are associated with Long QT syndrome (LQT3) indicated by (†) and with Brugada syndrome (BrS) by (#). LQT3 and BrS-associated residues implicated in binding of the DIII-DIV linker to the α-subunit and to Ca2+-calmodulin coloured orange and sky blue, respectively. In the $Na_V1.4$ sequence, residues whose mutations are associated with myotonia indicated by (|) and with paramyotonia congenita (PMC) by (‡). (B) Expanded view of the $Na_V1.5$ DIII-DIV linker (light grey), showing locations of the key residues coloured in (A), see text for details. (C). Binding of site A helix and site B helix to Ca2+-calmodulin C-lobe and N-lobe, respectively. Note the location of key site A and B residues coloured as in **(A)** and **(B)**.

The cleft present in the EFL binds the DIII-DIV linker (site A, Figure 1.5A,B,C)[235] by forming ionic bonds with residues in DIV S4 helix. Since the DIII-DIV linker contains the IFM motif, the CTD acts as a restraint for the inactivation gate from premature transition to the inactivated state. Site A and B of DIII-DIV linker also binds to the C- and N- lobes of calmodulin only in the presence of Ca^{2+} [242,243]. In $Na_v1.5$ disease causing mutations are found which weakens this binding, for example Y1494N affects binding of the C-lobe of CaM and I1521K affects the binding of N-lobe of CaM to the DIII-DIV linker[243].

The Na_v CTD can also bind calmodulin, its IQ motif binds the C- lobe of apo-calmodulin, whereas the N- terminal of helix 6 of CTD can bind the N- lobe of apo-calmodulin (Figure 1.4 A, Ba)[244]. In the presence of Ca^{2+}, the IQ motif of $Na_v1.5$ CTD can still bind Ca^{2+}-calmodulin, but the N- lobe of Ca^{2+}-calmodulin falls off the helix 6 and binds to a post IQ-motif NLBM (Figure 1.4 Bb). In another structure available of this binding (Figure 1.4 Bc) the N- lobe of Ca^{2+}-calmodulin appears to remain unbound to the N-lobe, however in that structure the post-IQ motif NLBM region is missing[245]. Mutations in this NLBM region are also associated with BrS, for e.g. A1924T (Table 1.2). Interestingly, a functioning NLBM region is missing in the $Na_v1.4$ CTD and although the $Na_v1.4$ CTD binds to apo-calmodulin in a similar fashion as the $Na_v1.5$ CTD, during its binding with Ca^{2+}-calmodulin, the N- lobe of the Ca^{2+}-calmodulin does not shift as dramatically as observed in the $Na_v1.5$ CTD (Figure 1.4 Bd,e)[245]. This suggests that even with such similar sequence homology between $Na_v1.4$ and $Na_v1.5$ CTD, they show different binding characteristics to Ca^{2+}/apo-calmodulin.

$Na_v1.5$ CTD also contains a PY motif that can bind Nedd4-2, which is upregulated by elevated Ca^{2+}, and be degraded[246].

Calmodulin could also potentially bind to N-terminal domain of $Na_v1.5$ CTD, with certain mutations which perturbs this interaction causing dominant negative effect on the channel function[247].

1.11 Aim of the project

All the voltage gated sodium ion channels subtypes have been associated with naturally occurring mutations that cause diseases that result in significant disability, developmental problems, early death and/or decrease in quality of life. Some of these mutations in $Na_V1.5$ alter amino acids in the extracellular turret loop regions of domains DII (R878, W879) and DIII (Y1426, D1430, W1440, E1441). Yet it is unclear how they affect channel gating. In the $Na_V1.5$ structure determined by cryogenic electron microscopy, the wild-type residues that correspond to these mutants appear to form a complex salt bridge at the interface between the DII and DIII turret loops (R878 containing the positively charged side chain with the negative charged side chain consisting of D1430 and E1441 residues). Furthermore, adjacent aromatic residues (W879, Y1426 and W1440) are likely to form cation-π interactions with the complex salt bridge. Here, we examine this region using site-directed mutagenesis, electrophysiology and *in silico* modelling. Since the location of these amino acids are not in a very critical area of the channel like the voltage sensor, pore, or the inactivation/activation gates, these might provide interesting insights into the mechanism of channel activation, inactivation, and recovery from inactivation. The hypothesis is that these cluster of amino acids stabilizes the etracellular loop region between DII and DIII and in extension contributes to the stability of Na_V. Disruption of the various bonds formed by these amino acids will likely lead to the destabilization of the Na_V structure resulting in drastic effects on the channel activity.

Moreover, as already discussed in detail previously, the Na_V channel shows Ca^{2+} dependent regulation through the association of its C-terminal domain with calmodulin. This project aims to understand this interaction between Na_V CTD and calmodulin and how this interaction is regulated in the presence and absence of Ca^{2+}. Since the CTD region mostly consists of a disordered region it has not been resolved with the full structure models recently made available by CryoEM. However, truncated CTD x-ray crystallography structures of $Na_V1.5$ and $Na_V1.4$ can be found in literature. Although very similar in homology, interesting differences in the binding of calmodulin can be observed in these available structures. The CTD, whether full or truncated, has not been resolved for $Na_V1.7$, so this project will also aim to resolve this structure using x-ray crystallography.

Finally, using phage displays single chain (scFv) antibodies will be selected against the CTD of $Na_v1.5$ and $Na_v1.7$. Since the CTD are known to bind the DIII-DIV linker, calmodulin and FGF13, an scFv binding to the CTD could potentially hamper or enhance these interactions. Being able to find an scFv antibody clone that can cause deregulation of CTD by, for instance preventing the binding of calmodulin, could have potential as a therapeutic agent. If the scFv could inhibit the binding of the DIII-DIV linker, which consists of the inactivation gate, to the CTD then it could potentially affect the inactivation and recovery from inactivation. Whether the scFvs elicit gain of function or loss of function to the channel, either way it can have therapeutic potential in different diseases. At the very minimum an antibody that selectively binds to $Na_v1.7$ and not to $Na_v1.5$ and vice versa can have promising role in diagnostics, detection in various experimental assays and help in structural determination. In this part of the project a 10^{12} scFv library (naïve human B Cell derived) will be screened to find clones that recognize selective $Na_v1.7$ and $Na_v1.5$ CTD. Selected clones will be studied using automated patch clamp to understand their effects on channel gating. It is expected that the clones could have effect on channel gating through inhibiting binding of other associated proteins with the CTD, like calmodulin, FGF13 etc.

Chapter 2

Materials and Methods

2. Materials and Methods

All chemicals were purchased from Sigma-Aldrich (Haverhill, UK), unless mentioned otherwise.

2.1 DNA constructs, primers, and site-directed mutagenesis

Bicistronic plasmids encoding $hNa_v1.5$ (pIRES2-EGFP-hNav1.5; also called hH1, accession no. M77235) and the R878C mutant (pIRES2-EGFP-R878C) together with a separately expressed EGFP were a gift from Dr. Ming Lei (University of Oxford, UK). All further mutations were introduced by site-directed mutagenesis (QuikChange Lightning kit, Agilent) according to the manufacturer's instructions with slight modifications which include use of additional 1 µl 100% DMSO (Thermo Scientific). The following reagents were mixed in a PCR tube: 5 µl of 10X reaction buffer, 2 µl of dsDNA template (100 ng), 2 µl of forward primer (125 ng), 2 µl of reverse primer (125 ng), 1 µl of dNTP mix, 1 µl of 100% DMSO, 1.5 µl of QuikSolution reagent. The volume was then made up to 50 µl using ultra-pure water (ddH_2O). Then following addition of 1 µl of QuikChange Lightning enzyme and a brief spin down, a run in a thermal cycle was performed with the following cycles: 95°C for 2 min, then 18 cycles of 95°C (20 sec), 60°C (10 sec), 68°C (30 sec/Kb of plasmid length) followed by a final step of 68°C for 5 min. 2 µl of *Dpn* I restriction enzyme was then added and kept at 37°C for 5 min after mixing thoroughly. 2 µl of this was then transformed in 45 µl of XL-10 Gold Ultracompetent cells (thawed for 5 min with 2 µl of β-ME mix, then *Dpn* I digested plasmid mixed gently with the cells for 30 min on ice) at 42°C for 30 sec, then immediately placed back on ice for 2mins, before transfer of the content to pre-heated 0.5 mL of 2TY Luria Broth (LB, 8 g Tryptone (Formedium), 5 g Yeast Extract (Formedium), 2.5 g NaCl (Fisher Scientific UK) in 500 ml dH_2O; sterilized by autoclaving) media at 37°C for 1 h at 250 rpm shaking. After transformation, the samples were streaked (50 µl and 200 µl of each sample separately) in 2TY agar (1.5%) plates. 1X Kanamycin Sulfate antibiotic (Gibco, Life technologies) was added to both the broth and agar media. Sigma GenElute HP Plasmid Midiprep Kit was used throughout for plasmid DNA extraction. Absorbance at 260/280 and 260/230 was used to determine DNA concentration and purity (BioPhotometer D30, Eppendorf). DNA sequencing confirmed whether nucleotide

exchange for mutant generation occurred successfully or not (Sanger Sequencing facility, Department of Biochemistry).

The following oligonucleotide primers were used for generating the mutants:

a. E1441C:
   5′-GGGTATGAAGAGCAGCCTCAGTGGTGCTACAACCTCTAC-3′ (+)
   5′-GTAGAGGTTGTAGCACCACTGAGGCTGCTCTTCATACCC-3′ (-)
b. E1441R:
   5′-TGAAGAGCAGCCTCAGTGGCGATACAACCTCTACATGTAC-3′ (+)
   5′-GTACATGTAGAGGTTGTATCGCCACTGAGGCTGCTCTTCA-3′ (-)
c. E1441Q:
   5′-GGGTATGAAGAGCAGCCTCAGTGGCAATACAACCTCTAC-3′ (+)
   5′-GTAGAGGTTGTATTGCCACTGAGGCTGCTCTTCATACCC-3′ (-)
d. E1441D:
   5′-GAAGAGCAGCCTCAGTGGGACTACAACCTCTACATGTACAT-3′ (+)
   5′-ATGTACATGTAGAGGTTGTAGTCCCACTGAGGCTGCTCTTC-3′ (-)
e. R878E:
   5′-CGACTCAGGCCTGCTGCCTCACTGGCACATGATG-3′ (+)
   5′-CATCATGTGCCACTCAGGCAGCAGGCCTGAGTCG-3′ (-)
f. R878D:
   5'-CAGGCCTGCTGCCTGACTGGCACATGATGG-3' (+)
   5'-CCATCATGTGCCAGTCAGGCAGCAGGCCTG-3' (–)
g. D1430R:
   5'-CATTATGTATGCAGCTGTGCGCTCCAGGGGGTATGAAGAG-3' (+)
   5'-CTCTTCATACCCCCTGGAGCGCACAGCTGCATACATAATG-3' (-)
h. D1430E:
   5'-TATGTATGCAGCTGTGGAATCCAGGGGGTATGAA-3' (+)
   5'-TTCATACCCCCTGGATTCCACAGCTGCATACATA-3' (-)
i. D1430C:
   5'- GACATTATGTATGCAGCTGTGTGTTCCAGGGGGTATGAAGAGCAG -3' (+)
   5'- CTGCTCTTCATACCCCCTGGAACACACAGCTGCATACATAATGTC -3' (-)
j. R878E/E1441R: R878E used as a template with E1441R oligonucleotide primers
k. R878C/E1441C: R878C used as a template with E1441C oligonucleotide primers
l. R878D/D1430R:R878D used as a template with D1430R oligonucleotide primers

m. R878C/D1430C:R878C used as a template with D1430C oligonucleotide primers

n. W879Y:

5'-GGCCTGCTGCCTCGCTATCACATGATGGACTTCT-3' (+)

5'-AGAAGTCCATCATGTGATAGCGAGGCAGCAGGCC-3' (–)

o. W879A:

5'-AGTCCATCATGTGCGCGCGAGGCAGCAGGC-3' (+)

5'-GCCTGCTGCCTCGCGCGCACATGATGGACT-3' (-)

p. Y1426A:

5'-AGGCTGGATGGACATTATGGCCGCAGCTGTGGACTCCAGG-3' (+)

5'- CCTGGAGTCCACAGCTGCGGCCATAATGTCCATCCAGCCT -3' (-)

q. Y1426W:

5'-CATTTAAAGGCTGGATGGACATTATGTGGGCAGCTGTGGACTC-3' (+)

5'-GAGTCCACAGCTGCCCACATAATGTCCATCCAGCCTTTAAATG-3' (–)

r. Y1426F:

5'- CATTTAAAGGCTGGATGGACATTATGTTCGCAGCTGTGGACTC -3' (+)

5'- GAGTCCACAGCTGCGAACATAATGTCCATCCAGCCTTTAAATG -3' (–)

s. W1440Y:

5'-GGTATGAAGAGCAGCCTCAGTATGAATACAACCTCTACATGTAC -3' (+)

5'-GTACATGTAGAGGTTGTATTCATACTGAGGCTGCTCTTCATACC -3' (-)

t. W1440A:

5'-GTATGAAGAGCAGCCTCAGGCGGAATACAACCTCTACATG -3' (+)

5'-CATGTAGAGGTTGTATTCCGCCTGAGGCTGCTCTTCATAC -3' (-)

u. Q1832E:

5'-GTATCGCCAAGCCCAACGAGATAAGCCTCATCAAC -3' (+)

5'-GTTGATGAGGCTTATCACGTTGGGCTTGGCGATAC -3' (-)

2.2 Cell culture and transfection

Human embryonic kidney (HEK293F) cells were cultured in DMEM/F-12 GlutaMAX medium (Invitrogen) supplemented with 10% fetal bovine serum at 37 °C and 5% CO_2. For patch-clamp experiments and confocal imaging, 0.5 µg of $Na_v1.5$ wild-type (WT) or appropriate mutant were transiently transfected using polyethylenimine (PEI, 1 µg/µl) at a DNA/PEI ratio of 1:4, on 18 mm coverslips in 6-well plates. For confocal imaging two changes were made, increase of plasmid to 1 µg and use of 22 mm coverslips. For the biotinylation assays, HEK293F cells were transiently transfected in 100 mm dishes with 8 µg of $Na_v1.5$ WT, mutant or empty vector pEGFP-N1 as a negative control, using a DNA/PEI ratio of 1:3. After 48 hours the transfected cells were harvested for further experimentation. Transfection efficiency was determined by Leica DMI 6000 CS microscope by the imaging of the GFP fluorescence.

2.3 Immunocytochemistry and imaging with confocal microscopy

The cover slips were initially washed with 100% ethanol, dried under UV overnight inside tissue culture hood and later processed with 0.01% poly-l-lysine (Merck Specialty Media) and again dried under UV overnight. After 48 h of transfection, the cover slips were washed three times with 1X Phosphate-buffered saline (PBS; pluriSelect Life Science) and fixed using 4% paraformaldehyde (PFA) for 10 min before being re-washed with 1X PBS. The permeabilization step was carried out by 0.1% Triton X solution (100 µl Triton X-100 in 100 ml 1X PBS prepared with Milli-Q ultrapure water) for 10 min at room temperature and pressure (rtp) under gentle shaking. Immediately, 1% Bovine Serum Albumin (BSA) (1 g BSA in 100 ml 1X PBS prepared with Milli-Q ultrapure water) blocking agent was added to the cover slips containing the transfected cells for 1 h. Overnight incubation with primary antibody Anti-Human $Na_v1.5$ (SKM2, SCN5A, polyclonal, rabbit, Alomone labs) prepared in 1% BSA solution followed with two different concentrations 1:250 and 1:500 and kept at 4°C under gentle shaking. On the next day, the cover slips were washed three times with 1X PBS and incubated with secondary antibody Alexa Fluor 647 (goat anti-rabbit; Invitrogen life technologies; A21245) for 2 h at 4°C under gentle shaking in darkness (plates covered with Aluminium foil). Cover slips were re-washed three times with 1X PBS and mounted on VWR SuperFrost Plus microscope slides using 4′,6-diamidine-2′-phenylindole dihydrochloride (DAPI; Duolink; Art no. 82040-0005) and sealed with

nail varnish (Boots, Cambridge). Images were captured using Olympus IX81 microscope by sequential scanning (for optimal signal-to-noise ratio) with 488nm (for EGFP) and 647nm (for Alexa 647).
Images were later processed using Fiji Image J software.

2.4 Co-immunoprecipitation (Co-IP) and Western Blotting

Transfected HEK293F cells on each 100 mm sterile dish were first washed three times with ice-chilled 1X PBS, pelleted by centrifugation at 1000 rpm for 5 min at rtp using swinging-bucket rotor centrifuge and every sample resuspended on 1ml Lysis Buffer (0.3g Tris (Melford Biolaboratories Ltd.), 0.44 g NaCl, 500 µl Triton X-100, Protease inhibitor tablet and made up to 50 ml with dH_2O; pH 7.4) and kept at 4°C on a rotating Eppendorf shaker for 30 min. The cell lysates were then separated after centrifugation at 10,000g, for 10 min at 4°C and Pierce BCA Protein Assay kit (Thermo Fisher Scientific) used to quantify and standardize the amount of protein in each sample before appropriate pulldown antibodies and 50 µl of Pierce Protein G Agarose (ThermoScientific, UK) (after three washes with lysis buffer) were added to each sample and kept at 4°C on rotating Eppendorf shaker overnight. On the next day the samples were spun down (2000g, 5 min, 4°C) and the supernatant collected on a fresh set of Eppendorf tubes. The protein G agarose beads were then washed three times with lysis buffer and the final wash collected on fresh Eppendorf tubes. Beads, supernatants and the washes collected were then mixed with Lithium dodecyl sulfate (LDS; Thermo Fisher Scientific Invitrogen NuPAGE LDS Sample Buffer (4X)) and Dithiothreitol (DTT; Melford Biolaboratories Ltd.), vortexed, kept at 80-90°C on a heating block for 10 min before being run on 3-8% Tris acetate gel (Thermo Fisher Scientific invitrogen) with 1X Tris Acetate SDS running buffer (novex by life technologies) for 1 h at constant 150 V on XCell SureLock container (novex by life technologies). The gel was then transferred to nitrocellulose membrane using regular iBlot gel transfer stacks (Invitrogen by Thermo Fisher Scientific). The membrane was then blocked in 5% milk (Marvel original dried skimmed milk) + TBST solution (6.06 g Tris, 8.7 g NaCl, 1 ml Tween20, made up to 1 L with dH_2O; pH 7.4) for 1 h on a shaker before being incubated with appropriate primary antibody on tube rollers at 4°C overnight. On the next day, the membranes were washed five times with TBST solution and incubated with appropriate HRP-conjugated secondary antibody on tube rollers for 1hour at rtp. The membranes were washed again five times with TBST,

soaked in Amersham ECL Western Blotting Detection Reagent (GE Healthcare) for 5mins, dried and processed on Amersham Hyperfilm ECL (GE Healthcare) in a dark room. If necessary, the membranes were washed with TBST solution again and stripped for 10 min using glycine buffer (7.5 g glycine, 0.5 g SDS, 5 ml Tween20, made up to 500 ml with dH_2O; pH 2.2). The membrane could then be made ready to re-probe with other antibodies after washing two times with 1X PBS and two times with TBST and blocking with 5% milk again for 1 h.

a) Pulldown antibodies used:
   i. HA-probe antibody (F-7): sc-7392, mouse, Santa Cruz Biotechnology
   ii. Anti-Human $Na_v1.5$ Antibody, SKM2, SCN5A - Cat#ASC-013, rabbit, allomone labs

b) Primary antibodies used:
   i. HA-probe antibody (Y-11): sc-805, rabbit, Santa Cruz Biotechnology
   ii. GFP antibody, GTX113617, rabbit, GeneTex
   iii. Anti-Myc Tag antibody, clone 4A6, HRP conjugate (#16-213), mouse, Merck Millipore

c) Secondary antibodies used:
   i. Goat Anti-Rabbit IgG (H + L)-HRP Conjugate #1706515, Bio-Rad

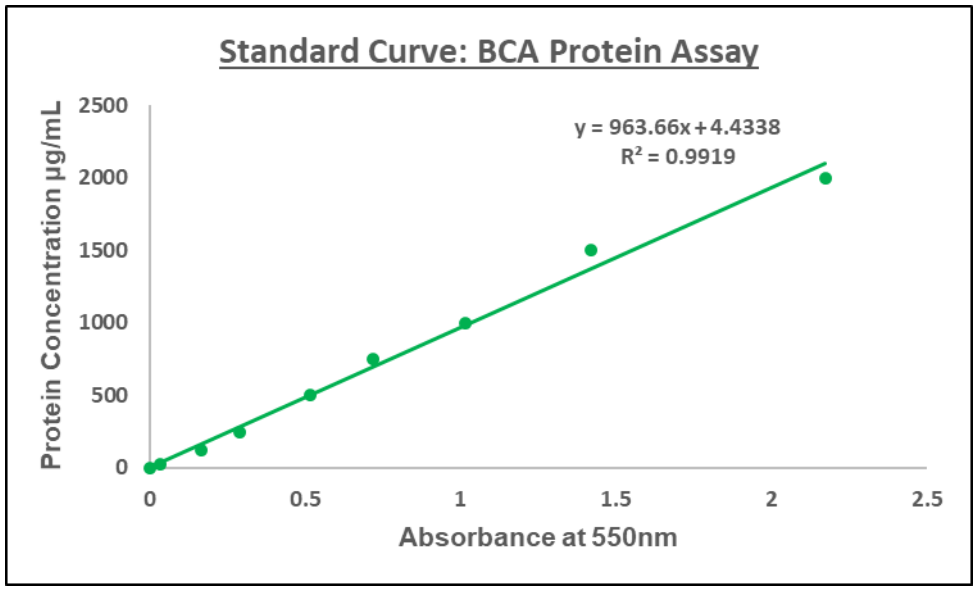

Figure 2.1. Standard curve to measure protein concentrations.

2.5 Cell surface biotinylation assay

Biotinylation assay was adapted from Laedermann *et* al., with slight modifications[248]. 48h after transiently transfecting HEK293F cells with appropriate plasmids, cells were washed twice with cold 1X PBS solution, then incubated with freshly prepared 0.5 mg/ml EZ-link™ Sulfo-NHS-SS-Biotin (Thermo Scientific, Cheshire, UK) in cold 1X PBS for 15 min at 4 °C. To quench and remove excess biotin the cells were washed twice with 200 mM glycine (in cold 1X PBS), and then twice with cold 1X PBS. Cells were then lysed in 1 ml of lysis buffer (50 mM HEPES pH 7.4; 150 mM NaCl; 1.5 mM $MgCl_2$; 1 mM EGTA pH 8; 10% Glycerol; 1% Triton X-100) supplemented with 1X Complete Protease Inhibitor Cocktail (Roche) at 4°C for 1 h, and then clarified by centrifugation; 16,000 X g for 15 min at 4 °C. 500 µg of the supernatant was incubated with 50 µl Pierce™ Streptavidin Agarose beads (Thermo Scientific, Cheshire, UK) overnight at 4 °C, while the remaining supernatant volume was kept as the input fraction. Following the overnight incubation, the Streptavidin beads were pelleted at 1000 X g for 1 min and washed thrice with cold 1X lysis buffer and then eluted with 50 µl of NuPAGE LDS Sample Buffer (4X; Invitrogen, Renfrewshire, UK) supplemented with 100 mM DTT at 37 °C for 30 min. The input fractions were similarly treated in LDS buffer + 100 mM DTT at equal final concentrations to function as a loading control indicating the total $Na_V1.5$ expression, while the biotinylated fractions represent just the $Na_V1.5$ expression at the cell surface.

The input (total $Na_V1.5$ expression) and biotinylated (cell surface-expressed $Na_V1.5$) samples were separated on NuPAGE 4–12% Bis-Tris gels (Invitrogen, ThermoFisher) and transferred to nitrocellulose membrane (iBlot transfer system, Invitrogen, ThermoFisher). Membranes were blocked with 5% milk in TBS-Tween (0.1%) for 45 mins at room temperature before overnight incubation of primary antibody at 4 °C. Primary rabbit polyclonal anti-(human $Na_V1.5$), (residues: 1978-2016) (#ASC-013, Alomone Labs, Jerusalem, Israel) and rabbit polyclonal anti-(actin) (A2066, Sigma), both used at a concentration of 1:200 were followed by a one-hour incubation with secondary Goat anti-(Rabbit IgG-HRP conjugate) (#1706515, Bio-Rad) at a concentration of 1:8000 at room temperature. Amersham ECL Western Blotting Detection Reagent (GE Healthcare, Hatfield, UK) was used to activate the HRP and the chemiluminescent signal

detected on Amersham Hyperfilm ECL (GE Healthcare). Immunoblot intensities were quantitated using Image J and normalized against their loading controls.

2.6 Electrophysiology

Electrophysiological experiments were carried out as previously described by Salvage *et* al., with slight modifications[249]. GFP fluorescence from pIRES vector helped visualize the efficiently transfected cells chosen for the whole-cell patch-clamp recordings which were made 48 h post-transfection. For all measurements, of inactivation, activation and recovery from inactivation, the whole-cell configuration of the patch-clamping technique was employed using an Axopatch 200 amplifier (Axon Instruments, CA, USA), Digidata 1322A digitizer (Axon Instruments, USA), and the Strathclyde Electrophysiology Software Package (WinWCP, Department of Physiology and Pharmacology, University of Strathclyde, UK). All the experiments were performed at room temperature (20-22°C). The extracellular bath solution used to superfuse the cells was set at a flow rate of 2–3 ml min^{-1} and was composed of 60 mM NaCl, 2 mM KCl, 1.5 mM $CaCl_2$, 10 mM glucose, 1 mM $MgCl_2$, 90 mM $CsCl_2$, 10 mM HEPES, pH 7.40 ± 0.01 adjusted with NaOH. The internal solution contained 35 mM NaCl, 105 mM CsF, 10 mM EGTA, 10 mM HEPES, pH 7.40 ± 0.01 adjusted with CsOH and filter sterilized (0.22 µm). Patch pipettes were prepared from borosilicate glass capillaries (1.2 mm OD, Harvard Apparatus, Cambridge, UK) using electrode puller model P87 (Sutter Instrument Co., CA, USA) with pipette resistance maintained between 1.5-2.5 MΩ. Signals were low-pass Bessel filtered at a cut-off frequency of 5 kHz and sampled at 125 kHz. Series resistance compensation (70–85%) was set for each recording, and leak currents were subtracted using a P/4 protocol. All recordings were made after allowing at least 3 min after membrane rupture. The liquid junction potential (2 mV) was not corrected for and data from cells with a clear loss of voltage control as demonstrated by poor I/V relationships were removed.

2.7 Voltage protocols

All protocols employed a holding potential of - 120 mV. The voltage dependences of steady-state activation and inactivation were examined using a 100 ms duration pulse, to activating test voltages ranging between - 140 mV to

+ 45 mV in 5 mV increments with each sweep, followed immediately by a pulse to a fixed voltage of -40 mV of 50 ms duration. For measurements of steady-state inactivation, peak currents elicited by each of the latter -40 mV pulses, were normalized to the maximum peak current generated and then plotted against the voltage of the preceding 100 ms conditioning pulse. The data assumed a sigmoid function, decreasing with positive shifts of membrane potential. For the activation protocol, peak current densities (pA/pF) were calculated by dividing the peak current amplitude by whole-cell capacitance and the current-voltage relationship plotted. Both inactivation and activation data were fitted with a single Boltzmann function:

$G/G_{max} = 1/(1+\exp((V-V_{1/2})/k)$ (Eq. 1)

where G/G_{max} is the normalized conductance or current, $V_{1/2}$ is the voltage of half-maximal activation or inactivation, *k* is the slope factor, and V is the test voltage or conditioning voltage. The G terms for each voltage V were calculated from observed peak currents I_{Na} and their reversal potential E_{Na} observed at large depolarizing activating test voltages as:

$G_{Na} = I_{Na}/(V-E_{Na})$ (Eq. 2)

The recovery from inactivation protocol employed a standard two-pulse protocol (P1) and (P2) both involving voltage steps to - 40 mV for 50 ms but separated by a return to the holding potential (-120 mV) of varying time courses between 1 to 200 ms. The ratio P2/P1 was then calculated to normalize the peak current, which indicated the fraction of current available for activation after depolarizations at varying durations. These plots were fitted with a double exponential function as follows:

$y = -A_1 \exp(-t/\tau_1) - A_2 \exp(-t/\tau_2)$ (Eq. 3)

In the above equation, A_1 and A_2 are the amplitudes of the fast and slow components respectively, τ_1 and τ_2 are the time constants of recovery from inactivation for the fast and slow components respectively and t is time.

2.8 Statistical analyses

Data from electrophysiological experiments were graphically presented using GraphPad Prism 9 software (GraphPad, CA, USA) and expressed as mean ± SEM. Statistical comparisons were performed using One-Way ANOVA followed by Dunnett post-hoc tests and statistical significance was assumed when $p < 0.05$. ANOVA was used since more than three independent groups of data needed to be analysed for statistical significance. Dunnet's post-hoc test was performed since only the control group was compared to all other mutants, however mutant groups were not compared to each other. The post-hoc analyses reduces the chance type I error (false positives) by controlling the experiment-wise error-rate. The data were automatically captured and analysed using the WinWCP (Electrophysiology software package, University of Strathclyde, UK). Normal distribution of data was assumed.

2.9 Application of veratridine

Veratridine (ab120279, Abcam, Cambridge, UK) was applied at 0.1 M final concentration, in the bath solution and continuously perfused during the whole-cell recording of HEK293F cells transiently transfected with the wild-type $Na_v1.5$ or those mutants which showed no detectable activation current[250]. Veratridine was allowed to perfuse the bath for at least 5 min before starting the recording. Effects of washing out the drug were not performed.

2.10 Disulfide locking experiment

Double cysteine mutations were carried out on the charged residues likely taking part in salt bridge formation (human R878C/E1441C and R878C/D1430C). Whole-cell recordings of HEK293F cells transfected with the wild-type $Na_v1.5$ or either of these two mutants were performed after continuously perfusing the bath solution with freshly prepared 1 mM ß-mercaptoethanol (ßME), allowing at least 5 min before the start of recording[36].

2.11 Molecular dynamics (MD) simulations and bioinformatics

The molecular dynamics (MD) simulations were performed by Manas Kohli (MPhil student, Dept. of Biochemistry, University of Cambridge, UK) and Dr. Taufiq Rahman (Lecturer, Dept. of Pharmacology, University of Cambridge, UK), as part of a close collaboration where I was part of the overall design and interpretation of the work.

The cryo-EM structure for rat $Na_V1.5$ (PDB ID: 6UZ3)[27] was used for the MD simulations. These were performed using NAMD 2.9[251] with CHARMM36 force fields[252]. All simulations were conducted at 310 K and 1 atm. For the wild-type structure, simulations were run on the original PDB structure: 6UZ3. Each of the mutants were engineered using the "Mutator" plugin of VMD 1.9.4[253].

To model the dynamics of each system, the protein was embedded into a lipid bilayer. Each protein was inserted into the palmitoyl-oleoyl-phosphatidylcholine (POPC) bilayer (containing 229 lipid molecules), which was then solvated by TIP3P waters (~ 36000 water molecules) and neutralized by 150 mM NaCl[251,252]. Parameters were taken from the work of Jounge *et al.*, to amend the interactions involving Na^+ ions[254]. All simulations were conducted in an NPT ensemble, with CMAP correction, where the pressure and temperature were held at 1 atm and 310 K by the Nose-Hoover Langevin piston and the Langevin thermostat respectively. Periodic boundary conditions (PBC) were applied in all directions. Simulations were preceded by a pre-equilibrium step. Firstly, the system was energy-minimized for 2000 steps and then equilibrated using a time step of 1 fs for 0.5 ns. To relax the lipid-protein interactions, all atoms were constrained except the lipid tails. Non-bonded Fix (NBFIX) parameters were utilised for this step as they are optimized for the specific case of ions interacting with carbonyl oxygen atoms[255]. This was followed by equilibration with the constrained protein to relax protein-water interactions. Subsequently, productive simulations were run for a duration of 15 ns with the same time step of 1 fs.

On successfully running the simulations, trajectory files (with a dcd extension) were generated and subsequently analysed to investigate the properties of the channel and region of interest. The RMSD values were generated through VMD's "RMSD Visualiser" tool which generated a value for every fs. VMD was used in the analysis of the DEKA ring. With VMD's 'Tkconsole', a tcl script was run to compute the atomic distances between the alpha carbons of the residues for every 1000 frames[256]. For the distances between residues of interest, distances between relevant charged groups on each residue was used. The last frame of every trajectory file was extracted into a pdb file using VMD. Thereafter, using these pdb files, appropriate pore profiles were obtained using MOLE2.0.

Sequence and structure alignments- Primary sequence alignments between the Na_v channel isoforms were conducted using Blastp[257]. Alignment between the rat and human $Na_v1.5$ structures was conducted using TopMatch[258].

2.12 Gateway cloning

Protein sequences were amplified by PCR with the primers below. The forward primers consisted of the *attB1* recombination site (12 nucleotides), the Shine-Dalgarno (translation initiation site in bacteria mRNA) and Kozak (translation initiation site in eukaryote mRNA) sequences, then start codon (ATG) followed by the sequence of our desired recombinant protein (first 7 nucleotides). The reverse primers consist of the two stop codons (TAA), *attB2* recombination site (12 nucleotides) and followed the last 7 nucleotides of our desired protein.

a. Full length $Na_v1.5$ CTD:

5'-AAAAAAGCAGGCTTCGAAGGAGATAGAACCATGCTGGAGAACTTCAGCGTGGCC-3' (F)

5'-AGAAAGCTGGGTGCTTATTATCACACGATGGACTCACGGTC-3' (R)

b. Full length $Na_v1.7$ CTD:

5'-AAAAAAGCAGGCTTCGAAGGAGATAGAACCATGCTGGAGAATTTTAGTGTTGCC-3' (F)

5'-AGAAAGCTGGGTGCTTATTACTATTTTTTGCTTTCCTTGCT-3' (R)

c. $Na_v1.5$ CTD EF-hand domain: same (F) primer as full length Nav1.5 CTD

5'-AGAAAGCTGGGTGCTTATTATTCGTGCTTGCGCCGGAGTGT-3' (R)

d. $Na_v1.7$ CTD EF-hand domain: same (F) primer as full length Nav1.5 CTD

5'-AGAAAGCTGGGTGCTTATTACTCTTGTTTCCGTTTTAGTGT-3' (R)

e. $Na_v1.5$ DIII-DIV linker:

5'-AAAAAAGCAGGCTTCGAAGGAGATAGAACCATGGACAACTTCAACCAACAGAAGGACAAC TTCAACCAACAGAAG-3' (F)

5'-AGAAAGCTGGGTGCTTATTAAGCGTAATCTGGAACATCGTATGGGTAGAATATGAAG CCCTGGTACTT-3' (R)

f. $Na_v1.7$ CTD DIII-DIV linker:

5'-AAAAAAGCAGGCTTCGAAGGAGATAGAACCATG GATAATTTCAACCAACAGAAA-3' (F)

5'-AGAAAGCTGGGTGCTTATTAAGCGTAATCTGGAACATCGTATGGAAATATACATCCTT GGATTTT-3' (R)

g. Calmodulin:

5'-AAAAAAGCAGGCTTCGAAGGAGATAGAACCATGATGGCTGACCAACTGACTGAA-3' (F)

5'-AGAAAGCTGGGTGCTTATTACTTTGCTGTCATCATTTGTAC-3' (R)

h. Universal *att*B1 adapter primer: 5'-GGGGACAAGTTTGTACAAAAAAGCAGGCT-3'
i. Universal *att*B2 adapter primer: 5'-GGGGACCACTTTGTACAAGAAAGCTGGGT-3'

Two step PCR protocol was performed using Qiagen Taq DNA polymerase kit. For both the PCR steps the thermal cycler steps were set as follows: 95°C for 3 min; 40 cycles of 95°C, 58-61°C, 72°C each for 1 min; and at the end 72°C for 15 min. For PCR step 1, the following were mixed in a PCR tube: 5 µL of 10X PCR buffer, 1 µL dNTP mix, 1 µL of desired DNA template (150ng), 1 µL of particular *attB1* primer (F) and 1 µL of *attB2* primer (R) (see list above), 10 µL of 5X Q-solution, 0.5 µL of Taq DNA polymerase and made volume up to 50 µL with ultrapure water. For PCR step 2, all the same chemicals as above were used except in place of the DNA template, 5 µL of the PCR step 1 product was used, and both the (F) and (R) primers were replaced by the universal *att*B1 and *att*B2 adapter primers.
With the *att*B-PCR product gel electrophoresis was performed on 1.8% Agarose gel (ethidium bromide). The band corresponding to the correct kbp was cut and QIAquick Gel Extraction kit used to extract the DNA fragments.
For BP reaction the following were mixed in a 1.5 ml tube: 150 ng of *att*B-PCR product (1-7 µl), 150 ng of pDonor221 vector (1 µl) and TE buffer (pH 8) to make it up to 8 µl. Finally added 2 µl of BP Clonase II enzyme mix and vortex briefly twice and microcentrifuge briefly. This mix was kept overnight at room temperature, or for 2-3h at 25 °C. To terminate the reaction 1 µl of Proteinase K was added at 37 °C for 10 minutes. 1 µl of BP reaction product was used to transform DH5α competent cells, plated on 2TY LB agar plates overnight at 37 °C. Individual colonies were picked to inoculate separate 3ml 2TY LB media for overnight growth at 37 °C, 250 rpm shaking. NEB plasmid extraction miniprep kit was used to extract the plasmid and DNA sequencing performed to confirm presence of the correct sequence in the entry clone.
For the LR reaction the following were mixed in a 1.5 ml tube: 150 ng of entry clone (1-7 µl), 150 ng of pDEST110 vector (1 µl) and TE buffer (pH 8) to make it up to 8 µl. Finally, 2 µl of LR Clonase II enzyme was added, followed by mixing and briefly vorticing twice and briefly microcentrifuging. This mix was kept at room temperature for 2-3 h. To terminate the reaction 1 µl of Proteinase K was added at 37°C for 10 min. 1 µl of LR reaction product was used to transform BL21 (DE3) competent cells that were then plated on a 2TY LB agar plate overnight at 37 °C Individual colonies

were picked to inoculate separate 3 ml 2TY LB media for overnight growth at 37°C, followed by 250 rpm shaking. NEB plasmid extraction miniprep kit was used to extract the plasmid and DNA sequencing performed to confirm presence of the correct sequence in the destination vector. To sequence the pDEST110 vector the following primers were used: GGGAATTGTGAGCGGATAAC (F) and AATGGTGATGGTGATGATGACC (R)

2.13 Protein expression

100-200 ng of destination vector product was transformed in 50 µl of BL21 (DE3) competent cells with heat shock at 42°C for 15 s followed by plating on 2TY LB agar plate containing 100 µg/ml ampicillin and 2% glucose and kept overnight at 37°C. A single colony was selected to prepare a starter culture of 5 mL 2TY LB media containing ampicillin and 2% glucose at 37 °C for 5-7 h. The culture was centrifuged at 250 rpm, and the pellets inoculated in 100 ml of the same media, freshly prepared, to grow overnight at 30°C. Next day the culture was centrifuged at 250 rpm, and the pellets transferred to 2L of LBE auto-induction media (supplemented with Ampicillin antibiotic) at 37°C for 3-4 h and later switched to 21°C over two nights.

Preparing 1L LBE media was made by adding together 10 g Bacto-tryptone (1%), 5 g Bacto-yeast (0.5%), 2.68 g ammonium chloride (50 mM), 0.71 g sodium sulphate (5 mM), 5 g glycerol (0.5%), 0.5 g glucose (0.05%), 2 g lactose (0.2%) and making up the solution to 1L with ultra-pure MilliQ water (ddH_2O). The solution was then autoclaved then cooled to room temperature for addition of the following, 1 mL 2M magnesium sulphate (2 mM, 0.22 µm filter sterilized), 40 mL of 1M K_2HPO_4 (40 mM, 0.22 µm filter sterilized), 10 mL of KH_2PO_4 (10 mM, 0.22 µm filter sterilized) and 1 mL of trace metal mix (0.22 µm filter sterilized). The trace metal mix was prepared as follows: 0.5 ml of 10 N HCl was added to 49.5 ml of ddH_2O to make 0.1 M HCl. In this was dissolved 1.35 g $FeCl_3 \cdot 6H_2O$. A further 36 mL of ddH_2O, followed by 2 ml of 1M $CaCl_2$, 1 ml of 1M $MnCl_2$, 1 ml of 1M $ZnSO_4$, 1 ml of 0.2 M $CoCl_2$, 2 ml of 0.1 M $CuCl_2$, 1 ml of 1M $NiCl_2$ were then added, and the solution finally made up to 100 mL using ddH_2O. The solution was then sterilized through a 0.22 µm filter and stored at room temperature.

2.14 Protein extraction

Post-auto induction, the cultures were centrifuged at 3000 rpm, 4°C for 20 min. The pellets were suspended in 20 mL DPBS and to lyse the cells sonication (DAWE soniprobe) was performed on ice at 70% power (100 watts), with four 15 s pulses. Centrifugation was repeated at 14,000 rpm, 4°C for 30 min and the supernatant collected and passed through 0.22 µm filter. 1 ml of pre-washed Qiagen Ni-NTA was added to the supernatant which was then kept on roller overnight at 4°C.

2.15 Protein purification

2.15.1 Affinity Chromatography

Purification of the extracted protein was performed in two steps. First, we employed affinity chromatography using Qiagen Ni-NTA beads which captured the N-terminal 10-His tags on our protein. The protein extract and Ni-NTA beads mix was first placed on gravity columns and the beads subsequently washed with PBS solution containing added 0.5M NaCl and 20 mM imidazole. Later, 14 ml of 500 mM imidazole solution in PBS/0.5M NaCl was used to elute the protein. The eluted proteins were centrifuged in appropriate MWCO vivaspin protein concentrators at 6000g, 4°C to concentrate to 2.5 mL volume. GE healthcare PD-10 desalting columns were later used to remove imidazole and exchange buffer to DPBS.

2.15.2 Size Exclusion Chromatography (AKTA)

Before injecting the protein sample into a Superdex 75 300/15 column (GE healthcare), the column was thoroughly washed with degassed 10% acetic acid and DPBS. Protein samples were also passed through a 0.22 µm filter to remove any debris that could clog the column. All the peaks (A_{280} absorption) were collected separately, and SDS-PAGE Western blot performed to check for the correct peak and its purity, visualized through Coomassie staining. The collected samples were concentrated again using appropriate molecular wight cut-off vivaspin protein concentrator and quickly frozen using liquid N_2 in small 50-100 µL aliquots and stored in a -80°C freezer.

The purity of the recombinant proteins were visually assessed by Western blot followed by Coomassie staining. At least 1 µg/well of purified protein sample mixed with the appropriate volume of 4X LDS buffer and 10mM DTT, was placed at 70°C for

10mins, then cooled down before running on 4-12% Bis-Tris SDS-PAGE gel (Invitrogen) with 1X MES buffer at 200 V for 30 min. After the end of the run, the gel was washed three times with distilled water and Coomassie blue stain (0.1% (w/v) Coomassie blue R350, 20% (v/v) methanol, and 10% (v/v) acetic acid) added and kept in shaking for 1h at room temperature. The gel was washed again three times with distilled water and destaining solution (50% (v/v) methanol in water with 10% (v/v) acetic acid) added and kept on shaking until protein bands became clearly visible from the background.

2.16 Phage display – Single chain fragment variable (ScFv)

Three 5 mL round bottom polystyrene tubes were coated overnight with 10 µg/mL protein (in PBS). The protein solution is then removed and 3% milk (in PBS) added for blocking for 1 h. Next the tubes were washed three times with PBS and 500 µL of phage were added to the negative selector ($Na_v1.5$ CTD for $Na_v1.7$ and vice versa) for 10 mins. The naïve scFv phage display library used has been made by Dr. Samir Hamaia (Dept. of Biochemistry, University of Cambridge, UK). Another round of deselection was repeated with the unbound phage. Next, the unbound phage in the supernatant were added to the target selection protein for 1 h followed by ten times washing with PBS + 0.05% Tween20 and ten times with PBS to fully remove unbound phage. 50 ul Trypsin (2 µl/ml Trypsin, 50mM Tris, 0.1mM $CaCl_2$) was added for 15 min to elute the bound phage which were incubated with 5 ml TG1 E. coli, OD_{600} 0.5 (37°C, 170 rpm, 1 h). Centrifugation was performed at 3000 rpm for 7 min at rtp to remove the media and the pellets were gently resuspended in 2TY LB media. 150 µl were added on two 2TY LB agar plates for incubation overnight at 30°C. (A 10-fold serial dilution was also carried out, with 50 µl of each dilution plated, to give an indication of clone diversity and library size). Next, the bacteria were harvested using freezing media (65% 2TY, 2% glucose, 17% glycerol, 100 µg/ml ampicillin). The volume required for OD_{600} of 0.1 was added to 5 ml of 2TY media and incubated (37°C, 180rpm, 1 h). 100 µl helper phage were added and incubation was continued for 1 hr at a lower speed of 165 rpm to facilitate phage binding to bacterial surface receptors. The culture was centrifuged twice at 3000 rpm for 5 min at rtp, to remove the glucose containing media completely. The bacteria were incubated overnight at 30°C in 10 ml 2TY media (100 µg/ml ampicillin, 50 µg/ml kanamycin, no glucose)

before centrifugation (13000 rpm, 10 min) to isolate phage. This was repeated for a second cycle with the infected bacteria inoculated in 10 mL 2TY to give OD_{600} of 1 (37°C, 180 rpm, 2 h). After centrifugation (7830 rpm, 5 min, rtp), the media was replaced with 0.5 ml PBS and a miniprep was carried out using QIAcube. 10 µl of Nco1 and Not1 restriction enzyme were added to 50 µl pSANG4 plasmid to excise the scFv gene[259,260]. 10 µl were added to 3 µl of pSANG10 vector with 4µl T4 ligase in 13 µl H_2O and left for 2.5 h. 8 µl ligated plasmid were transformed into 50 µl Bl21 bacteria (42°C, 15s heat shock).

Using sterile pipette tips, colonies were added to wells of a 96-well plate containing 100 µl 2xTY (50 µg/ml kanamycin), and to wells containing 150 µl LBE (50 µg/ml kanamycin). The plates were incubated overnight (400 rpm, 37°C). 25 µl glycerol was added to the 2xTY plates for freezing at -80°C.

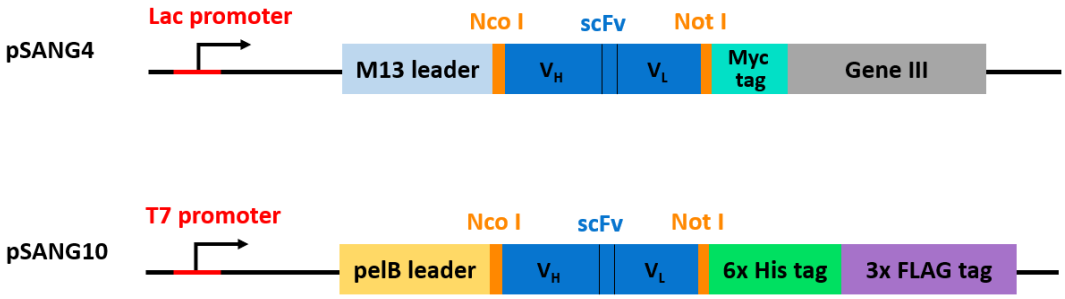

For the screening assay, 50 µl of 3% milk were added to the LBE wells to make up for volume lost through evaporation.

Figure 2.2. Phagemid pSANG4 vector and bacterial pSANG10 vector (based on Martin *et* al., 2006 and Schofield *et* al., 2006). The scFv gene, fused to Gene III, is encoded between Nco I and Not I restriction sites, allowing excision from pSANG4 and ligation into pSANG10. pSANG10 was then used for periplasmic expression of scFv, as the pelB leader sequence helps direct the expressed protein to the periplasm. The 6x His tag was used for purification using Ni-NTA beads and 3x FLAG tag for detection. This image was made by Roshni Mistry (part II student, Dept. of Biochemistry, University of Cambridge)

2.17 ScFv screening assay

96 well Immulon 2B ELISA plates were coated overnight at 4°C in pairs, either with 100 µL (10 µg/mL in PBS) of $Na_v1.5$ CTD or with $Na_v1.7$ CTD. On the following day the protein solution were removed and 200 µL of 3% milk added for blocking for 1h, to reduce non-specific binding. The milk was then removed and the plate washed three times with PBS + 0.05% Tween20 and 50 µl of ScFV clones from the LBE wells were added to the corresponding wells of pairs of plates for 1-2h. Plates were washed again three times with PBS + 0.05% Tween20. 100 µL of anti-FLAG (HRP) antibody was added at a concentration of 1:10,000 for 30mins followed by washing steps for three more times. Next 100 µL of TMB substrate was added and blue coloration observed within few minutes (maximum wait time 10 min) and immediately 100 µL of 2M H_2SO_4 added to stop the reaction. The plates were then read for absorbance at 450 nM using plate reader.

Clones that recognized specifically one type of the CTD and not the other and showed the largest absorbance value were chosen to be grown in 3 mL 2TY culture for plasmid extraction. These plasmids were then sequenced to check for unique clones.

2.18 ScFv clone expression

200 ng plasmids of the selected clones were transformed in BL21 (DE3) using heat shock at 42°C for 15 s and plated on 2TY LB agar plate containing 2% glucose and kanamycin (50 µg/ml) and kept at 37 ºC overnight. A single colony was selected to prepare a starter culture of 5 mL 2TY LB media containing kanamycin and 2% glucose at 37°C for 6 h at 250 rpm. The culture was centrifuged, and the pellets inoculated in freshly prepared 100ml of the same media to grow overnight at 30°C at 250 rpm. Next day the culture was centrifuged, and the pellets transferred to 1L of LBE auto-induction media (containing all the added supplements as mentioned previously) at 37°C for 3-4 h at 200 rpm and later switched to 30°C overnight and on the next day 21°C overnight.

2.19 ScFV clone extraction and purification

For periplasmic extraction, first the 1L cultures were centrifuged at 3000 rpm for 20 min at 4°C. Next, 50 mL of cold TES buffer (30 mM Tris-HCl, 1 mM EDTA, 20% sucrose, pH 8) supplemented with one Roche cOmplete Protease Inhibitor cocktail tablet and 100 µL of deoxyribonuclease I from bovine pancreas were added and the pellets suspended. After 10-20 min on ice, centrifugation at 9000 rpm, 4°C for 20 min was performed and the supernatant stored on ice. The pellets were resuspended on 50 mL of 5 mM $MgSO_4$ supplemented with one Roche cOmplete Protease Inhibitor cocktail tablet and 100 µL of deoxyribonuclease I from bovine pancreas. After 10-20 min on ice, centrifugation at 9000 rpm, 4°C for 20 min was performed and the supernatant stored added to the previously collected supernatant. The combined supernatants were centrifuged at 14000 rpm, 4°C for 30 min to remove any remaining cell debris and passed through 0.22 µM filter. The volume of TES buffer and 5 mM $MgSO_4$ used for the extraction was adjusted according to the volume of the pellet in the ratio 1:20.

For purification of these His-tagged scFv, every 50 mL of lysates were mixed with 1 mL of Ni-NTA beads (Qiagen), overnight on a roller at 4°C. Next day this mixture was placed on a gravity filter and beads collected at the bottom of the tube as the lysates were allowed to pass through. These beads were washed with PBS solution containing extra 0.5M NaCl and 20 mM Imidazole. Later, 14 ml of 500 mM imidazole solution in PBS/0.5M NaCl was used to elute the protein. The eluted proteins were centrifuged in 10 kDa molecular weight cut-off vivaspin protein concentrators at 6000g, 4°C for buffer exchange to DPBS. 50 µL aliquots of were flash frozen using liquid Nitrogen and stored at -80°C. Purity of the scFv were ascertained by Western blotting followed by Coomassie staining.

2.20 ELISA

2.20.1 Interaction between $Na_v1.7$ CTD (C7) and calmodulin (CaM)

Immulon 2HB 96-well ELISA plates (Fisher) were used for this assay. The wells were coated with 100 µL of either 10 µg/mL $Na_v1.7$ CTD (C7), 10 µg/mL $Na_v1.7$ CTD EF hand (7EF), or 3% BSA (bovine serum albumin), overnight at 4°C. The C7 and 7EF samples were either prepared in 5 mM $CaCl_2$, 5 µM $CaCl_2$, or 10 mM EGTA and wells were coated separately with each. The next day, after removing the coating solution,

all the wells were blocked with 200 µL of 3% BSA for 1 h at room temperature (rtp). The plate was then washed with PBST (0.05% Tween20) three times and 100 µL of 10 µg/mL calmodulin added to each well, Ca^{2+}-CaM being added to wells that were coated with samples containing Ca^{2+} in the buffer, while apoCaM (10 mM EGTA) was added to the wells coated with samples containing 10 mM EGTA. After 2 h, the plate was washed four times with PBST. Next, 100 µL of anti-calmodulin antibody (ThermoFisher) at 1:3000 concentration was added to all the wells for 2 h, followed by four times PBST washes. Next, 100 µL of secondary goat anti-mouse -HRP antibody was added to all the wells for 1h followed by four times washing with PBST. Then 100 µL of TMB substrate (ThermoFisher) was added to all the wells and the characteristic blue coloration observed in wells where TMB interacted with HRP. This reaction was allowed to continue for 10mins before addition of 100 µL of 2M H_2SO_4 to terminate, turning the blue colors to yellow. Fluostar optima plate reader was then used to measure absorbance at 450 nM. Results were analysed using two-tailed student's t-test and statistical significance was assumed when $p < 0.05$.

2.20.2 Examining whether C5 and C7 specific scFv clones recognized their respective truncated version, 5EF and 7EF

96 well ELISA plates were coated with 100 µL of 10 µg/mL C5, 5EF, C7, 7EF and BSA (control) in separate wells, overnight at 4°C. The samples were removed, and the wells blocked with 200 µL of 3% BSA for 1h at room temperature. Three times PBST washes were then performed before addition of 50 µL of the C5 specific clones (3A5, 3A11, 3B5, 3C5, 3D9, 3G9, 3H1, 4B3), from LBE cultures grown overnight, on the wells coated with C5, 5EF, C7 (to confirm deselection) and BSA for 1h at rtp. The same was done for the C7 specific clones (2G11, 4G9, 5C4, 5D7, 6A4, 7A12, 7D6) which were added to C7, 7EF, C5 (to confirm deselection) and BSA. Next four times PBST wash followed by addition of 100 µL anti-FLAG-HRP antibody (Abcam) at 1:20,000 dilution (in 3% BSA) for 1h at rtp. This step is followed by four PBST washes, then addition of 100 µL of TMB substrate for 10mins before adding 100 µL of 2M sulphuric acid. Absorbance reading at 450nM was then performed using the plate reader.

After further purification of selected few scFvs (3C5 and 3H1 of C5 specific and 5C4 and 5D7 of C7 specific), the ELISA mentioned above was repeated and 100 ng of scFv clone used per well.

2.20.3 Effect of apoCaM on scFv binding to C5 and C7

Multiple wells were separately coated with 100 µL of 10 µg/mL of either C5 or C7 prepared in PBS buffer containing 10 mM EGTA, overnight at 4°C. Some wells were coated with 3% BSA as control. Next day, samples were removed from the wells and four PBST washes performed. Then 100 µL of 10 µg/mL of apoCaM (made in PBS containing 10 mM EGTA) were added to all the wells for 1h at rtp. Four more PBST washes followed and then the scFv clones specific to each subtype of Na_v CTD were added accordingly at 100 µL of 1 µg/mL, for 1h at rtp. Next four washing steps with PBST was performed again and 100 µL anti-FLAG-HRP antibody (Abcam) at 1:20,000 dilution (in 3% BSA) for 1h at rtp added. This step was followed by four PBST washes, then addition of 100 µL of TMB substrate for 10 min before adding 100 µL of 2M H_2SO_4. Absorbance reading at 450 nM was then performed using the plate reader. Results were analysed using two-tailed student's t-test and statistical significance was assumed when $p < 0.05$.

2.21 Isothermal Titration Calorimetry (ITC)

Purified recombinant proteins, $Na_v1.5$ CTD, $Na_v1.7$ CTD and calmodulin were dialysed using 2 kDa molecular weight cut-off membranes (ThermoFisher) overnight at 4°C with slow stirring in 1L DPBS (pH 7.4) mixed with either 5 mM $CaCl_2.2H_2O$ or 10 mM EDTA. The protein concentrations were quantified using nanodrop A_{280} reading and diluted with respective dialysate to 30 µM for the CTDs and 300 µM for calmodulin. This step ensures that all the proteins are in identical buffer which will reduce large heats of dilution (background heats) from masking the experimental observations. The dialysates were then used to wash the cell and syringe three to four times. Next, one of the CTDs was loaded inside the cell taking care not to introduce any bubbles. The syringe was then filled with the calmodulin solution and the needle placed inside the cell before the start of the experiment. During the run the stirring was maintained at 750 rpm and temperature at 25°C. Injections were started once the DP (µcal/s) reached at least 5.0. After the initial 0.4 µL injection, total 20 injections were made of 2 µL each, every 2 mins. All data were collected, using the MicroCal

iTC200 (Ge Healthcare), and analyzed using the Origin Plugin (OriginLabs) provided with the instrument for subtracting reference and fitting of a standard one site binding model.

2.22 Biolayer interferometry (BLI)

The machine was switched on ahead of time to allow enough time for the lamp to warm up which helps minimize noise and drift in recordings. The temperature was set at 25 °C and shake speed at 1000 rpm. Measurements were made using the OctetRed96 (ForteBio) using Anti-Penta-HIS (HIS1K) Dip and Read Biosensors (ForteBio). The biosensor was hydrated in a 96-well plate on 200 µl PBS buffer (same as used for protein) for 10 min. All the protein sample buffers contained 0.05% Tween20 and 10mM EDTA. The experiment was started with a 60 s baseline step with the sensors in the buffer. Next for the loading step 200 µL of the His-tagged proteins (10 µg) were allowed to immobilize on the sensor for 300s. To wash away any unbound non-immobilized protein, an additional 60s of baseline step was performed. This step also established a new baseline with the anti-His sensors now bound to the His-tagged proteins. Next, a 60 s association step was performed with 4 different concentrations of calmodulin (1000 nM, 200 nM, 40 nM and 8nM) followed by a 120s dissociation step with the sensors being placed back into wells containing just the buffer. Finally for regeneration the sensors were place in wells containing 10 mM glycine, pH 1.5 for 30s. The same experiment was repeated with buffer containing 5 mM $CaCl_2$ and then again by increasing concentration of calmodulin 100-fold i.e. 100 µM, 20 µM, 4 µM and 0.8 µM. A further control step was also performed where the binding partner, calmodulin, was added to sensors before immobilization of His-tagged proteins. Data was analyzed and graph fitted with global fitting (model 1:1).

2.23 X-ray crystallography

The full length and truncated ($Na_v1.7$ EF-hand) $Na_v1.7$ CTD, at a concentration of 11 mg/mL and 15 mg/mL respectively, were chosen for crystallization trials. Protein expression and purification was performed as mentioned previously. The proteins were in a buffer containing 50 mM Tris HCl, 140 mM NaCl, pH 7.4. The sitting drop vapour diffusion method was used for the crystallization trial experiment on 96 wells, 2 drops, MRC-type plates (compatible with Rock Imager software) using Mosquito from FORMULATRIX. The crystallization drops contained protein solution and

crystallization condition in either 2:1 or 1:1 ratio, for e.g. 200 nL of protein solution with 100 nL and 200 nL of crystallization condition in the two separate wells. For optimization, up to 400 nL of protein solution and crystallization condition were used. Initially the following commercially available crystallization screens were used: JCSG+ (Molecular Dimension), BCS (Molecular Dimension), LMB Screen (Molecular Dimension), PACT Suite (Molecular Dimension), MIDAS (Molecular Dimension), Morpheus (Molecular Dimension), Wizard I and II (Molecular Dimension), Wizard III and IV (Molecular Dimension), Classic Lite Suite (Qiagen), PEGS I Suite (Qiagen) and PEGS II Suite (Qiagen). Initial screening mostly produced thin needle like and rod-shaped crystals from Morpheus, Wizard III and IV, PACT, JCSG+ and BCS plates. Images were taken under bright, UV and cross-polarized light. Crystals were fished using Cryoloops (0.1-0.2 mm) and flash frozen in liquid nitrogen. The loops were then stored in pucks and sent to Diamond Light Source. 3D-diffraction data from all the crystals were collected at the beamlines IO4 or I24 of the synchrotron at Diamond Light Source, shot at a wavelength of 0.9999 Å, exposure of 0.050s.

2.24 Automated Patch clamp

The same protocols for steady-state activation, steady-state inactivation and recovery from inactivation were employed as mentioned previously. The only difference made was the second fixed voltage pulse was set at -10 mV for the $Na_V1.7$ expressing cells compared to the -40 mV usually used for $Na_V1.5$ expressing cells. Nanion's patchliner (Nanion Technologies, Munich, Germany) was used for automatic whole cell patching of HEK293F cells stably expressing either $Na_V1.5$ or $Na_V1.7$. The stable cell lines were made by Hengrui Liu (PhD student, Tony Jackson group, Dept. of Biochemistry, University of Cambridge, UK). The same pipette solution and bath solution were used as mentioned previously, except either 500 nM of scFv or equal volume of the scFv buffer (PBS) was added to the pipette solution. The same statistical analysis was also performed.

2.25 *In silico* docking

To better understand how and where the scFvs were binding to the CTDs, *in silico* docking was performed using ClusPro 2.0 server[261]. The advanced option of antibody mode was employed without automatic masking of non-CDR regions[262]. The results were then analyzed and imaged using PyMol software and statistical analysis, two-tailed Student's t-test, performed using GraphPad Prism 9 software.

Chapter 3

Structural and Functional role of extracellular loops

3.1 Introduction

Germline *SCN5A* mutations that reduce or abolish channel activity are associated with inherited, autosomal dominant cardiopathologies, including Brugada syndrome (BrS) and sinus node dysfunction (SND). BrS is characterized by ventricular tachyarrhythmias and syncope. SND is also associated with bradyarrhythmias involving the sinus node; although in practice, the BrS and SND phenotypes can clinically overlap. BrS accounts for a significant fraction of sudden death in young to middle-aged patients[263]. Because almost all BrS and SND patients are heterozygous, they typically exhibit about a 50% reduction in the level of functional $Na_v1.5$ compared to phenotypically normal individuals. This reduction can compromise action potential conduction velocities and precipitate arrhythmogenicity[264]. Several *SCN5A* deletion and missense mutations associated with BrS and SND, prevent the folding of the $Na_v1.5$ channel and lead to its retention in the endoplasmic reticulum (ER)[265]. Other missense mutations do not prevent folding but disrupt channel activity because they occur in regions known to be functionally important, such as the S4 helices or the inactivation gate[266]. However, some BrS/SND missense mutations occur in regions where the association with sodium channel function is less clear. Such mutations are likely to be particularly informative, both structurally and therapeutically, as they may reveal new insights into Na_v channel behaviour. This class of mutation is exemplified in an individual with a BrS/SND-like pathology who was heterozygous for the $Na_v1.5$ missense mutation R878C, a residue located on the DII extracellular turret loop connecting its S5 and re-entrant P1 helices (Figure 3.1A). When tested by heterologous expression, the mutant displayed a complete loss of function, despite normal $Na_v1.5$ expression on the plasma membrane[154]. Two similar BrS-associated $Na_v1.5$ mutations, D1430N and E1441Q are located on the DIII extracellular turret loop connecting its S6 and re-entrant P2 helices (Figure 3.1A). The D1430N mutant displays a complete loss of function[98]. In the case of E1441Q, no experimental analysis of its gating behaviour has yet been described[80].

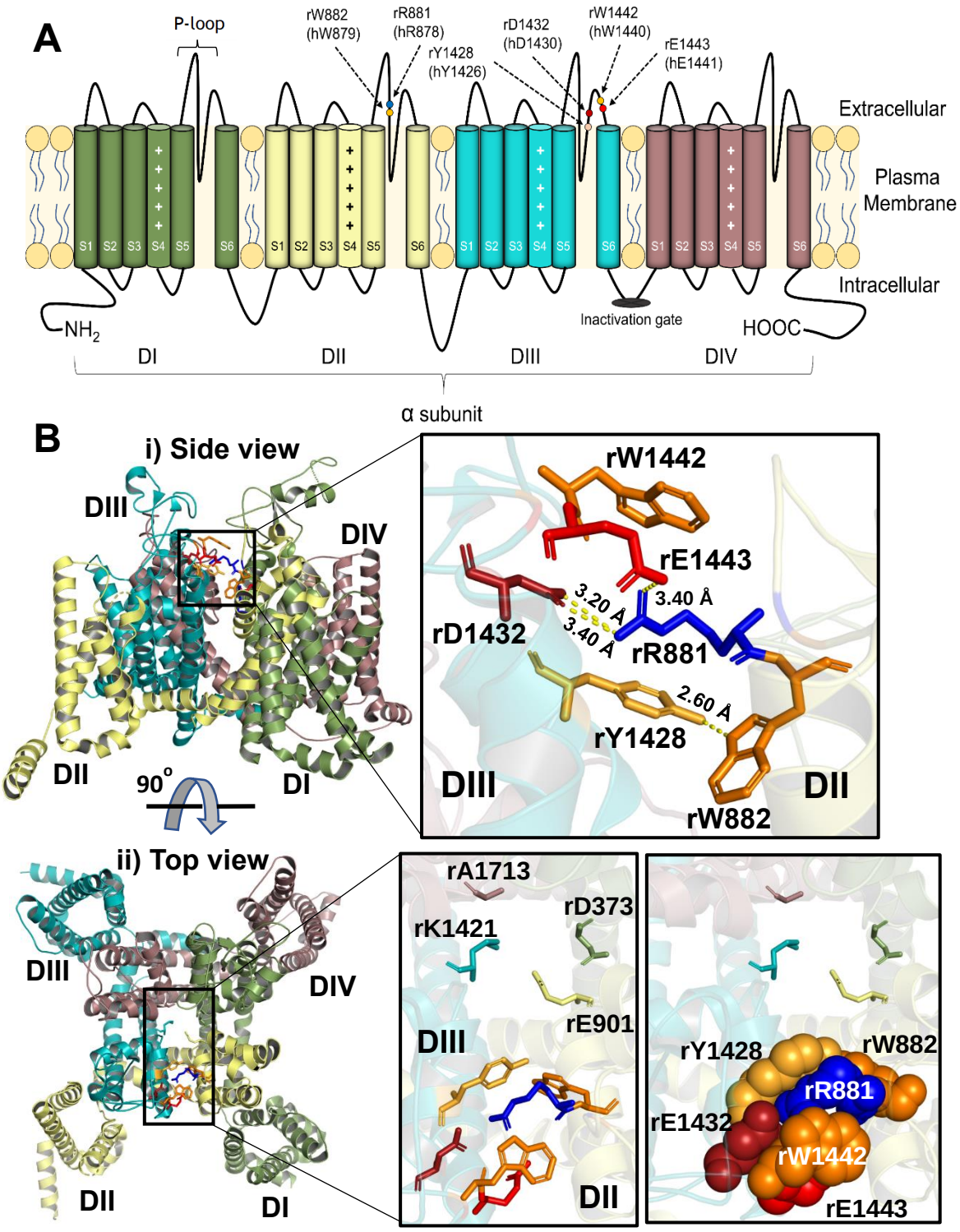

Figure 3.1. A complex salt bridge and cation-π interactions within the Nav1.5 DII-DIII extracellular turret. A. Schematic representation of the Nav1.5 channel. The N and C-termini, the inactivation gate, the four homologous domains, DI-DIV, the transmembrane alpha-helices S1-S6 and the DI p-loops are indicated. The positive charges on the S4 helices of each domain are also indicated. The helices S5 and S6 line the channel pore and the positively charged S4 helices function as the voltage sensor. The positions of amino acid residues at the extracellular turret DII-DIII interface studied in this project are indicated for both human (h) and rat (r) Nav1.5 sequences. **B.** The rat Nav1.5 structure (PDB ID: 6UZ3), showing the topology of the channel from i), the side view and ii), the top view. The DII-DIII turret interface residues are highlighted in the enlarged images. In i), the enlarged image shows the approximate bond distances. In ii), the right-hand enlarged image displays the interface residues as spheres, to show their packing. The left-hand enlarged image shows the position of the DEKA residues relative to the DII-DIII interface.

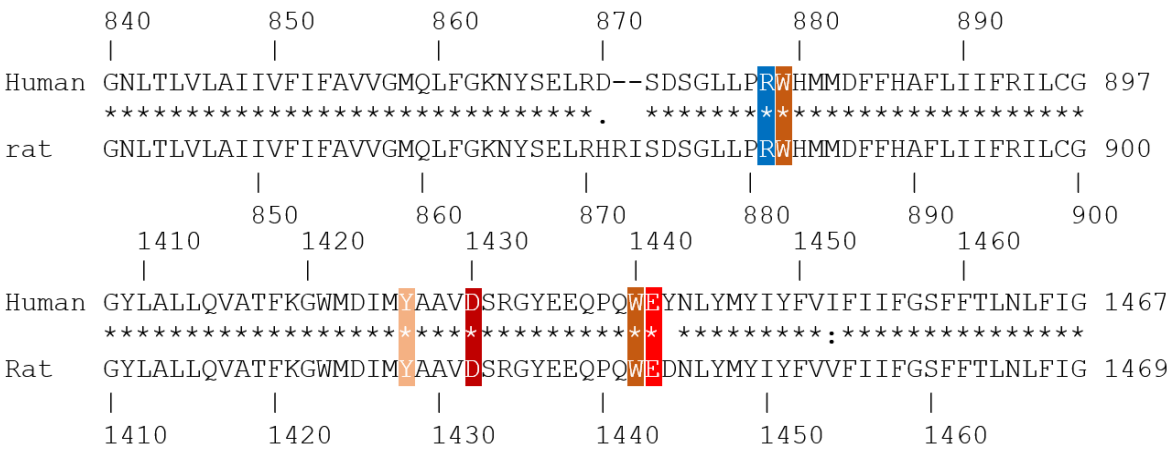

Figure 3.2. Primary sequence alignments of human Nav1.5 (Uniprot ID: Q14524-1) and rat Nav1.5 (Uniprot ID: P15389-1). The residues discussed in the text are highlighted in color.

* Amino acids that are identical between species.

: Amino acids that show conservative changes between species.

. Amino acids that show semiconservative changes between species.

Table 3.1. Left: The equivalent human (h) and rat (r) residues for the amino acids studied in this current work are listed. Right: The human (h) Nav1.5 mutations used in the electrophysiological and biochemical assays and the equivalent rat (r) Nav1.5 mutants examined by MD simulation are shown.

Human	Rat
R878	R881
W879	W882
Y1426	Y1428
D1430	D1432
W1440	W1442
E1441	E1443

Human Nav1.5 mutations used in functional assays	Equivalent rat Nav1.5 mutations, modelled by MD simulation
W1440Y	W1442Y
W1440A	-
Y1426F	-
Y1426W	-
Y1426A	-
E1441D	E1443D
D1430E	-
E1441Q	E1443Q
R878C	-
W879Y	-
W879A	-
R878E/E1441R	-
R878C/E1441C	-
R878D/D1430R	R881D/D1432R
R878C/D1430C	-

Figure 3.3. Sequence alignment analysis using Clustal Omega, of all the different isoforms of hNa_v show that the $Na_v1.5$ D1430 and E1441 are entirely conserved whereas other than the Histidine residue in place of arginine in $Na_v1.9$, the R878 is also well conserved. It is interesting to observe that arginine of $Na_v1.9$ has been replaced by Histidine which also contains positively charged side chain, ensuring conservation of a positive charged moiety in that region among all isoforms. The hydrophobic residues W879, Y1426 are fully conserved and in the position of W1440, some Nav contain Tyrosine and $Na_v1.9$ contains Phenylalanine, changes which are considered very conservative within the subtypes.

* Amino acids that are identical between species.

: Amino acids that show conservative changes between species.

. Amino acids that show semiconservative changes between species.

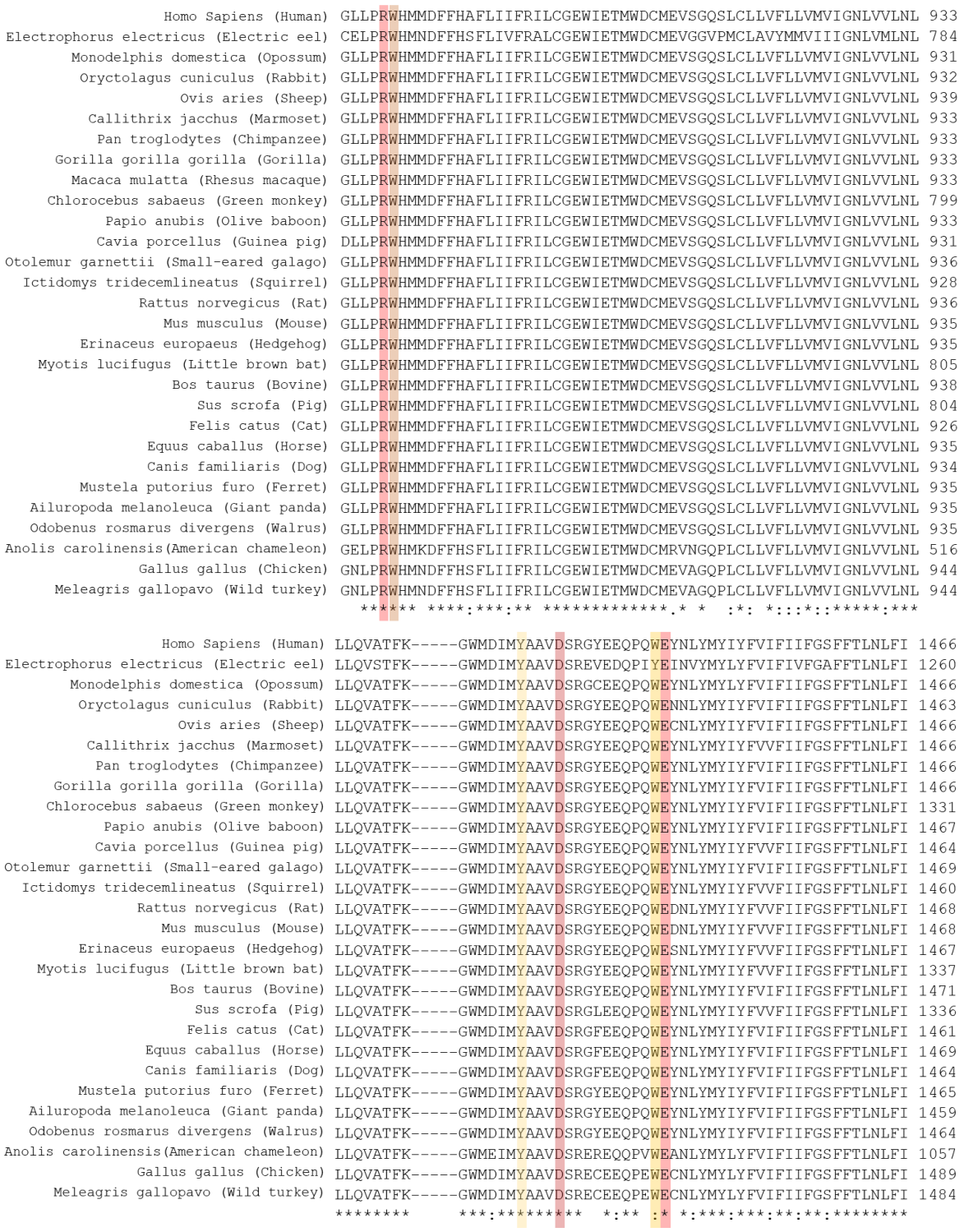

Figure 3.4. Sequence alignment analysis using Clustal Omega of $Na_V1.5$ among different species shows that both the salt bridge forming residues R878, D1430 and E1441 are highly conserved and the hydrophobic residues W879 and Y1426 are also fully conserved, while W1440 is highly conserved among all the species.

* Amino acids that are identical between species.

: Amino acids that show conservative changes between species.

. Amino acids that show semiconservative changes between species.

The structure of rat $Na_v1.5$ has been determined by cryo-EM[27] and hence can be used to identify the locations of these residues. However, there are small insertions and deletions between the human and rat sequences, so that the corresponding residue positions are not identical (Figure 3.2). Thus, human R878 is equivalent to rat R881, human D1430 corresponds to rat D1432 and human E1441 corresponds to rat E1443. For clarity, both the human and the equivalent rat $Na_v1.5$ residues that were experimentally studied are indicated in (Figure 3.1 A) and are summarized in Table 3.1.

Interestingly, in the rat $Na_v1.5$ structure, the positively charged guanidinium group of R881 on the DII turret lies less than 4Å from the negatively charged carboxylate groups of D1432 and E1443 on the adjacent DIII turret (Figure 3.1B)[27]. This arrangement is consistent with a complex salt bridge, in which more than two charged residues interact[267,268]. Moreover, the charged residues are sandwiched between the side chains of rat Y1428 (equivalent to human Y1426) and rat W1442 (equivalent to human W1440) on the DIII turret, such that both the aromatic rings lie in register with, and less than 4Å, from the delocalised positive charge on the R881 guanidinium group. This is consistent with cation-π interactions[269]. In addition, residue Y1428 on the DIII turret forms a hydrogen bond with W882 (equivalent to human W879) on the DII turret (Figure 3.1B). Thus, several independent $Na_v1.5$ mutants that are associated with BrS/SND occur in residues that together form a structurally interacting cluster at the DII-DIII turret-loop interface. Moreover, all these residues are very highly conserved, not only among all the human Na_v subtypes but also across species as indicated in Figure 3.3 and Figure 3.4.

3.2 Objectives and Hypothesis

The overall aim of the present study was to investigate the existence and functional consequences of predicted complex salt bridge interactions between the highly conserved R878 (DII, S5-6), D1430 (DIII, S5-6) and E1441 (DIII, S5-6) in Na^+ channel function. Furthermore, the predicted cation-π interaction between Y1426 (DIII, S5-6) and W1440 (DIII, S5-6) with the delocalized positive charge of R878 would also be looked at and its importance in channel function determined. Finally, Y1426 is predicted to form hydrogen bond with W879 (DII, S5-6), which could have effects on channel gating, would be further investigated. I have adopted the following steps in my approach.

I first investigated whether, in common with Na_v channels that contain the R878C and D1430N mutations, channels containing the Na_v E1441Q mutation, similarly a natural mutation associated with BrS, also successfully trafficked to the plasma membrane. Moreover, the W1440 residue will be mutated to W1440Y, a conservative mutation, and W1440A which should show the most drastic effect since Alanine has no hydrophobic side chain. Similar mutations will be made on the W879 and Y1426 residues. Additionally, for Y1426, an even more conservative mutation to Y1426F will be made, since Phenylalanine simply has a single hydroxyl group missing, this mutant would be unable to take part in hydrogen bonding with W879. To check plasma membrane trafficking, immunostaining followed by confocal microscopy and cell surface biotinylation would be employed. The fact that R878C and D1430N are trafficked has already been demonstrated [98,154].Patch clamp experiments will then confirm whether, and how the mutation affects channel activity. Although there are published reports describing expression and functional Na_v changes associated with the R878C and D1430N mutants, similar reports are not available for E1441Q or the rest of the mutants that would be generated. Seeing how the sliding-helix model predicts how the channel S5-S6 helices move during different states of the channel (closed, activated, or inactivated), these salt bridge and cation-π interactions could show dynamic behaviour, being formed and broken as the channel moves between different states[31,270]. If any channel shows loss of activity, like in the case of R878C, veratridine, Na_v channel activator, will be used to try and rescue its activity.
I will next perform extensive disulphide-locking experiments using the R878C/E1441C and R878C/D1430C double mutants. Again, due to proximity of both the residues,

this should form a di-sulphide bond, locking the channel in either the activated or inactivated state. Conversely, adding ß-mercaptoethanol should help break the di-sulphide bond and release the channel from the locked open or close position, showing up as either sudden emergence of current or sudden termination of current, during repetitive depolarizations, depending on whether the channel gets locked in the activated or inactivated state [271].

To the latter end, I will generate double mutants R878E/E1441R and R878D/D1430R, which should then allow the channel to regain the activity that was lost in the R878C mutant. Thus, the double mutation would then retrieve the potential salt bridge formation.

Also, it has recently been observed that the Ig domains of ß3-subunits can form trimers which means that they can potentially induce oligomerization of at least up to three α-subunits[46]. Whether the R878C mutation, in the DII, S5-S6 extracellular pore-loop region, disrupt the binding of ß3-subunit to $Na_V1.5$ will be tested using co-immunoprecipitation.

Finally, as part of a very close collaboration, where I was involved with the overall design and interpretation of the work, Manas Kohli and Dr. Taufiq Rahman (Pharmacology, University of Cambridge) performed the molecular dynamics (MD) simulation of some of the key residues (Table 3.1) using Gromacs 2020.4 with CHARMM36 force fields, on the cryo-EM structure for rat $Na_V1.5$ (PDB ID: 6UZ3). This should inform us whether these mutations affect the global and local stability of channel and any long-range disruption they may cause, e.g., to the pore geometry.

3.3 DNA sequencing confirms successful generation of mutants

Figure 3.5. DNA sequencing confirm successful mutant generation.

Few examples of the sequences of mutants used in this study (Seq_2) are aligned with the WT Nav1.5 sequence (Seq_1) to show the location of the mutations (boxed in red).

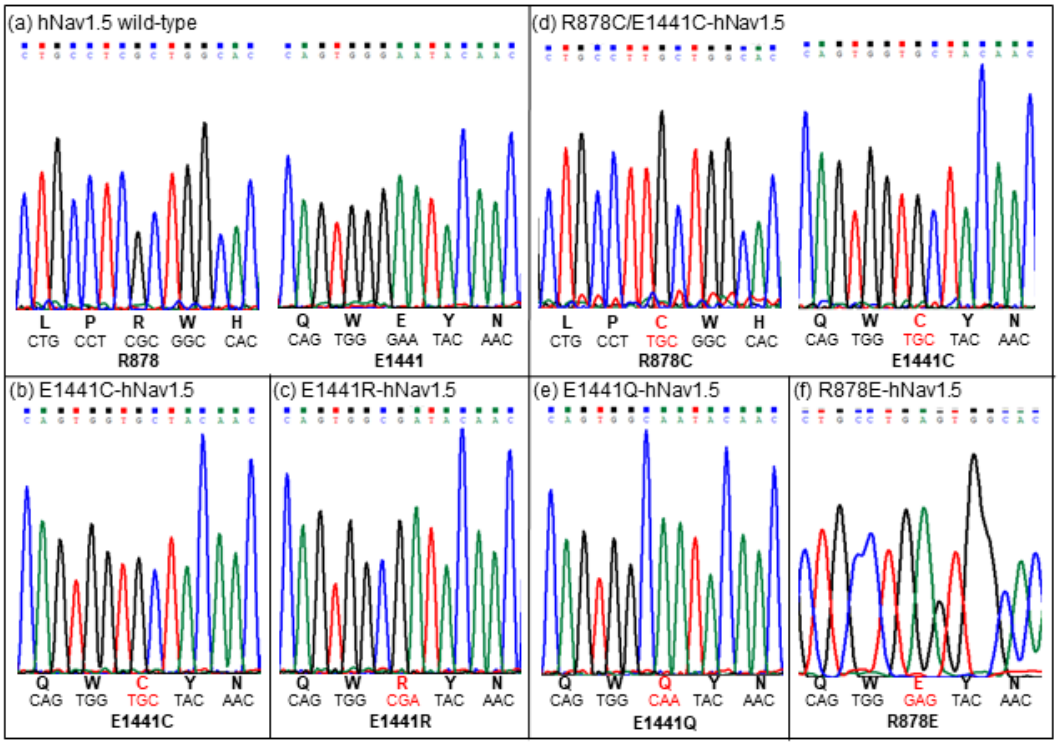

Figure 3.6 Chromatogram showing the sequences of WT hNav1.5 (a) and sequences of some of the mutated hNav1.5 with the nucleotide changes made to generate the point mutations highlighted (b,c,d,e,f).

3.4 HEK293f transfection efficiency

Transfection of HEK293f cells using PEI has been performed for patch clamp, co-immunoprecipitation, and confocal microscopy experiments. As can be observed in Figure 3.7, using Leica DMI 6000 CS microscope to image GFP fluorescence, the transfection efficiency remained unchanged for mutants when co-transfected with either $Na_v1.5$ WT or ß3 subunit. These initial characterizations were performed in a limited number of mutants since more robust methods to study plasma membrane trafficking has been employed as discussed below.

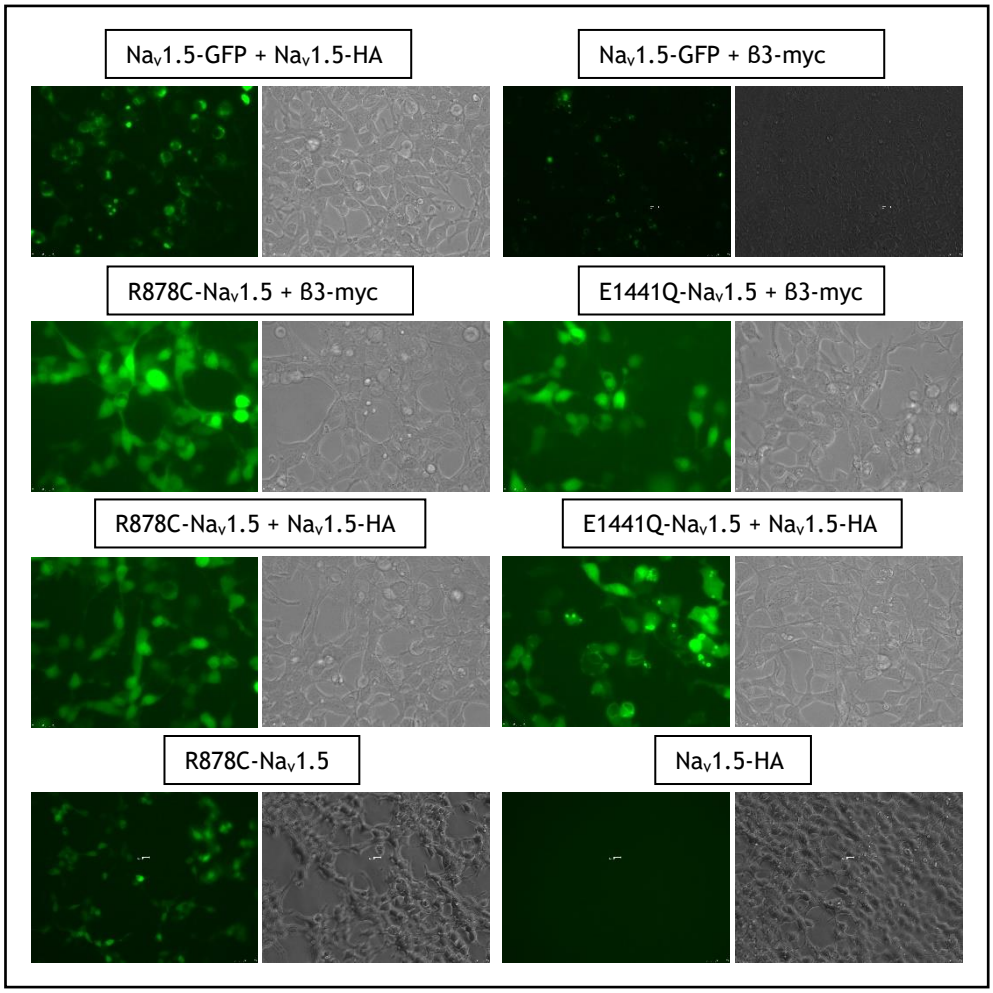

Figure 3.7. Transfection efficiency was determined by Leica DMI 6000 CS microscope by the imaging of the GFP fluorescence and phase contrast post 48h of transfecting 8µg of total plasmid DNA as shown in the label of the images. Unlike the $Na_v1.5$-GFP which is cloned in pcDNA3.1-GFP, the R878C and E1441Q were cloned in bicistronic pIRES vector which expresses GFP unlinked to the mutant channel protein, hence the more diffused signal observed in the microscope images. $Na_v1.5$-HA was used as a negative control for GFP fluorescence.

3.5 Plasma membrane trafficking of mutant $Na_v1.5$ channels

Mutations in the channel can compromise its ability to fold properly and hence its trafficking to the cell membrane surface. To test this possibility, initially immunostaining was used followed by confocal microscopy to visualize the localization of the channels. The images confirmed that the mutants were trafficking on the cell surface with no visual difference compared to the WT (Figure 3.8). To get a better quantifiable comparison surface biotinylation followed by western blotting was performed to measure the fraction of wild-type and mutant human $Na_v1.5$ channels on the plasma membrane of transfected HEK293F cells[248,272]. Western blots detected $Na_v1.5$ channels in the transfected cells (but not in the EGFP-transfected control) as a broad band of Mwt > 250 kDa (Figure 3.9). This is a somewhat higher Mwt than is usually observed[249]. The reason is unclear, but similar electrophoretic behaviour has been noted for $Na_v1.5$ in other reports[273].

As a positive control, the trafficking-defective human $Na_v1.5$ channel mutant Q1832E was included, which has previously been shown to exhibit a 48% reduction in surface expression compared to the wild-type channel[274]. Biotinylation of this mutant detected about a 50% reduction in surface labelling compared to wild-type human $Na_v1.5$ (Figure 3.9). By contrast, both the wild-type human $Na_v1.5$ and all the mutant channels were detected on the plasma membrane to a similar extent (Figure 3.9 A, B).

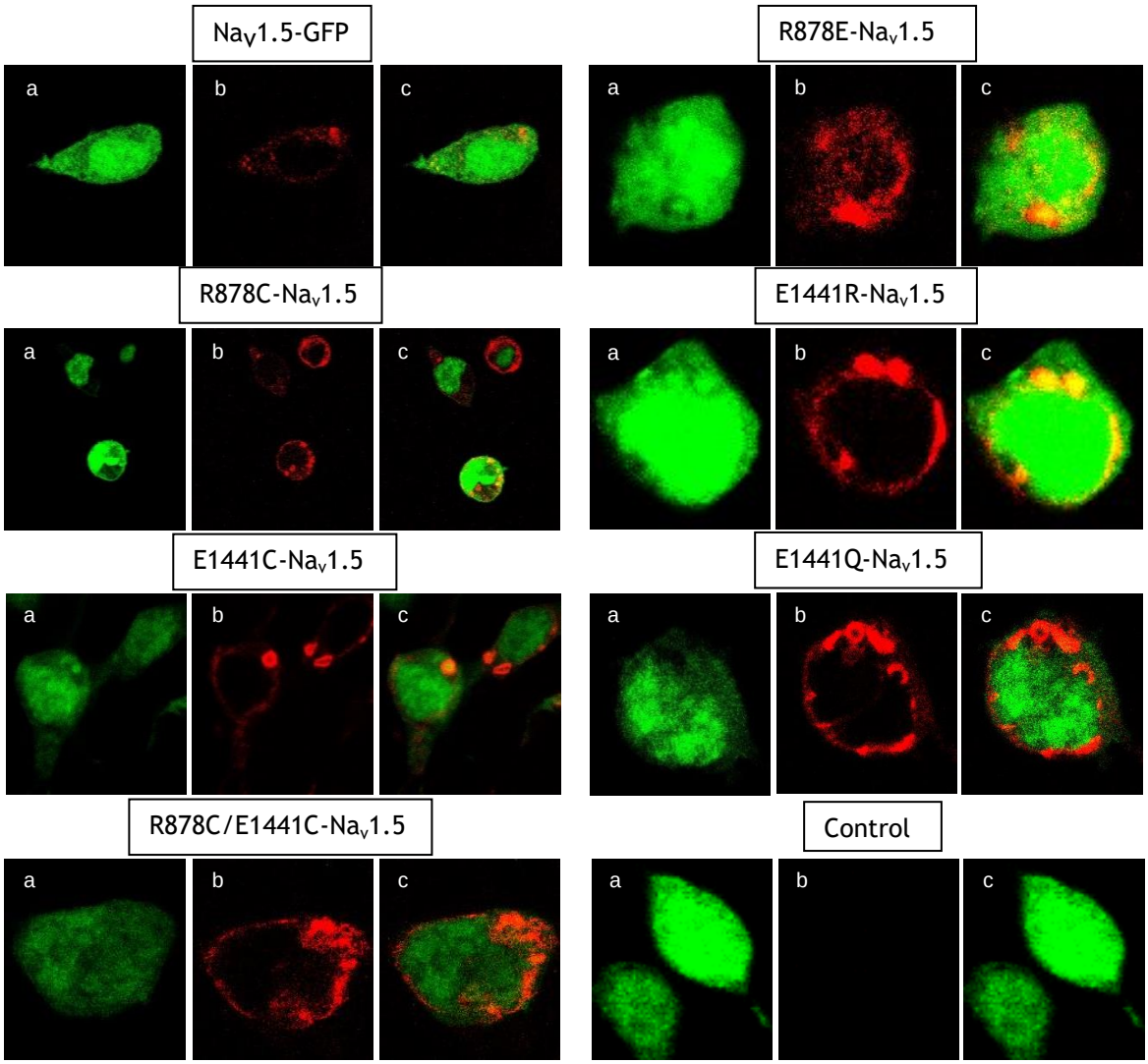

Figure 3.8. Surface membrane trafficking of both WT and mutated Na$_v$1.5 is observed in confocal microscopy. a) GFP fluorescence of HEK293F cells transfected with either the WT (Nav1.5-GFP in pcDNA3.1-GFP plasmid) or mutated Nav1.5 (in pIRES bicistronic plasmid expressing GFP unlinked to Nav protein). b) Membrane staining by anti-Nav1.5 antibody (targets intracellular, c-terminus, amino acid residues 1978-2016 of NaV1.5). c) Merging of (a) and (b). Control was transfected with the Nav1.5-GFP WT but incubation with the primary anti-Nav1.5 antibody missing.

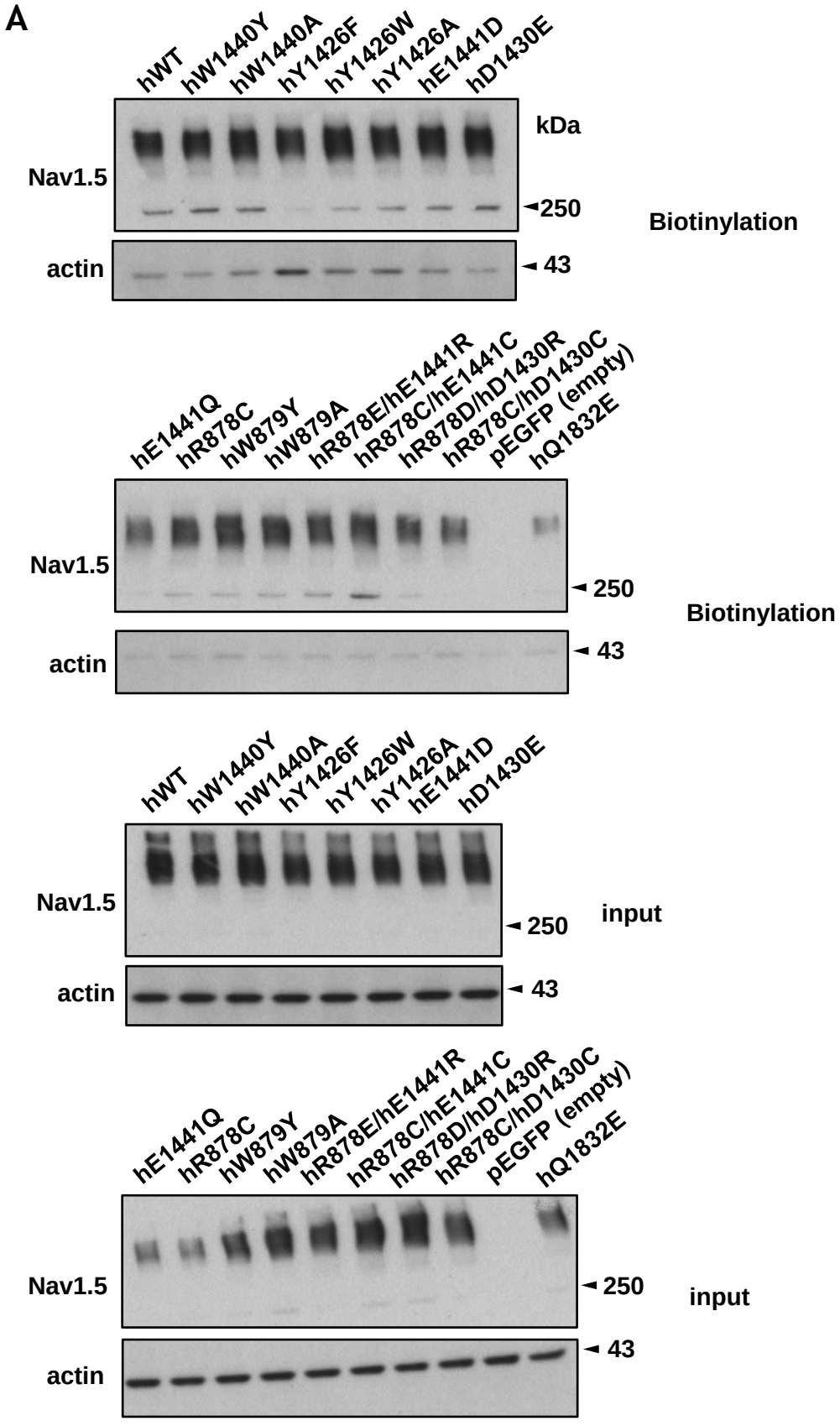
A
hWT
hW1440Y
hW1440A
hY1426F
hY1426W
hY1426A
hE1441D
hD1430E
kDa
Nav1.5
250
Biotinylation
actin
43
hE1441Q
hR878C
hW879Y
hW879A
hR878E/hE1441R
hR878C/hE1441C
hR878D/hD1430R
hR878C/hD1430C
pEGFP (empty)
hQ1832E
Nav1.5
250
Biotinylation
actin
43
hWT
hW1440Y
hW1440A
hY1426F
hY1426W
hY1426A
hE1441D
hD1430E
Nav1.5
250
input
actin
43
hE1441Q
hR878C
hW879Y
hW879A
hR878E/hE1441R
hR878C/hE1441C
hR878D/hD1430R
hR878C/hD1430C
pEGFP (empty)
hQ1832E
Nav1.5
250
input
actin
43

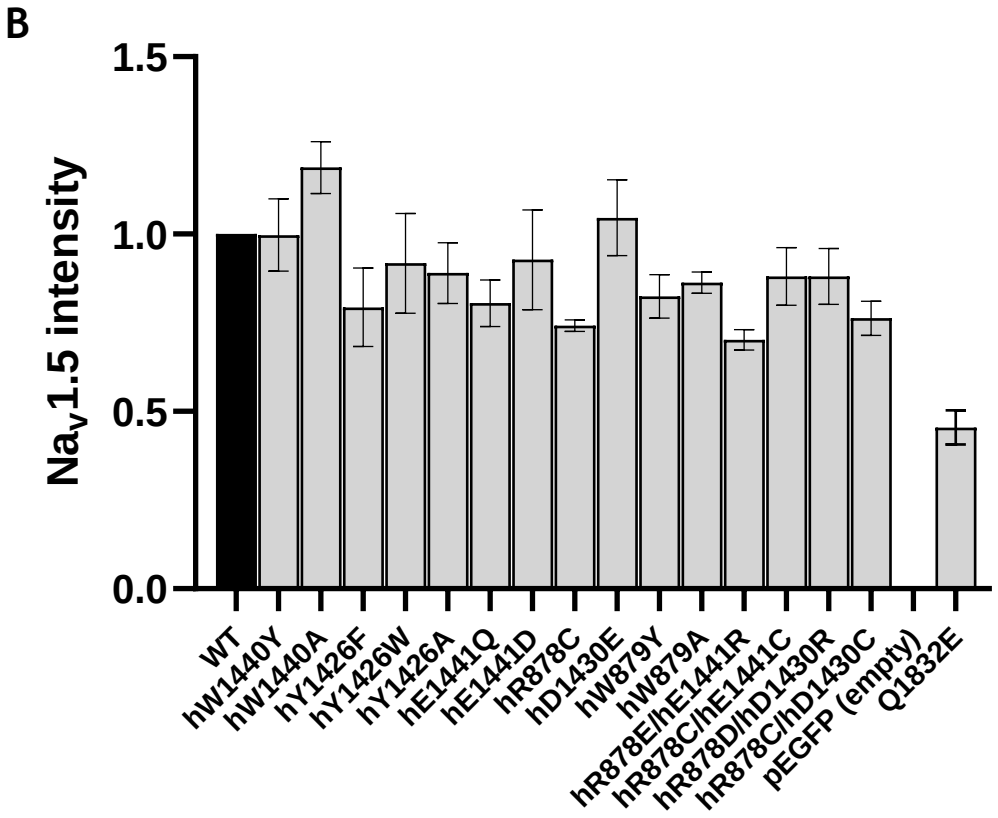

Figure 3.9 Cell surface biotinylation assay. **A.** Representative western blots of biotinylated cell surface fraction and total lysate of HEK293F cells transiently transfected with wild-type or mutant human (h), wild-type and mutant $Na_V1.5$ channels. Actin was used as a loading control. **B.** Quantitation of the $Na_V1.5$ intensities (n=3). Normalized intensities for each channel are presented relative to the normalized intensity for the wild-type $Na_V1.5$. No significant differences were seen between the wild-type and mutant channels.

3.6 Immunoprecipitation confirms interaction between the WT hNa$_v$1.5 α-α and α-β3 subunits and between mutated hNa$_v$1.5 α-β3 subunits

This study also confirms the previously observed interactions between Na$_v$1.5 α-α subunits and α-β3 subunits, and the mutations R878C and E1441Q did not abolish these interactions (Figure 3.10)[53]. One interesting observation in Western Blot analysis is that the mutated α-subunits preferentially bound with the higher glycosylated β3 subunits, while the WT α-subunits preferentially interacted with the core-glycosylated form of β3 subunits.

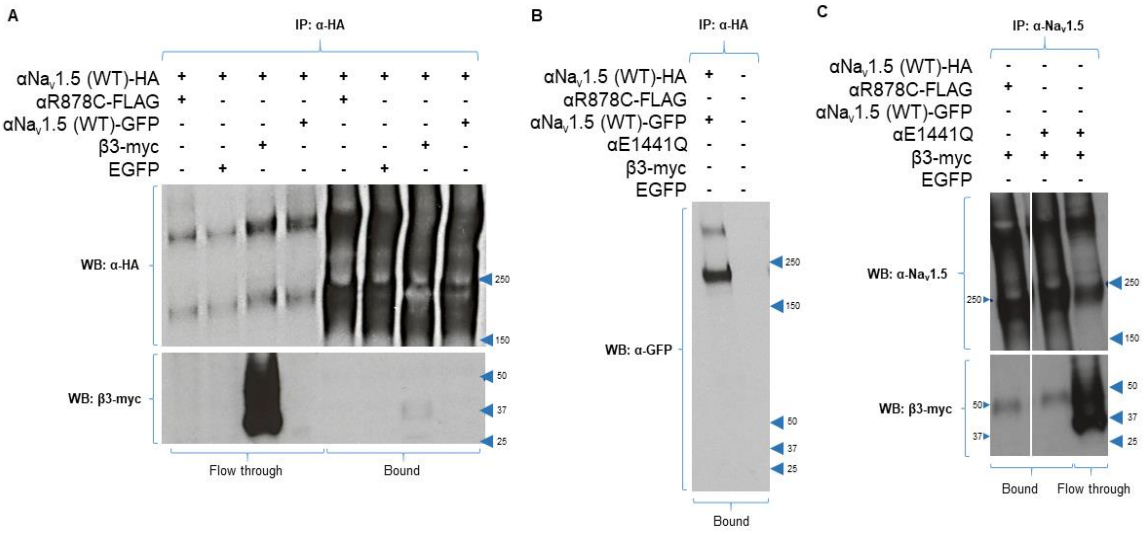

Figure 3.10. Immunoprecipitation (IP) shows interaction between two WT α subunits and between β3 and WT and mutated α subunits. **A.** Successful IP using anti-HA antibody to pulldown HA-tagged α subunit, as represented by the first four columns of the blot (from right) showing bands near 250 kDa and one more at a higher molecular weight (glycosylated fraction). Column two (from right) also shows band near 37kDa which represents β3 being pulldown by WT α subunit. Left column shows the unbound fractions. **B.** IP using anti-HA antibody also pulled down GFP-tagged WT α subunit, confirming α-α subunit interaction. **C.** Both the αR878C and E1441Q mutant pulled down β3. Interestingly, the mutated α subunits preferentially pulled down the higher glycosylated form of β3 (band just below 50kDa).

3.7 Whole cell patch clamp

Steady-state activation properties of the transiently transfected human $Na_v1.5$ WT and mutant channels were compared using whole cell patch clamp (Table 3.1). Under the steady-state activation protocol the human pathological BrS/SND mutation, R878C[154] and the putative human BrS mutation, E1441Q[80] were first examined. In agreement with previous work[154], I failed to detect any electrophysiological activity from the R878C mutant (Figure 3.15). The E1441Q mutation was similarly inactive, thus corroborating its previously inferred role as causative for BrS[80] (Figure 3.19). Given the structural insights noted above, this data supports a functional role for a salt bridge between human R878 and E1441. To extend this observation and guided by the rat $Na_v1.5$ structure, individual conservative mutations in human $Na_v1.5$: E1441D were generated (Figure 3.19) and D1430E (Figure 3.15) and tested them for electrophysiological behaviour compared to wild-type human $Na_v1.5$. The E1441D mutant displayed a 93% reduction in peak current activity, compared to the wild-type value ($p<0.0001$). Nevertheless, the currents were large enough to measure additional gating parameters. Compared to wild-type $Na_v1.5$, the E1441D mutant displayed a significantly increased slope factor (*k*) for activation ($p<0.0001$). However, there was no effect of the E1441D mutation on the steady-state $V_{1/2}$ of activation ($p=0.0585$). By contrast, there was no detectable current from the D1430E mutation (Figure 3.14). Both the charge swap mutants, R878E/E1441R and R878D/D1430R, and double cysteine mutants did not conduct any current (Figure 3.15).

Next the functional importance of the aromatic residues surrounding the complex salt bridge was examined (Figure 3.1B). The human W1440Y mutation was functional and showed no statistically significant differences in peak current ($p=0.9996$), or steady-state gating parameters compared to human wild-type $Na_v1.5$. In contrast, the human W1440A mutation, which lacked any aromatic residue at this position, had a significantly (~80%) reduced peak current relative to wild-type human $Na_v1.5$ ($p<0.0001$) and a significantly increased slope factor (*k*) for activation (Figure 3.12). The functional importance of the Y1426 aromatic residue in human $Na_v1.5$ was similarly investigated by replacing it with alanine. The Y1426A mutant displayed a 70% reduction in peak current relative to wild-type $Na_v1.5$ and a significant increase in (*k*) activation (Figure 3.13). Thus, the separate removal of each of the aromatic

groups that form the putative cation-π interactions with the R878 guanidinium group, significantly reduced but did not abolish channel activity.

Based on the rat $Na_v1.5$ structure, it was inferred that human Y1426 on the DIII turret additionally forms a hydrogen bond with human W879 on the DII turret (Figure 3.1B). To test the importance of this interaction, first the human Y1426 residue was replaced with a bulkier tryptophan residue. This change would be expected both to abolish the hydrogen bond with human W879 and to also perturb the packing at the DII and DIII turret interface, whilst retaining the cation-π bond itself. The human Y1426W mutation displayed a significant reduction in peak current and an increase in the slope factor (*k*) for activation (Figure 3.13). To specifically test the role of the hydrogen bond, a human Y1426F mutant was generated. This mutant should largely retain its cation-π bonding potential relative to wild-type human $Na_v1.5$, with minimum disturbance to side-chain packing, whilst being unable to form a hydrogen bond with W879. The human Y1426F mutant displayed a 50% reduction in peak current, with no significant effect on steady-state gating parameters. Finally, the role of the human W879 residue by generating a human W879A and a W879Y mutant was examined. No current responses could be detected in either of these cases (Figure 3.15). Since this was a more severe phenotype than displayed by the Y1426F mutant, it suggests an important stabilising role for the tryptophan residue at position 879 of human $Na_v1.5$, acting in addition to its hydrogen bonding potential with Y1426.

A charge-swap approach has been previously used to study ion channel salt bridges[275,276]. Here, the positively and negatively charged residues were reversed by site-directed mutagenesis. The extent to which a given function was maintained or modified by this procedure reflects the structural constraints on the salt bridge in the wild-type protein. A double mutation in human $Na_v1.5$ was generated: R878E with E1441R and a separate double mutation: R878D with D1430R. Strikingly, neither of the charge swap mutants exhibited any detectable currents (Figure 3.15). Double cysteine mutations were also made which similarly did not conduct any current (Figure 3.15).

A major effect of the mutations is on the magnitude of their peak currents relative to wild-type $Na_v1.5$, which could indicate that severely compromised mutants, particularly those that lack detectable gating activity, fail to traffic to the plasma membrane, however, it has already been established through surface biotinylation

that there were no significant difference between the trafficking of the WT and the mutants (Figure 3.9).

3.7.1 Steady state activation

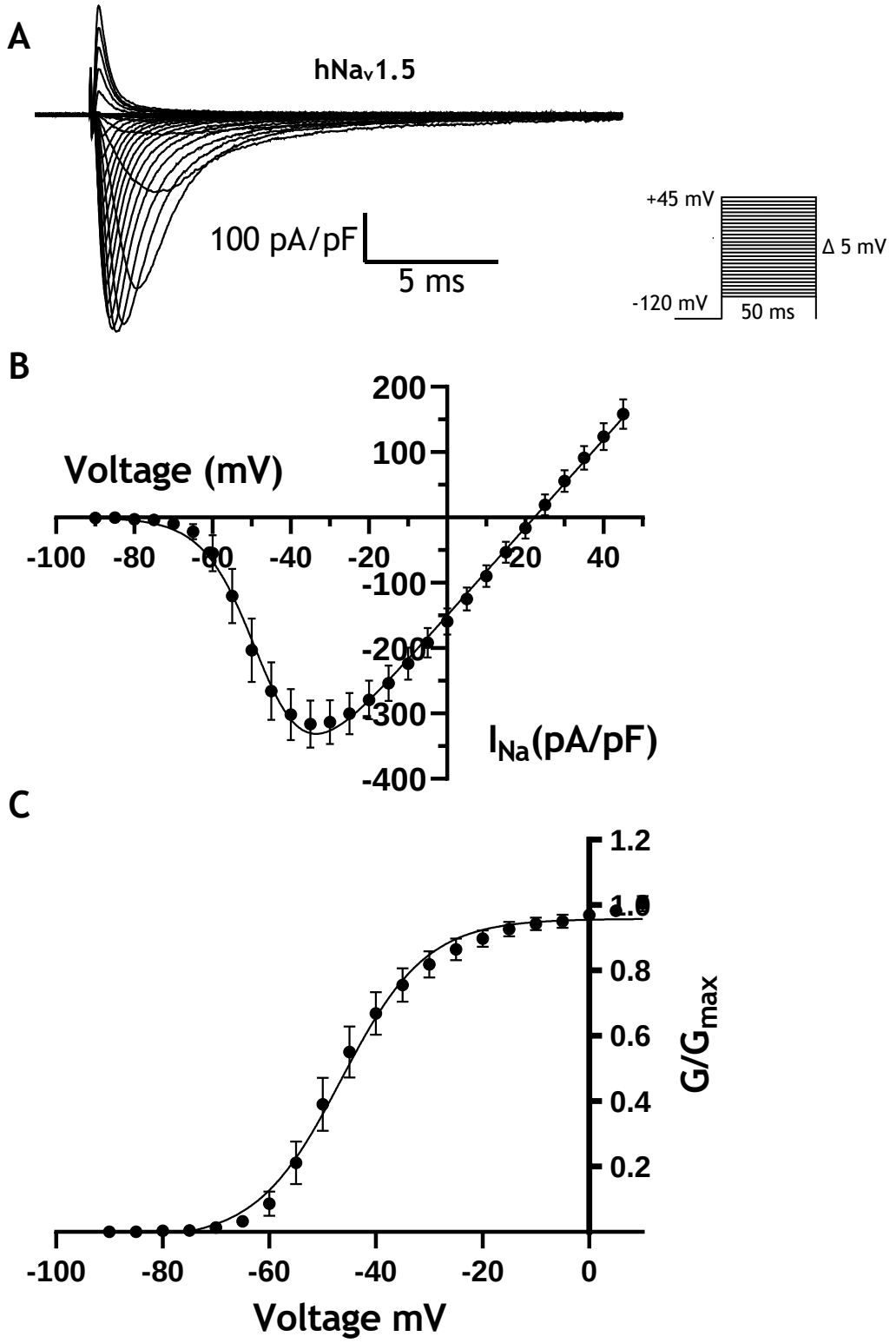

Figure 3.11. Steady-state activation properties of wild-type (WT) $Na_v1.5$ channel. **A.** Typical whole-cell current trace from HEK293F cells transfected with human (h), wild-type Nav1.5 channel under the activation protocol as outlined in Methods. **B.** Currents, normalized to whole-cell capacitance, versus voltage curves. **C.** Channel conductance as a function of voltage. Curves were fitted to a Boltzmann function as outlined in Methods. The data are means ± SEMs. (n = 9).

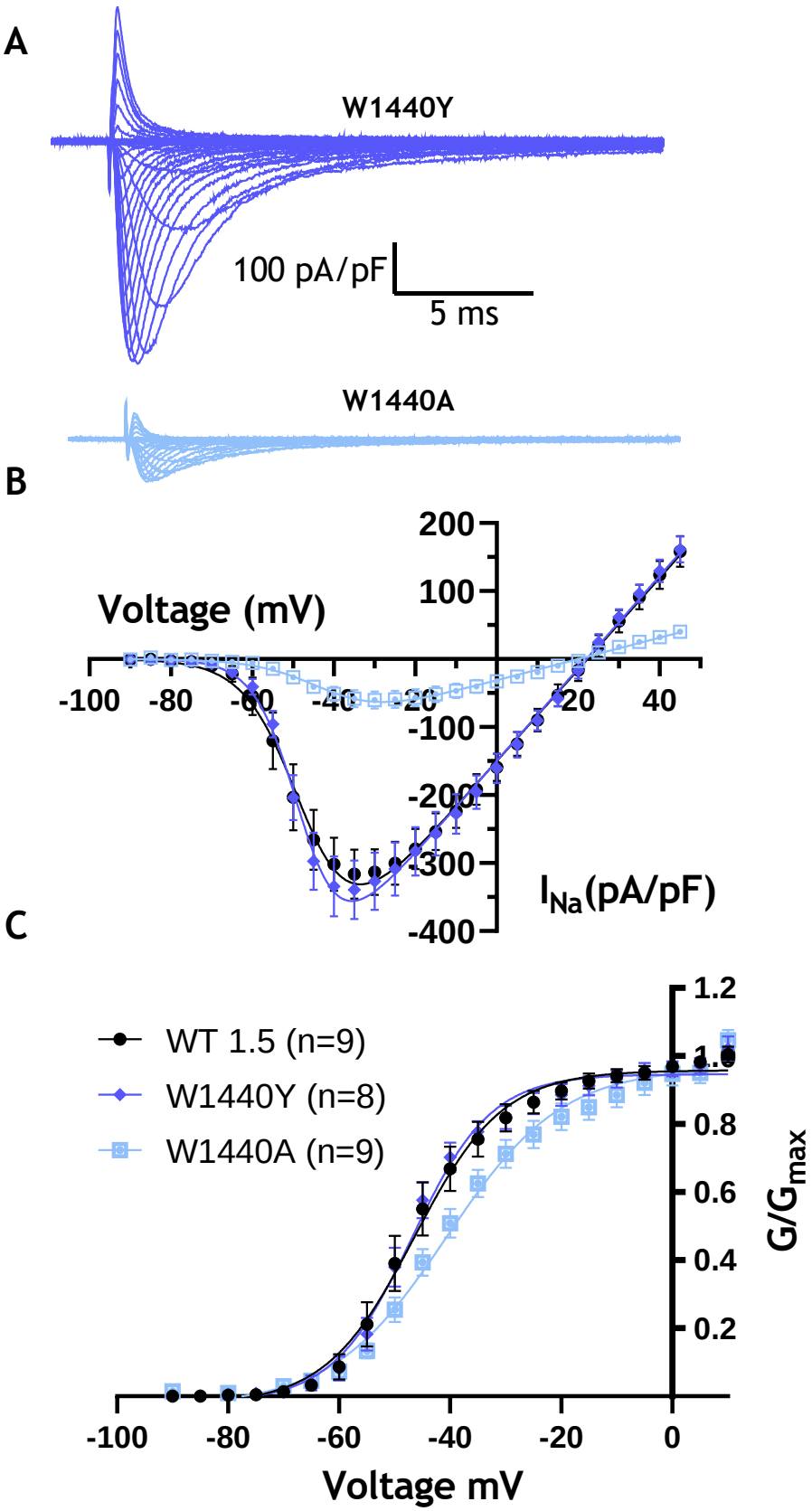

Figure 3.12. Steady-state activation properties of WT $Na_v1.5$ channel versus W1440Y and W1440A mutants. **A.** Typical whole-cell current trace from HEK293F cells transfected with W1440Y and W1440A $Na_v1.5$ channel under the activation protocol as outlined in Methods. **B.** Currents, normalized to whole-cell capacitance, versus voltage curves for the WT and mutants. **C.** Channel conductance as a function of voltage for WT and mutants. Curves were fitted to a Boltzmann function as outlined in Methods. The data are means ± SEMs. W1440Y (n = 8), W1440A (n=9).

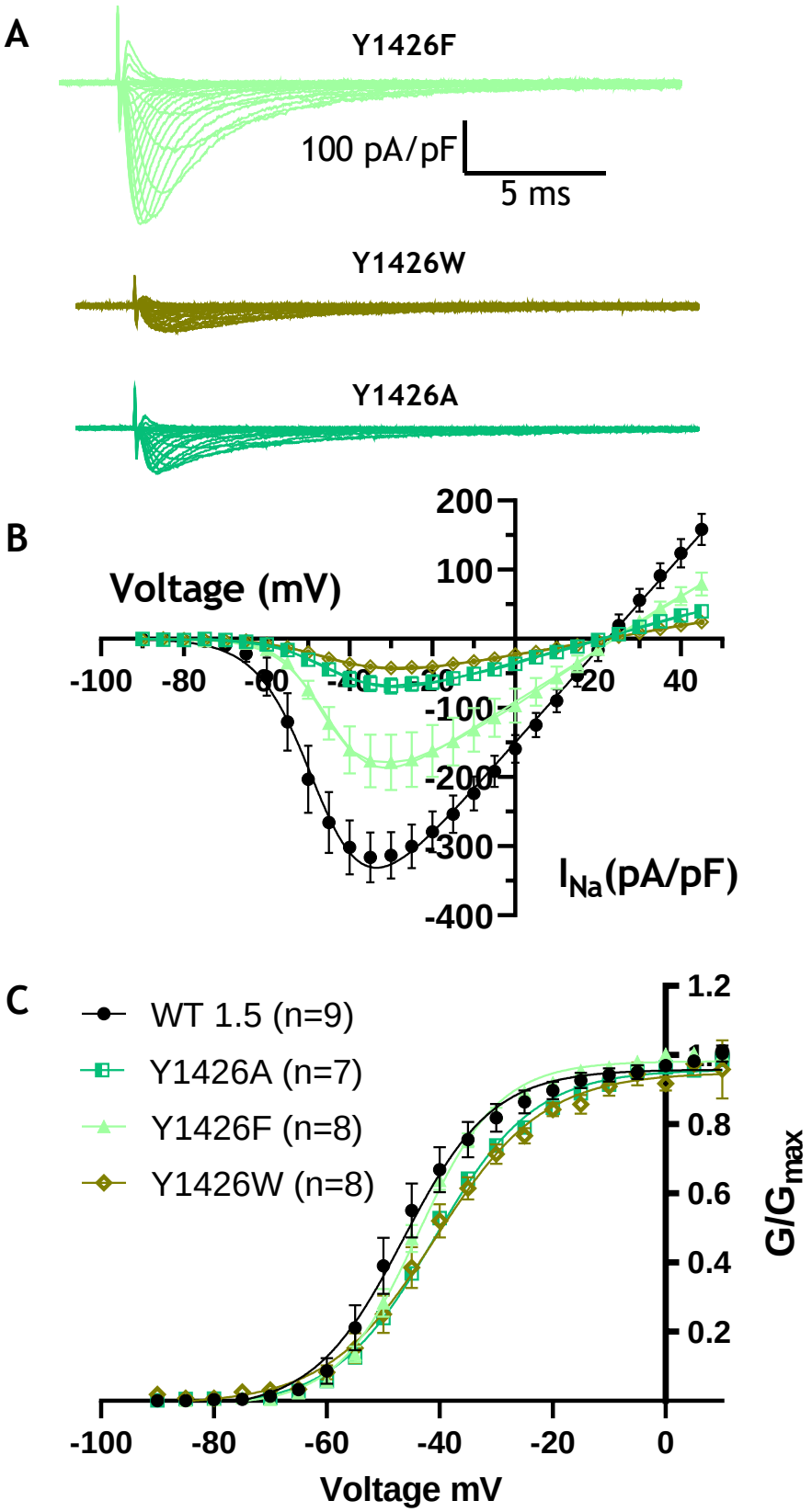

Figure 3.13. Steady-state activation properties of WT $Na_v1.5$ channel versus Y1426F, Y1426W and Y1426A mutants. **A.** Typical whole-cell current trace from HEK293F cells transfected with Y1426F, Y1426W and Y1426A $Na_v1.5$ channel under the activation protocol as outlined in Methods. **B.** Currents, normalized to whole-cell capacitance, versus voltage curves for the WT and mutants. **C.** Channel conductance as a function of voltage for WT and mutants. Curves were fitted to a Boltzmann function as outlined in Methods. The data are means ± SEMs. Y1426F (n = 8), Y1426W (n=8), Y1426A (n=7).

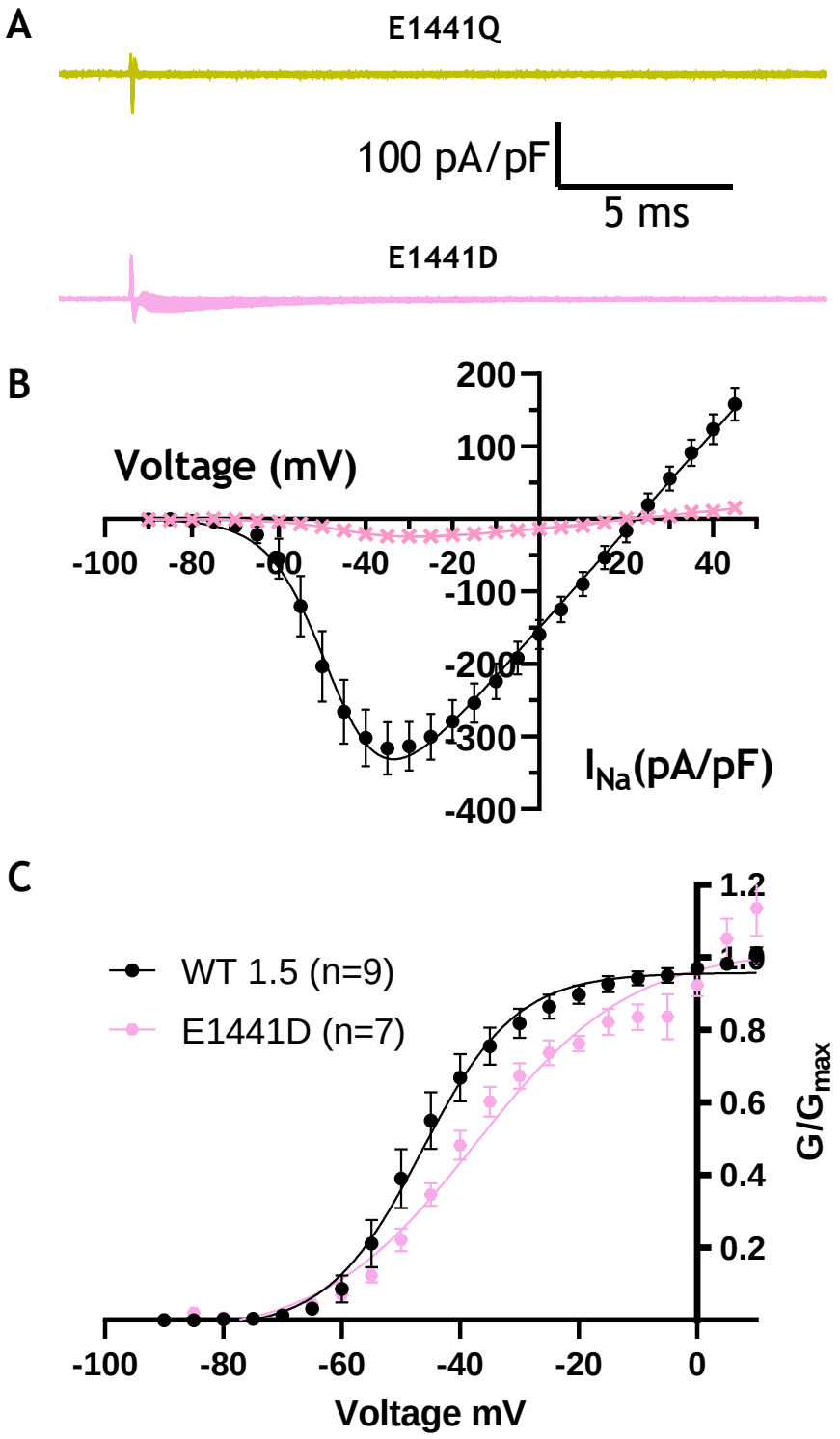

Figure 3.14. Steady-state activation properties of WT $Na_v1.5$ channel versus E1441D mutant. **A.** Typical whole-cell current trace from HEK293F cells transfected with E1441Q and E1441D $Na_v1.5$ channel under the activation protocol as outlined in Methods. **B.** Currents, normalized to whole-cell capacitance, versus voltage curves for the WT and mutants. **C.** Channel conductance as a function of voltage for WT and mutants. Curves were fitted to a Boltzmann function as outlined in Methods. The data are means ± SEMs. E1441D (n = 7).

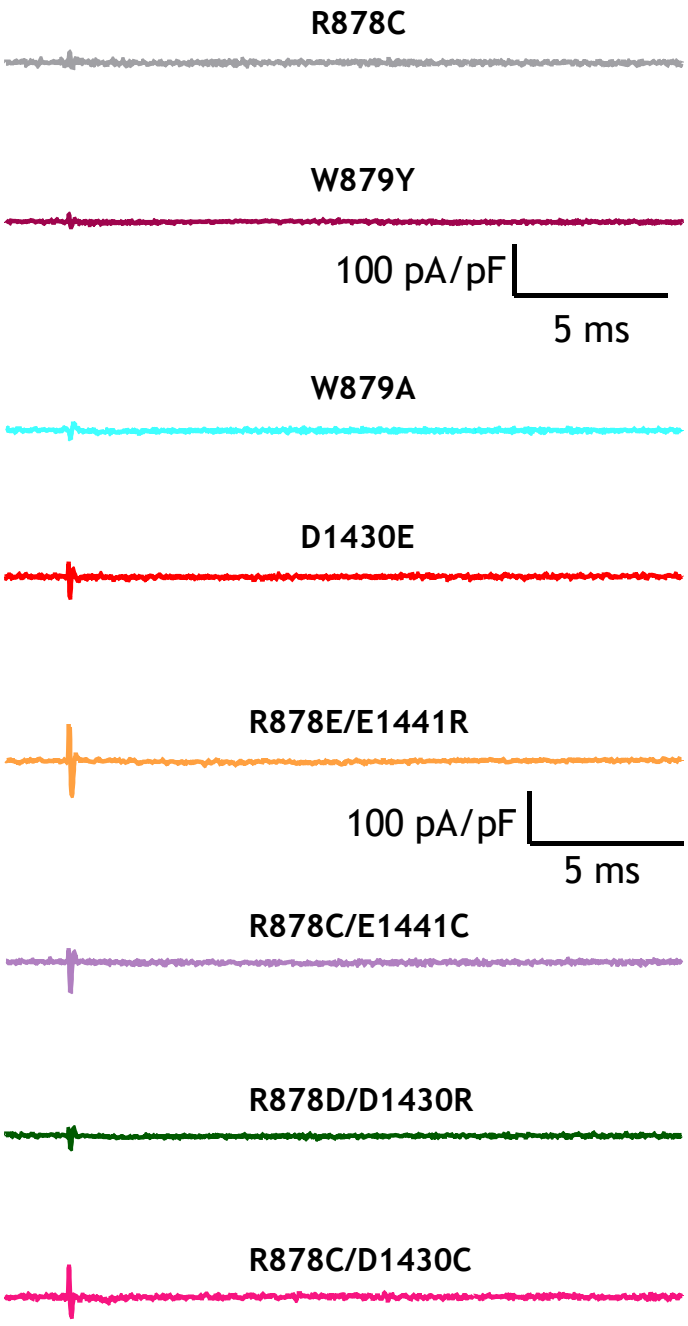

Figure 3.15. Typical whole-cell current trace from HEK293F cells transfected with the mutant channel under the activation protocol as outlined in Methods. For all the mutants (n=3).

Table 3.2. Parameters from whole-cell patch-clamp steady-state activation data. The data were fitted using a Boltzmann function to deduce all the parameters. The data are expressed as mean ± SEM and One-Way ANOVA statistical analysis followed by Dunnett post-hoc tests performed to determine the statistical significance between each mutant and the wild-type $Na_v1.5$ channel. *p<0.05, **p<0.01, ***p<0.001, ****p<0.0001.

	Peak I_{Na}	$V_{1/2}$(mV)	k(mV)	n
HEK293F cells				
WT	-332.29 ± 36.27	-46.89 ± 2.43	5.22 ± 0.35	9
hW1440Y	-342.46 ± 42.15	-47.89 ± 1.47	5.27 ± 0.45	8
hW1440A	-60.85 ± 13.01****	-41.77 ± 1.51	7.85 ± 0.40***	9
hY1426F	-180.47 ± 40.13**	-44.4 ± 0.95	5.98 ± 0.28	8
hY1426W	-44.23 ± 7.54****	-41.83 ± 1.84	7.86 ± 0.47***	8
hY1426A	-68.44 ± 11.25****	-41.61 ± 1.41	7.22 ± 0.17**	7
hE1441D	-24.83 ± 2.23****	-40.57 ± 1.55	8.16 ± 0.64****	7

3.7.2 Steady state inactivation

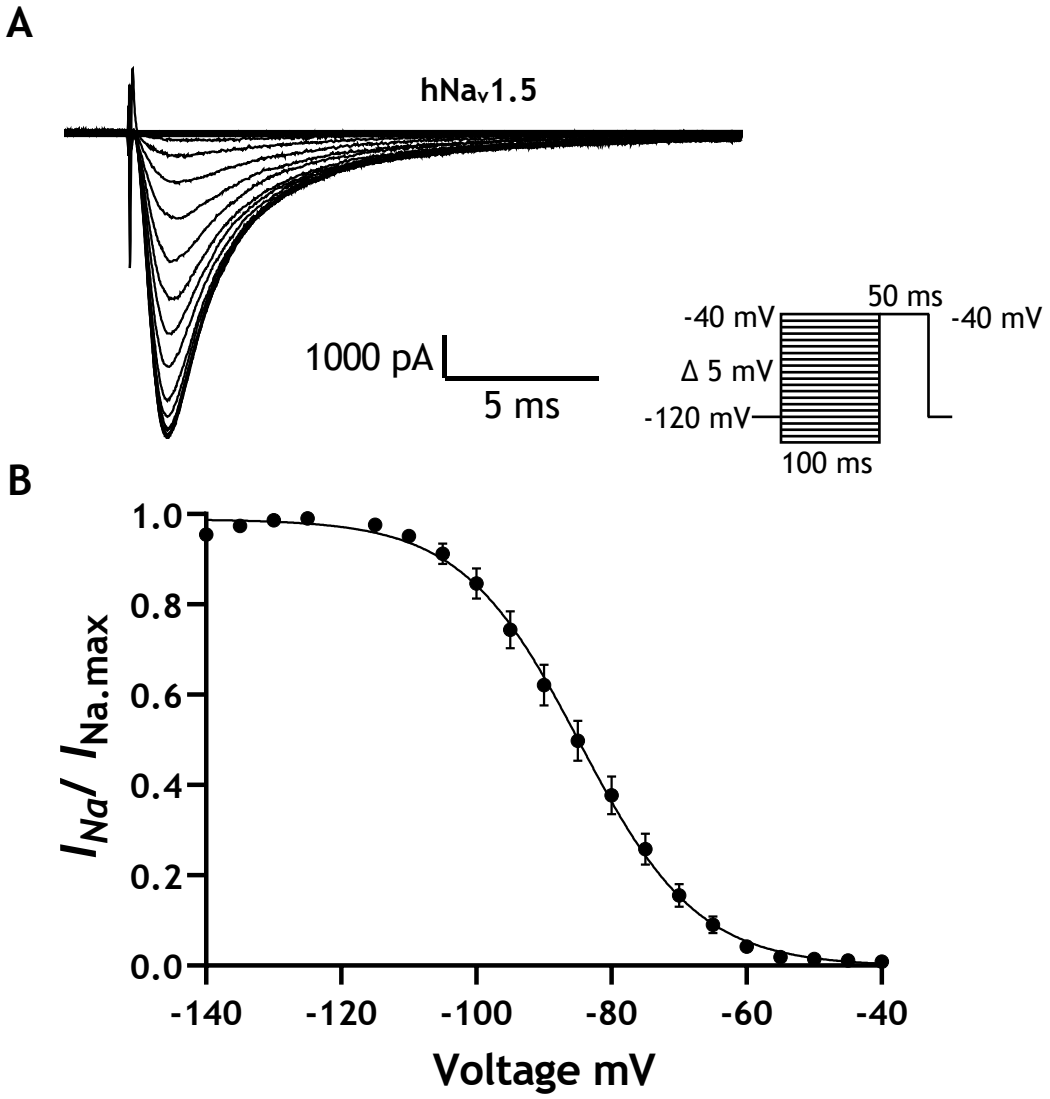

Figure 3.16. Steady-state inactivation properties of wild-type human $Na_v1.5$ channel. **A.** Typical whole-cell current traces from HEK293F cells transfected with Nav1.5 channel under the steady-state inactivation protocols described in Methods. **B.** Current-voltage curve with peak I_{Na} of each step normalized with maximum peak I_{Na} and plotted against test pre-pulse potential. The data are means ± SEMs (n=14).

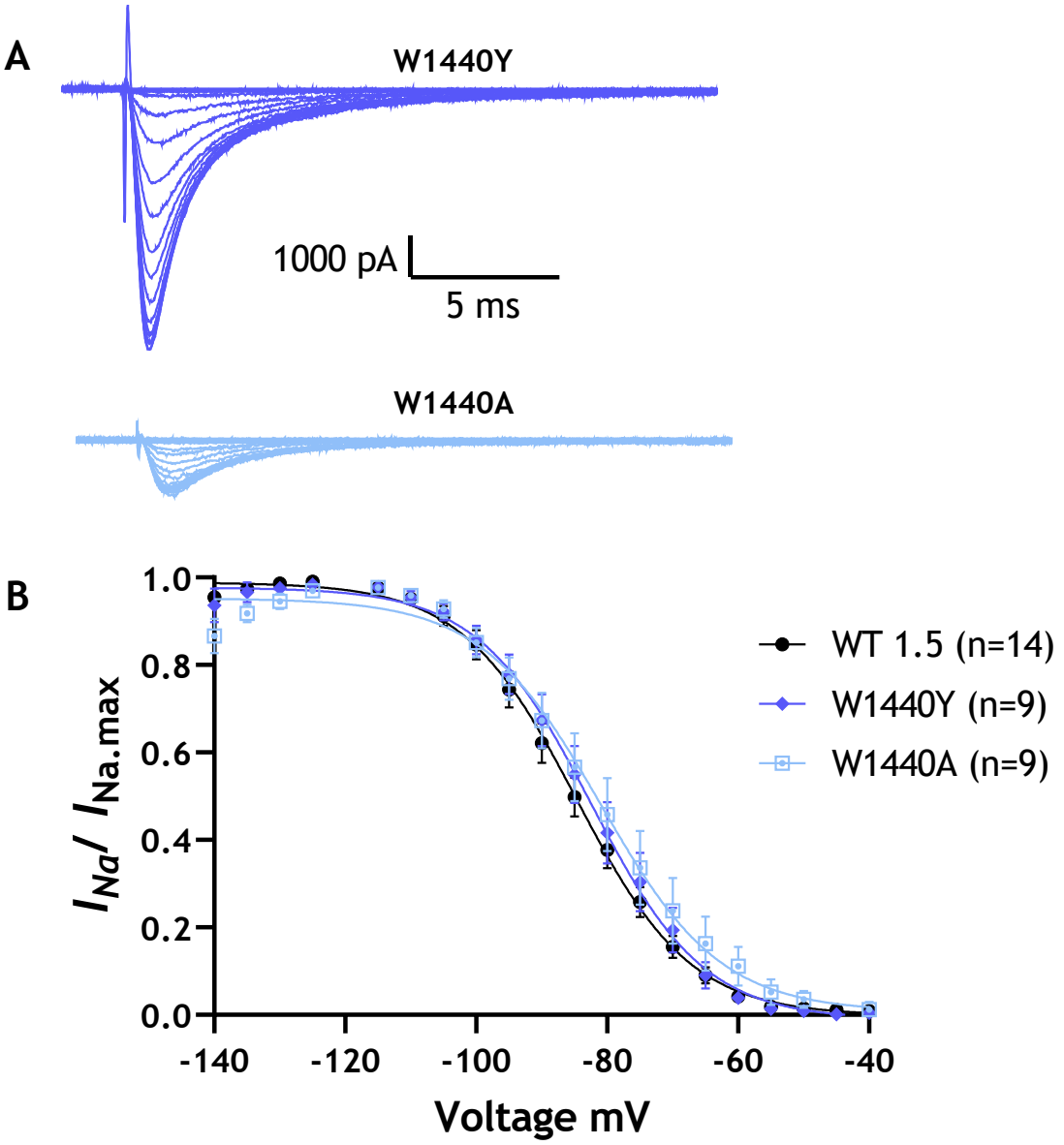

Figure 3.17. Steady-state inactivation properties of W1440Y and W1440A versus wild-type human $Na_v1.5$ channel. **A.** Typical whole-cell current traces from HEK293F cells transfected with Nav1.5 channel under the steady-state inactivation protocols described in Methods. **B.** Current-voltage curve with peak I_{Na} of each step normalized with maximum peak I_{Na} and plotted against test pre-pulse potential. The data are means ± SEMs.

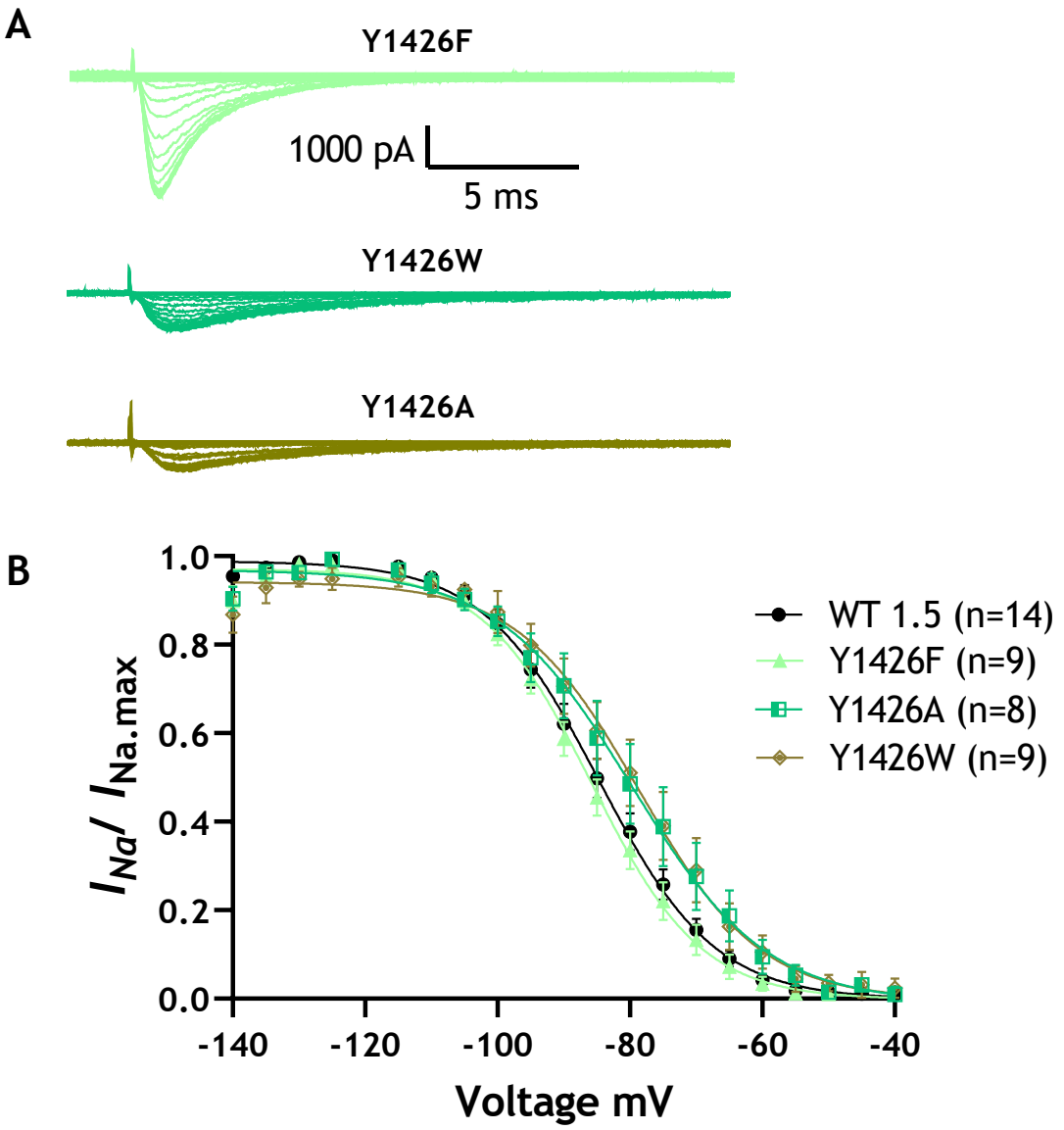

Figure 3.18. Steady-state inactivation properties of Y1426F, Y1426W and Y1426A versus wild-type human $Na_v1.5$ channel. **A.** Typical whole-cell current traces from HEK293F cells transfected with Nav1.5 channel under the steady-state inactivation protocols described in Methods. **B.** Current-voltage curve with peak I_{Na} of each step normalized with maximum peak I_{Na} and plotted against test pre-pulse potential. The data are means ± SEMs.

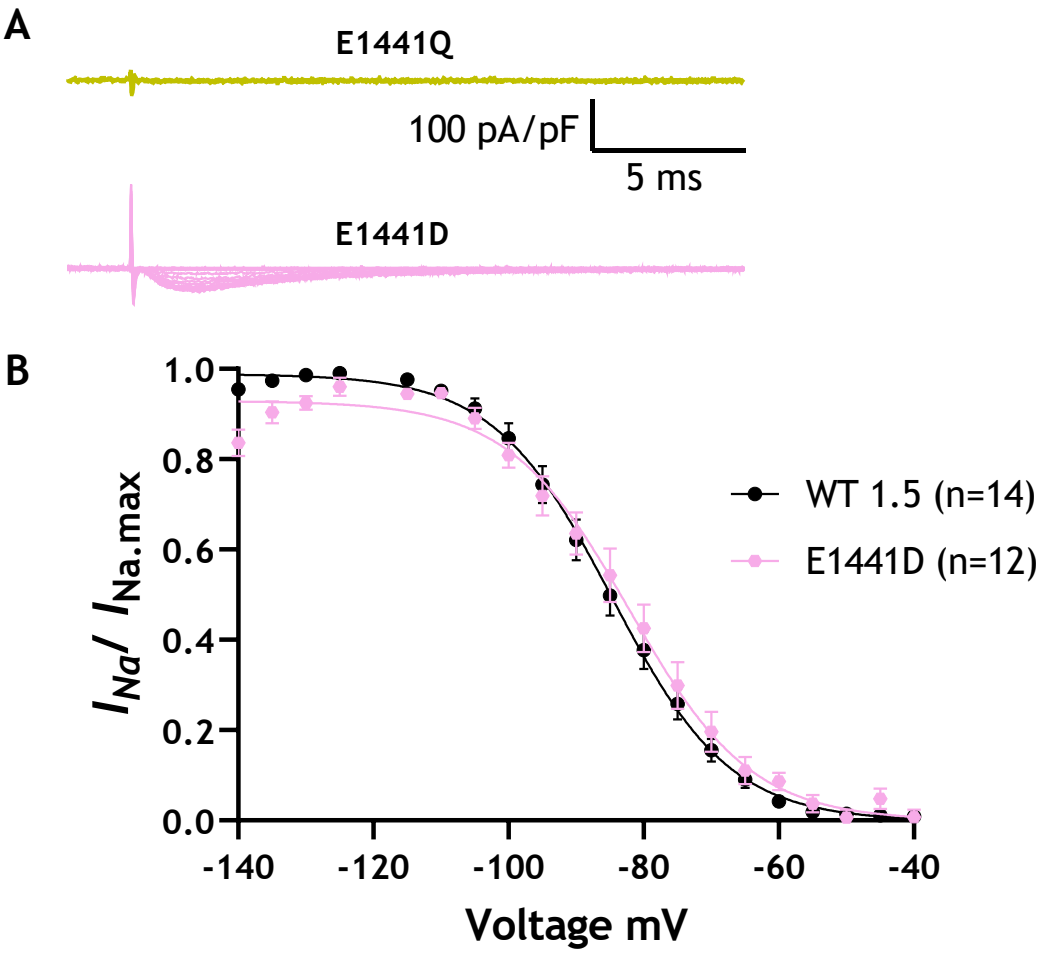

Figure 3.19. Steady-state inactivation properties of E1441D versus wild-type human $Na_v1.5$ channel. **A.** Typical whole-cell current traces from HEK293F cells transfected with $Na_v1.5$ channel under the steady-state inactivation protocols described in Methods. **B.** Current-voltage curve with peak I_{Na} of each step normalized with maximum peak I_{Na} and plotted against test pre-pulse potential. The data are means ± SEMs.

Table 3.3. Parameters from whole-cell patch-clamp steady-state inactivation data. **D**ata were fitted using a Boltzmann function to deduce all the parameters. The data are expressed as mean ± SEM and One-Way ANOVA statistical analysis followed by Dunnett post-hoc tests performed to determine the statistical significance between each mutant and the wild-type $Na_v1.5$ channel. *p<0.05, **p<0.01, ***p<0.001, ****p<0.0001.

	$V_{1/2}$(mV)	k(mV)	n
HEK293F cells			
WT	-84.75 ± 1.70	-7.925 ± 0.24	14
hW1440Y	-82.52 ± 2.60	-7.351 ± 0.33	9
hW1440A	-80.49 ± 3.27	-7.606 ± 0.46	9
hY1426F	-85.57 ± 1.96	-7.894 ± 0.24	9
hY1426W	-78.48 ± 3.27	-7.942 ± 0.36	8
hY1426A	-79.81 ± 3.47	-7.888 ± 0.46	8
hE1441D	-82.17 ± 2.40	-7.394 ± 0.46	12

3.7.3 Recovery from inactivation

In addition to steady-state parameters, recovery from inactivation kinetics were also examined in detail (Figure 3.20, Figure 3.21, Figure 3.22). As noted previously[249], recovery from inactivation was best fitted to a double exponential curve corresponding to a fast and slow component. However, there were no statistically significant differences in the kinetics of either of these components between any of the mutants and wild-type channels.

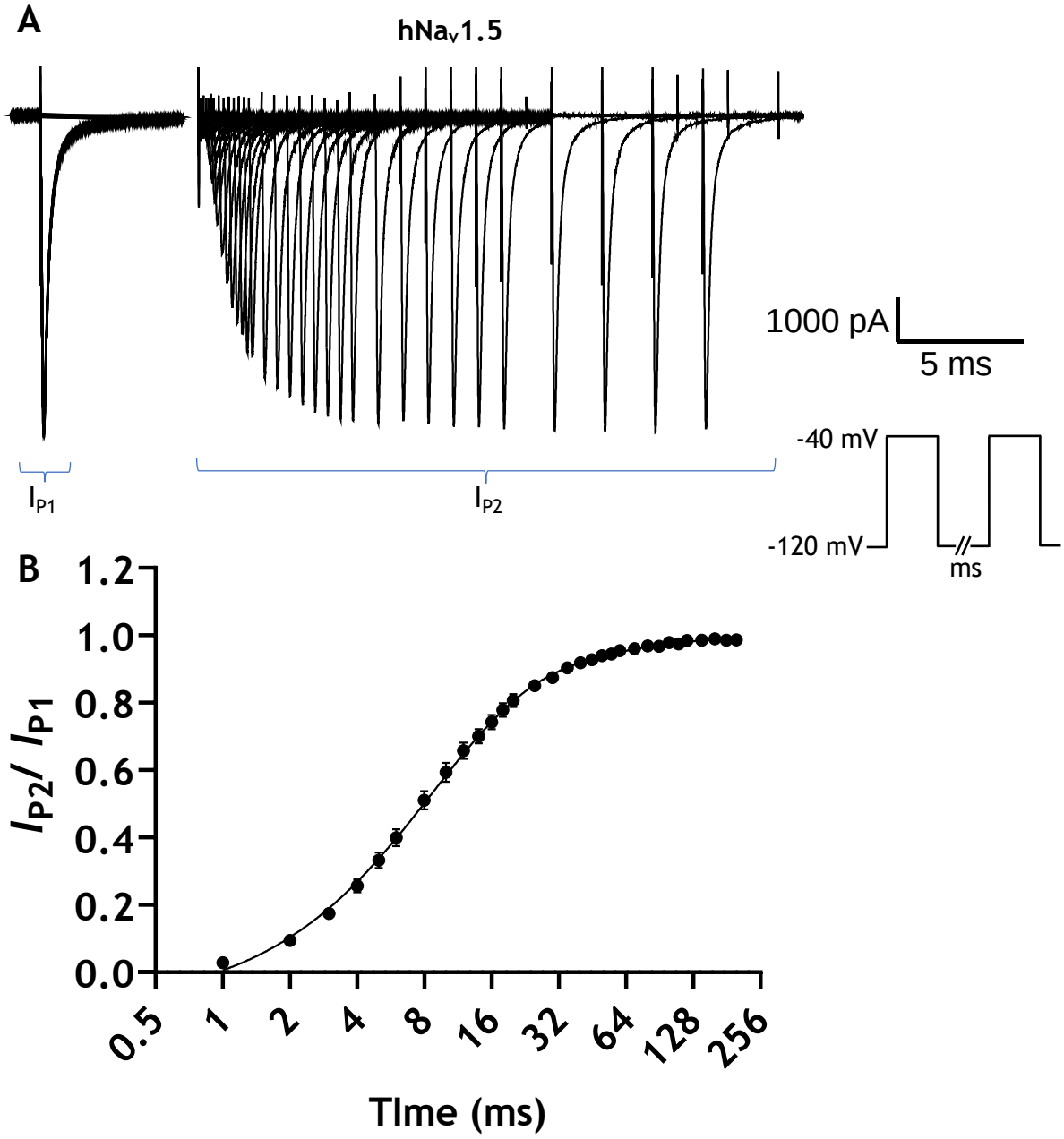

Figure 3.20. Recovery from inactivation properties of wild-type human $Na_v1.5$ channel. **A.** Representative whole-cell traces from recovery from the inactivation protocol as outlined in Methods. **B.** The fraction of $Na_v1.5$ channel I_{Na} recovering from the inactive state plotted against the increasing time duration between the two depolarizing pulses.

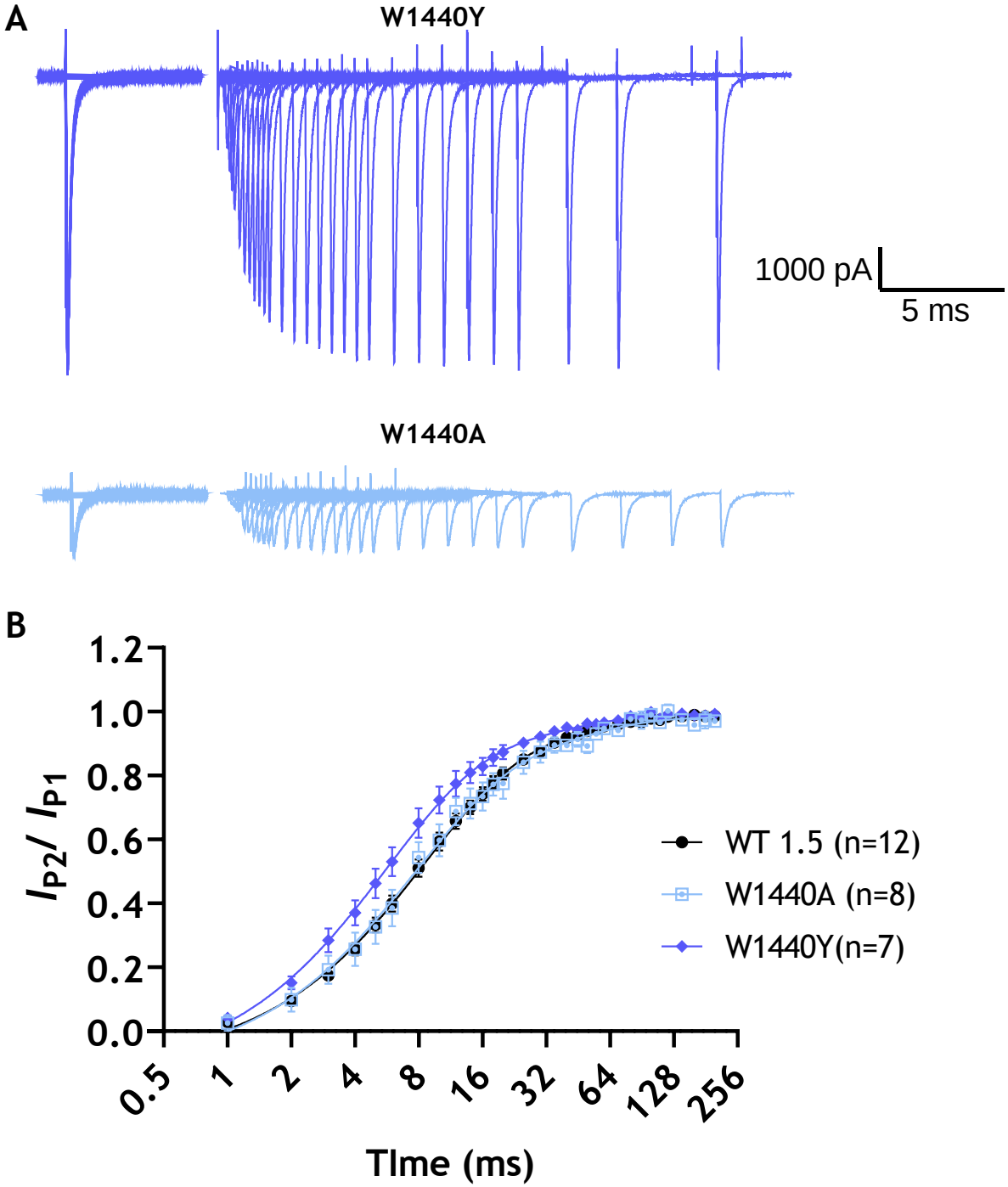

Figure 3.21 Recovery from inactivation properties of W1440Y, W1440A and WT human $Na_v1.5$ channel. **A.** Representative whole-cell traces from recovery from the inactivation protocol as outlined in Methods. **B.** The fraction of mutant and WT $Na_v1.5$ channel I_{Na} recovering from the inactive state plotted against the increasing time duration between the two depolarizing pulses.

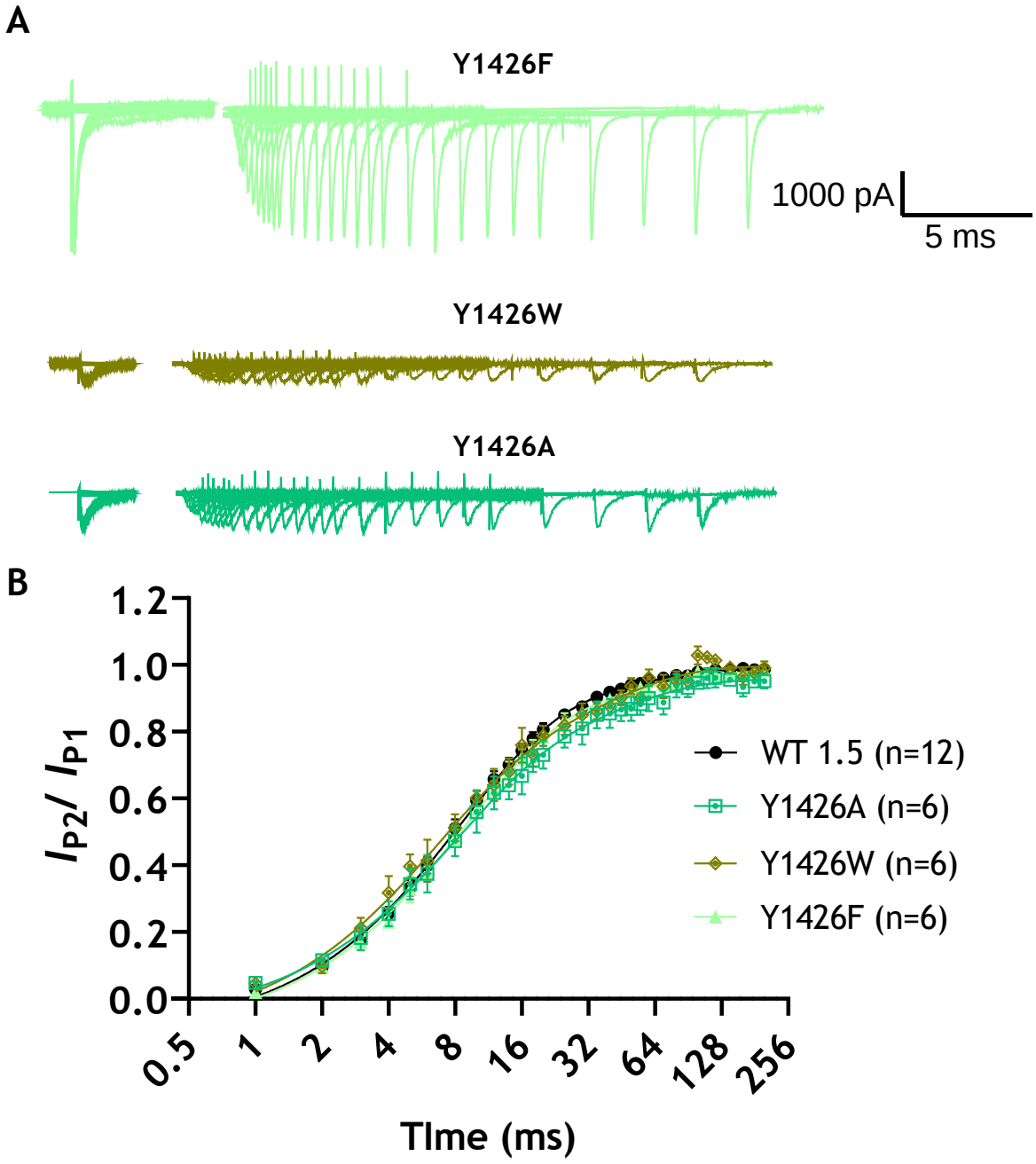

Figure 3.22. Recovery from inactivation properties of Y1426F, Y1426W, Y1426A and WT human $Na_v1.5$ channel. **A.** Representative whole-cell traces from recovery from the inactivation protocol as outlined in Methods. **B.** The fraction of mutant and WT $Na_v1.5$ channel I_{Na} recovering from the inactive state plotted against the increasing time duration between the two depolarizing pulses.

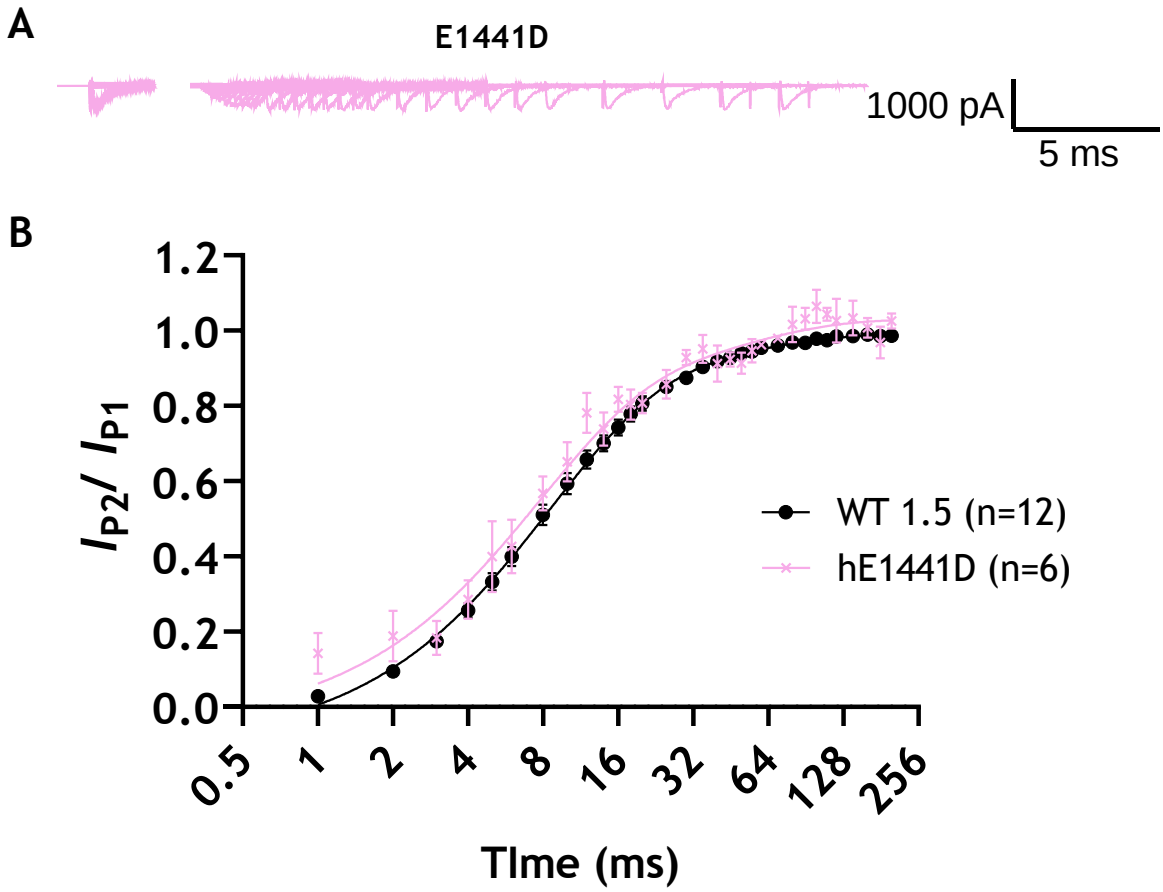

Figure 3.23. Recovery from inactivation properties of E1441D and WT human $Na_v1.5$ channel. **A.** Representative whole-cell traces from recovery from the inactivation protocol as outlined in Methods. **B.** The fraction of mutant and WT $Na_v1.5$ channel I_{Na} recovering from the inactive state plotted against the increasing time duration between the two depolarizing pulses.

Table 3.4. Parameters from whole-cell patch-clamp recovery from inactivation data. A double exponential function was used to fit the data and expressed as mean ± SEM. Statistical significance was analysed using a one-way ANOVA, followed by Dunnett post-hoc tests performed to determine the statistical significance between each mutant and the wild-type $Na_V1.5$ channel. *p<0.05, **p<0.01, ***p<0.001, ****p<0.0001.

	k_{fast}	k_{slow}	τ_{fast} (ms)	τ_{slow} (ms)	$t_{1/2\ fast}$ (ms)	$t_{1/2\ slow}$ (ms)	n
HEK293F cells							
WT	0.122 ± 0.008	0.022 ± 0.002	8.611 ± 0.524	48.47 ± 3.747	5.969 ± 0.363	33.60 ± 2.597	12
hW1440Y	0.183 ± 0.021	0.029 ± 0.004	5.905 ± 0.669	39.05 ± 5.210	4.093 ± 0.464	27.07 ± 3.610	7
hW1440A	0.144 ± 0.015	0.026 ± 0.002	7.472 ± 0.709	39.99 ± 3.431	5.179 ± 0.492	27.72 ± 2.378	8
hY1426F	0.120 ± 0.010	0.020 ± 0.002	8.658 ± 0.757	54.45 ± 5.037	6.000 ± 0.524	37.74 ± 3.492	6
hY1426W	0.185 ± 0.040	0.026 ± 0.005	6.709 ± 1.332	48.08 ± 10.54	4.650 ± 0.923	33.33 ± 7.302	6
hY1426A	0.152 ± 0.020	0.035 ± 0.011	7.377 ± 1.234	42.64 ± 10.25	5.113 ± 0.855	29.55 ± 7.107	6
hE1441D	0.160 ± 0.020	0.022 ± 0.002	6.999 ± 1.221	49.04 ± 4.993	4.852 ± 0.846	33.99 ± 3.461	6

3.8 Application of Na_v agonist veratridine

Veratridine failed to rescue the human $Na_v1.5$ null-mutations. The steroidal alkaloid Na_v channel activator veratridine inhibits channel transitions from the open to the inactivated state[277]. Veratridine binds to an intracellular site, located between DI and DIV, that is distinct and quite separate from the extracellular DII-DIII turret interface[278]. If the turret null mutations were driving the channel into the inactivated state, then it would be expected of veratridine to overcome, or at least attenuate inactivation and hence restore some activity. If on the other hand, the mutations were preventing the earlier activation step, then veratridine should not influence these channels. 0.1 mM veratridine, a concentration that is known to be saturating for wild-type $Na_v1.5$[279], was found to induce a clear tail current in the wild-type human $Na_v1.5$ channel, but failed to rescue any of the human $Na_v1.5$ null-mutants (Figure 3.24). Therefore, the $Na_v1.5$ mutations most likely interfered with conformational movements normally required for the activation step, for example pore opening.

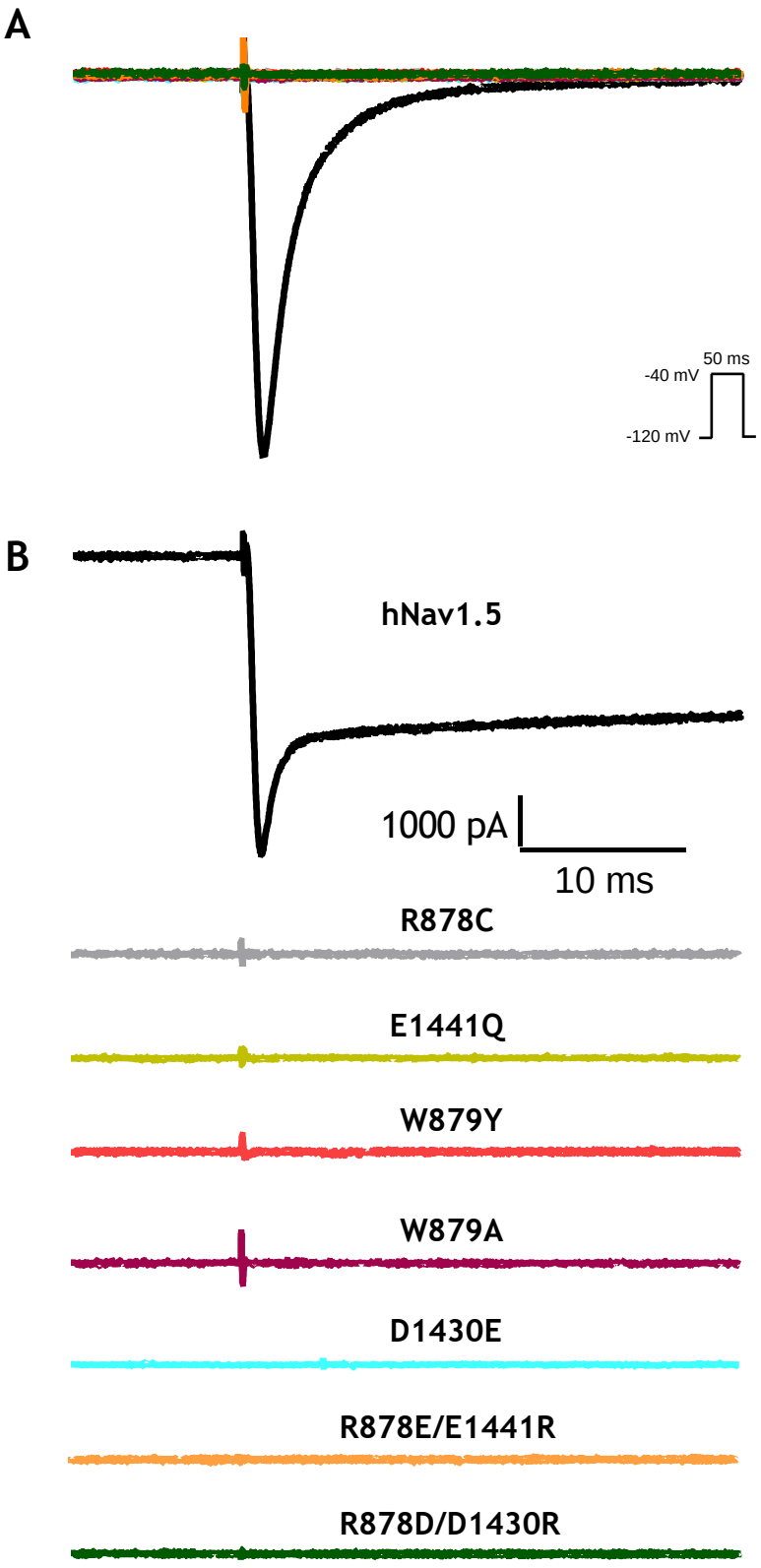

Figure 3.24. The sodium channel activator veratridine does not rescue human $Na_v1.5$ null-mutants. The gating responses of the human $Na_v1,5$ WT and null-mutants were tested **A.** in the absence, or **B.** in the presence of 0.1 mM veratridine (VTD); representative traces for the WT $Na_v1.5$ channel show the classic tail current, caused by veratridine-induced stabilization of the active Na_v channel state. However, none of the mutants showed any sign of re-activation.

3.9 Di-sulfide locking

Double cysteine substitutions were also made at the location of the salt bridge. This method has provided important structural and functional insights into ion channel behavior[36,280]. Here, the D1430 and E1441 residues of the human R878C mutant were separately replaced with cysteine. If any activity was restored in these mutants, it would indicate that a disulfide bond could form between the two DII and DIII turret interface cysteines and provide a functional replacement for the salt bridge[36]. However, neither mutation (either with or without prior reduction using ß-mercaptoethanol) exhibited any detectable current (Figure 3.15, Figure 3.25). Taken together, these experiments underscore the tight functional constraints that apply to the complex salt bridge residues.

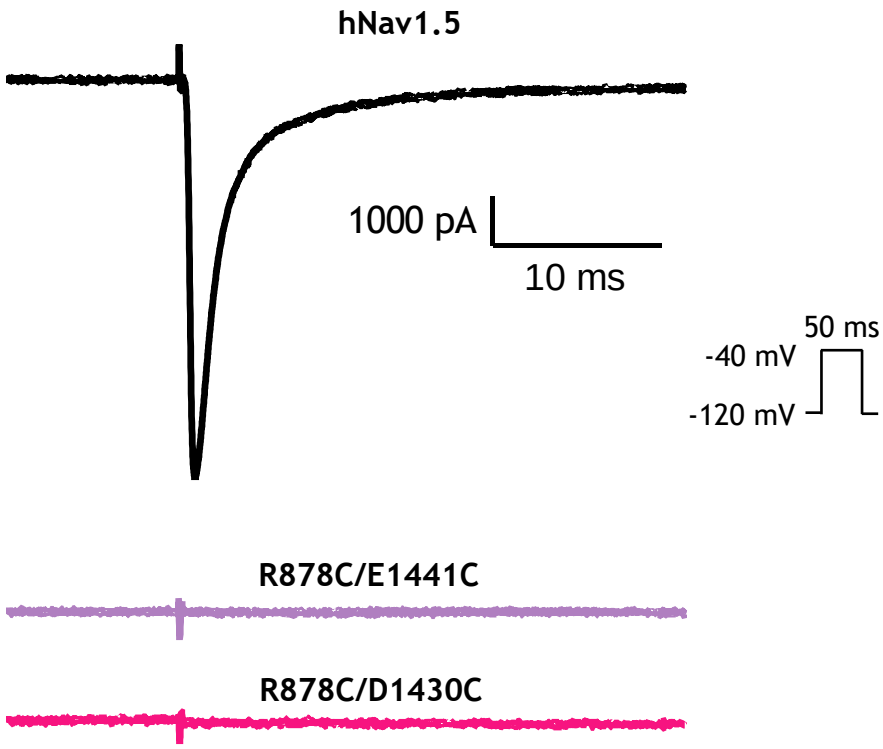

Figure 3.25. Representative traces from the di-sulfide locking experiment. The di-sulfide reducing agent ß-mercaptoethanol does not rescue human: R878C/E1441C or the human: R878C/D1430C double mutants.

3.10 MD simulation

Based on the electrophysiological, biochemical, and pharmacological evidence presented above, it was hypothesized that mutations in the DII-DIII turret interface of $Na_v1.5$ perturb the turret structure, which then allosterically disrupts pore geometry and/or global channel flexibility, to impair sodium ion permeability. To address this question, atomistic MD simulations was carried out[281,282] of the wild-type $Na_v1.5$ structure and mutants generated by *in silico* mutagenesis[253]. The rat $Na_v1.5$ structure[27] was used as the template because this was the only high-resolution $Na_v1.5$ structure available during the experiments. However, it should be noted that very recently, Li, *et al.*, reported the structure of human $Na_v1.5$[283]. As expected, the human and rat $Na_v1.5$ ($rNa_v1.5$) structures are extremely similar, both within the DII-DIII turret region and throughout the whole channel. Importantly, there are no significant differences in the geometry or relative positions of the residues of interest between the two $Na_v1.5$ structures (Figure 3.26).

Since it was impractical to simulate all the mutants that was characterised experimentally, a sub-set of specific mutants was chosen as a model, both pathological and artificial, that together represent illustrative examples from the range of recorded gating activities. The mutations that were examined by MD simulation are summarized in Table 3.1 and represent three functional classes, as informed by the electrophysiological data (Table 3.2, Table 3.3, Table 3.4). They are:

(i) Rat W1422Y. This is the rat equivalent to human W1440Y, a mutation that incorporates a natural Na_v channel isoform polymorphism into a $Na_v1.5$ background and whose electrophysiological gating behavior does not differ from the wild-type protein.

(ii) Rat E1443D. This is the rat equivalent to human E1441D, a mutation with a conservative charge replacement, yet with a significantly reduced peak current and altered slope factor.

(iii) Rat E1443Q and rat R881D/D1432R. These mutants are equivalent to the human putative BrS mutant E1441Q and the human R878D/D1430R mutant respectively. Both human mutants produce inactive channels.

For all structures simulated, channel stability was assessed as measured through Root-Mean Square Deviation (RMSD) values. Pore and turret interface stabilities were assessed through RMSD values and residue distances in each structure.

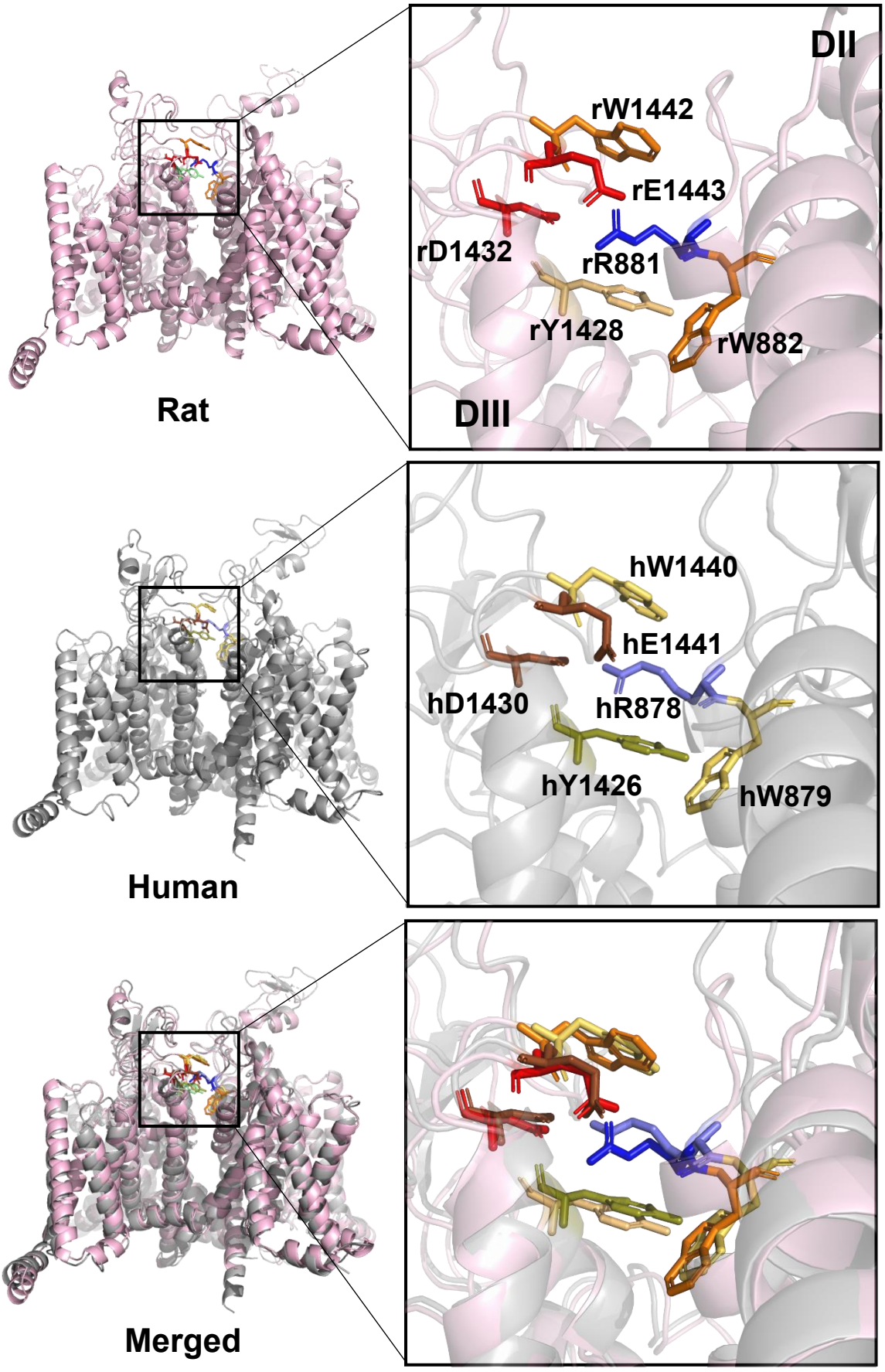

Figure 3.26. Human (PDB: 7DTC) and rat $Na_v1.5$ (6UZ3) channel structures are very similar with no significant differences in the geometry or relative position of the residues of interest

3.10.1 Global and local stabilities of the simulated rNa$_v$1.5 channel

Mutations of the turret interface affect both global and local stability of the Na$_v$1.5 structure - RMSD backbone values were used to examine the structural flexibility of the whole channels (Figure 3.28A), the residues of the S5-S6 helices that line the inner pore (Figure 3.28B) and the residues within the turret interface (Figure 3.28C). In these experiments, the relative stabilities of wild-type and mutant channels within a 15ns window were compared. This time range was chosen to be long enough to record side-chain rearrangements of interest[284], whilst being computationally tractabe[285–287]. In all cases, the time was sufficient to establish steady-state residue positions in the wild-type channel (Figure 3.27) with which to compare mutants. Further still for two of the mutants and WT, a longer simulation of 100ns was run (Figure 3.29A,B) to confirm that equilibrium was established in less than 15ns that remained stable for the entire 100ns simulation.

For the case of global stability and the stability of the S5-S6 pore residues, the E1443D, E1443Q and R881D/D1432R mutants showed evidence of reduced stability relative to the wild-type model, whilst the W1442Y mutant was most similar to the wild-type channel (Figure 3.28 A, B). This is consistent with the electrophysiological data for the human W1440Y mutant, which shows no significant differences with the wild-type channel in any gating parameter, including peak current. The RMSD backbone values for the turret interface residues (Figure 3.28C) provided a finer-grained analysis. For example, the flexibility of the E1443D mutant was comparable to the wild-type, and the W1442Y mutant and was now distinct from the higher flexibility shown by the R881D/D1432R and E1443Q mutations. The human versions of R881D/D1432R and E1443Q were devoid of any detectable gating behavior, whilst the human version of E1443D retained some peak current activity (Figure 3.14. Table 3.2). Hence, the modelled stability of the turret interface region provided the clearest relationship with function, even in the presence of some global destabilization.

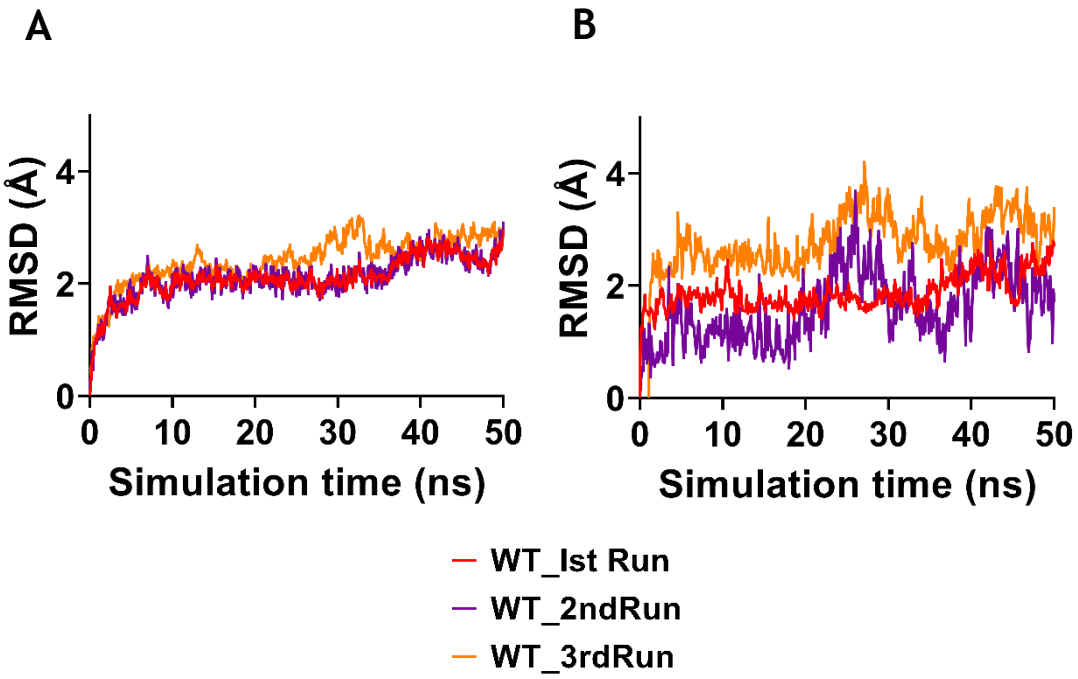

Figure 3.27. MD simulations of the global and local stabilities of the simulated rat $Na_v1.5$ channels. RMSD values of protein backbone of the wild-type (WT) channels in three separate runs. The first frame of the MD simulation as a function of time was examined for: **A.** all residues in the protein; **B.** residues of the complex salt-bridge and cation-π bonds connecting the DII-DIII turret interface.

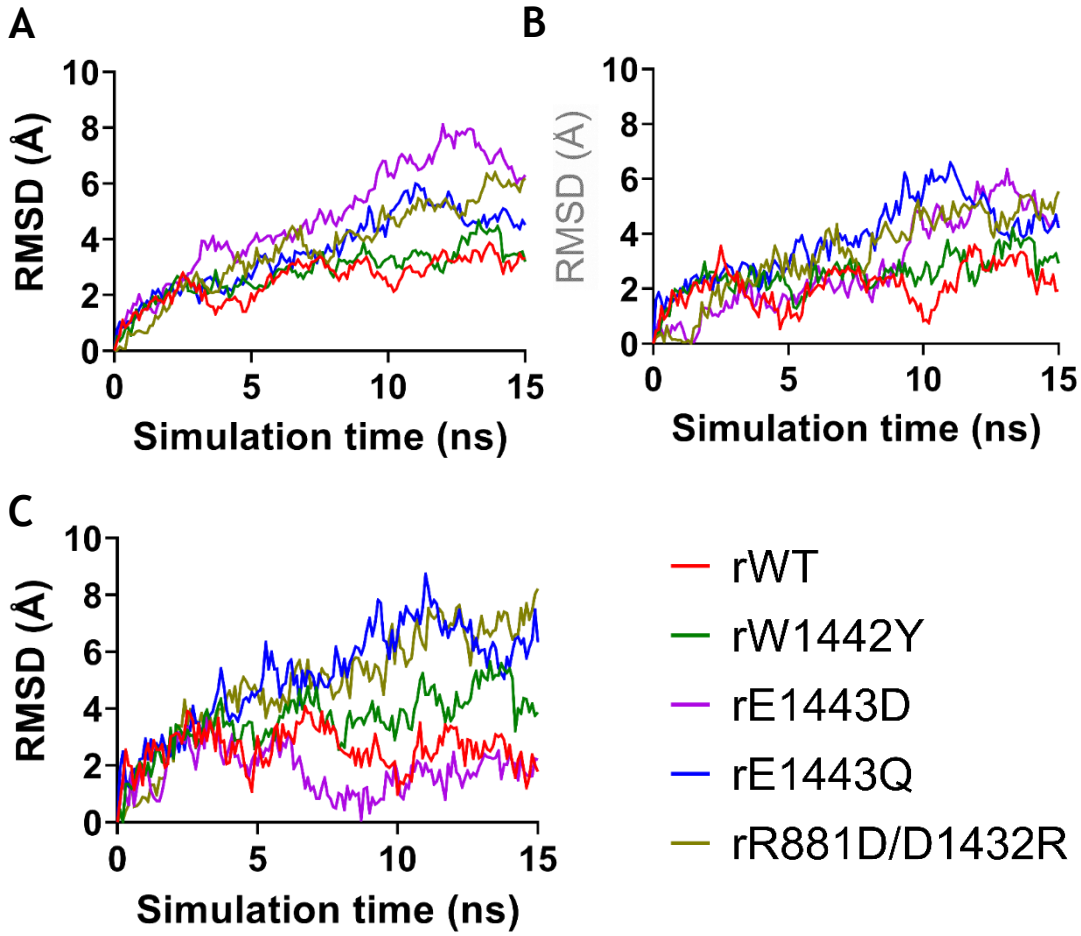

Figure 3.28. RMSD values of C(α) atoms of the wild-type (WT) and mutant rat (r) Nav1.5 channels. The first frame of the MD simulation as a function of time was examined for, **A.** all residues in the protein, **B.** residues of the S5-S6 helices lining the pore of the channel and **C.** residues of the complex salt-bridge and cation-π bonds connecting the DII-DIII turret interface.

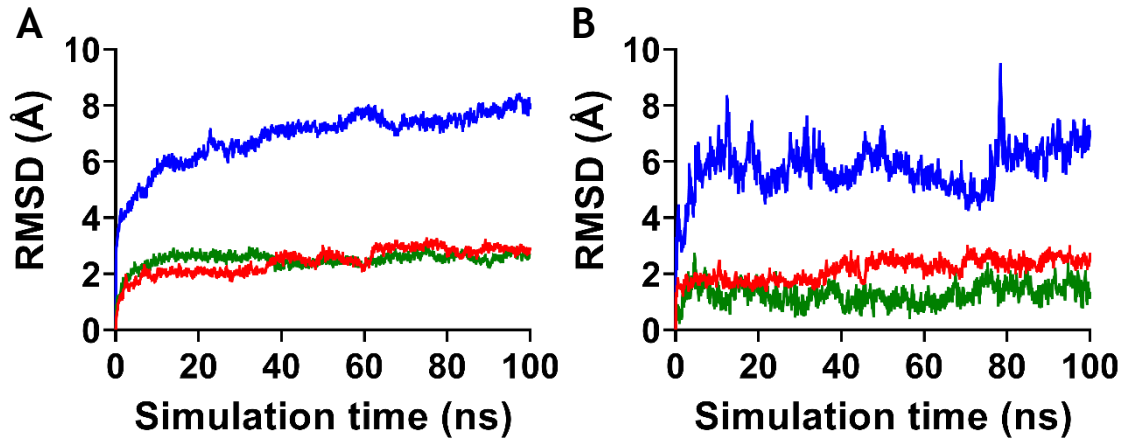

Figure 3.29. 100ns MD simulation of the global and local stabilities of WT, positive control W1442Y and salt-swap (R881D/D1432R) mutant which showed the least stability from previous runs. **A.** all residues in the protein; **B.** residues of the complex salt-bridge and cation-π bonds connecting the DII-DIII turret interface.

3.10.2 Bond distance analysis

Mutant-specific destabilization of the turret interface- To better understand how the mutations affect the local stability at the DII-DIII turret interface, MD simulations was applied to calculate distance values for the salt-bridges and the cation-π interactions, as analysed across the entire time course of the simulation (Figure 3.30). In the wild-type simulation, these estimated bond distances (~3-5 Å) indicated stable salt-bridge and cation π interactions over the time course of the simulation. The bond distances exhibited in the modelled rat W1442Y mutant were similar to those of the wild-type channel (Figure 3.30). This is consistent with the electrophysiological data showing no differences in gating behavior for the human W1440Y mutant compared to the human wild-type $Na_v1.5$ (Table 3.2). For the case of the modelled rat E1443D mutant, the equilibrium distance between the D1443 and R881 residues was about 10 Å. This increased distance is probably too far to form a strong salt bridge[288] and likely reflects the smaller size of the aspartate compared to the glutamate side chain. Nevertheless, none of the other bond distances were significantly different from the wild-type simulation (Figure 3.30). In the modelled rat E1443Q mutant, the presence of glutamine at position 1443 will prevent the formation of a salt bridge with R881. This probably explains the increased distance between Q1443 and R881. The distance between R881 and the W1442 residue was also significantly disrupted, to the point where the cation π bond was unlikely to be maintained. In the salt-swapped mutant, rat R881D/D1432R, the E1443-R881 salt-bridge distance and the W1442-R881 cation π bond distances both changed during the simulation, but in opposite directions (Figure 3.30), suggesting a more dynamic destabilization.

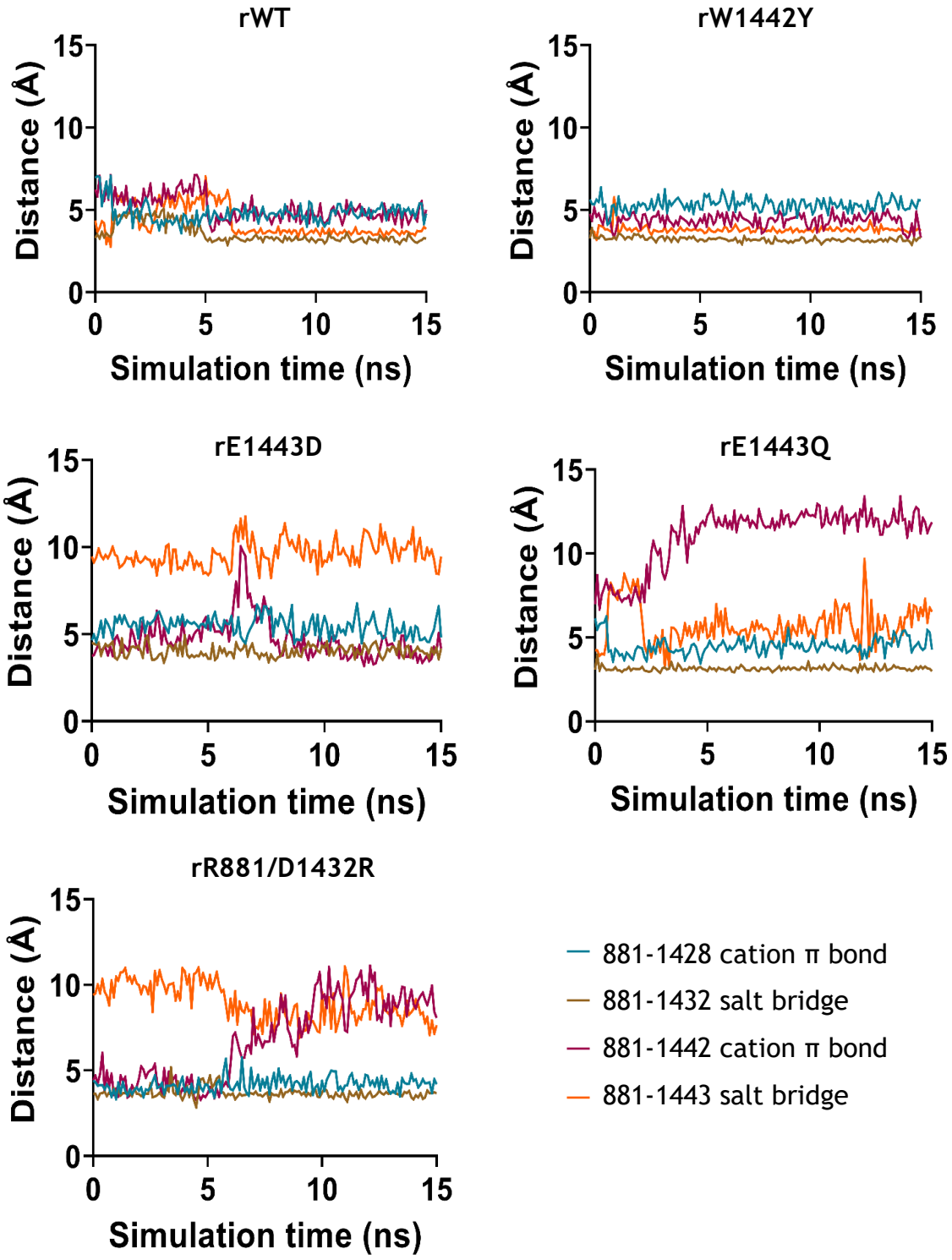

Figure 3.30. Comparative analyses of the bond distances for specific pairs of residues in the DII-DIII turret interfaces of the simulated rat Nav1.5 channels, studied across the entire time course of the simulation. Distance values are presented for every 0.1 ns frame of the MD simulation as indicated.

3.10.3 Effect of the DII-DIII turret mutations on the geometry of the DEKA selectivity ring

Mutations in the turret interface perturb the geometry of the DEKA selectivity ring, reduce the radius of the pore and reduce sodium ion penetration- It was hypothesized that the mutation-induced instability within the DII-DIII turret region may allosterically distort the DEKA selectivity filter and/or the pore geometry. The distance between each pair of residues in the selectivity ring of the wild-type and mutant rat $Na_v1.5$ channels using MD simulation were calculated (Figure 3.31, Figure 3.32). All distances equilibrated well before the end of the simulation.

When the position of the DEKA residues in the selectivity filter was looked at (Figure 3.32), for the WT and rW1442Y mutant it was observed that all the four amino acids were pointing away from the pore, enabling a cavity in the middle which can conduct the Na^+ ions. For the rE1443D mutant, the E and K residues were shifted slightly to a point they started pointing towards the pore, whereas for the rE1443Q and rR881D/D1432R mutant the positively charged Lysine (K) amino acid clearly sticks outwards into pore, essentially occluding it.

The D-A distances were similar for all the simulated channels, including the wild-type $Na_v1.5$. However, for the other distances, each mutation displayed distinct and shorter geometries compared to the wild-type channel (Figure 3.31, Figure 3.32). For the simulated r1443Q mutant, the clearest change was a reduced distance between the D and E residues. Whilst for the simulated rR881D/D1432R mutant, the E-K distance showed the largest reduction compared to the wild-type simulation. Although the D-K distances for all the mutants were noticeably smaller compared to the wild-type channel, this was least obvious for the rW1442Y mutant (Figure 3.31, Figure 3.32).

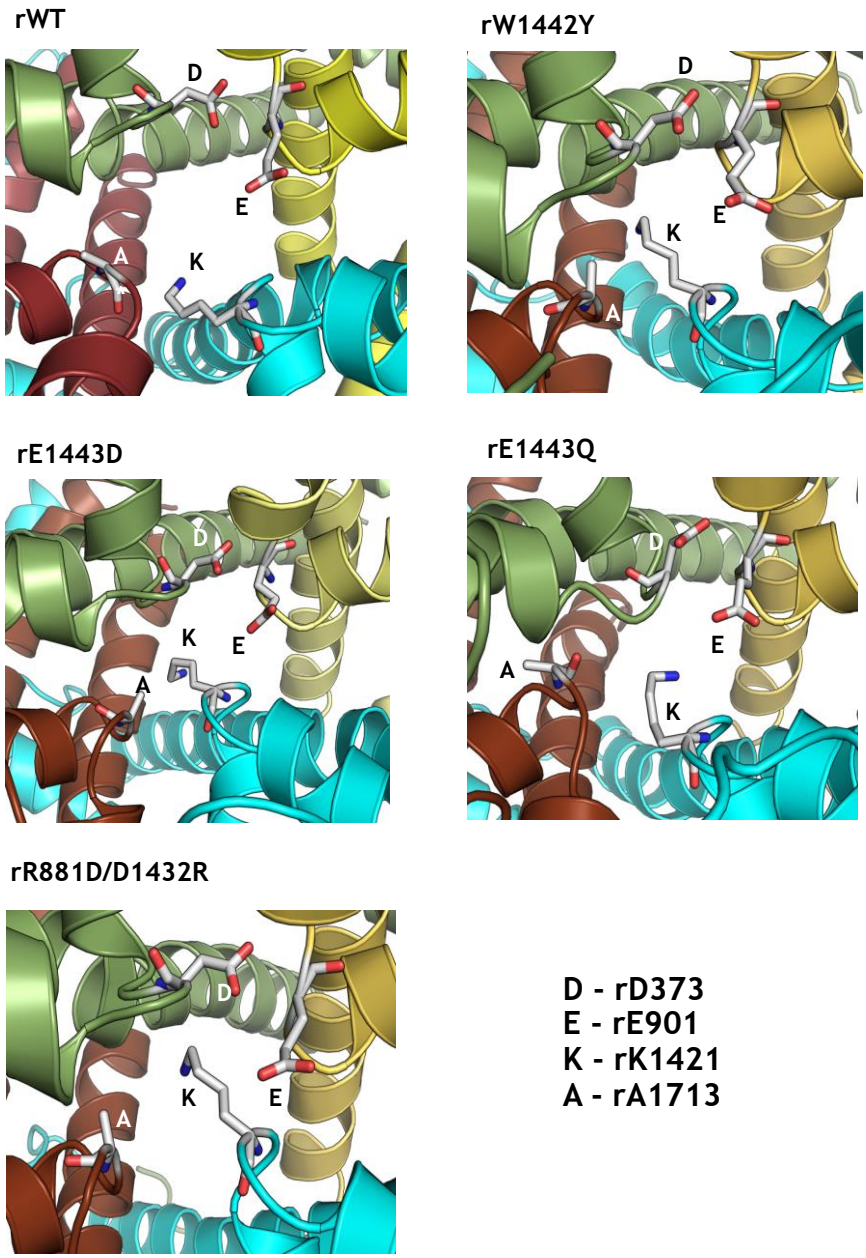

Figure 3.31. Effect of the DII-DIII turret mutations on the geometry of the DEKA selectivity ring of the simulated rat Nav1.5 channels. Diagrammatic representation of the contraction of the DEKA selectivity ring at 15 ns, for the simulated wild-type (WT) and mutant rat (r) $Na_v1.5$ channels, as indicated.

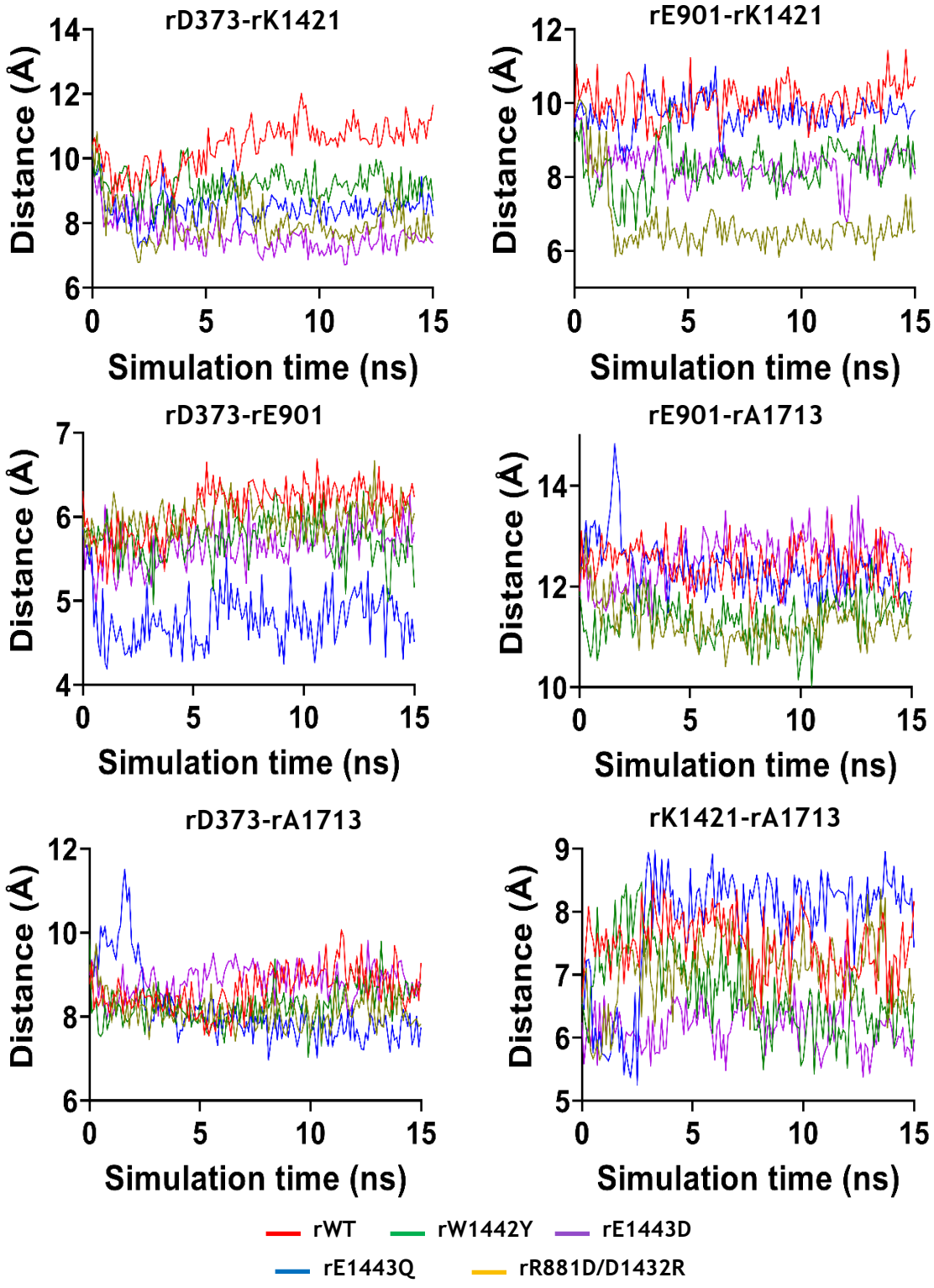

Figure 3.32. Distances between pairs of residues in the DEKA ring, as indicated, equilibrated throughout a 15 ns simulation.

3.10.4 Effect of the DII-DIII turret mutations on pore geometry

The topology of the inner pore vestibule for each structure over a 15 ns simulation was modelled. Firstly, MOLE 2 program[289] was used to provide a pseudo-three dimensional rendering of the pore profile. Secondly, for each mutant, the pore radius profile from the DEKA ring to the intracellular activation gate compared to the pore radius profile of the wild-type channel was calculated (Figure 3.33). The red line in the graph indicated how the pore radius changes along the whole pore. For instance, the largest pore radius is observed to be about 4.5 Å and the shortest is around 2.5 Å for the WT. In both the wild-type and W1442Y mutant structures, the DEKA constriction point and the inner vestibule[38] were clearly identified and remained stable during the simulation. In contrast, the remaining mutants all exhibited degrees of time-dependent and localized structural instability, leading to a reduced pore radius throughout the length of the channel (Figure 3.33). The most striking example of this behavior was shown by the rR881D/D1432R mutant. Although initially, the pore profile closely matched the wild-type topology, by the end of the simulation, pore could not be computed (Figure 3.33). Hence, the occlusion of sodium is predicted to be particularly severe in this mutant and is consistent with the complete absence of gating activity for the human equivalent mutant.

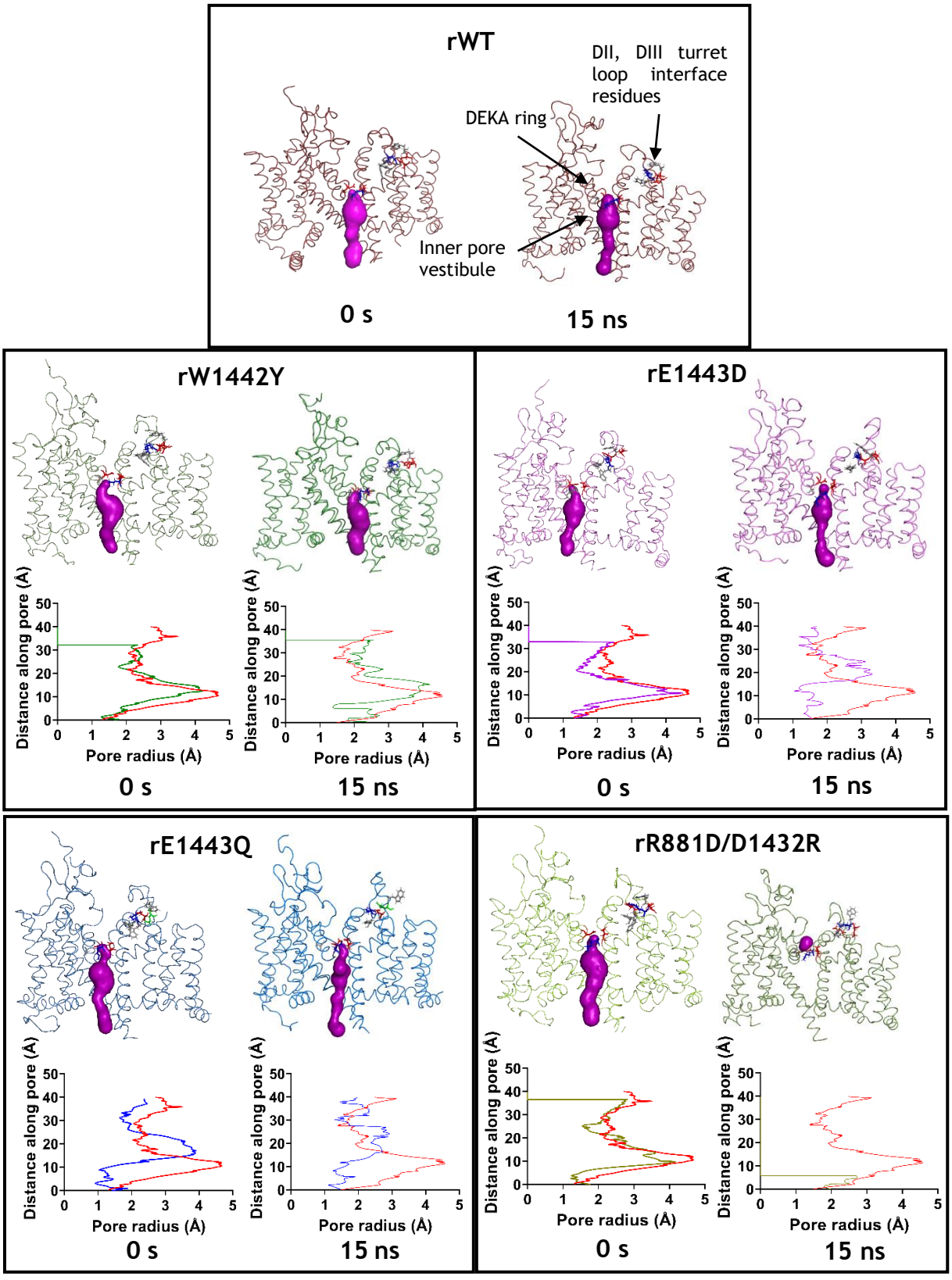

Figure 3.33. Effect of the DII-DIII turret mutations on pore geometry of the simulated rat $Na_v1.5$ channels. The channel cross-sectional profiles for the first (0 s) and last (15 ns) frames of the simulation are shown. Pore profiles, as predicted using MOLE 2 are highlighted in purple. The locations of key regions are indicated for the wild-type channel. Underneath each mutant channel cross-section, the pore radius profiles at 0 sec and 15 ns are shown, relative to that of the simulated WT, and computed to the intracellular surface of the channel. The distance along the pore starts from the DEKA selectivity ring at 0Å and ends at the intracellular activation gate at 50Å.

3.11 Discussion

In this work, a conserved, complex salt-bridge with associated cation-π bonds, that connects the DII and DIII extracellular turret loops and helps encase the $Na_v1.5$ outer vestibule was highlighted. Using the combined approaches of mutagenesis, electrophysiology and MD simulations, it was shown that targeted mutations to these residues significantly compromise $Na_v1.5$ gating behaviour and provide new structural insights into the pathological human BrS/SND mutations that occur in this region.

All the mutants studied were generated by site-directed mutagenesis and conformed by DNA sequencing (Table 3.1, Figure 3.5, Figure 3.6). The mutants were transiently transfected in HEK293f cells, and the efficiency of transfection was confirmed using Leica DMI 6000 CS microscope and was consistently found to be above 80% (Figure 3.7).

The effect of the naturally occurring R878C and E1441Q mutations on the α-α subunit dimerization and the α-ß3 interaction with co-immunoprecipitation were first examined (Figure 3.10). The mutations had no effect on these interactions. This was expected, as ß3 subunit transmembrane region is expected to bind near DIII of Na_v, and its Ig domain is expected to bind on the extracellular loop covering DI and D4. This is based on the similarity in structure of ß3 subunit with ß1 subunit, for which a cryoEM structure confirms its binding to Na_v[25]. The only interesting observation was that the mutated α subunits preferentially precipitated with the higher glycosylated ß3 subunits compared to the WT α-subunits. Previous reports on $hNa_v1.7$ suggested roles of ß1 and ß3 on regulating glycosylation levels of $hNa_v1.7$ α-subunit, however the reverse i.e. any hNa_v α-subunit modulating ß-subunits is not found[248]. Functionally relevant sialic acids, affecting gating parameters such as voltage of half-activation, the voltage of half-inactivation, the time constants for fast inactivation, and the time constants for recovery from inactivation, were found to be localized in the DI/S5-S6 loop region in $hNa_v1.4$, while $hNa_v1.5$ remained unaffected [43]. The negative charges from these sugars probably influences the local electrostatic field near the pore region [48].

Both the wild-type human $Na_v1.5$ and all the mutant channels were detected on the plasma membrane to a similar extent (Figure 3.9). This result agrees with previous reports that the human R878C and the human D1430N BrS mutants were expressed on the plasma membrane[98,154]. There are multiple and extensive quality-control mechanisms within the secretory pathway that can efficiently detect and destroy aberrantly folded proteins before they reach the plasma membrane[290]. Hence, the compromised gating behaviour of the mutant $Na_v1.5$ channels is unlikely to be explained by a large-scale misfolding of the channels. Rather, the mutations are more likely to introduce relatively small structural changes, which nonetheless block one or a small number of gating steps.

For the human mutants that retained some gating activity, only the peak currents and steady-state activation parameters were significantly different from those of the wild-type channel. Steady-state inactivation parameters and recovery from inactivation kinetics were not affected (Table 3.2, Table 3.3). Taken together with the failure of veratridine to rescue the null mutants (Figure 3.24), this suggests that disruption of the extracellular DII-DIII interface on the outer vestibule turrets selectively inhibits one or more of the conformational changes that underlie channel activation. Yet channel activation depends on conformational changes that occur deeper within the pore and within the peripheral voltage-sensors, which are physically distant from the DII-DIII interface on the extracellular turret[27]. Hence, the DII-DIII mutations are likely to induce longer-range, allosteric perturbations.

Complex salt bridges play an important role in stabilizing secondary structures and adjacent domains within proteins[291]. The appropriate ionic contacts between residues of the complex salt bridge depend not only on their charge but also on their precise geometry and orientation. In these situations, arginine is significantly more common than lysine as the cation partner. This is because the delocalized positive charge on the arginine guanidinium group can simultaneously facilitate multiple electrostatic interactions[267]. Thus, in the wild-type rat $Na_v1.5$ structure, the η1 and η2 nitrogens of the R881 guanidinium group individually contact the carboxylate groups of residues D1432 and E1443 respectively, whilst the ε nitrogen lies over the aromatic group of Y1428, contributing to the cation-π interaction (Figure 3.1B). The positive charge on a lysine side chain cannot do this as easily because it is more tightly localised. These considerations probably explain why even lysine cannot functionally substitute for residue R878 in human $Na_v1.5$[154].

In the modelled rat E1443Q mutant (equivalent to the putative human BrS null-mutant E1441Q, (Tabe 3.1), the normal salt bridge between residues 881 and 1443 clearly cannot form. Yet, the major perturbation was to increase the distance between R881 and W1442 (Figure 3.30), thus likely weakening – if not abolishing - the cation-π bond between these two residues. By comparison, the distances between the salt-bridge residues R881 and D1432 and the cation-π bond residues R881 and Y1428 were relatively unaffected compared to the wild-type simulation (Figure 3.30). The second null-mutant examined by MD simulation was R881D/D1432R, in which the charged residues R881 and D1432 were reciprocally swapped. This arrangement did not affect the bond distance between the 881 and 1432 residues. Strikingly, however, the bond distance for the 881-1443 salt-bridge became smaller as the 881-1442 cation-π bond became larger during the simulation, suggesting a dynamic rearrangement within this mutant over the time scale studied (Figure 3.30). Thus, the MD simulations suggest important contributions from both the complex salt bridge and cation-π bonds in maintaining the DII-DIII interface structure. Estimating the quantitative contribution of these individual interactions is difficult using MD simulations[284]. However, of the nine null-mutations studied, seven were targeted to the complex salt-bridge and of the six mutants that retained some gating activity, five were targeted to the cation-π bonds. This could suggest that the complex salt bridge provides a major role in stabilizing the DII-DIII turret interface and the cation-π bonds contribute secondary, although still important reinforcement.

The individual replacement of each of the aromatic residues, human W1440 and Y1426 with alanine significantly reduced peak current but had no significant effects on steady-state gating or kinetic parameters. However, the replacement of human W1440 with tyrosine showed no significant gating effects compared to wild-type human $Na_v1.5$ (Table 3.2). Thus, the precise form of the aromatic amino acid at this position is not critical and indeed, tyrosine not tryptophan is present at this position in most Na_v channel isoforms (Figure 3.3). By contrast, there are more constraints on the second cation-π-forming aromatic residue (human Y1426/rat Y1428). For example, even the replacement of this tyrosine with phenylalanine reduced peak current by about 50% for the human mutant (Table 3.2). This suggests that the tyrosine hydroxyl group is functionally important and in the rat structure, Y1428 forms a hydrogen bond with the DII W882 residue (Figure 3.1), thus holding either or

both the W882 and Y1428 residues in a constrained orientation that may further stabilize the DII DIII turret interface.

To investigate the effect of the turret mutations on the DEKA ring and pore geometry, MD simulations was performed. In the channel structure on which these simulations were based, the cytoplasmic inactivation gate (Figure 3.1) is engaged with its DIV binding site and is therefore thought to represent the inactivated state[27]. Therefore, it was not expected that the sodium ions will fully traverse the channel in this conformation. However, given the differences in pore geometries between the wild-type and mutant structures, important insights are still likely to be obtained. For example, previous MD simulations of Na_v channels have used inactivated state structures as templates[292].

The DEKA ring acts as a constriction point and selectively favoured sodium ion permeability over other cations. The detailed mechanism by which selectivity is achieved is uncertain, but site-directed mutagenesis experiments[293] and the use of cryo-EM structures[294], suggest that the geometry of both the DEKA ring acidic groups and the DIII lysine residue are important[282,295]. MD simulations performed indicate notable differences in the RMSD distances between these side-chains in the mutants compared to the wild-type $Na_v1.5$ (Figure 3.31, Figure 3.32). These misalignments, together with possible steric interference from the enhanced flexibility of the DII-DIII turret (Figure 3.28B, Figure 3.29C), offer clues to the gating disruption shown by the mutants. Interestingly, of all the simulated mutants examined, the rat W1442Y showed the least discrepancy in DEKA ring and pore geometry compared to the wild-type channel and indeed, the electrophysiological properties of the human equivalent mutant were not significantly different from the human wild-type channel (Table 3.2).

It is conceivable that perturbation of the DEKA ring may relax ion selectivity. However, this is unlikely to be the case for those human mutants that display a complete absence of current gating since the external bath solution contained 2 mM KCl and 1.5 mM $CaCl_2$. For those human $Na_v1.5$ channels that retained some gating activity, the ion-selectivity of the channel can be investigated by comparing their reversal potentials[293,296]. Importantly, the reversal potentials of the functional mutants were not significantly different from the wild-type value (Figure 3.11, Figure 3.12, Figure 3.13, Figure 3.14). This supports the view that the DEKA rings in each of

the active human mutants retained selectivity for sodium ions, despite their altered geometry.

The most dramatic changes predicted from the MD simulations occurred in the dimensions, geometries and stabilities of the inner pore. In particular, the increased pore radius corresponding to the inner vestibule was prominent in the rat wild-type and W1442Y mutants and remained stable during the simulations. In contrast, by the end of the simulation, the inner vestibule was significantly attenuated in the rat E1443Q mutant and absent altogether in the rat R881D/D1432R mutant (Figure 3.33). Both equivalent human mutations were electrophysiologically inactive (Figure 3.14, Figure 3.15). This attenuation in the inner vestibule radius was less dramatic in the modelled rat E1443D mutant (whose human equivalent retained about 6% of the wild-type peak current activity) but was still noticeable compared to the wild-type and W1442Y profiles (Figure 3.33). Hence, the degree of pore constriction in the MD simulations for the mutants – particularly within the inner vestibule – broadly correlated with the gating activity of the equivalent human mutants.

Except for the human W1440Y and Y1426F mutants, all other human activity-retaining mutants exhibited significantly higher values of the slope-factor, *k* (activation) compared to the wild-type channel (Table 3.2). This slope factor is inversely proportional to the effective charge (*z*) transferred across the membrane during activation[297,298]. The larger values of *k* (activation) therefore imply that the voltage-sensing movements in the VSDs of the mutants are restricted relative to the wild-type channel. These movements are normally tightly coupled to pore opening and thus perhaps to pore geometry[38]. In further work, it will be interesting to monitor the S4 helix movements within the individual VSDs of each mutant, for example by using conformationally-sensitive biophysical methods[249,299]. However, to follow such conformational changes by MD simulations will require extended simulation times that run into the hundreds of ns – ms range[284]. Ultimately, the predictions from the MD simulations will also require direct comparison to high-resolution structures of the individual mutants.

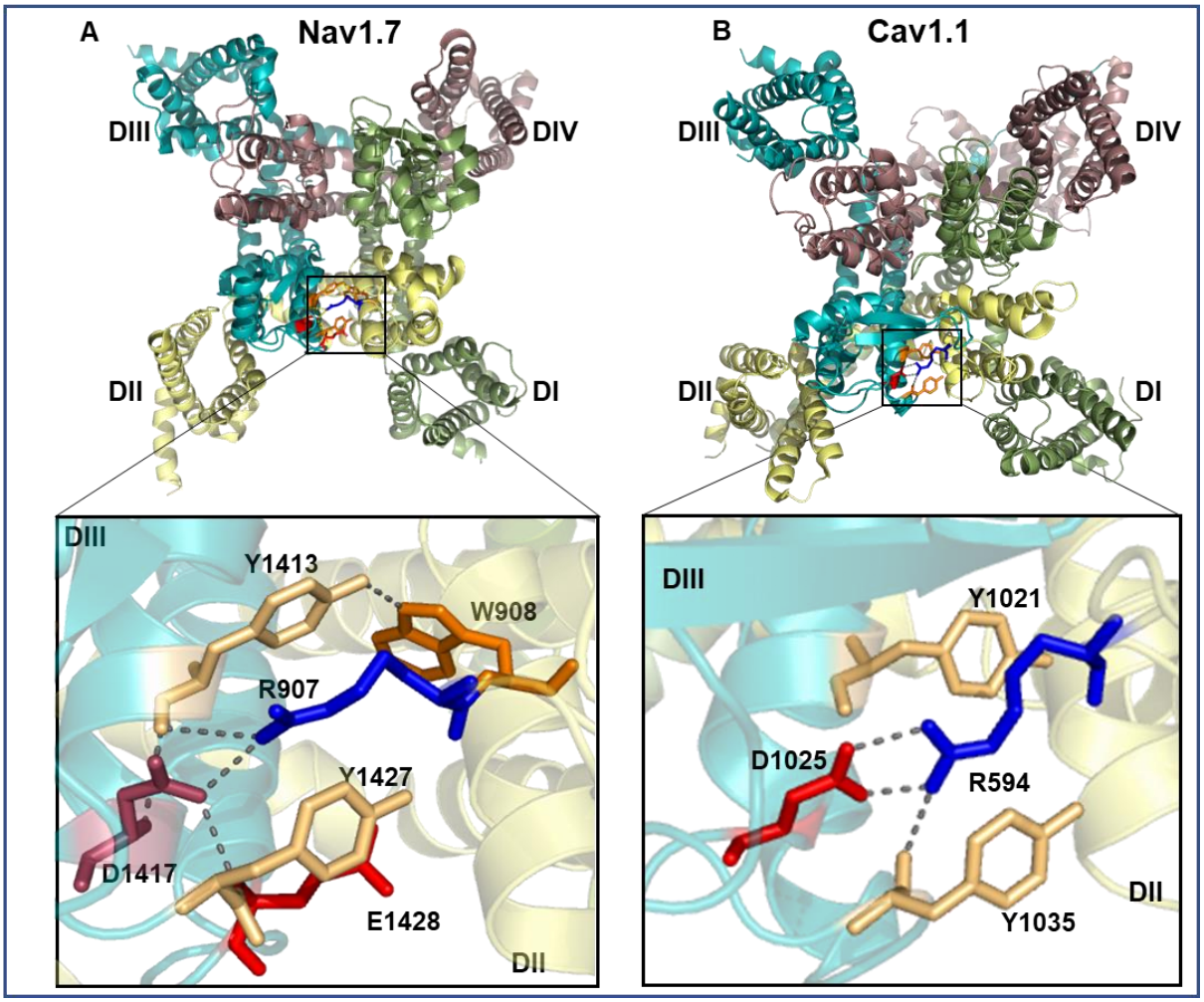

Figure 3.34. CryoEM structure of A. $Na_v1.7$ and B. $Ca_v1.1$, showing the DII-DIII interface with the complex salt bridge and cation-π interaction.

The existing cryo-EM structures of $Na_v1.2$, $Na_v1.4$ and $Na_v1.7$ all reveal the same cation-π bonded complex salt-bridge at the DII-DIII turret interface[25,28]. Furthermore, the critical residues that form this interface are completely conserved in all Na_v channel isoforms (Figure 3.3), suggesting that all Na_v channel isoforms will display this structural feature. Interestingly, several independent missense mutations corresponding to these residues in human $Na_v1.1$ are associated with inherited epileptic encephalopathy[182]. Also, an arginine to glutamine missense null-mutation in human $Na_v1.7$ is associated with congenital insensitivity to pain. This $Na_v1.7$ residue is designated R896[113] or R907[182] (Figure 3.34), depending on the alternatively spliced $Na_v1.7$ isoform, and is equivalent to human $Na_v1.5$ R878 and rat R881. Hence our current work not only provides insights into $Na_v1.5$-associated cardiopathologies but also into similar pathological mutations in other Na_v channels. Finally, eukaryotic voltage-gated sodium channels and voltage-gated calcium channels are derived from a common ancestor by gene duplication[300]. The Cav1.1

family of voltage-gated calcium channels similarly contains a salt bridge, bounded by likely cation-π bonds at the equivalent DII-DIII extracellular turret interface[301] (Figure 3.34). To my knowledge, there are no clinical reports of mutations affecting these Cav1.1 residues. However, if such mutations are discovered, it can be predicted that the channels will either be non-functional or severely compromised and are likely to have pathological consequences.

Chapter 4

Regulation of Na_V by Calmodulin

4.1 Introduction

The C-terminal domains (CTD) of all the Na_vs share high sequence similarity, particularly their proximal half, the EF hand region (Figure 4.1). The CTDs primarily affect the kinetics and voltage dependence of Na_v inactivation. Thus, it is well documented that the brain $Na_v1.2$, inactivates more rapidly than the cardiac $Na_v1.5$. Furthermore, chimeras made by exchanging the CTD of $Na_v1.5$ for that of the $Na_v1.2$, results in a channel with a faster inactivation kinetics similar to that of $Na_v1.2$. Conversely, exchanging the CTD of $Na_v1.2$ for that of $Na_v1.5$, results in a slowed inactivation. In addition, although the effects on inactivation of CTD are mostly attributed to the proximal half, known to bind calmodulin (CaM), fibroblast growth factor (FGF) and the DIII-DIV linker (inactivation gate), truncation of the distal half (post IQ motif) also causes 3 mV negative shifts in steady-state inactivation of $Na_v1.2$. In contrast, complete removal of the $Na_v1.2$ CTD causes a -12 mV shift[302].

Calmodulin (CaM) comprises two globular, N- and C- terminal domains connected by a flexible linker of around eight turns (Figure 4.2)[303]. It is highly conserved amongst eukaryotes functioning as a Ca^{2+} sensor that can bind four Ca^{2+} at the four EF-hand like (helix-loop-helix) binding sites. The CaM then undergoes a conformational change which allows it to interact and regulate other proteins. CaM also interacts with other cellular proteins in its *apo* form i.e., with no Ca^{2+} bound to it. CaM regulates the function of many cellular enzymes including CaM-dependent kinases and phosphatases, plasma membrane Ca^{2+}-ATPases, nitric oxide synthase, and glutamate decarboxylase. Interactions with other cellular proteins have also been reported, for example interaction with myosin V heavy chain, the C-terminal domain of the Ca^{2+} channel (Cav1.2), Ca^{2+}-activated K^+ channels, and voltage-gated Na^+ channels ($Na_v1.2$ and 1.5). CaM utilizes non-polar interactions and the flexibility of its linker to wrap around its target protein[304].

```
Nav1.9 LENFNTATEESEDPLGEDDFDIFYEVWEKFDPEATQFIKYSALSDFADALPEPLRVAKPN   60
Nav1.8 LENFNVATEESTEPLSEDDFDMFYETWEKFDPEATQFITFSALSDFADTLSGPLRIPKPN   60
Nav1.4 LENFNVATEESSEPLGEDDFEMFYETWEKFDPDATQFIAYSRLSDFVDTLQEPLRIAKPN   60
Nav1.5 LENFSVATEESTEPLSEDDFDMFYEIWEKFDPEATQFIEYSVLSDFADALSEPLRIAKPN   60
Nav1.6 LENFSVATEESADPLSEDDFETFYEIWEKFDPDATQFIEYCKLADFADALEHPLRVPKPN   60
Nav1.1 LENFSVATEESAEPLSEDDFEMFYEVWEKFDPDATQFMEFEKLSQFAAALEPPLNLPQPN   60
Nav1.7 LENFSVATEESTEPLSEDDFEMFYEVWEKFDPDATQFIEFSKLSDFAAALDPPLLIAKPN   60
Nav1.2 LENFSVATEESAEPLSEDDFEMFYEVWEKFDPDATQFIEFAKLSDFADALDPPLLIAKPN   60
Nav1.3 LENFSVATEESAEPLSEDDFEMFYEVWEKFDPDATQFIEFSKLSDFAAALDPPLLIAKPN   60
       ****..***** :**.****: *** ******:****: :  *::*. :*  ** : :**

Nav1.9 KYQFLVMDLPMVSEDRLHCMDILFAFTARVLGGSDGLDSMKAMMEEKFMEANPLKKLYEP   120
Nav1.8 RNILIQMDLPLVPGDKIHCLDILFAFTKNVLGESGELDSLKANMEEKFMATNLSKSSYEP   120
Nav1.4 KIKLITLDLPMVPGDKIHCLDILFALTKEVLGDSGEMDALKQTMEEKFMAANPSKVSYEP   120
Nav1.5 QISLINMDLPMVSGDRIHCMDILFAFTKRVLGESGEMDALKIQMEEKFMAANPSKISYEP   120
Nav1.6 TIELIAMDLPMVSGDRIHCLDILFAFTKRVLGDSGELDILRQQMEERFVASNPSKVSYEP   120
Nav1.1 KLQLIAMDLPMVSGDRIHCLDILFAFTKRVLGESGEMDALRIQMEERFMASNPSKVSYQP   120
Nav1.7 KVQLIAMDLPMVSGDRIHCLDILFAFTKRVLGESGEMDSLRSQMEERFMSANPSKVSYEP   120
Nav1.2 KVQLIAMDLPMVSGDRIHCLDILFAFTKRVLGESGEMDALRIQMEERFMASNPSKVSYEP   120
Nav1.3 KVQLIAMDLPMVSGDRIHCLDILFAFTKRVLGESGEMDALRIQMEDRFMASNPSKVSYEP   120
          :: :***:*  *::**:*****:* .*** *. :* ::  **::*: :*  *  *:*

Nav1.9 IVTTTKRKEEERGAAIIQKAFRKYMMKVTKGDQGDQNDLENGPH-SPLQTLCNGDLSSFG   179
Nav1.8 IATTLRWKQEDISATVIQKAYRSYVLHRSMALSNTPCVPRAEEE---AASLPDEGFVAFT   177
Nav1.4 ITTTLKRKHEEVCAIKIQRAYRRHLLQRSMKQASYMYRHSHDGS--GDDAPEKEGLLANT   178
Nav1.5 ITTTLRRKHEEVSAMVIQRAFRRHLLQRSLKHASFLFRQQAGSGLSEEDAPEREGLIAYV   180
Nav1.6 ITTTLRRKQEEVSAVVLQRAYRGHLARRGFICKKTTSNK--------------------L   160
Nav1.1 ITTTLKRKQEEVSAVIIQRAYRRHLLKRTVKQASFTYNKNKIKGGAN--LLIKEDMIIDR   178
Nav1.7 ITTTLKRKQEDVSATVIQRAYRRYRLRQNVKNISSIYIKDGDRD-DD--LLNKKDMAFDN   177
Nav1.2 ITTTLKRKQEEVSAIIIQRAYRRYLLKQKVKKVSSIYKKDKGKECDG--TPIKEDTLIDK   178
Nav1.3 ITTTLKRKQEEVSAAIIQRNFRCYLLKQRLKNISSNYNKEAIKGRID--LPIKQDMIIDK   178
       *.** : *.*:  *  :*: :* :  :

Nav1.9 VAKGKVHCD-------------------------------------------------------   188
Nav1.8 ANENCVLPDKSE----------------------TASATSFPPS---YESVTRGLSDRV   211
Nav1.4 MSKMYGHENGNSSSPSPEEKGEAGDAGPTMGLMPISPSDTAWPPAPPPGQTVRPGVKESL   238
Nav1.5 MSENFSRPLGPPSS-----------SS---------ISSTSFPPS---YDSVTRATSDNL   217
Nav1.6 ENGGTHR---EKKE-----------ST---------PST-ASLPS---YDSVTKPEKEKQ   193
Nav1.1 INENSIT---EKTD-----------LT---------MSTAACPPS---YDRVTKPIVEKH   212
Nav1.7 VNENSSP---EKTD-----------AT---------SST-TSPPS---YDSVTKPDKEKY   210
Nav1.2 LNENSTP---EKTD-----------MT---------PST-TSPPS---YDSVTKPEKEKF   211
Nav1.3 LNGNSTP---EKTD-----------GS---------SST-TSPPS---YDSVTKPDKEKF   211


Nav1.9 -------------------------------- 188
Nav1.8 NMRTSSSIQNEDEATSMELIAPGP-------- 235
Nav1.4 --------------------------------V 239
Nav1.5 QVRGSDYSHSEDL----ADFPPSPDRDRESIV 245
Nav1.6 QRAEEGRRERAKR---QKEV-------RESKC 215
Nav1.1 EQEGKDEKAKGK---------------------- 224
Nav1.7 EQDRTEKEDKGK------DS-------KESKK 229
Nav1.2 EKDKSEKEDKGK------DI-------RESKK 230
Nav1.3 EKDKPEKESKGK------EV-------RENQK 230
```

Figure 4.1. Clustal omega alignment of the C-terminal domain of all the human Na_V.
* Amino acids that are identical between species.
: Amino acids that show conservative changes between species.
. Amino acids that show semiconservative changes between species.

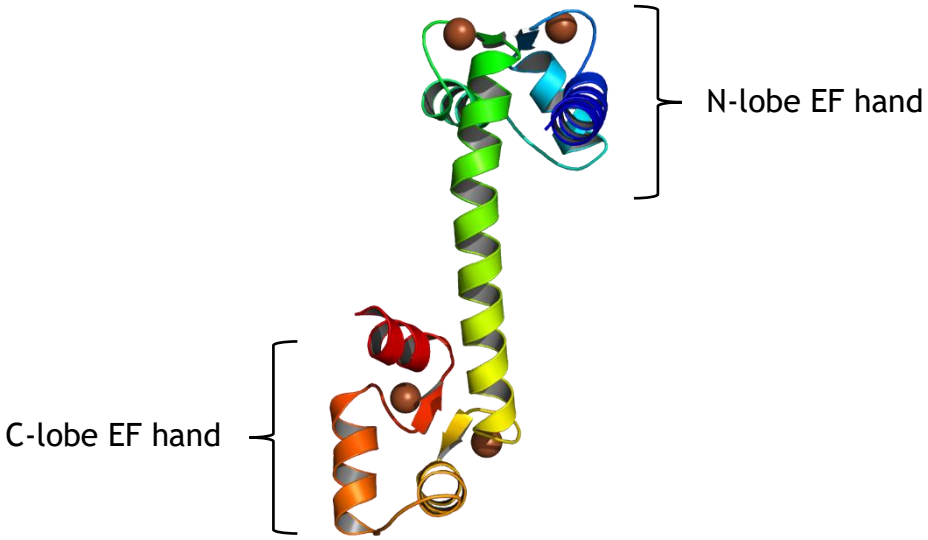

Figure 4.2. The Human Calmodulin structure (PDB ID: 3CLN), colored in rainbow (N to C terminus) with the N-terminus in blue and C-terminus in red. The N-lobe and C-lobe EF hands connected by an α-helix linker are also indicated along with the Ca^{2+} (brown spheres) binding sites.

The Na_v C-terminal domain (CTD) of Na_v consists of an IQ motif that can bind the C-lobe of CaM, and EF-hand like domain that can bind the N-lobe of CaM. The N-lobe of CaM can also bind to a post-IQ motif present in some Na_v subtypes. This interaction of CaM with Na_v channels accelerates inactivation. Disruption of apoCaM binding of to the IQ motif of $Na_v1.5$ CTD increases persistent current. Conversely, the physiological persistent $Na_v1.6$ current in cerebellar Purkinje cells can be diminished by increasing CaM availability[305,306]. Naturally occurring mutations in $Na_v1.5$ CTD residues involved in their interaction with CaM are associated with both BrS and LQT3. For example the Q1909R mutation in the $Na_v1.5$ CTD which is implicated in LQT3, significantly reduces apoCam binding and results in persistent Na^+ current[306]. Mixed phenotypes of the same mutation presenting as BrS in some patients and LQT3 in others have also been observed. Since binding of apoCaM can increase peak channel open probability, affecting the binding of apoCaM would thus result in a decrease in channel open probability and hence contribute to a BrS phenotype. On the other hand, since broken interaction of apoCaM with the $Na_v1.5$ CTD can cause persistent tail current, this may affect normal repolarization of action potential hence resulting in a LQT3 phenotype[307]. Furthermore, de novo mutations in CaM have been associated with cardiopathologies such as ventricular arrhythmias with recurrent cardiac arrest[308].

Binding of the truncated WT CTD of $Na_v1.2$, $Na_v1.5$ and $Na_v1.6$ have been investigated by several groups using Isothermal Titration Calorimetry (ITC)[306,309,310]. Yan et al., 2018 reported a K_D of 99 ± 4 nM between the WT $Na_v1.5$ CTD (1773-1940 a.a) and apoCaM, while Wang et al., 2014 found the K_D to be 88 ± 6 nM. In the case of Ca^{2+}-CaM, a slightly higher K_D value of 132 ± 9 nM was found by Wang et al., 2014. Gabelli et al., 2014 reported a K_D of 46 ± 33 nM to 105±15 nM with Ca^{2+}-CaM, with a slightly smaller CTD protein 1773-1929, however the resulting complex still involved the CaM C-lobe binding αVI helix of the CTD, including the suggested CaM N-lobe binding motif (NLBM). All the data above were obtained from microCal ITC-200 at 20-28 °C, with the $Na_v1.5$ CTD in the cell (20-75 μM) titrated with apoCaM (200-1000 μM). In the case of the $Na_v1.2$ CTD (1777-1937 a.a) with apoCaM, K_D of 36 ± 6 nM and with Ca^{2+}-CaM 1713 ± 333 nM were reported. Only Gabelli et al., 2014 studied the $Na_v1.6$ CTD (1769-1926 a.a) interaction with apoCaM and found the K_D to be 276 ± 63 nM.

Furthermore, CaM has been reported to also bind the DIII-DIV linker of Na_v, which consist of the inactivation gate. A K_D of 66 ± 11 nM has been reported for Ca^{2+}-CaM binding to the $Na_v1.5$ DIII-DIV linker[243].

Fibroblast Growth Factors (FGF) are a structurally related diverse group of 22 polypeptides involved in numerous cellular processes including cell differentiation, proliferation, and apoptosis especially during embryonic development. In mature organisms they play key roles in tissue repair and angiogenesis. Changes in expression of FGF and its receptors have been implicated in tumour progression and metastasis. Paracrine and endocrine roles of FGF are well characterized with paracrine FGFs, through interaction with FGF receptors (FGFR) co-factored with heparin, being involved in repair functions. In contrast, endocrine FGFs affect metabolism through interactions with FGFR having α-Klotho or ß-Klotho as a co-factor. Role of intracrine FGFs in neuronal function, with no association with the FGFR, are less understood.

X-ray structures of $Na_v1.2$ with FGF13U and $Na_v1.5$ with FGF12B and FGF13 indicate binding of FGF to the globular EF-hand domains in both cases. Recently, it has been shown that loss of FGF13 in the DRG neurons of mice, removed the ability to perceive painful stimuli. This attributed to an interaction of FGF13 with the $Na_v1.7$ CTD, which ensures localization of $Na_v1.7$ in the membrane during noxious stimuli like heat, and thus increases Na^+ current. Inhibiting this interaction significantly reduced action potential firing in response to heat stimuli[311]. In the heart, the predominantly expressed FHF, FGF12, has been associated with BrS in a single patient to date. Mouse models with the Q7R mutation in FGF12 showed a reduction in Na^+ current density. This mutation reduced binding of FGF12 to $Na_v1.5$ CTD[312].

4.2 Objectives and Hypothesis

As discussed above, Ca^{2+} exerts its regulatory effect on $Na_v1.4$ and $Na_v1.5$ through association with calmodulin. However, such association has not been explored in $Na_v1.7$. Here, I first investigated whether calmodulin interacts with $Na_v1.7$ in presence and absence of Ca^{2+}. Next, I compared this interaction with the interaction of calmodulin with $Na_v1.5$ again in the presence and absence of Ca^{2+}. This protein-protein interaction was studied using two different binding assays: Isothermal Titration Calorimetry (ITC) and Biolayer Interferometry (BLI).

Structures of $Na_v1.4$ CTD and $Na_v1.5$ CTD bound to CaM reveals the residues involved in this interaction. Interestingly, CaM binding to the CTDs differ substantially according to the Na_v subtype. Interaction of $Na_v1.7$ CTD and CaM has not been studied. Structures of the complete CTD have not been solved for any of the Na_v subtypes, although truncated structures of some of the Na_vs are available. Thus, I will try to solve the crystal structure of the complete $Na_v1.7$ C-terminal domain. This will provide us with better insight about the binding sites present in the $Na_v1.7$ CTD and how its amino acids are arranged.

4.3 DNA sequencing confirms successful recombinant protein generation

The Gateway cloning method has been used to clone the full-length C-terminal domain (CTD) of $Na_v1.5$ (C5) and $Na_v1.7$ (C7), truncated versions consisting of the globular EF hand domains, 5EF and 7EF, and the DIII-DIV linker consisting of the inactivation gate (5D3D4 and 7D3D4). Finally, using the same process human calmodulin (CaM) was cloned. As shown in Figure 4.3 and Figure 4.4, all the recombinant proteins consisted of 10-His tags at the N-terminus while the DIII-DIV linkers had additional HA tag at the C-terminus. DNA sequencing confirmed that the cloning was 100% successful with the cloned recombinant proteins when aligned against the WT sequence show 100% identical sequence.

A

```
Expression C5   HHHHHHHHHHTSLYKKAGFEGDRTMLENFSVATEESTEPLSEDDFDMFYEIWEKFDPEAT  60
Nav1.5 CTD      ----------------------------LENFSVATEESTEPLSEDDFDMFYEIWEKFDPEAT  35
                                            **********************************

Expression C5   QFIEYSVLSDFADALSEPLRIAKPNQISLINMDLPMVSGDRIHCMDILFAFTKRVLGESG  120
Nav1.5 CTD      QFIEYSVLSDFADALSEPLRIAKPNQISLINMDLPMVSGDRIHCMDILFAFTKRVLGESG  95
                ************************************************************

Expression C5   EMDALKIQMEEKFMAANPSKISYEPITTTLRRKHEEVSAMVIQRAFRRHLLQRSLKHASF  180
Nav1.5 CTD      EMDALKIQMEEKFMAANPSKISYEPITTTLRRKHEEVSAMVIQRAFRRHLLQRSLKHASF  155
                ************************************************************

Expression C5   LFRQQAGSGLSEEDAPEREGLIAYVMSENFSRPLGPPSSSSISSTSFPPSYDSVTRATSD  240
Nav1.5 CTD      LFRQQAGSGLSEEDAPEREGLIAYVMSENFSRPLGPPSSSSISSTSFPPSYDSVTRATSD  215
                ************************************************************

Expression C5   NLQVRGSDYSHSEDLADFPPSPDRDRESIV***  270
Nav1.5 CTD      NLQVRGSDYSHSEDLADFPPSPDRDRESIV---  245
                ******************************
```

B

```
Expression 5EF  HHHHHHHHHHTSLYKKAGFEGDRTMLENFSVATEESTEPLSEDDFDMFYEIWEKFDPEAT  60
Nav1.5 CTD      ----------------------------LENFSVATEESTEPLSEDDFDMFYEIWEKFDPEAT  35
                                            **********************************

Expression 5EF  QFIEYSVLSDFADALSEPLRIAKPNQISLINMDLPMVSGDRIHCMDILFAFTKRVLGESG  120
Nav1.5 CTD      QFIEYSVLSDFADALSEPLRIAKPNQISLINMDLPMVSGDRIHCMDILFAFTKRVLGESG  95
                ************************************************************

Expression 5EF  EMDALKIQMEEKFMAANPSKISYEPITTTLRRKHE**----------------------  155
Nav1.5 CTD      EMDALKIQMEEKFMAANPSKISYEPITTTLRRKHEEVSAMVIQRAFRRHLLQRSLKHASF  155
                ***********************************
```

C

```
Expression 5D3D4 HHHHHHHHHHTSLYKKAGFEGDRTMDNFNQQKKKLGGQDIFMTEEQKKYYNAMKKLGSKK 60
Nav1.5 D3D4      ----------------------------DNFNQQKKKLGGQDIFMTEEQKKYYNAMKKLGSKK 35
                                             **********************************

Expression 5D3D4 PQKPIPRPLNKYQGFIFYPYDVPDYA**  86
Nav1.5 D3D4      PQKPIPRPLNKYQGFIF-----------  52
                 *****************
```

D

```
Expression CaM  HHHHHHHHHHTSLYKKAGFEGDRTMMADQLTEEQIAEFKEAFSLFDKDGDGTITTKELGT  60
CaM             ----------------------------MADQLTEEQIAEFKEAFSLFDKDGDGTITTKELGT  35
                                             **********************************

Expression CaM  VMRSLGQNPTEAELQDMINEVDADGNGTIDFPEFLTMMARKMKDTDSEEEIREAFRVFDK  120
CaM             VMRSLGQNPTEAELQDMINEVDADGNGTIDFPEFLTMMARKMKDTDSEEEIREAFRVFDK  95
                ************************************************************

Expression CaM  DGNGYISAAELRHVMTNLGEKLTDEEVDEMIREADIDGDGQVNYEEFVQMMTAK**      174
CaM             DGNGYISAAELRHVMTNLGEKLTDEEVDEMIREADIDGDGQVNYEEFVQMMTAK--      149
                ************************************************************
```

Figure 4.3. DNA sequencing of **A.** $Na_v1.5$ C-terminal domain (C5); **B.** EF hand motif of $Na_v1.5$ C-terminal domain (5EF); **C.** DIII-DIV linker consisting of the inactivation gate of Nav1.5 (5D3D4); and **D.** Human calmodulin (CaM). Sequences A, B and C are aligned with the sequence of the human Nav1.5 C-terminal domain, isoform 1 (UniProtKB - Q14524). All the recombinant proteins consist of 10-His tags on the N-terminal (highlighted in yellow). Stop codons are highlighted in red. 5D3D4 has an extra FLAG tag at its c-terminal which is highlighted in cyan.

A

```
Expression C7   HHHHHHHHHHTSLYKKAGFEGDRTMLENFSVATEESTEPLSEDDFEMFYEVWEKFDPDAT  60
Nav1.7 CTD      ----------------------------LENFSVATEESTEPLSEDDFEMFYEVWEKFDPDAT  35
                                            **********************************

Expression C7   QFIEFSKLSDFAAALDPPLLIAKPNKVQLIAMDLPMVSGDRIHCLDILFAFTKRVLGESG  120
Nav1.7 CTD      QFIEFSKLSDFAAALDPPLLIAKPNKVQLIAMDLPMVSGDRIHCLDILFAFTKRVLGESG  95
                ************************************************************

Expression C7   EMDSLRSQMEERFMSANPSKVSYEPITTTLKRKQEDVSATVIQRAYRRYRLRQNVKNISS  180
Nav1.7 CTD      EMDSLRSQMEERFMSANPSKVSYEPITTTLKRKQEDVSATVIQRAYRRYRLRQNVKNISS  155
                ************************************************************

Expression C7   IYIKDGDRDDDLLNKKDMAFDNVNENSSPEKTDATSSTTSPPSYDSVTKPDKEKYEQDRT  240
Nav1.7 CTD      IYIKDGDRDDDLLNKKDMAFDNVNENSSPEKTDATSSTTSPPSYDSVTKPDKEKYEQDRT  215
                ************************************************************

Expression C7   EKEDKGKDSKESKK***      254
Nav1.7 CTD      EKEDKGKDSKESKK---      229
                **************
```

B

```
Expression 7EF  HHHHHHHHHHTSLYKKAGFEGDRTMLENFSVATEESTEPLSEDDFEMFYEVWEKFDPDAT  60
Nav1.7 CTD      ----------------------------LENFSVATEESTEPLSEDDFEMFYEVWEKFDPDAT  35
                                            **********************************

Expression 7EF  QFIEFSKLSDFAAALDPPLLIAKPNKVQLIAMDLPMVSGDRIHCLDILFAFTKRVLGESG  120
Nav1.7 CTD      QFIEFSKLSDFAAALDPPLLIAKPNKVQLIAMDLPMVSGDRIHCLDILFAFTKRVLGESG  95
                ************************************************************

Expression 7EF  EMDSLRSQMEERFMSANPSKVSYEPITTTLKRKQE**----------------------  155
Nav1.7 CTD      EMDSLRSQMEERFMSANPSKVSYEPITTTLKRKQEDVSATVIQRAYRRYRLRQNVKNISS  155
```

C

```
Expression 7D3D4 HHHHHHHHHHTSLYKKAGFEGDRTMDNFNQQKKKLGGQDIFMTEEQKKYYNAMKKLGSKK  60
Nav1.7 D3D4      ----------------------------DNFNQQKKKLGGQDIFMTEEQKKYYNAMKKLGSKK  35
                                             **********************************

Expression 7D3D4 PQKPIPRPGNKIQGCIFPYDVPDYA**  85
Nav1.7 D3D4      PQKPIPRPGNKIQGCIF----------  52
                 *****************
```

Figure 4.4. DNA sequencing of **A.** $Na_v1.7$ C-terminal domain (C7); **B.** EF hand motif of $Na_v1.7$ C-terminal domain (7EF); and **C.** DIII-DIV linker consisting of the inactivation gate of Nav1.7 (7D3D4). Sequences A, B and C are aligned with the sequence of the human Nav1.7 C-terminal domain, isoform 1 (UniProtKB – Q15858). All the recombinant proteins consist of 10-His tags on the N-terminal (highlighted in yellow). Stop codons are highlighted in red. 7D3D4 has an extra FLAG tag at its c-terminal which is highlighted in cyan.

4.4 Recombinant protein purification

Recombinant proteins that were successfully cloned were then transformed into BL21(DE3) E.Coli competent bacteria for expression using autoinduction. BL21 (DE3) strains consist of chromosomal copies of the T7 RNA polymerase gene under control of lacUV5 promoter which is ideal for the pDEST110 expression vector used in this study. It has also been reported that for pDEST110 vectors BL21 (DE3) strains exhibit the maximum expression level of recombinant protein[313]. The fact that this strain is also deficient in ion and ompT proteases is also very helpful. For purification, a two-step approach was taken. First, since all the recombinant proteins contained 10-His tags, Ni-NTA beads were used to purify them. Next, for further purity, size exclusion chromatography (AKTA) was performed. Thus, Figure 4.5 shows the AKTA chromatogram of $Na_V1.5$ CTD (C5). Although, two peaks can be observed, upon running SDS-PAGE followed by Coomassie staining, both the peaks appeared to be the $Na_V1.5$ CTD. The peak that showed the higher purity was chosen for downstream applications. These double peaks are sometimes observed when the concentration of protein is very high resulting in overloading of the AKTA column. Also, parameters like salt concentration in the buffer, temperature and pH can cause these double peaks[314]. This same phenomenon was observed for the other recombinant proteins.

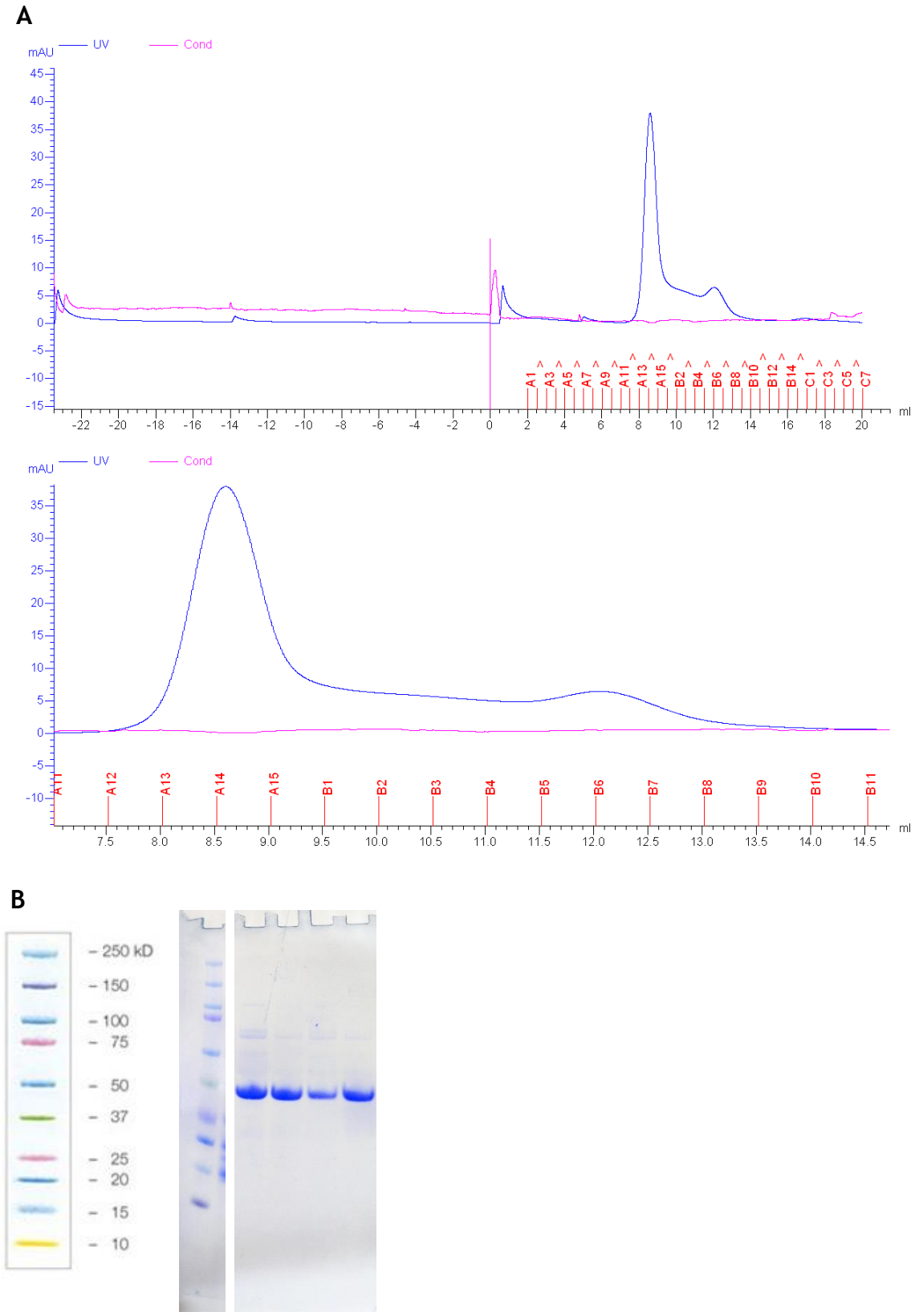

Figure 4.5. $Na_v1.5$ c-terminal domain protein (C5) purification with size exclusion chromatography (AKTA); **A.** The blue peaks corresponding to $Na_v1.5$ CTD, zoomed in image of the peaks is shown below. **B.** Sample from different regions of the peaks were run in a SDS-PAGE gel and stained with Coomassie blue

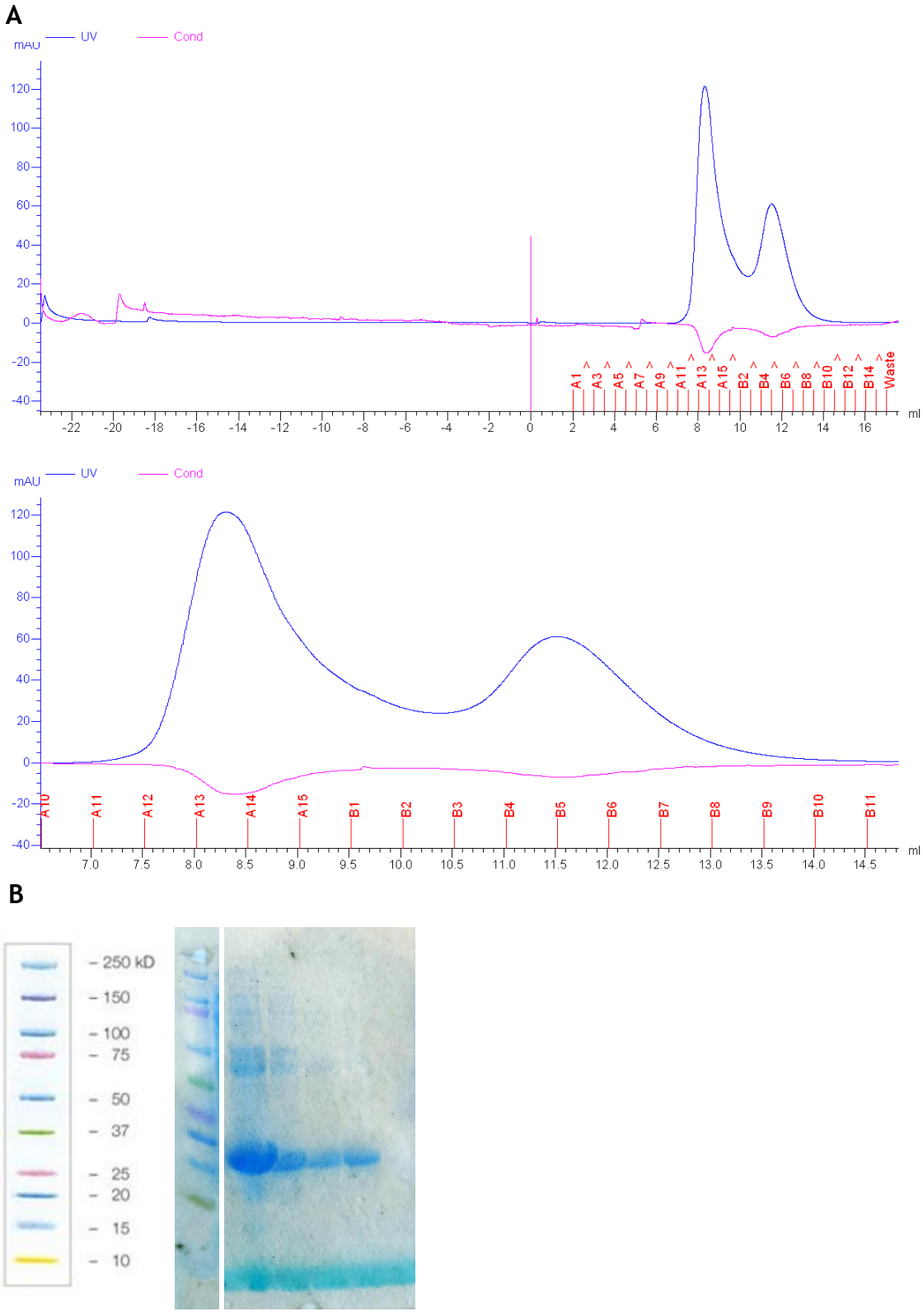

Figure 4.6. $Na_v1.5$ C-terminal domain EF hand domain protein (5EF) purification with size exclusion chromatography (AKTA); **A.** The blue peaks corresponding to $Na_v1.5$ CTD EF hand, zoomed in image of the peaks are shown below. **B.** Sample from different regions of the peaks were run in a SDS-PAGE gel and stained with Coomassie blue.

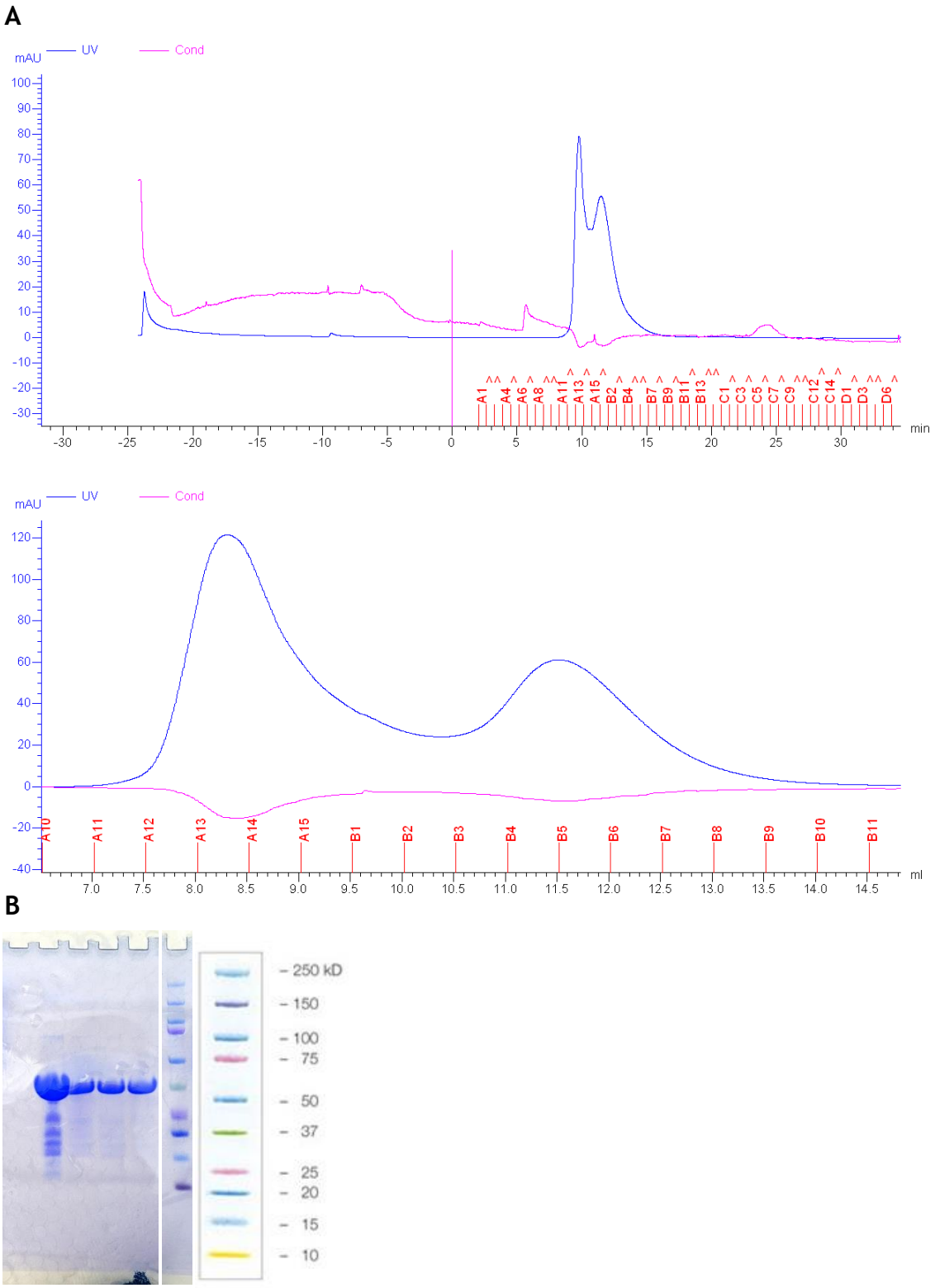

Figure 4.7. $Na_v1.7$ C-terminal domain protein (C7) purification with size exclusion chromatography (AKTA); **A.** The blue peaks corresponding to $Na_v1.7$ CTD, zoomed in image of the peaks are shown below. **B.** Sample from different regions of the peaks were run in a SDS-PAGE gel and stained with Coomassie blue.

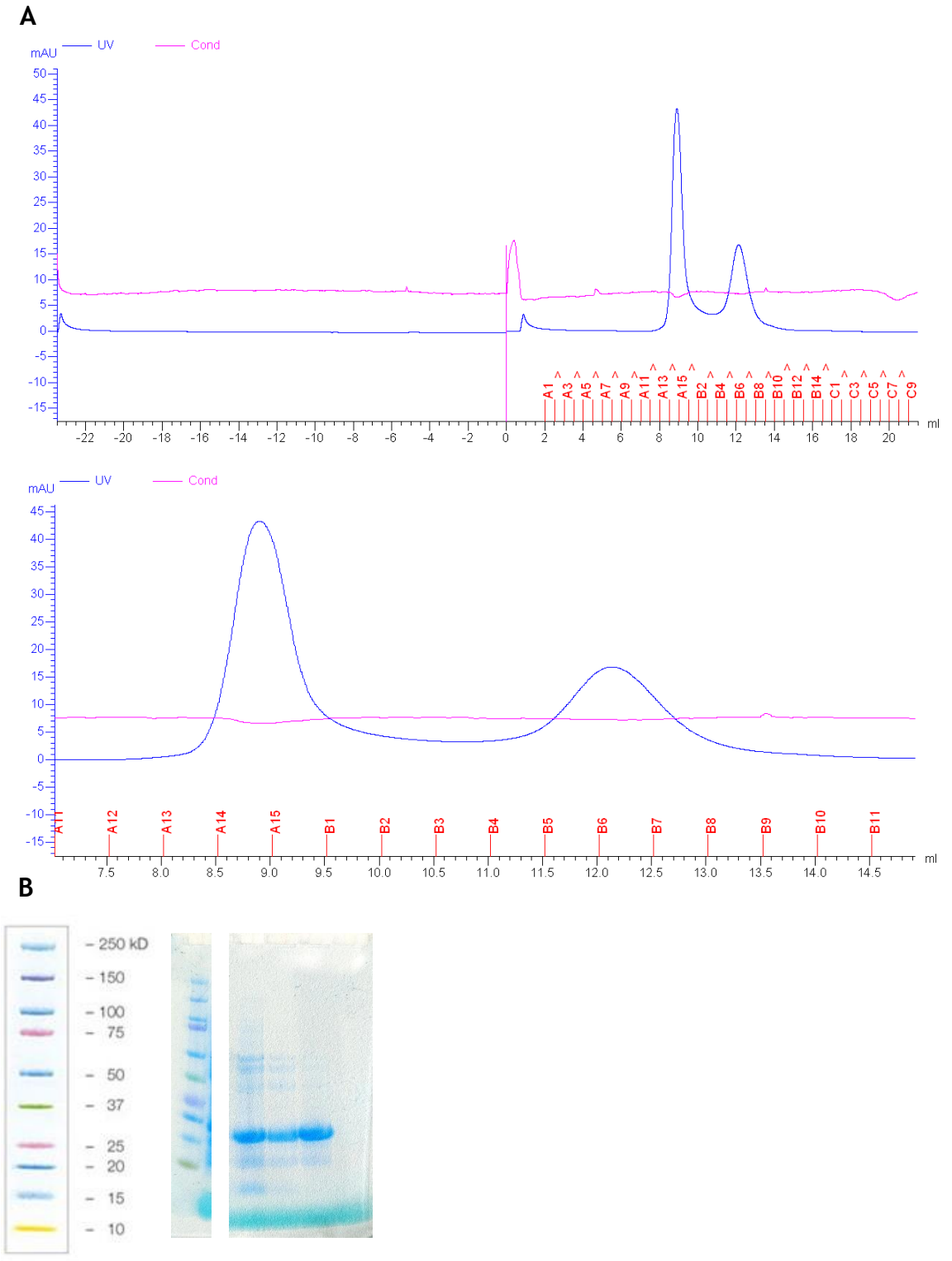

Figure 4.8. $Na_v1.7$ C-terminal domain EF hand domain protein (7EF) purification with size exclusion chromatography (AKTA); **A.** The blue peaks corresponding to $Na_v1.7$ CTD EF hand, zoomed in image of the peaks are shown below. **B.** Sample from different regions of the peaks were run in a SDS-PAGE gel and stained with Coomassie blue.

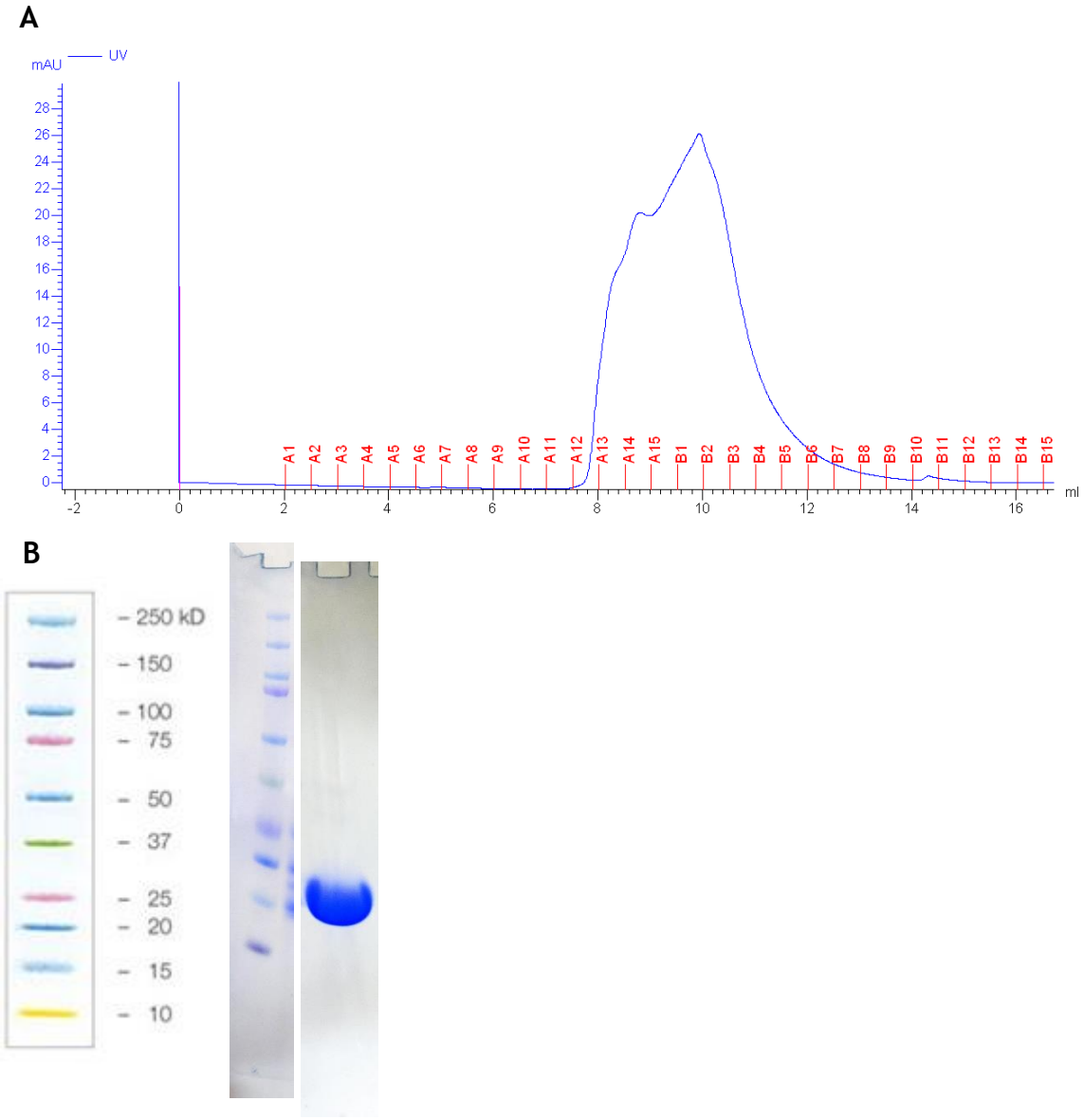

Figure 4.9. Human Calmodulin protein (CaM) purification with size exclusion chromatography (AKTA); **A.** The blue peaks corresponding to CaM. **B.** Sample from the peak was run in a SDS-PAGE gel and stained with Coomassie blue.

4.5 Protein-protein interaction: ELISA

Interaction of the cloned recombinant $Na_v1.7$ CTD (C7) or the truncated EF hand (7EF) with calmodulin (CaM) were tested by ELISA, in presence and absence of Ca^{2+} (Figure 4.10). In presence of 5 mM $CaCl_2$ no interaction was observed. 1000-fold dilution of $CaCl_2$ to 5 µM still resulted in no interaction. Only in presence of 10 mM EGTA, which chelates all the Ca^{2+}, an interaction was observed between both C7 and 7EF with CaM.

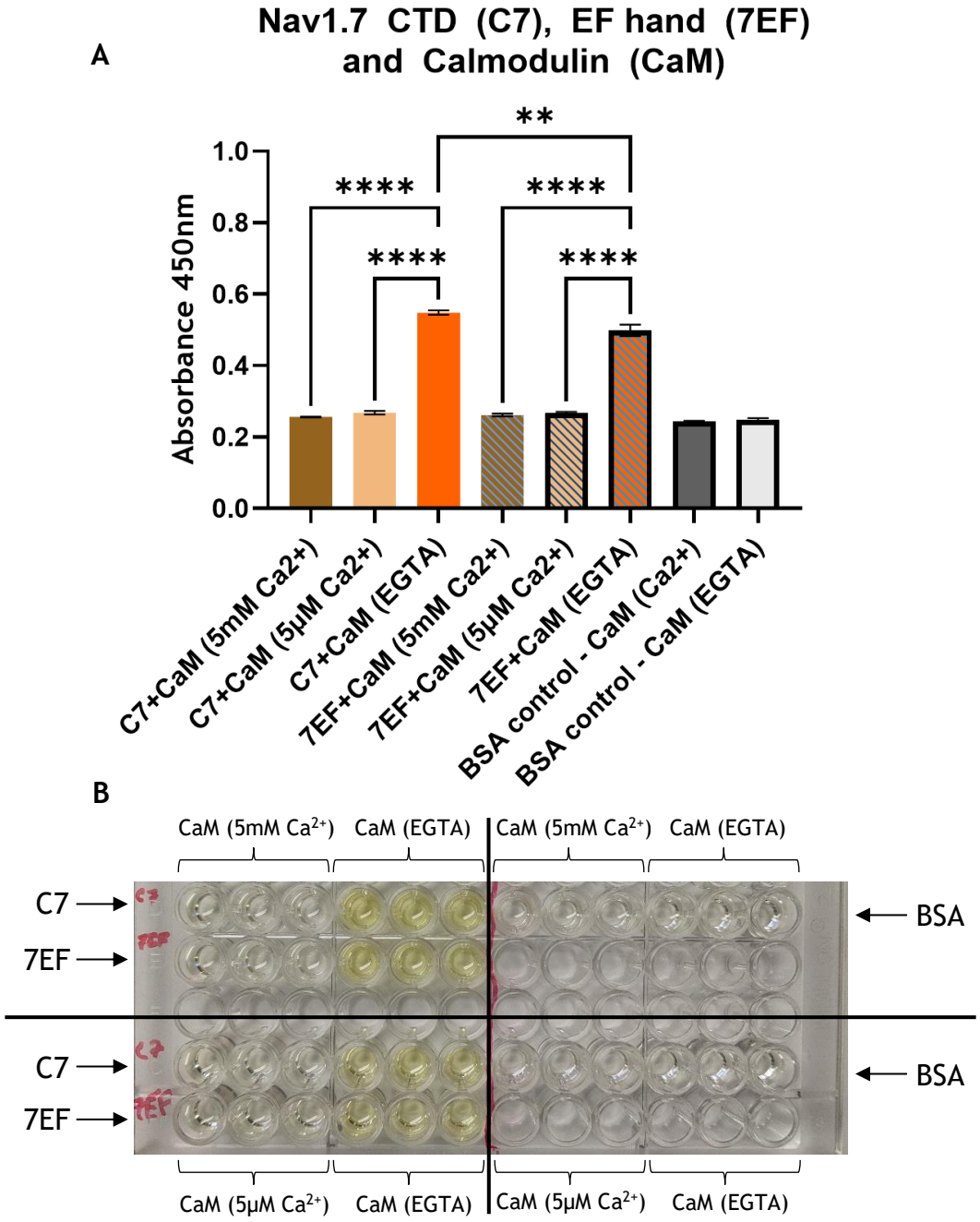

Figure 4.10. Interaction of $Na_v1.7$ CTD (C7) and $Na_v1.7$ CTD EF hand (7EF) with calmodulin (CaM). **A.** The interaction was tested in presence of 5 mM Ca^{2+}, 5 µM Ca^{2+} and 10 mM EGTA. **B.** 96 well plate image of the experiment after addition of 2M sulphuric acid to stop the TMB substrate-HRP reaction.

4.6 Protein-protein interaction: Isothermal titration calorimetry (ITC)

The isothermal titration calorimetry (ITC) results agreed with the ELISA results. Both showed that CaM binds to C7 and $Na_V1.5$ CTD (C5) in the absence of Ca^{2+} (Figure 4.12). The thermograms (top graph of Figure 4.12 A and B) peaks are representative of each injection of CaM into the cell containing either C7 or C5. For C7 after the curve was fitted to one binding site model, the following parameters were also computed: stoichiometry (N) of 1.04 ± 0.00741 sites, enthalpy (ΔH) of -11.93 ± 0.17 kcal/mol, entropy (ΔS) of -6.57 cal/mol/deg, and equilibrium dissociation constant (K_D) of 48.78 ± 12.23 nM. When repeated (Figure 4.12 A ii.) the following values were obtained: N of 1.06 ± 0.00458 sites, ΔH of -6.24 ± 0.05 kcal/mol, ΔS of 12.70 cal/mol/deg and K_D of 44.84 ± 10.95 nM.
For C5 the parameters are, N of 0.958 ± 0.0223 sites, ΔH of -2.97 ± 0.13 kcal/mol, ΔS of 22.2 cal/mol/deg, and K_D of 93.46 ± 19.78 nM.

The ITC results obtained for binding of $Na_V1.5$ CTD (C5) and $Na_V1.7$ CTD (C7) with CaM in the presence of 5 mM $CaCl_2$, show that there is possibly no interaction or a very weak one. The raw data was difficult to fit in 1:1 binding model. For C7 (Figure 4.14 A), N of 1.03 ± 0.129 sites, ΔH of 1.28 ± 0.24 kcal/mol, ΔS of 31.5 cal/mol/deg, and K_D of 1.15 ± 6.67 μM. For C5 (Figure 4.14 B), N of 0.132 ± 0.039 sites, ΔH of -3.37 ± 1.27 kcal/mol, ΔS of 15.9 cal/mol/deg, and K_D of 1.10 ± 5.96 μM.

4.6.1 $Na_v1.7$ CTD and $Na_v1.5$ CTD with apoCaM

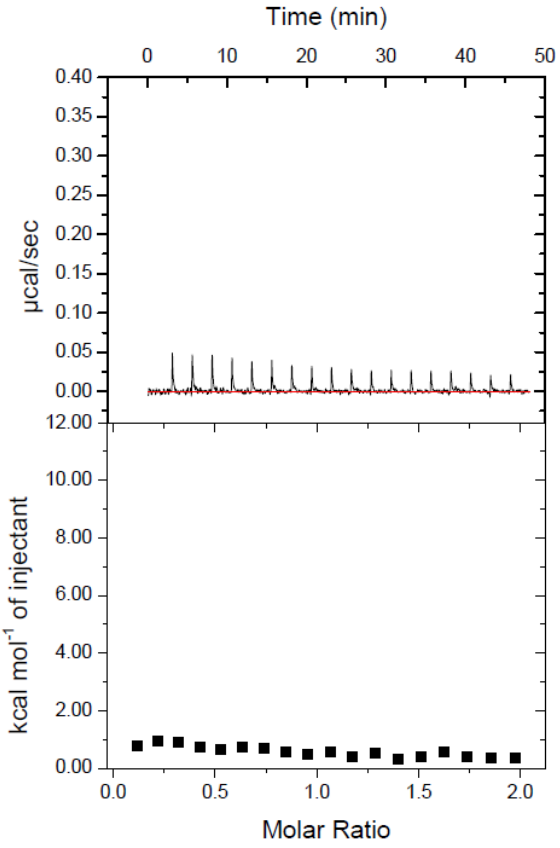

Figure 4.11. ITC sensorgram to measure baseline heat change of adding apoCalmodulin (apoCaM) from syringe into the cell containing the buffer used to prepare $Na_v1.5$ and $Na_v1.7$ CTD. All the buffers contained 10 mM EDTA to chelate any Ca^{2+} ion. Raw ITC data trace (Top) and the integrated heats of the measured interaction (bottom).

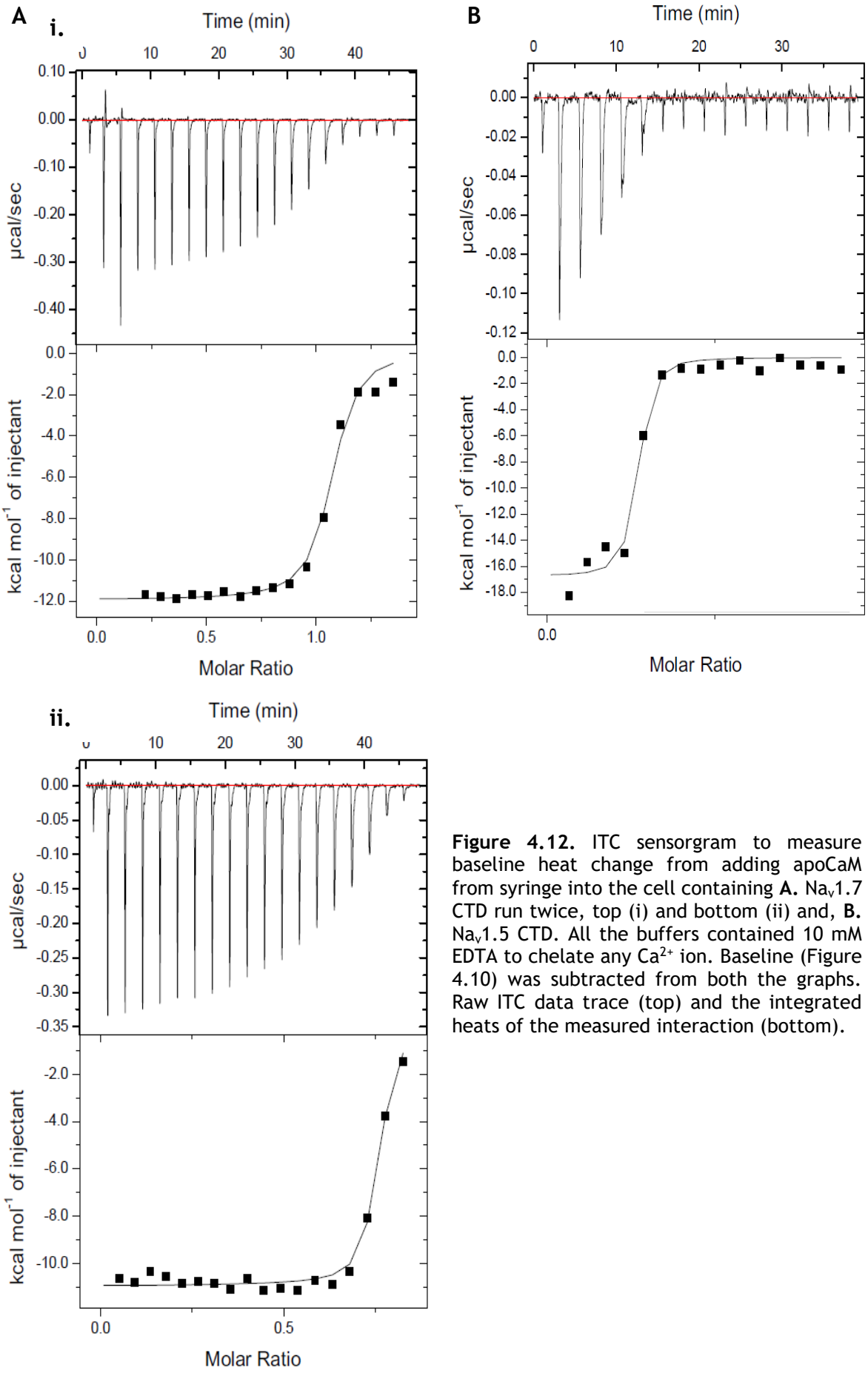

Figure 4.12. ITC sensorgram to measure baseline heat change from adding apoCaM from syringe into the cell containing **A.** $Na_v1.7$ CTD run twice, top (i) and bottom (ii) and, **B.** $Na_v1.5$ CTD. All the buffers contained 10 mM EDTA to chelate any Ca^{2+} ion. Baseline (Figure 4.10) was subtracted from both the graphs. Raw ITC data trace (top) and the integrated heats of the measured interaction (bottom).

4.6.2 $Na_v1.7$ CTD and $Na_v1.5$ CTD with Ca^{2+}-CaM

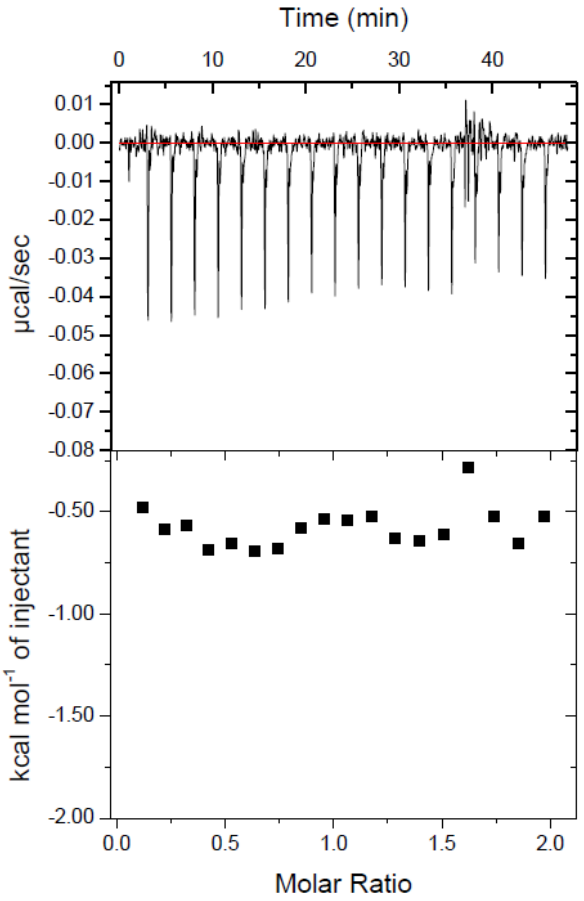

Figure 4.13. ITC sensorgram to measure baseline heat change of adding Ca^{2+}-CaM from syringe into the cell containing the buffer used to prepare $Na_v1.5$ and $Na_v1.7$ CTD. All the buffers contained 5 mM $CaCl_2$. Raw ITC data trace (top) and the integrated heats of the measured interaction (bottom).

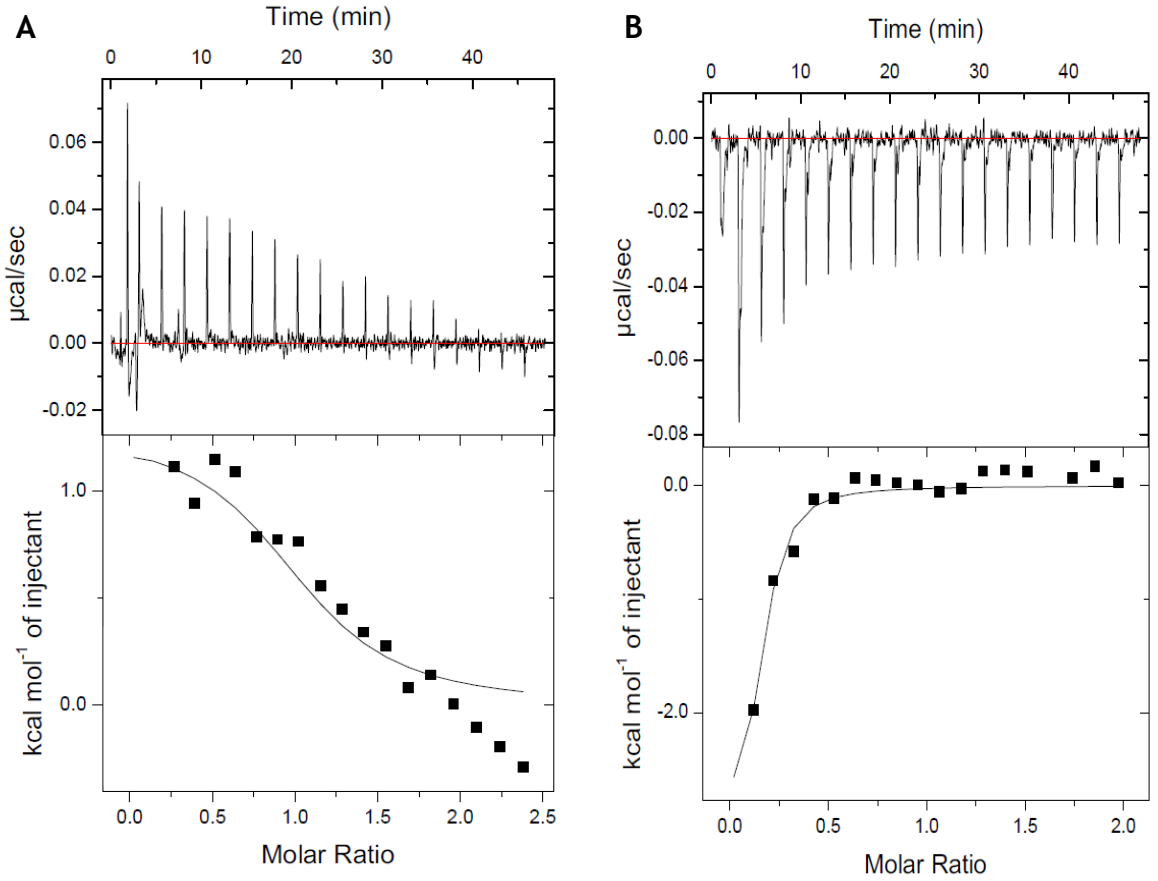

Figure 4.14. ITC sensorgram to measure baseline heat change of adding Ca^{2+}-CaM from syringe into the cell containing **A.** $Na_v1.7$ CTD and, **B.** $Na_v1.5$ CTD. All the buffers contained 5 mM $CaCl_2$. Baseline (Figure 4.11) was subtracted from both the graphs. Raw ITC data trace (top) and the integrated heats of the measured interaction (bottom).

4.7 Protein-protein interaction: Bio-layer interferometry (BLI)

The interaction of $Na_v1.5$ CTD (C5) and $Na_v1.7$ CTD (C7) with CaM was repeated using bio-layer interferometry technique using an OctetRed 96 instrument. In the absence of Ca^{2+}, the K_D obtained for C7 interaction with CaM (EDTA) was 50 ± 1.62 nM, and the K_D for C5 interaction with CaM (EDTA) was 164 ± 8.31 nM (Figure 4.15). Interaction could not be detected in the presence of 5 mM Ca^{2+} (Figure 4.17). Interaction was also not detected when the truncated CTDs were used i.e. the EF hand domains of $Na_v1.5$ (5EF) and $Na_v1.7$ (7EF) in the presence or absence of Ca^{2+} (Figure 4.16, Figure 4.18).

4.7.1 Calmodulin (EDTA) with $Na_v1.7$ CTD and $Na_v1.5$ CTD

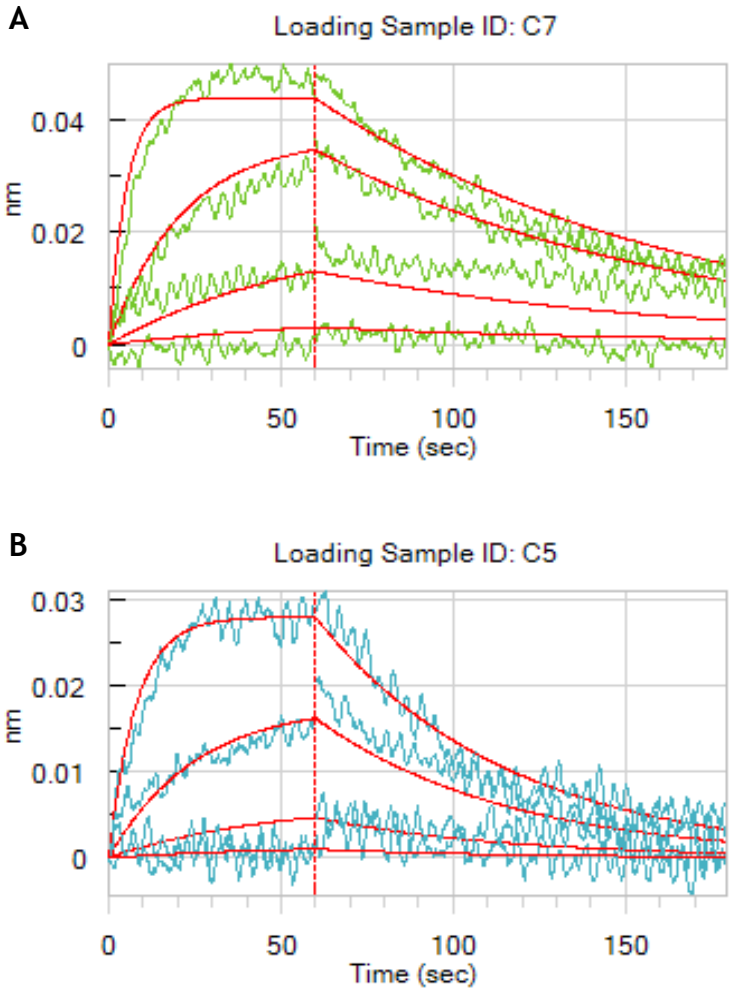

Figure 4.15. Determination of equilibrium dissociation constants (K_D) of the interaction between four different concentrations of calmodulin (1000 nM, 200 nM, 40 nM and 8nM), in the presence of 10 mM EDTA, and **A.** $Na_v1.7$ CTD (C7), and **B.** $Na_v1.5$ CTD (C5).

4.7.2 Calmodulin (EDTA) with the EF hand domain of $Na_v1.7$ CTD and $Na_v1.5$ CTD

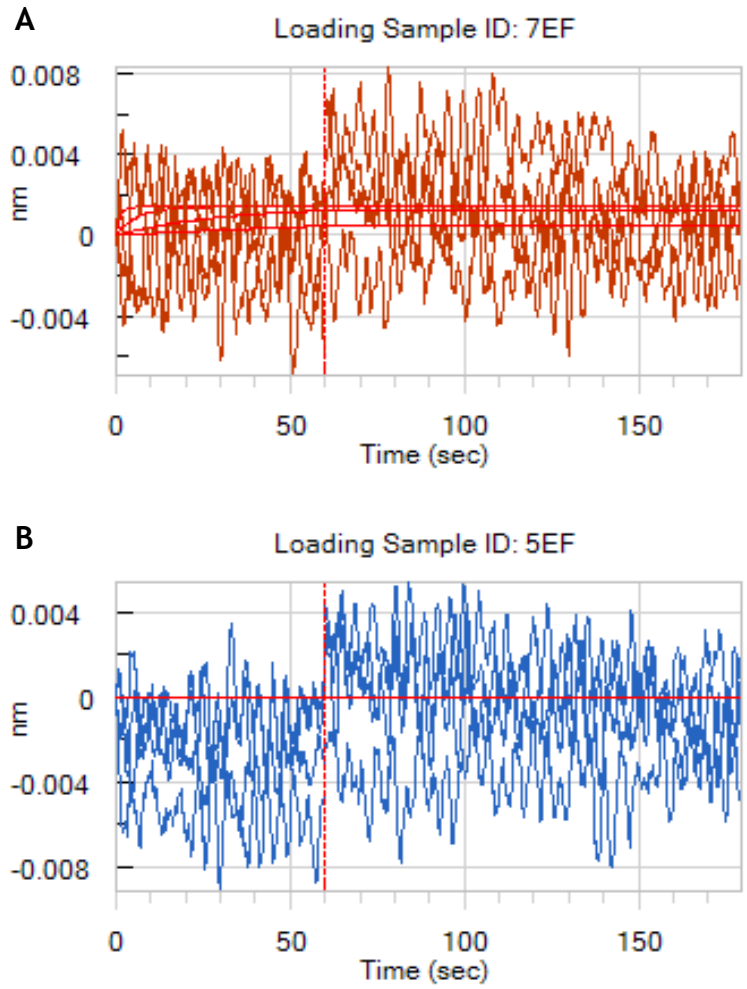

Figure 4.16. Determination of equilibrium dissociation constants (K_D) of the interaction between four different concentrations of calmodulin, in the presence of 10 mM EDTA and **A.** $Na_v1.7$ CTD EF hand (7EF), and **B.** $Na_v1.5$ CTD EF hand (5EF).

4.7.3 Calmodulin (Ca^{2+}) with $Na_v1.7$ CTD and $Na_v1.5$ CTD

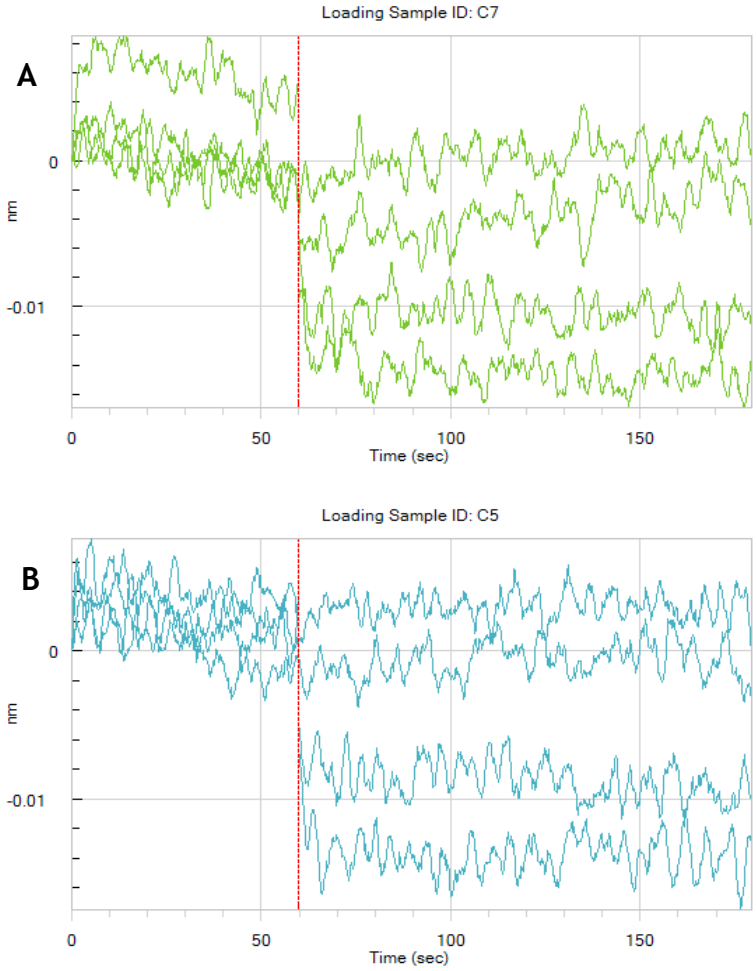

Figure 4.17. Determination of equilibrium dissociation constants (K_D) of the interaction between four different concentrations of calmodulin, in the presence of 5 mM $CaCl_2$ and **A.** $Na_v1.7$ CTD (C7), and **B.** $Na_v1.5$ CTD (C5).

4.7.4 Calmodulin (Ca^{2+}) with EF hand domain of $Na_v1.7$ CTD and $Na_v1.5$ CTD

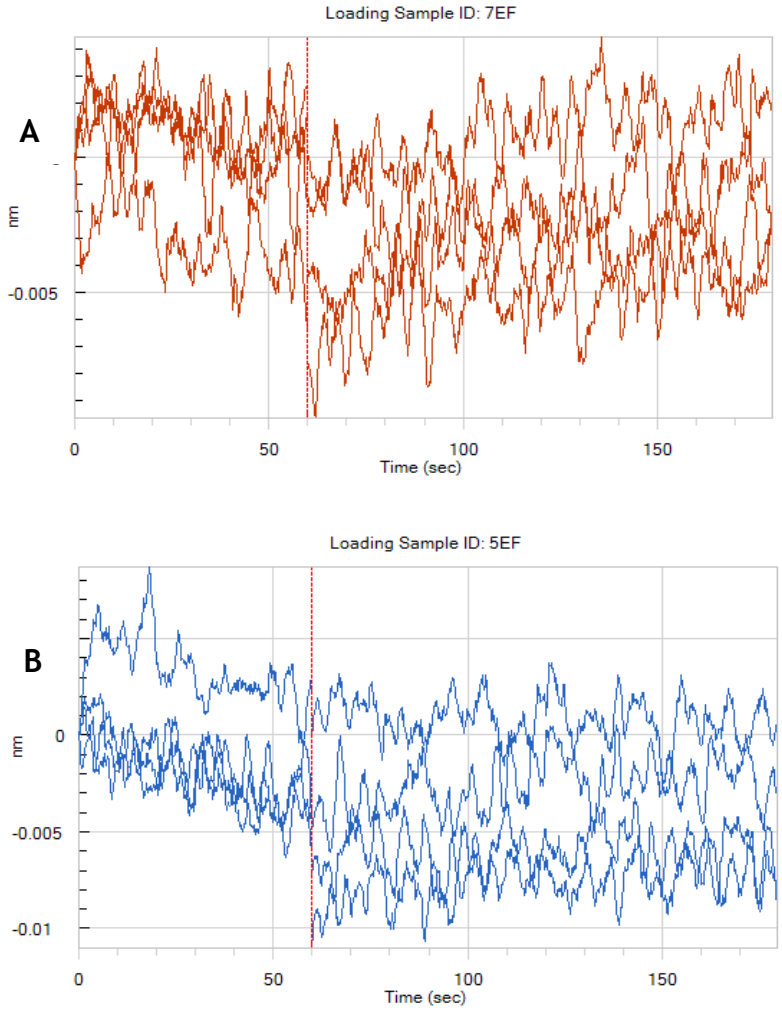

Figure 4.18. Determination of equilibrium dissociation constants (K_D) of the interaction between four different concentrations of calmodulin, in the presence of 5 mM $CaCl_2$ and **A.** $Na_v1.7$ CTD EF hand (7EF), and **B.** $Na_v1.5$ CTD EF hand (5EF).

4.8 X-ray crystallography

Crystal trials were set up using commercially available 96 wells, 2 drops, MRC-type plates, for full length $Na_v1.7$ CTD (C7) and the truncated EF hand (7EF). More than a thousand different conditions were tested, and crystals obtained from certain conditions were imaged using the Rock Imager software (Figure 4.19, Figure 4.20). Optimization of some conditions were also performed (Figure 4.21) and selected crystals sent for x-ray diffraction at Diamond Light Source (Figure 4.22). Unfortunately, none of the crystals turned out be protein, some crystals did not diffract at all, from the diffraction patterns of some of the others it could be concluded that they were either ice rings or salt crystals.

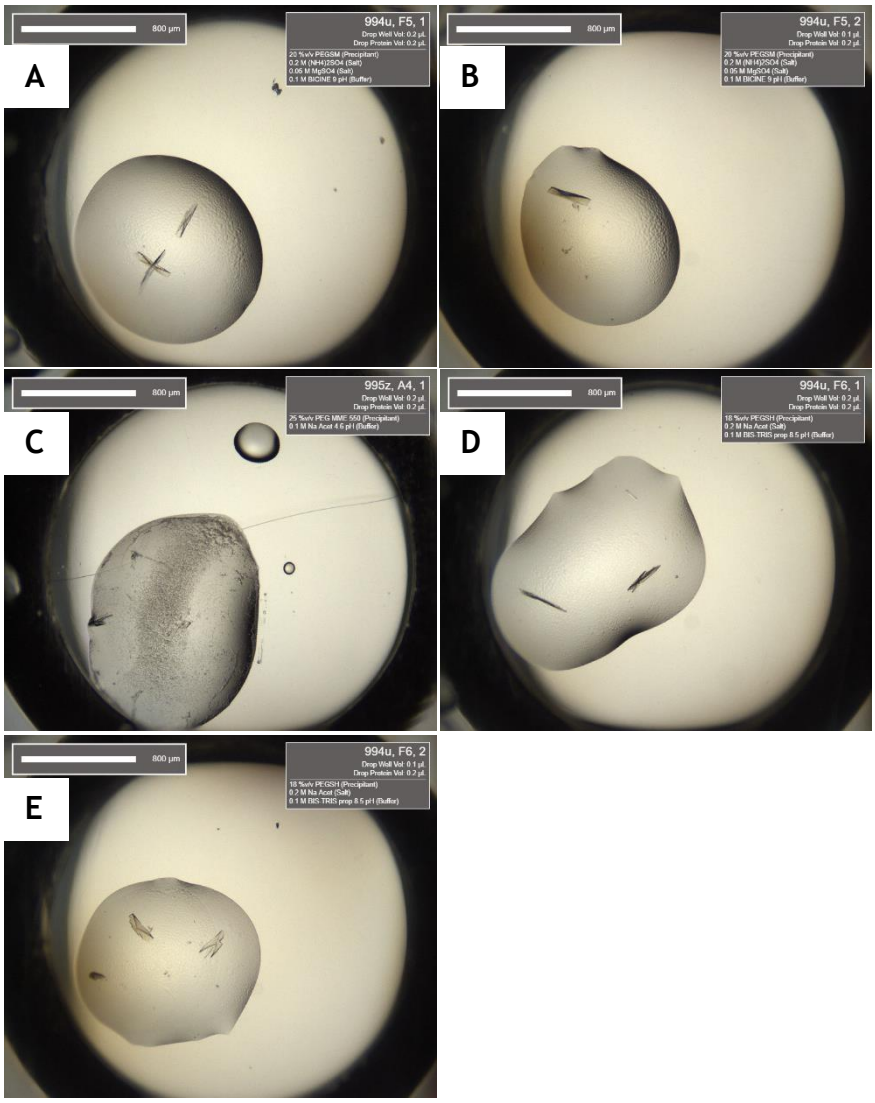

Figure 4.19. Crystals of full length $Na_v1.7$ CTD obtained from different conditions. Protein drops were either 100 or 200 nL, and the condition volume was kept constant at 200 nL. **A.** 20% v/v PEGSM (precipitant), 0.2M $(NH_4)_2SO_4$, 0.06M $MgSO_4$, 0.1M Bicine pH 9; **B.** 20% v/v PEGSM (precipitant), 0.2M $(NH_4)_2SO_4$, 0.05M $MgSO_4$, 0.1M Bicine pH 9; **C.** 25% v/v PEG MME 550 (precipitant), 0.1M Sodium Acetate pH 4.6; **D.** 18% v/v PEGSH (precipitant), 0.2M Sodium Acetate, 0.1M BIS-TRIS propane pH 8.5; **E.** 18% v/v PEGSH (precipitant), 0.2M Sodium Acetate, 0.1M BIS-TRIS propane pH 8.5.

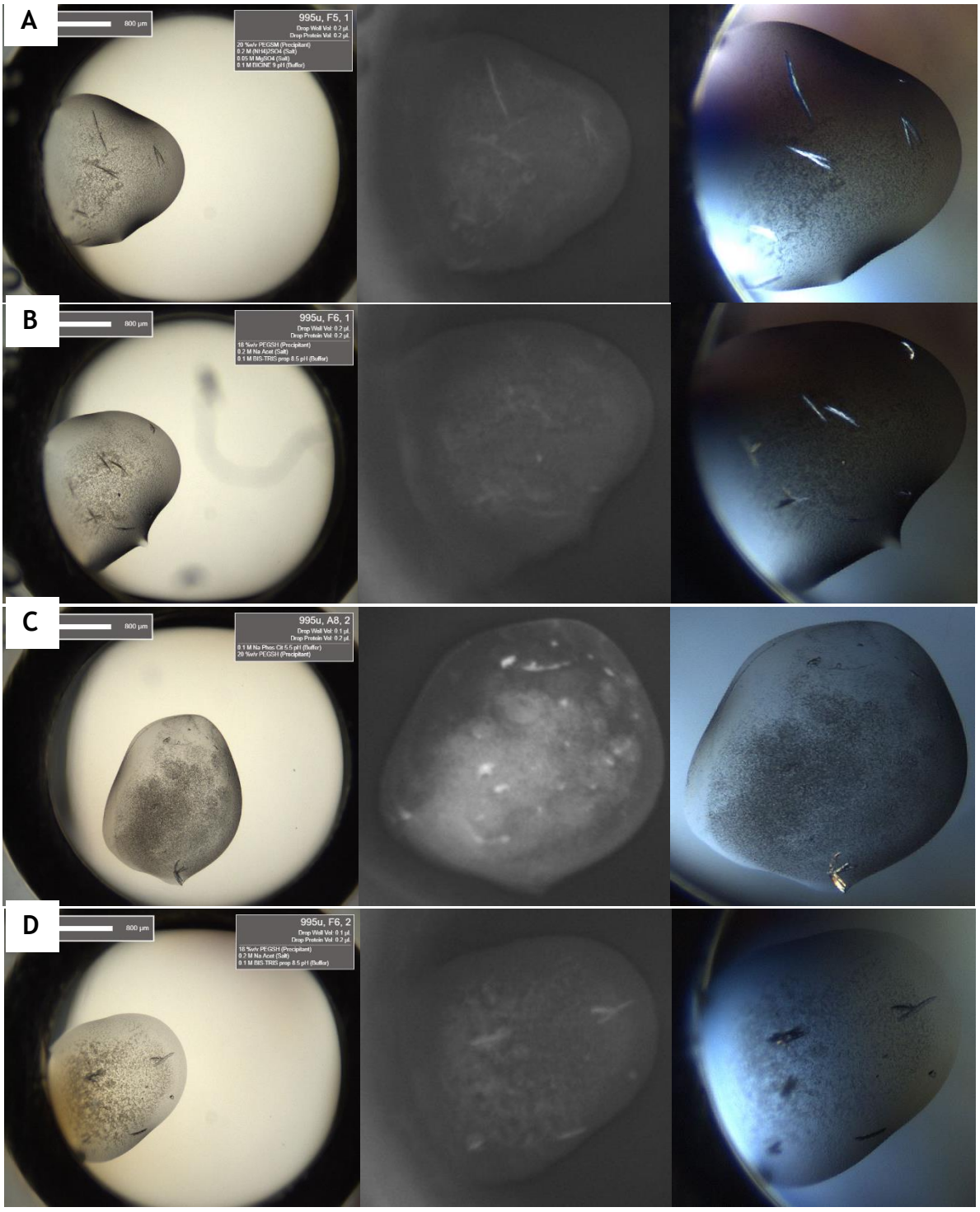
A
800 µm
995u, F5, 1
Drop Well Vol: 0.2 µl
Drop Protein Vol: 0.2 µl
20 %v/v PEGSM (Precipitant)
0.2 M (NH4)2SO4 (Salt)
0.05 M MgSO4 (Salt)
0.1 M BICINE 9 pH (Buffer)
B
800 µm
995u, F6, 1
Drop Well Vol: 0.2 µl
Drop Protein Vol: 0.2 µl
18 %v/v PEGSH (Precipitant)
0.2 M Na Acet (Salt)
0.1 M BIS-TRIS prop 8.5 pH (Buffer)
C
800 µm
995u, A8, 2
Drop Well Vol: 0.1 µl
Drop Protein Vol: 0.2 µl
0.1 M Na Phos Cit 5.5 pH (Buffer)
26 %v/v PEGSH (Precipitant)
D
800 µm
995u, F6, 2
Drop Well Vol: 0.1 µl
Drop Protein Vol: 0.2 µl
18 %v/v PEGSH (Precipitant)
0.2 M Na Acet (Salt)
0.1 M BIS-TRIS prop 8.5 pH (Buffer)

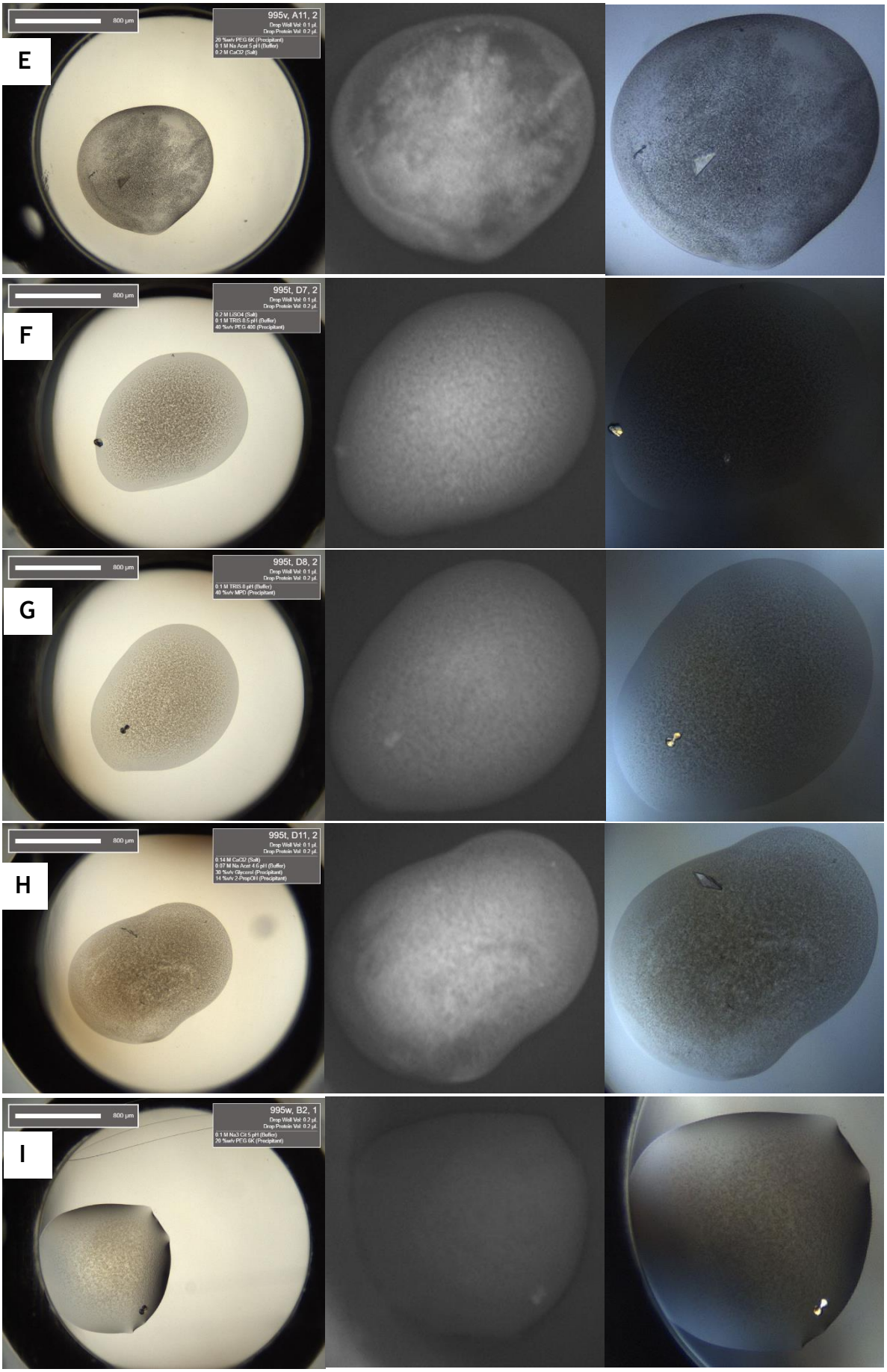

Figure 4.20. Crystals of full length $Na_V1.7$ CTD EF hand obtained from different conditions. Protein drops were either 100 or 200 nL, and the condition volume was kept constant at 200 nL. Every row

first image is bright field, second is high-definition UV and the third is polarized light, of the same crystal.
A. 20% v/v PEGSM (precipitant), 0.2M $(NH_4)_2SO_4$, 0.05M $MgSO_4$, 0.1M Bicine pH 9; **B.** 18% v/v PEGSH (precipitant), 0.2M Sodium Acetate, 0.1M BIS-TRIS propane pH 8.5; **C.** 20% v/v PEGSH, 0.1M Sodium Phosphate Citrate pH 5.5; **D.** 18% v/v PEGSH (precipitant), 0.2M Sodium Acetate, 0.1M BIS-TRIS propane pH 8.5; **E.** 20% w/v PEG 6K (precipitant), 0.1M Sodium Acetate pH 5, 0.2M $CaCl_2$. **F.** 0.2M Li_2SO_4, 0.1M TRIS pH 8.5, 40% v/v PEG 400 (precipitant); **G.** 0.1M TRIS pH 8, 40% v/v MPD (precipitant); **H.** 0.14M $CaCl_2$, 0.07M Sodium Acetate pH 4.6, 30% v/v Glycerol (precipitant), 14% v/v 2-propanol (precipitant); **I.** 0.1M Sodium Citrate pH 5, 20% w/v PEG 6K (precipitant).

Optimisation: NaV_1p7_EF_hand_MPD.dfy

dragonfly

	1	2	3	4	5	6	7	8	9	10	11	12
A	20% v/v PEGSM, 0.2M $(NH_4)_2SO_4$, 0.1M Bicine pH 9				MPD: 21.00uL, 30.00%v/v Tris pH8 (pH: 8): 7.00uL, 100.00mM	MPD: 23.00uL, 32.86%v/v Tris pH8 (pH: 8): 7.00uL, 100.00mM	MPD: 25.00uL, 35.71%v/v Tris pH8 (pH: 8): 7.00uL, 100.00mM	MPD: 27.00uL, 38.57%v/v Tris pH8 (pH: 8): 7.00uL, 100.00mM	MPD: 29.00uL, 41.43%v/v Tris pH8 (pH: 8): 7.00uL, 100.00mM	MPD: 31.00uL, 44.29%v/v Tris pH8 (pH: 8): 7.00uL, 100.00mM	MPD: 33.00uL, 47.14%v/v Tris pH8 (pH: 8): 7.00uL, 100.00mM	MPD: 35.00uL, 50.00%v/v Tris pH8 (pH: 8): 7.00uL, 100.00mM
B					MPD: 21.00uL, 30.00%v/v Tris pH8 (pH: 8): 7.00uL, 100.00mM	MPD: 23.00uL, 32.86%v/v Tris pH8 (pH: 8): 7.00uL, 100.00mM	MPD: 25.00uL, 35.71%v/v Tris pH8 (pH: 8): 7.00uL, 100.00mM	MPD: 27.00uL, 38.57%v/v Tris pH8 (pH: 8): 7.00uL, 100.00mM	MPD: 29.00uL, 41.43%v/v Tris pH8 (pH: 8): 7.00uL, 100.00mM	MPD: 31.00uL, 44.29%v/v Tris pH8 (pH: 8): 7.00uL, 100.00mM	MPD: 33.00uL, 47.14%v/v Tris pH8 (pH: 8): 7.00uL, 100.00mM	MPD: 35.00uL, 50.00%v/v Tris pH8 (pH: 8): 7.00uL, 100.00mM
C					MPD: 21.00uL, 30.00%v/v Tris pH8 (pH: 8): 7.00uL, 100.00mM	MPD: 23.00uL, 32.86%v/v Tris pH8 (pH: 8): 7.00uL, 100.00mM	MPD: 25.00uL, 35.71%v/v Tris pH8 (pH: 8): 7.00uL, 100.00mM	MPD: 27.00uL, 38.57%v/v Tris pH8 (pH: 8): 7.00uL, 100.00mM	MPD: 29.00uL, 41.43%v/v Tris pH8 (pH: 8): 7.00uL, 100.00mM	MPD: 31.00uL, 44.29%v/v Tris pH8 (pH: 8): 7.00uL, 100.00mM	MPD: 33.00uL, 47.14%v/v Tris pH8 (pH: 8): 7.00uL, 100.00mM	MPD: 35.00uL, 50.00%v/v Tris pH8 (pH: 8): 7.00uL, 100.00mM
D					MPD: 21.00uL, 30.00%v/v Tris pH8 (pH: 8): 7.00uL, 100.00mM	MPD: 23.00uL, 32.86%v/v Tris pH8 (pH: 8): 7.00uL, 100.00mM	MPD: 25.00uL, 35.71%v/v Tris pH8 (pH: 8): 7.00uL, 100.00mM	MPD: 27.00uL, 38.57%v/v Tris pH8 (pH: 8): 7.00uL, 100.00mM	MPD: 29.00uL, 41.43%v/v Tris pH8 (pH: 8): 7.00uL, 100.00mM	MPD: 31.00uL, 44.29%v/v Tris pH8 (pH: 8): 7.00uL, 100.00mM	MPD: 33.00uL, 47.14%v/v Tris pH8 (pH: 8): 7.00uL, 100.00mM	MPD: 35.00uL, 50.00%v/v Tris pH8 (pH: 8): 7.00uL, 100.00mM
E					MPD: 21.00uL, 30.00%v/v Tris pH8 (pH: 8): 7.00uL, 100.00mM	MPD: 23.00uL, 32.86%v/v Tris pH8 (pH: 8): 7.00uL, 100.00mM	MPD: 25.00uL, 35.71%v/v Tris pH8 (pH: 8): 7.00uL, 100.00mM	MPD: 27.00uL, 38.57%v/v Tris pH8 (pH: 8): 7.00uL, 100.00mM	MPD: 29.00uL, 41.43%v/v Tris pH8 (pH: 8): 7.00uL, 100.00mM	MPD: 31.00uL, 44.29%v/v Tris pH8 (pH: 8): 7.00uL, 100.00mM	MPD: 33.00uL, 47.14%v/v Tris pH8 (pH: 8): 7.00uL, 100.00mM	MPD: 35.00uL, 50.00%v/v Tris pH8 (pH: 8): 7.00uL, 100.00mM
F					MPD: 21.00uL, 30.00%v/v Tris pH8 (pH: 8): 7.00uL, 100.00mM	MPD: 23.00uL, 32.86%v/v Tris pH8 (pH: 8): 7.00uL, 100.00mM	MPD: 25.00uL, 35.71%v/v Tris pH8 (pH: 8): 7.00uL, 100.00mM	MPD: 27.00uL, 38.57%v/v Tris pH8 (pH: 8): 7.00uL, 100.00mM	MPD: 29.00uL, 41.43%v/v Tris pH8 (pH: 8): 7.00uL, 100.00mM	MPD: 31.00uL, 44.29%v/v Tris pH8 (pH: 8): 7.00uL, 100.00mM	MPD: 33.00uL, 47.14%v/v Tris pH8 (pH: 8): 7.00uL, 100.00mM	MPD: 35.00uL, 50.00%v/v Tris pH8 (pH: 8): 7.00uL, 100.00mM
G			20% v/v PEGSM, 0.2M $(NH_4)_2SO_4$, 0.05M $MgSO_4$, 0.1M Bicine pH 9		MPD: 21.00uL, 30.00%v/v Tris pH8 (pH: 8): 7.00uL, 100.00mM	MPD: 23.00uL, 32.86%v/v Tris pH8 (pH: 8): 7.00uL, 100.00mM	MPD: 25.00uL, 35.71%v/v Tris pH8 (pH: 8): 7.00uL, 100.00mM	MPD: 27.00uL, 38.57%v/v Tris pH8 (pH: 8): 7.00uL, 100.00mM	MPD: 29.00uL, 41.43%v/v Tris pH8 (pH: 8): 7.00uL, 100.00mM	MPD: 31.00uL, 44.29%v/v Tris pH8 (pH: 8): 7.00uL, 100.00mM	MPD: 33.00uL, 47.14%v/v Tris pH8 (pH: 8): 7.00uL, 100.00mM	MPD: 35.00uL, 50.00%v/v Tris pH8 (pH: 8): 7.00uL, 100.00mM
H					MPD: 21.00uL, 30.00%v/v Tris pH8 (pH: 8): 7.00uL, 100.00mM	MPD: 23.00uL, 32.86%v/v Tris pH8 (pH: 8): 7.00uL, 100.00mM	MPD: 25.00uL, 35.71%v/v Tris pH8 (pH: 8): 7.00uL, 100.00mM	MPD: 27.00uL, 38.57%v/v Tris pH8 (pH: 8): 7.00uL, 100.00mM	MPD: 29.00uL, 41.43%v/v Tris pH8 (pH: 8): 7.00uL, 100.00mM	MPD: 31.00uL, 44.29%v/v Tris pH8 (pH: 8): 7.00uL, 100.00mM	MPD: 33.00uL, 47.14%v/v Tris pH8 (pH: 8): 7.00uL, 100.00mM	MPD: 35.00uL, 50.00%v/v Tris pH8 (pH: 8): 7.00uL, 100.00mM

Figure 4.21. Optimization of conditions for crystal growth, with double the volume of protein and condition used which is 400 nL. For Column 1 and 2, 20% v/v PEGSM, 0.2M $(NH_4)_2SO_4$, 0.1M Bicine pH 9; for clumn 3 and 4 the same condition was use as 1 and 2 with the addition of 0.05M $MgSO_4$; for 5-12 0.1M TRIS pH 8 was used with a gradient of MPD concentration from 30-50%.

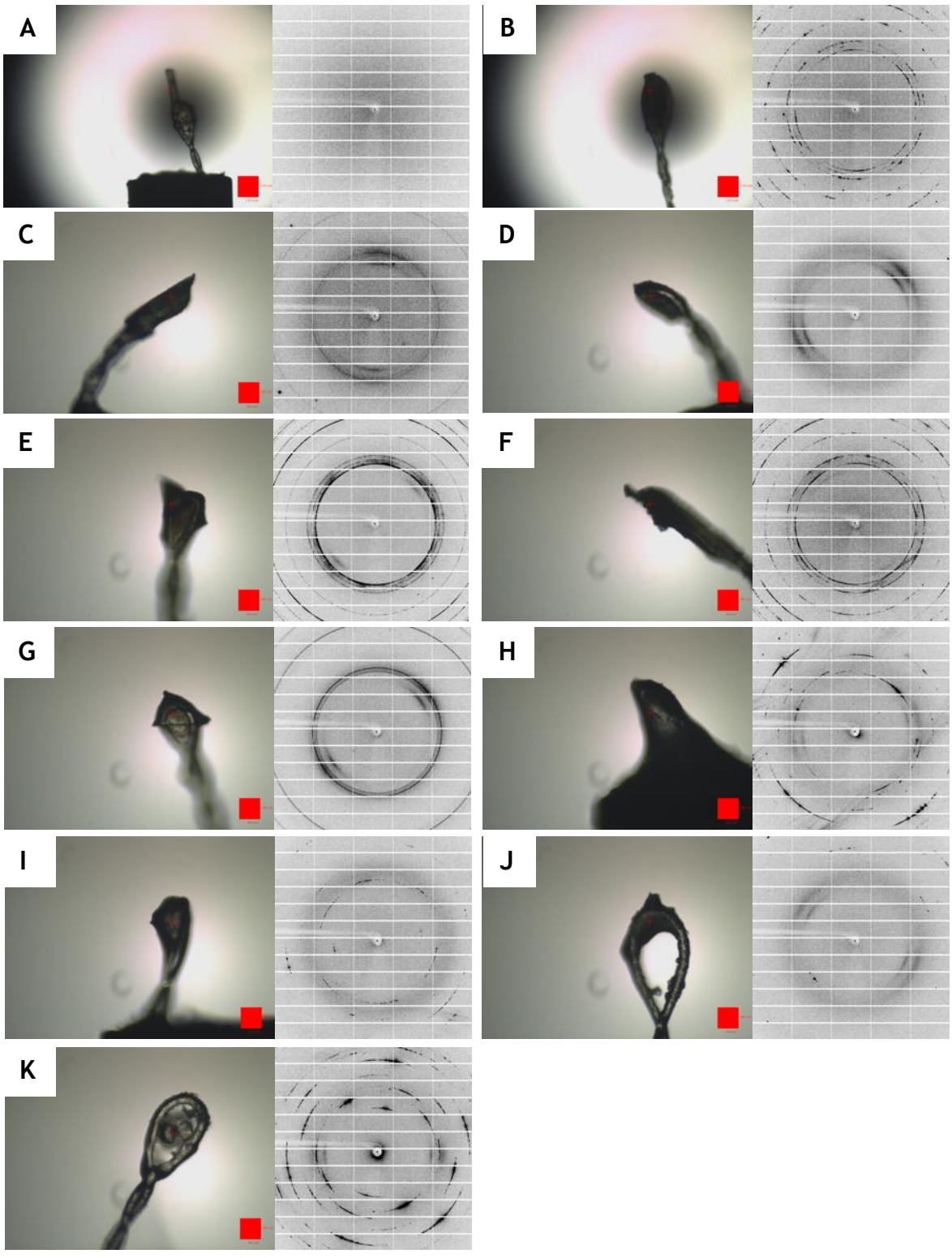

Figure 4.22. X-ray diffraction analysis of crystals obtained from different crystallization trial conditions. The first image shows the crystal mounted on a loop and the second image is of the diffraction pattern observed.

4.9 Predicted model of full length $Na_v1.7$ CTD using Phyre 2 and FoldIndex

Since there is still no available structure of the C-terminal domain of $Na_v1.7$ (C7), structure determination was performed using *in silico* methods. First, FoldIndex predicts that other than the initial globular EF hand domain, most of the C7 protein will remain unfolded, which could directly affect crystal formation (Figure 4.23 A). In contrast Phyre2 server predicts that 59% of the C7 protein will consist of alpha helices, 3% beta sheets and 38% disordered (Figure 4.23 B). The predicted model, Figure 4.23 C, shows the predicted cartoon structure of C7.

A

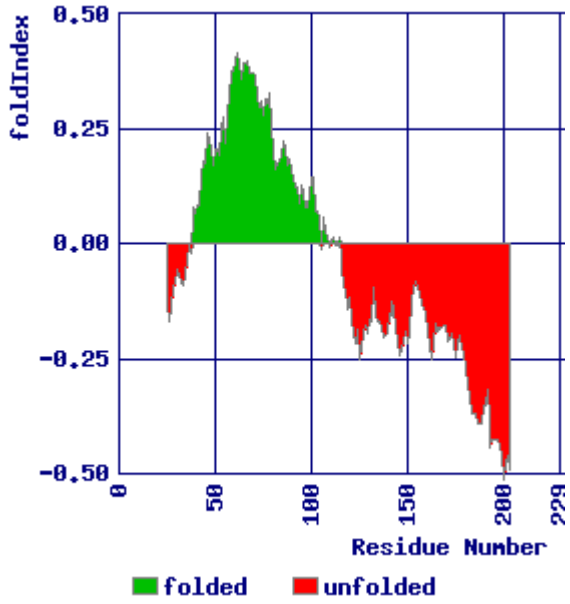

B

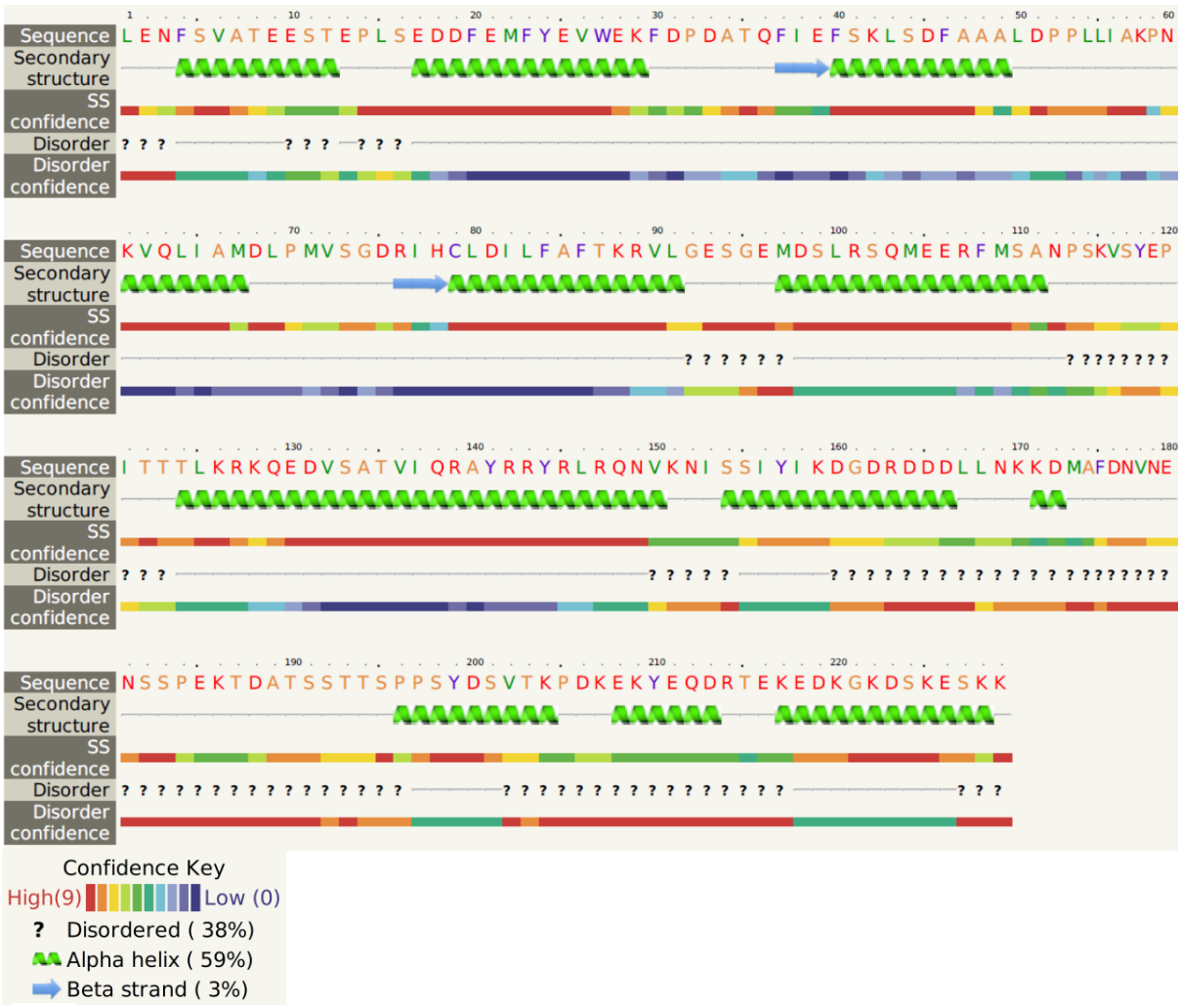

C

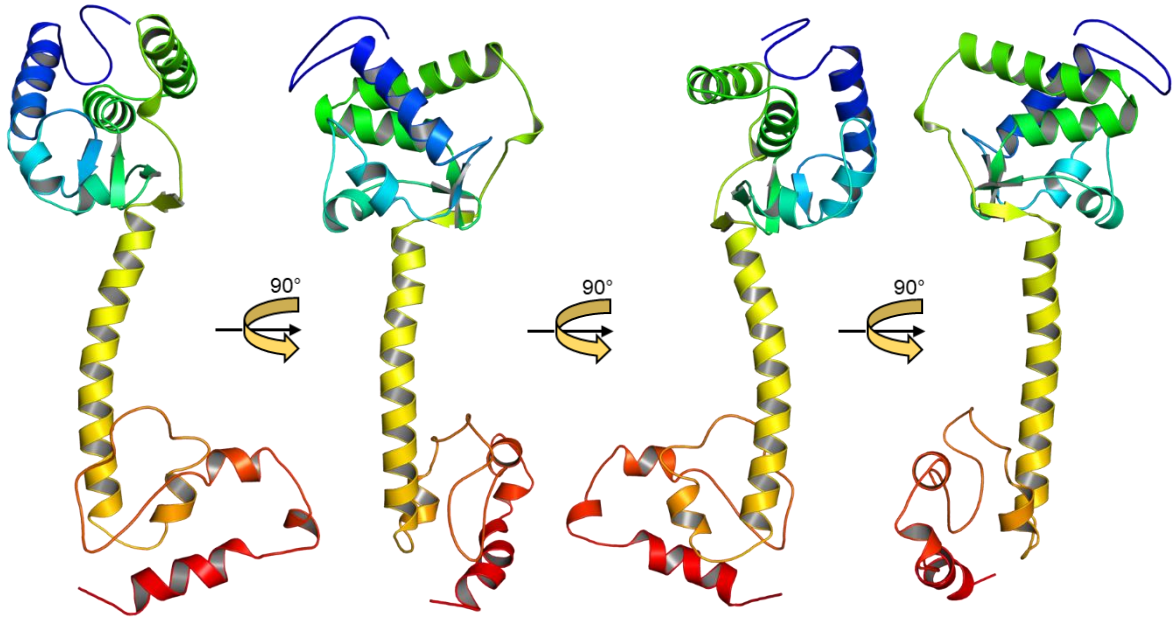

Figure 4.23 $Na_v1.7$ CTD protein structure prediction. **A.** FoldIndex© predicts that the $Na_v1.7$ CTD consists mainly of disordered region which would remain unfolded. **B.** Phyre2, in contrast, predicts that majority of the protein will be folded and form alpha helices, with high confidence. **C.** The topology of the CTD from the side at 90° anticlockwise rotations is also illustrated, with the structure being colored in rainbow (N to C terminus) with the N-terminus in blue and C-terminus in red.

Discussion

This study investigated the protein-protein interaction between human $Na_V1.5$ CTD (C5) and $Na_V1.7$ CTD (C7) with calmodulin (CaM). An attempt was also made to solve the x-ray crystal structure of the full length of C7. All the recombinant proteins were cloned using Gateway cloning in pDest vector, expressed in BL21 (DE3) competent cells through auto-induction and purified using affinity and size exclusion chromatography.

Before expressing the proteins, vector DNA was sequenced to confirm the success of the cloning process and presence of N-terminus 10-His tag which was essential for the Ni-NTA purification (Figure 4.3, Figure 4.4). A second step purification was performed using Superdex 75 10/300 GL column and sample from the peaks were run on SDS-PAGE gel to gauge purity. Greater than 90% purity was achieved for all the samples (Figure 4.5, Figure 4.6, Figure 4.7, Figure 4.8, Figure 4.9).

From various reports it is well established that the C-terminal domains of $Na_V1.2$, $Na_V1.4$, $Na_V1.5$ and $Na_V1.6$ are regulated by CaM. C-lobe of CaM binds to the αVI helix of the CTDs, which consist of IQ motif, whereas the N-lobe of CaM binds either to the EF-hand domain or post-IQ motif of the CTDs depending on the presence or absence of Ca^{2+}. In this study we found that both the full length $Na_V1.7$ CTD (C7) and EF hand domain of $Na_V1.7$ CTD (7EF) bind to CaM only in the absence of Ca^{2+} (i.e. apoCaM). Detection of binding was not observed even at 1000-fold decrease in Ca^{2+} concentration (from 5 mM to 5 µM). Only when all the Ca^{2+} in the buffer was chelated by the addition of 10 mM EGTA, did C7 interact with CaM. To confirm this observation, it was repeated using ITC, which has the advantage of being a lot more sensitive and provide additional parameters like dissociation constant, enthalpy, entropy, and stoichiometry. ITC results found a dissociation constant of 48.78 ± 12.23 nM for C7 with apoCaM and 93.46 ± 19.78 nM for C5 with apoCaM. This value is within the range of K_D values previously reported of truncated C5 with apoCaM that ranges between 88 to 99 nM. This study is the first to report K_D value of this interaction using the full length of the CTD of both $Na_V1.5$ and $Na_V1.7$. Considering how the post-IQ motif disordered region of the C5 appears to fold back on itself (Figure 1.3), this could affect both the C-and N-lobe binding of CaM to C5. Also, when the same interaction of C5 with apoCaM was repeated using BLI (OctetRed), the K_D value was

found to be 164 nM. The K_D value of C7 with apoCaM using BLI was 50 nM which is consistent with the ITC result. Since ITC measures the interaction in solution, all the surfaces of both the interacting proteins are available for interaction, which might be masked when adsorbed to sensor surface of BLI. Hence, the K_D value of 93.46 ± 19.78 nM for C5 with apoCaM is most likely the more accurate representation of the interaction.

When we closely examined the predicted full-length structure of C7, compared to C5, the very tail end of C7 (post-IQ region) does not loop back on itself, but rather formed a semi globular structure at the end (Figure 4.23). In this arrangement unlike the tail end of the C5, C7's tail end does not come near the CaM binding IQ-motif and EF hand regions, hence most likely does not cause any steric hindrance. This could be one explanation for why the affinity of apoCaM is consistently found to be at least two to three times more for C7 than C5. The importance of the IQ motif for binding of CaM can be ascertained from the reported complete loss of this binding when the IQ amino acid residues are mutated to two Alanines (AA)[306].

Using ITC, the interaction of Ca^{2+}-CaM with C5 and C7 was found to be very weak, about 1 μM range, with very low enthalpy, which resulted in a poor curve fit to 1:1 binding model. The experiment was repeated with BLI, which failed to detect any interaction. Expectedly, even the truncated 5EF and 7EF recombinant protein did not to bind to Ca^{2+}-CaM, same as seen with apoCaM. Some reports do suggest a K_D of around 132 nM for C5 with Ca^{2+}-CaM[306], however a greatly truncated version of C5 was used in those experiments. As mentioned previously, the full-length C5 introduces more complexity to the overall arrangement of the protein which can have drastic effects on its interactions with other proteins.

The full-length CTD structure is yet to be determined. X-ray crystallography structures of truncated $Na_V1.5$ can be found in the literature. This study attempted to solve the full-length structure of C7, for which even the truncated structure is not available. However, the crystals obtained from the trials using hundreds of different conditions and optimizations, failed to diffract under x-ray examination. This was unusual as many of the crystals were found to light up on UV and show distinct refraction of cross-polarized light indicative of presence of protein crystal. FoldIndex

predicted that majority of C7 protein consists of disordered region, especially at its tail-end (Figure 4.23). Phyre2, although predicted presence of some alpha helices towards the tail-end nonetheless agrees with FoldIndex, in that most of the protein is largely unstructured, which could explain the difficulty faced in solving this structure using x-ray crystallography. NMR and CryoEM techniques could be employed next as further attempts to reveal the structure of C7 which could potentially give us valuable insight into how this protein takes part in its regulatory role of the $Na_V1.7$ ion channel. Also, differences in structures with other Na_V subtypes, which if found could be utilized to screen for subtype specific drugs and markers.

Chapter 5

Isolation of single chain fragment variable (scFv) antibody against $Na_V1.5$ and $Na_V1.7$ C-terminal domain

5.1 Introduction

Today, of the top 10 drugs by worldwide sale, six are biologics, all of which are monoclonal antibodies (mAbs), accounting for revenues of nearly USD 163 billion[315,316]. Therapeutic mAbs have more than double the rate of Food and Drugs Administration (FDA) approval following Phase I clinical trials compared to other drug classes and more than 100 are currently approved for different stages of clinical trials [317]. MAbs can be engineered in various formats to increase their target specificity, clearance, and overall functionality (Figure 5.1)[318].

Hybridoma technology had initially been used to produce mAbs in mice, which was revolutionary at the time[319]. However, being murine-derived mAbs posed particular challenges. For example, in humans, injected mAbs are neutralized by human anti-mouse antibodies, which result in a more rapid clearance of murine mAbs. Murine mAbs are also associated with severe allergic reactions. These problems have been addressed by using humanized antibody made by fusing the murine complementarity determining regions (CDRs) with the human constant regions (like the Fc domain). Furthermore, entirely human mAbs can now be produced using transgenic mice like HuMabMouse, where using gene editing, human loci for the immunoglobulin gene (Ig) replace the mouse one[320].

Phage display libraries provide an alternative approach to screening and isolating antibody targets to specific proteins or non-proteins[321]. Blood is collected from either immunized or non-immunized human donor and their IgG or IgM antibodies are isolated respectively to create single chain fragment variable (scFv) libraries. To make naïve libraries, total RNA is isolated from B-lymphocytes from healthy donor blood. Reverse transcriptase can then be used to convert the RNA into cDNA. Next, the variable region heavy (V_H) and light (V_L) chains can be separately amplified and then linked using a protease resistant $(Glycine_4Serine_1)_3$ linker to make the scFvs. These scFvs are then fused with the pIII gene of phage and cloned into a phagemid vector. Phagemid vectors are simple plasmids which carry origins of replication for both bacteria and phage. Use of phagemid vectors instead of phage vectors increases the transformation efficiencies, hence construction of larger libraries can be

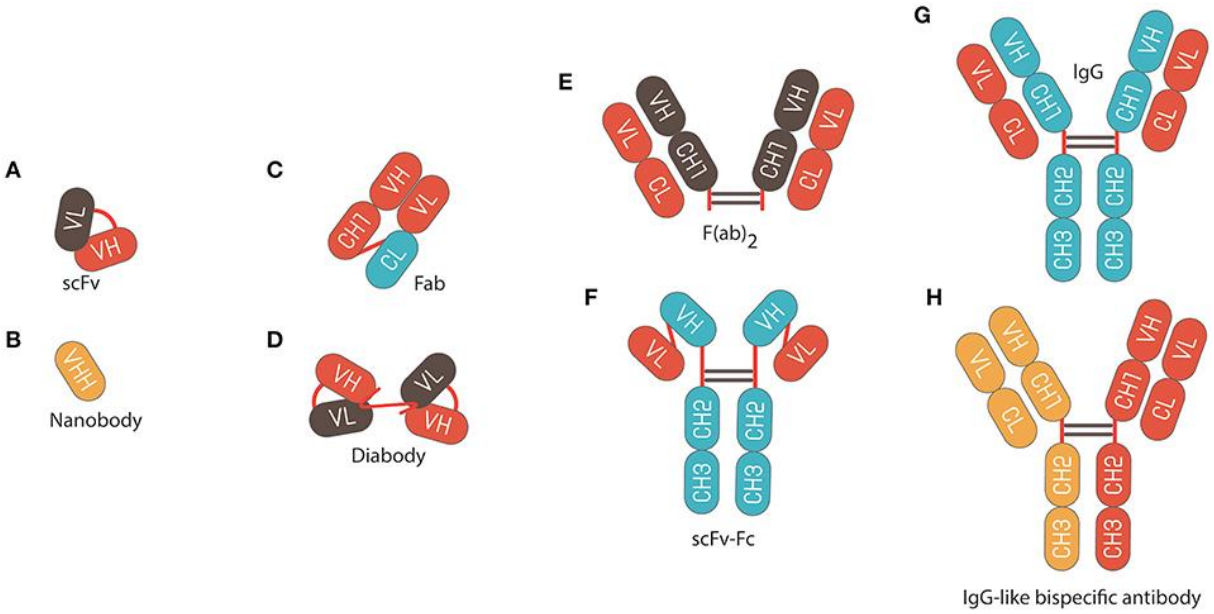

Figure 5.1. Different antibody formats. (A) Single chain fragment variable (scFv) composed of variable regions of the light chain (VL) linked to variable regions of the heavy chain (VH) by a flexible glycine-serine linker (Gly4Ser)3. (B) Nanobody fragments. (C) Fragment of antigen binding (Fab) composed of VL and a constant domain of the light chain (CL) linked to VH and constant domain 1 of the heavy chain (CH1) by a disulphide bond between the CL and CH1 domains. (D) Diabody composed of VL linked to variable heavy VH by a pentameric (Gly4Ser). (E) F(ab)2 fragment composed of 2 × Fab fragments joined by an Immunoglobulin G (IgG) hinge region. (F) scFv fusion with an Fc IgG. (G) IgG composed of constant fragment (Fc), which can bind and stimulate immune effector cells, and Fab, which comprises the variable domains that contain the antigen binding regions. (H) Bispecific IgG antibody.

achieved[322]. These libraries then are displayed on the surfaces of bacteriophage viruses such as T4 lambda and M13 filamentous phage.

The most widely used bacteriophage for phage display are the M13 filamentous phages (Ff phages) which infect E.Coli strains that express F pili, where the viral coat protein binds. The phage consists of a circular single-stranded DNA with nine genes which encode for 11 proteins (5 of which are coat proteins pIII, pVIII, pVI, pVII, and pIX). Antibody genes can be fused with the pIII coat protein expressing gene, and thus be displayed alongside the pIII protein, without this attachment protein losing its adsorption and extrusion properties[323]. Due to their smaller size, it is easier to express scFv recombinant antibodies in bacteria and then through gene fusion with pIII display on the phage surface (Figure 5.1)[324].

The six complementarity determining regions (CDRs) of the V_H and V_L fragments of scFvs, play the most crucial part in recognizing and binding to the antigen target. Most frequently the CDR3 region of the V_H fragment is found to be involved in

antibody-antigen interactions[325,326]. These CDR3 loops vary in lengths from about 5 to up to 30 amino acids, with longer loops dominating the binding to antigen entirely, whereas shorter CDR3 loops are generally assisted by other CDR regions for binding. To make larger libraries with greater diversity, random integration of CDRs, with different length and sequence of loops, can be achieved using PCR.
Adalimumab (Humira®) is the highest selling drug in the world. It is derived from fully human antibody and was developed through the utilization of phage display. It can bind to tumour necrosis factor-alpha and inhibit its binding to its receptor, by which it imparts its anti-inflammatory effect. It has initially gained approval as a drug against rheumatoid arthritis, although currently it is being used to treat a variety of other conditions such as ankylosing spondylitis, Crohn's disease, ulcerative colitis and fingernail psoriasis.

Despite the large number of mAb that undergoing clinical trials and gaining FDA approvals for treatment of various diseases, there is no current ion channel targeted mAb approved for clinical use. Many pharmaceutical companies tried to utilize the high selectivity, affinity and low toxicity that mAbs offer to find drugs that act on ion channels, but so far have failed to do so. A lot of work has been done with $Na_V1.7$ as a target with the hopes of finding an antibody that binds to $Na_V1.7$ and provide analgesic effect. For example SVmab1, a mouse derived mAb, was first thought to inhibit $Na_V1.7$ by binding to its domain II voltage sensing domain, and give analgesic effects to mice, however other groups could not replicate these findings, resulting in the original article eventually being retracted[228]. Currently, a Japanese pharmaceutical company called Shionogi claims to have a $Na_V1.7$ targeting mAb in the discovery phase. Other larger pharmaceutical companies like Pfizer, Roche and Biogen also tried to formulate small molecules that inhibit $Na_V1.7$, but in all the cases the drugs were discontinued after phase II clinical trials as effects observed on the bench failed to translate in clinical setting[327].

5.2 Objectives and Hypothesis

The C-terminal domain of Na_Vs interact with numerous other proteins including the inactivation gate (IG), calmodulin (CaM) and fibroblast growth factors (FGFs) through which it affects channel gating. The objective of this study was to find single chain fragment variable (scFv) antibodies that target and bind specifically the $Na_V1.5$ CTD and $Na_V1.7$ CTD (C7) and some that could potentially recognize both. The effect of this binding of scFv to its target would then be studied using automated patch clamp. Whether this binding is affected by the interaction of CaM with the CTDs would also be investigated. Finally, the location of the binding of selective scFv clones would be ascertained using truncated CTDs and eventually by using *in silico* docking.

5.3 Biopanning with scFv phage display library selected for $Na_v1.5$ CTD (C5) and $Na_v1.7$ CTD (C7)

Biopanning of a naïve ScFv phage display library against $Na_v1.5$ CTD (C5) and $Na_v1.7$ CTD (C7) produced hundreds of positive hits (Figure 5.2, Figure 5.3). Since an initial three step deselection step was performed with C7, before the selection step with C5, most of the positive hits displayed specificity to C5. The same is true for most of the clones that recognized the C7 clones, since deselected with C5, did not cross react with C5.

Clones that showed the largest absorbance 450 nm signal (>1) were selected and ELISA repeated to confirm their specificity to C5 (Figure 5.4) and C7 (Figure 5.5). In the repeat ELISA, some of the selected clones, although continued to show specificity, showed absorbance 450 nM values that were not as high as observed initially, for example 3F5, 3G9 and 4B3 of the C5 selective clones and 2G9, 4D12, 4E11, 4G8, 5E11 and 6H9 of the C7 selective clones. These were hence not used for further experiments.

Regardless of the deselection steps, possibly due to high sequence similarity between C5 and C7, biopanning did result in some clones that recognized both the CTDs. Some of these clones were also selected and ELISA repeated for confirmation (Figure 5.6). Some of the clones however, in this repeated ELISA, turned out to not recognize either of C5 or C7, for example 1A12, whereas 1E4 turned out be sonly elective for C5.

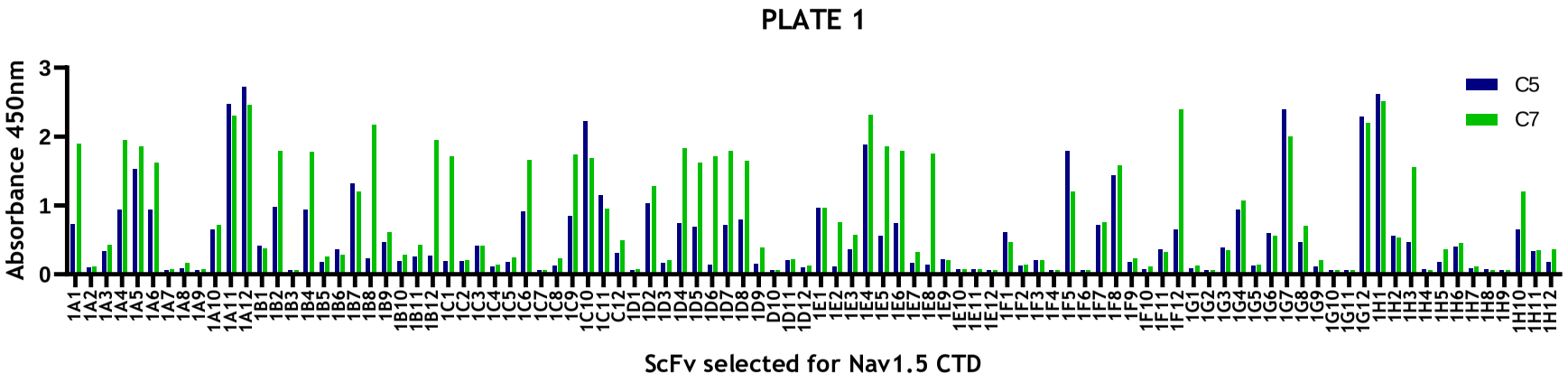
PLATE 1
Absorbance 450nm
C5
C7
ScFv selected for Nav1.5 CTD

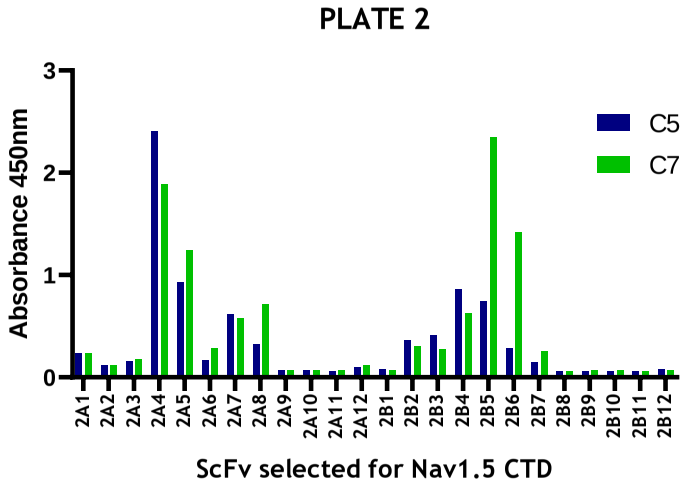
PLATE 2
Absorbance 450nm
C5
C7
ScFv selected for Nav1.5 CTD

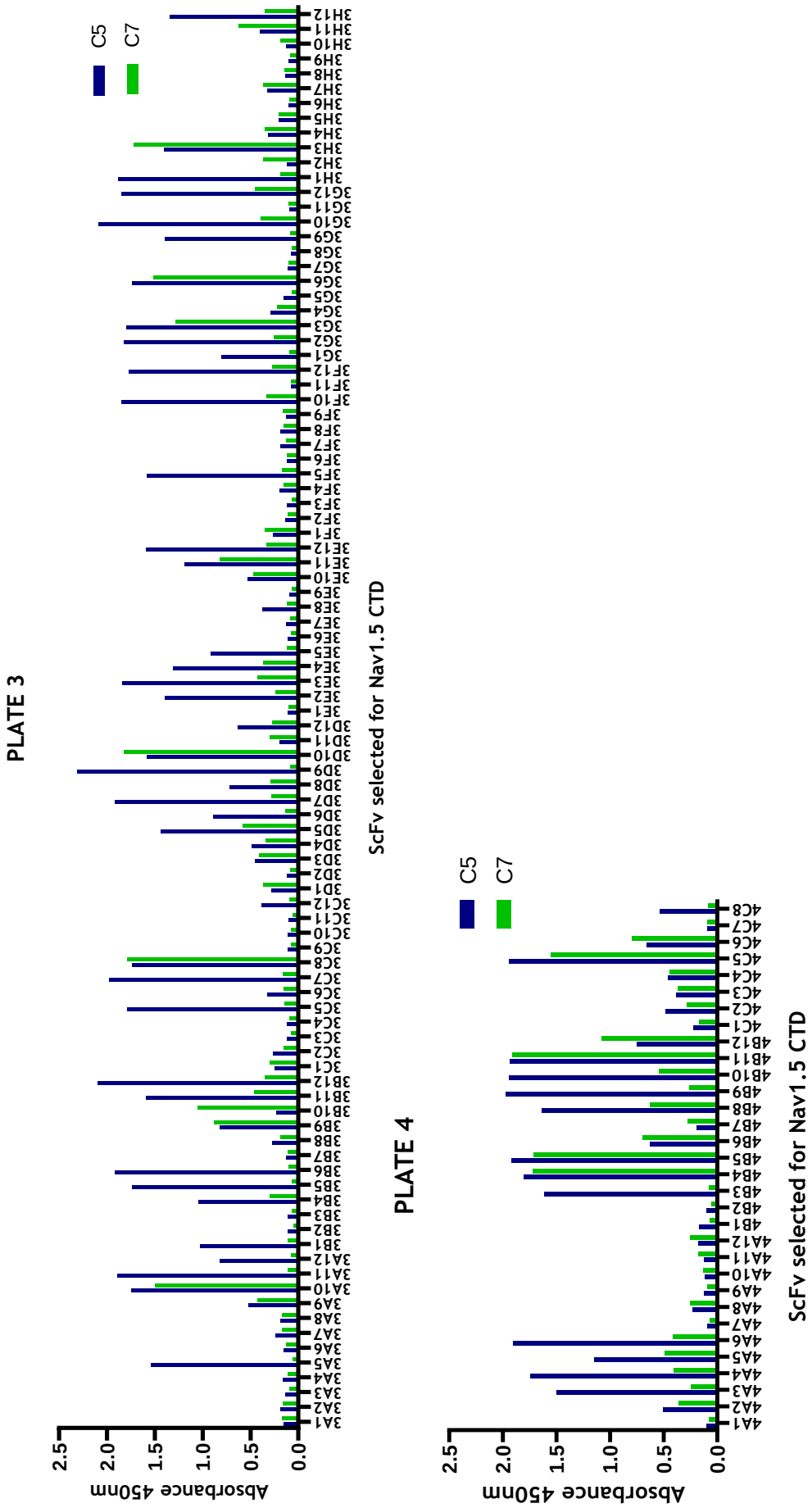

Figure 5.2. 96 well ELISA plate results for clones that were selected for $Na_v1.5$ CTD (C5, blue) and deselected for $Na_v1.7$ CTD (C7, green).

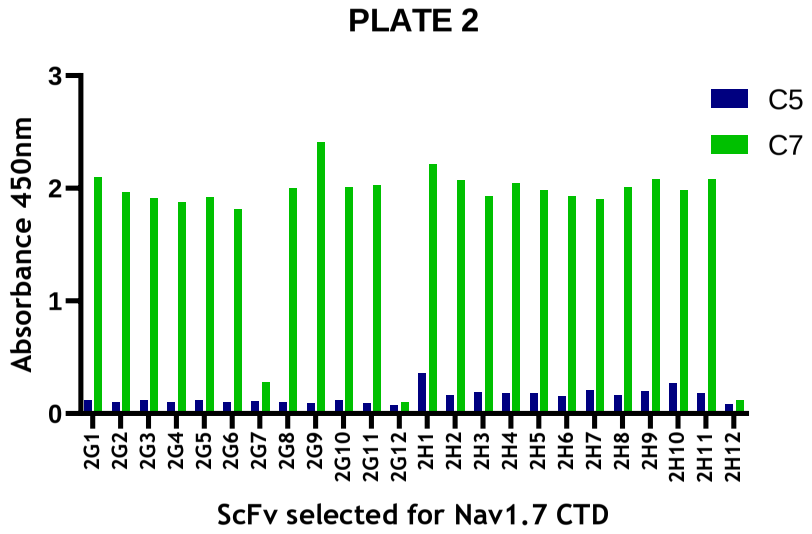
PLATE 2
Absorbance 450nm
3
2
1
0
C5
C7
2G1
2G2
2G3
2G4
2G5
2G6
2G7
2G8
2G9
2G10
2G11
2G12
2H1
2H2
2H3
2H4
2H5
2H6
2H7
2H8
2H9
2H10
2H11
2H12
ScFv selected for Nav1.7 CTD

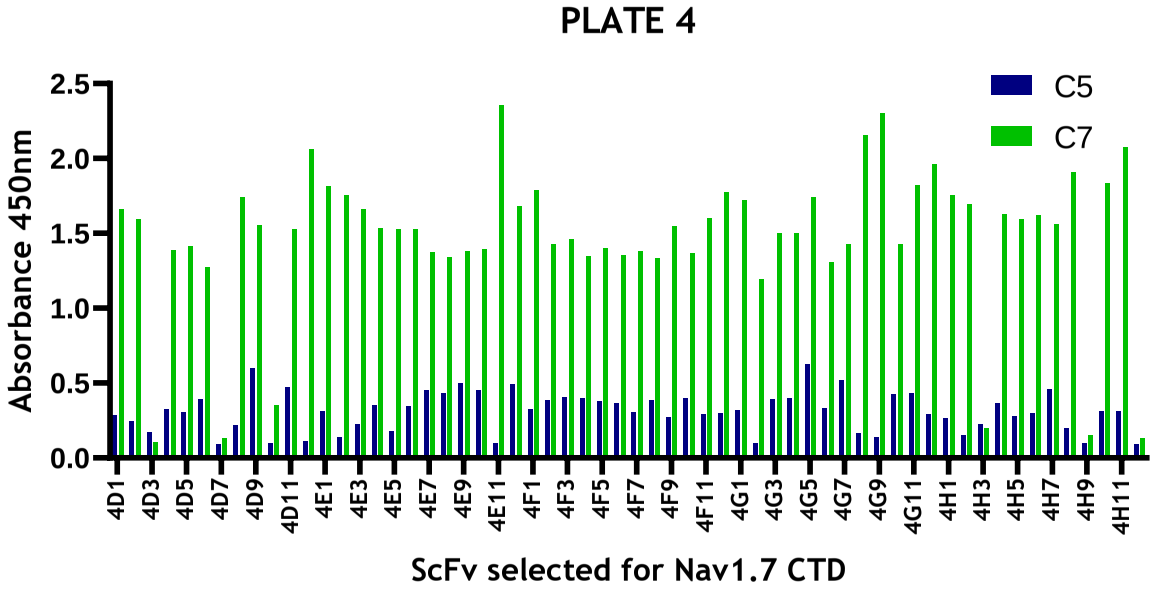
PLATE 4
Absorbance 450nm
2.5
2.0
1.5
1.0
0.5
0.0
C5
C7
4D1
4D3
4D5
4D7
4D9
4D11
4E1
4E3
4E5
4E7
4E9
4E11
4F1
4F3
4F5
4F7
4F9
4F11
4G1
4G3
4G5
4G7
4G9
4G11
4H1
4H3
4H5
4H7
4H9
4H11
ScFv selected for Nav1.7 CTD

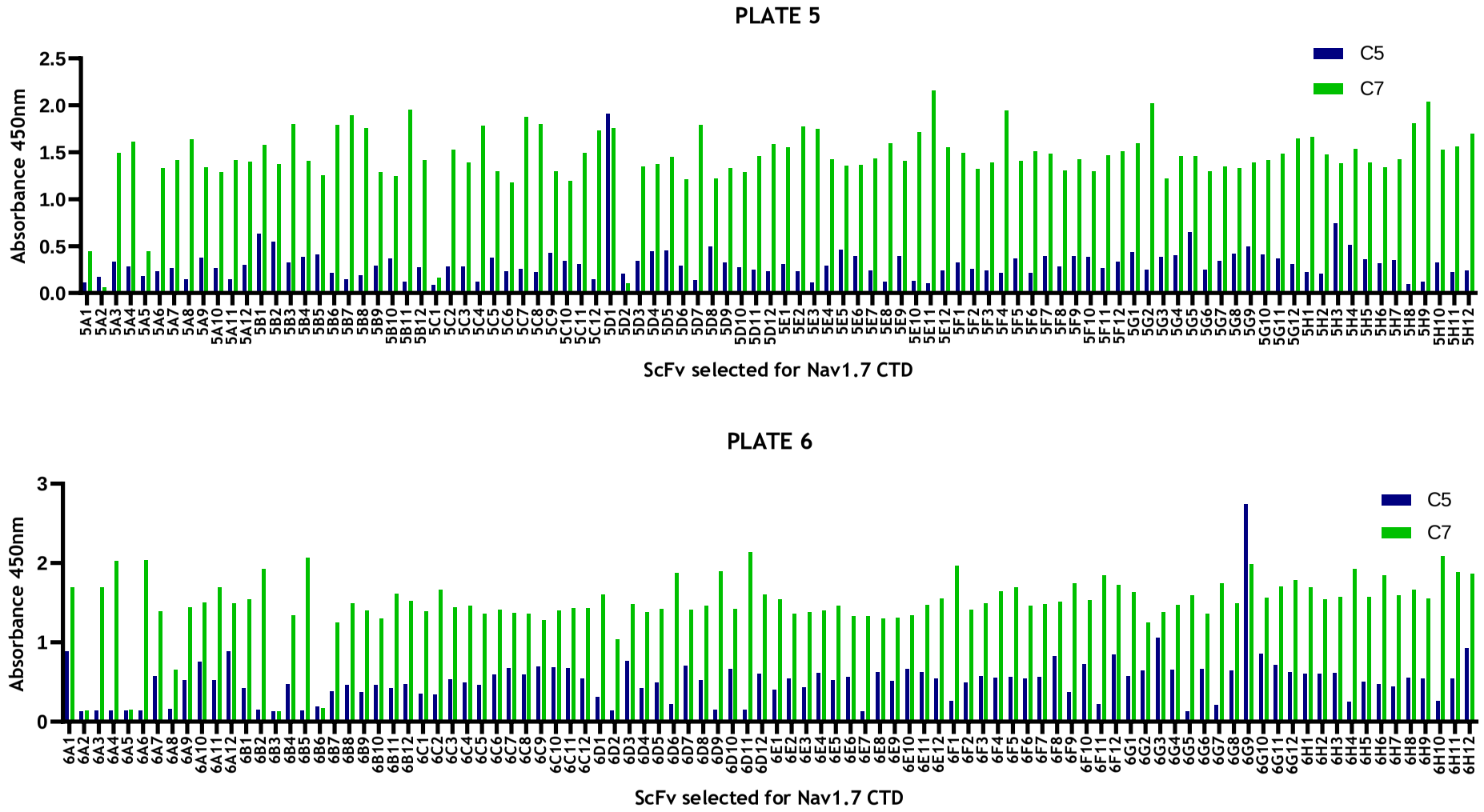
PLATE 5
Absorbance 450nm
2.5
2.0
1.5
1.0
0.5
0.0
C5
C7
5A1 5A2 5A3 5A4 5A5 5A6 5A7 5A8 5A9 5A10 5A11 5A12 5B1 5B2 5B3 5B4 5B5 5B6 5B7 5B8 5B9 5B10 5B11 5B12 5C1 5C2 5C3 5C4 5C5 5C6 5C7 5C8 5C9 5C10 5C11 5C12 5D1 5D2 5D3 5D4 5D5 5D6 5D7 5D8 5D9 5D10 5D11 5D12 5E1 5E2 5E3 5E4 5E5 5E6 5E7 5E8 5E9 5E10 5E11 5E12 5F1 5F2 5F3 5F4 5F5 5F6 5F7 5F8 5F9 5F10 5F11 5F12 5G1 5G2 5G3 5G4 5G5 5G6 5G7 5G8 5G9 5G10 5G11 5G12 5H1 5H2 5H3 5H4 5H5 5H6 5H7 5H8 5H9 5H10 5H11 5H12
ScFv selected for Nav1.7 CTD
PLATE 6
Absorbance 450nm
3
2
1
0
C5
C7
6A1 6A2 6A3 6A4 6A5 6A6 6A7 6A8 6A9 6A10 6A11 6A12 6B1 6B2 6B3 6B4 6B5 6B6 6B7 6B8 6B9 6B10 6B11 6B12 6C1 6C2 6C3 6C4 6C5 6C6 6C7 6C8 6C9 6C10 6C11 6C12 6D1 6D2 6D3 6D4 6D5 6D6 6D7 6D8 6D9 6D10 6D11 6D12 6E1 6E2 6E3 6E4 6E5 6E6 6E7 6E8 6E9 6E10 6E11 6E12 6F1 6F2 6F3 6F4 6F5 6F6 6F7 6F8 6F9 6F10 6F11 6F12 6G1 6G2 6G3 6G4 6G5 6G6 6G7 6G8 6G9 6G10 6G11 6G12 6H1 6H2 6H3 6H4 6H5 6H6 6H7 6H8 6H9 6H10 6H11 6H12
ScFv selected for Nav1.7 CTD

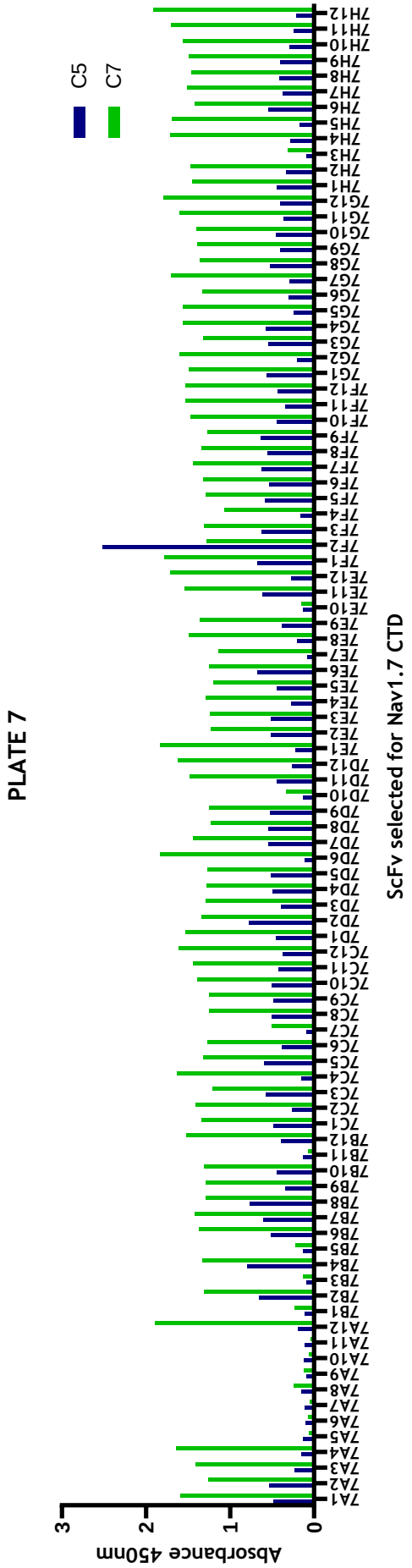

Figure 5.3. 96 well ELISA plate results for clones that were selected for $Na_v1.7$ CTD (C7, green) and deselected for $Na_v1.5$ CTD (C5, blue).

5.4 Shortlisted scFv

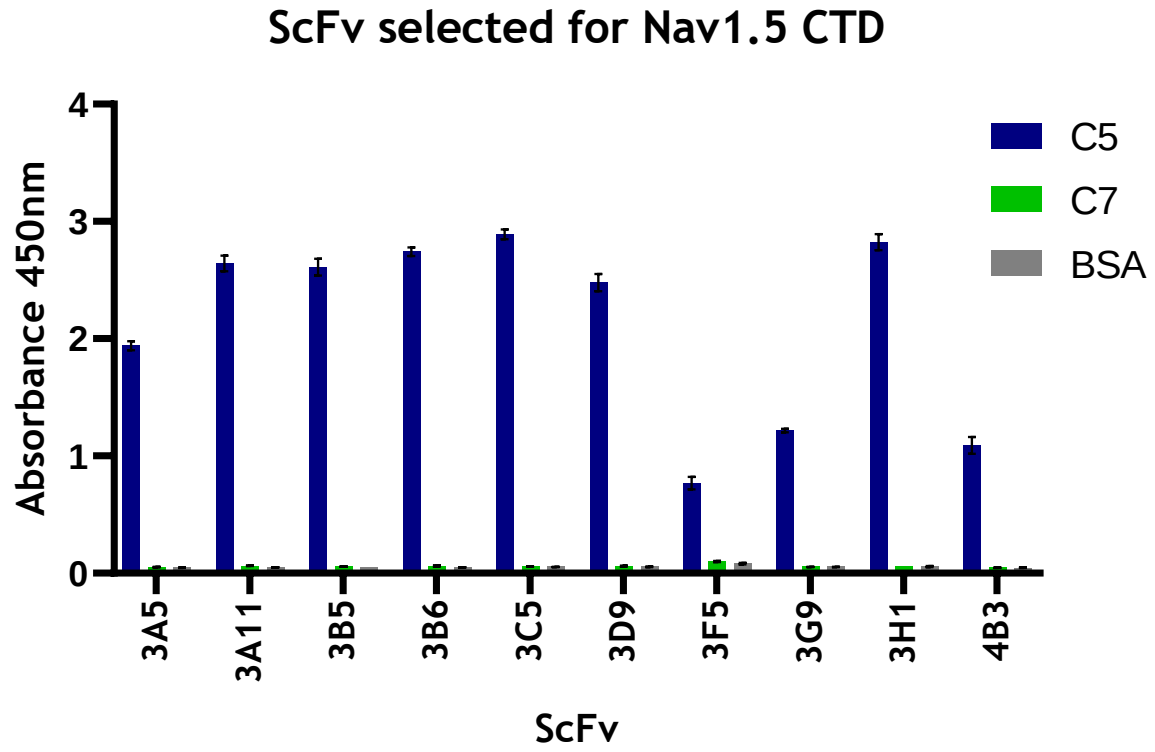

Figure 5.4. 96 well ELISA plate repeated for shortlisted clones that were specifically recognizing $Na_v1.5$ CTD (C5, blue).

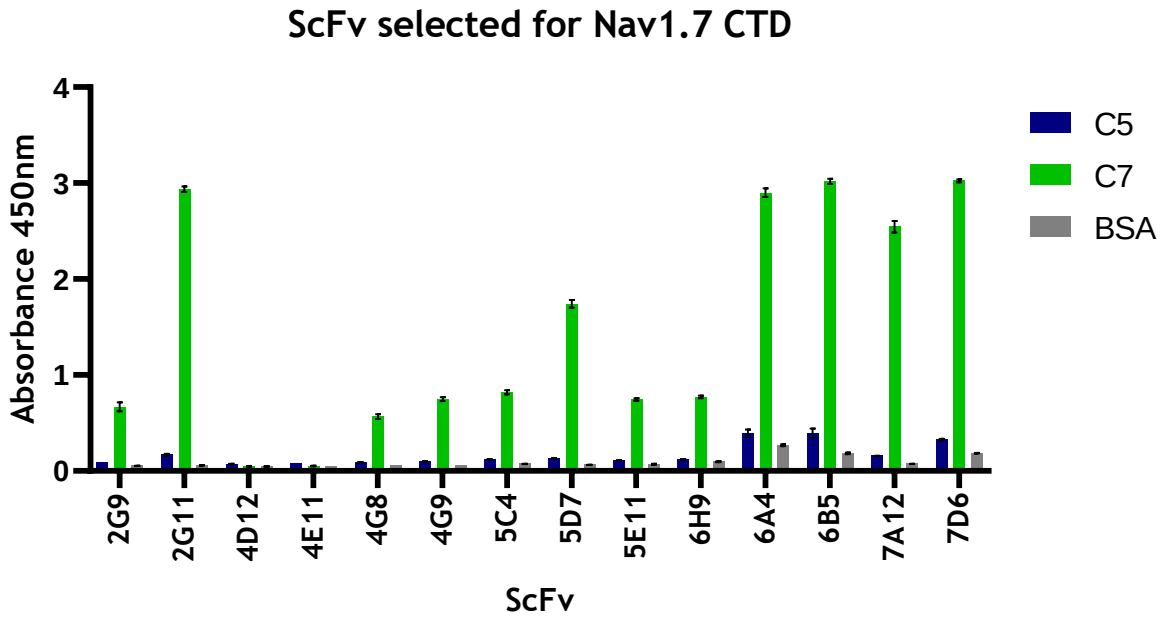

Figure 5.5. 96 well ELISA plate repeated for shortlisted clones that were specifically recognizing $Na_v1.7$ CTD (C7, green).

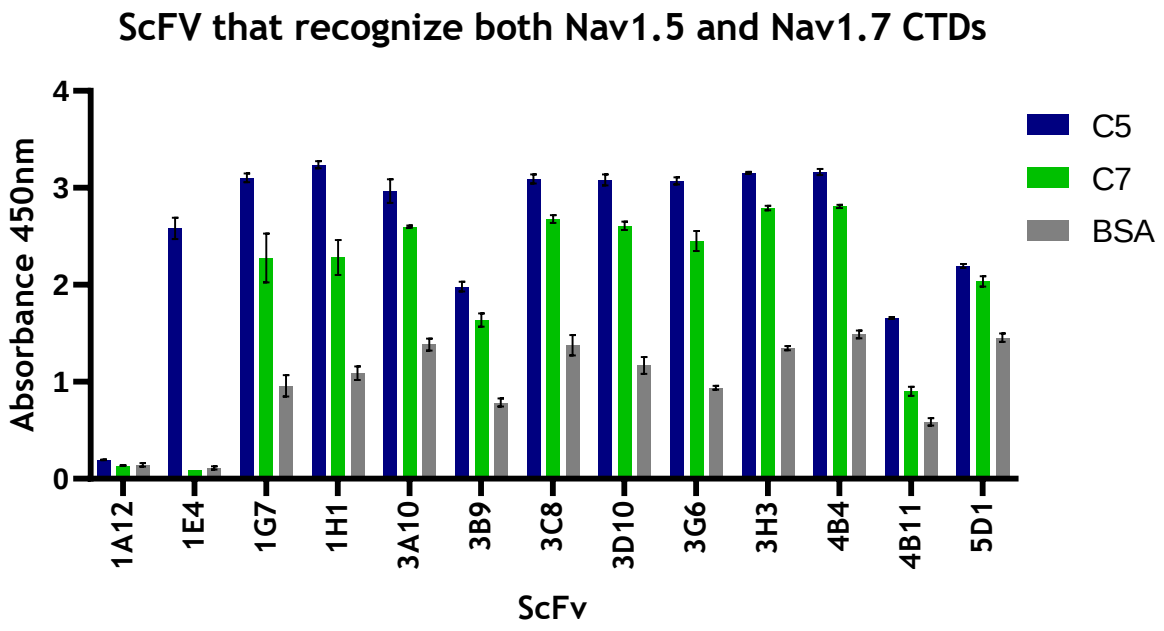

Figure 5.6. 96 well ELISA plate repeated for shortlisted clones that were recognizing both $Na_v1.5$ CTD (C5, blue) and $Na_v1.7$ CTD (C7, green).

5.5 Selected scFv to $Na_v1.5$ CTD (C5) probed on $Na_v1.5$ CTD EF hand (5EF)

To determine the region of C5 the scFv clones specific to C5 bind, ELISA was performed with the clones to determine whether they recognized the truncated $Na_v1.5$ CTD EF-hand (5EF) (Figure 5.7). All the clones recognized both C5 and 5EF, while some of them appeared to bind with higher affinity to 5EF compared to C5, namely 3A5, 3B5, 3G9 and 3H1. Figure 5.7B shows the ELISA plates after TMB substrate was added and before 2M Sulphuric acid was added to neutralize the reaction. The relative intensity of the blue color corresponds to the level of absorbance 450 nM signal which is an indication of binding affinity. Note also how the BSA control did not give any signal as expected. Figure 5.8 confirms that the clones selective to C5 that were also recognizing 5EF, were still deselected for C7.

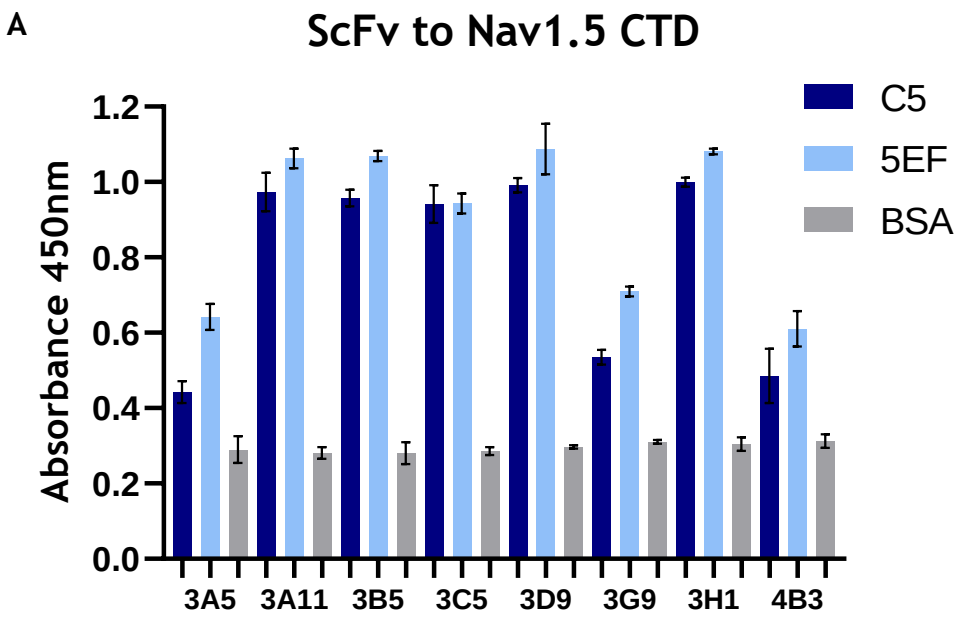

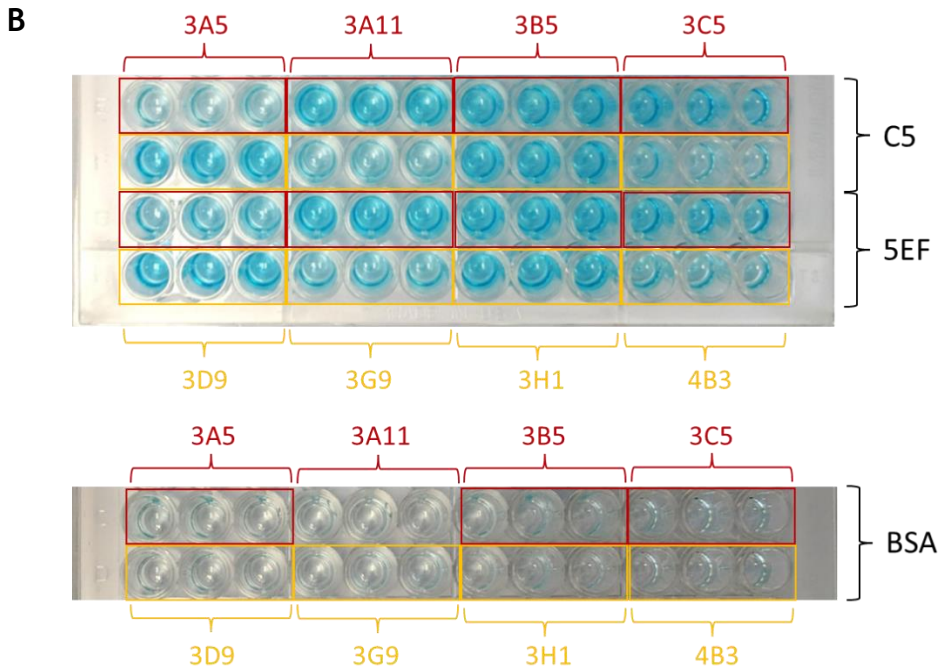

Figure 5.7. To narrow down where the $Na_v1.5$ CTD (C5) selective scFv clones bind, they were screened against the Nav1.5 CTD EF hand domain (5EF). **A.** Absorbance reading at 450 nm **B.** Image of the actual 96 well plate of the results graphically presented in (A).

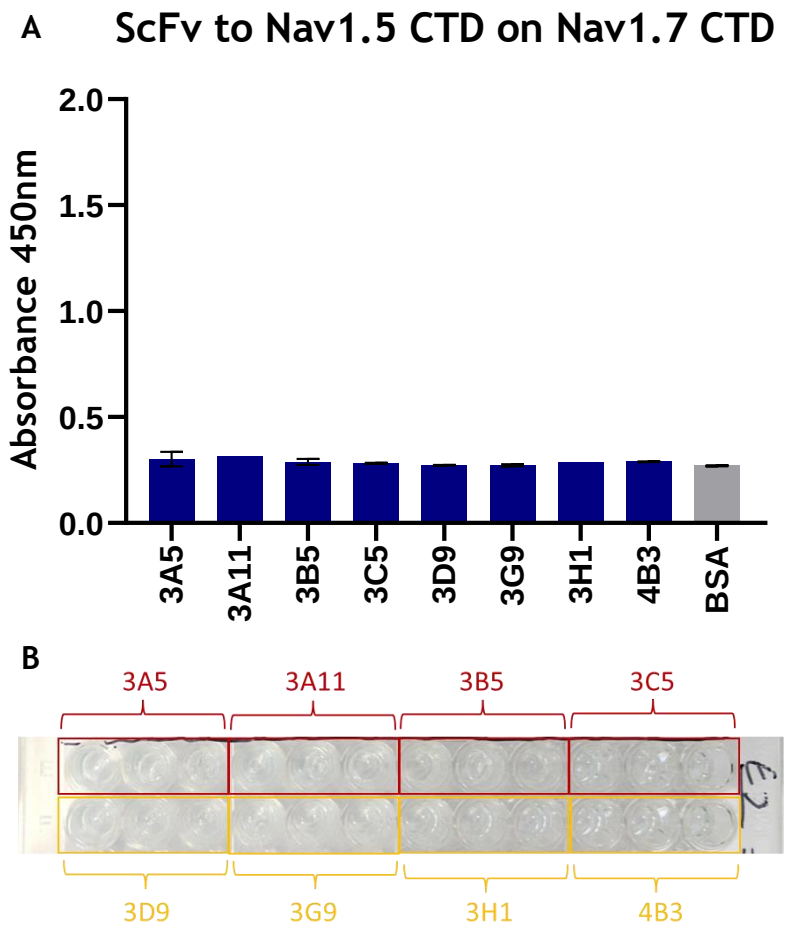

Figure 5.8. To confirm that the clones recognizing Nav1.5 CTD are not also recognizing $Na_v1.7$ CTD, ELISA was repeated. **A.** Absorbance reading at 450 nm **B.** Image of the actual 96 well plate of the results graphically presented in (A).

5.6 Selected scFv to $Na_v1.7$ CTD (C7) probed on $Na_v1.7$ CTD EF hand (7EF)

The same test, for the clones that selectively recognize C7, was performed to better understand broadly the region at which they were binding. Therefore, the clones were used to determine whether they recognized the truncated $Na_v1.7$ CTD EF-hand (7EF) along with the full length $Na_v1.7$ CTD (Figure 5.9). Unlike clones to C5, none of the clones specific to C7 bound to the 7EF region, suggesting that they were recognizing a region towards the latter half of C7, which consists of a more disordered region.

Figure 5.10 confirms that the clones selective to C7 were still deselected for C5.

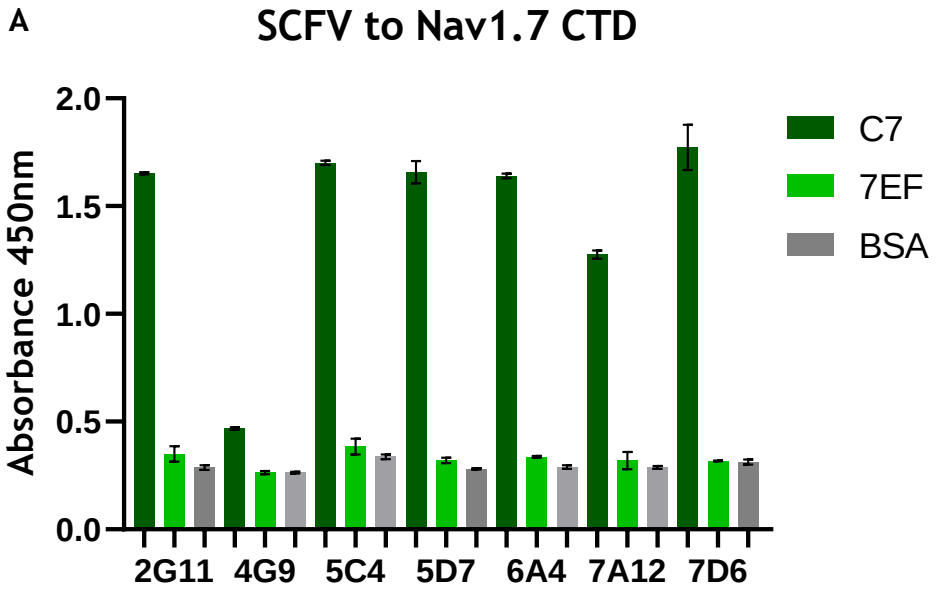

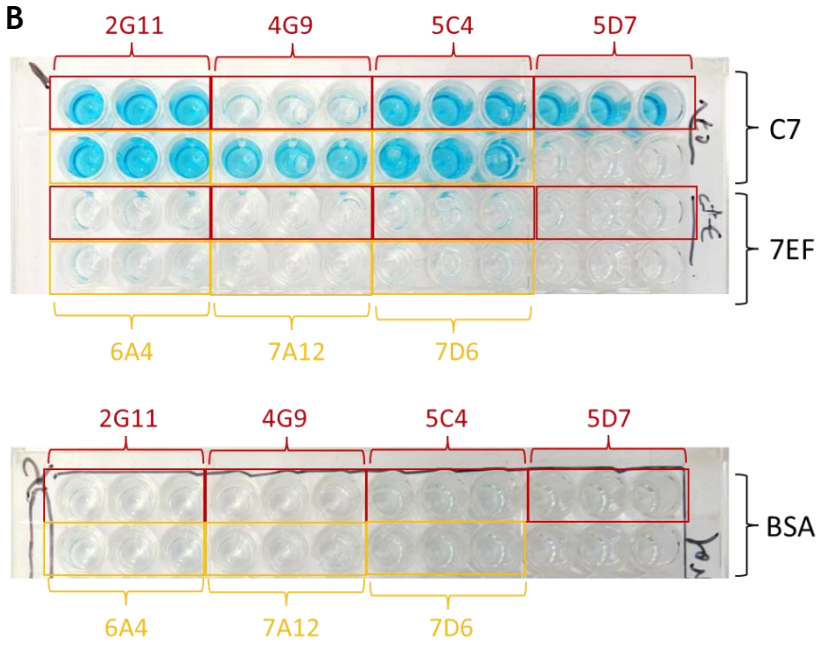

Figure 5.9. To narrow down where the $Na_v1.7$ CTD (C7) selective scFv clones bind, they were screened against the Nav1.7 CTD EF hand domain (7EF). **A.** Absorbance reading at 450 nm **B.** Image of the actual 96 well plate of the results graphically presented in (A).

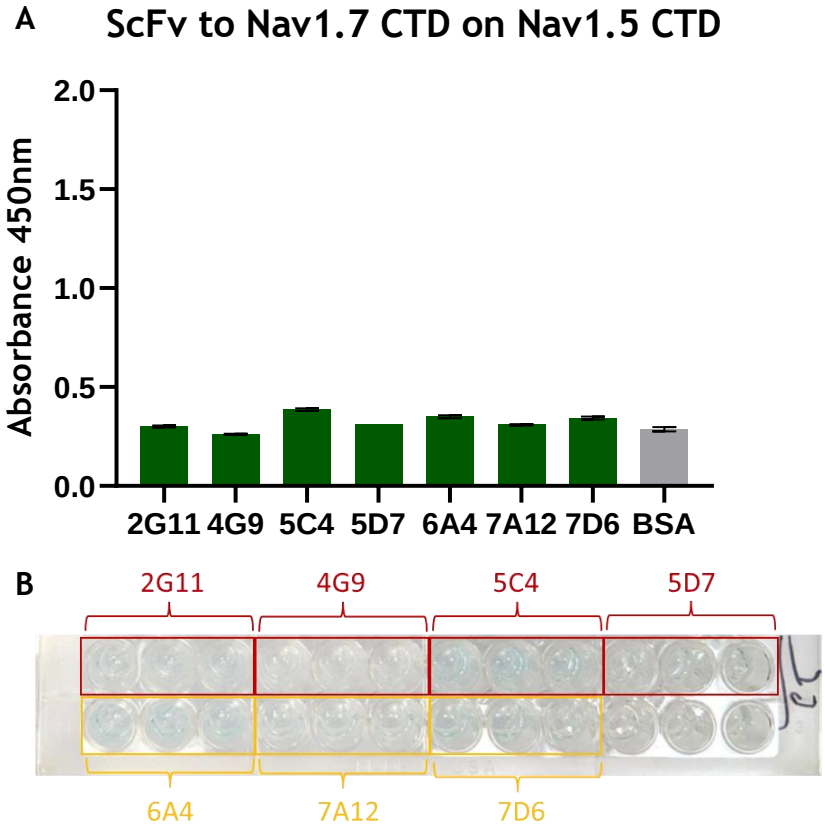

Figure 5.10. To confirm that the clones recognizing Nav1.7 CTD are not also recognizing $Na_v1.5$ CTD, ELISA was repeated. **A.** Absorbance reading at 450 nm **B.** Image of the actual 96 well plate of the results graphically presented in (A).

5.7 Purified scFv clones for $Na_v1.5$ CTD (C5) and $Na_v1.7$ CTD (C7)

DNA sequencing of three of the purified clones binding to C5 (Figure 5.11A) revealed that the clones 3D9 and 3H1 were the same, showing 100% identical complementarity determining regions (CDRs) of both the variable regions, heavy (V_H) and light (V_L). Therefore, between the two, 3H1 was chosen for further work. CDRs are basically the regions which takes the leading role in antigen binding. Similarly, 5C4 and 6A4, purified clones binding to C7, turned out to be the same (Figure 5.11B), so only 5C4 was chosen for further work.

Figure 5.12 reconfirms the nature of the selected clones and their deselection were intact after periplasmic extraction and purification.

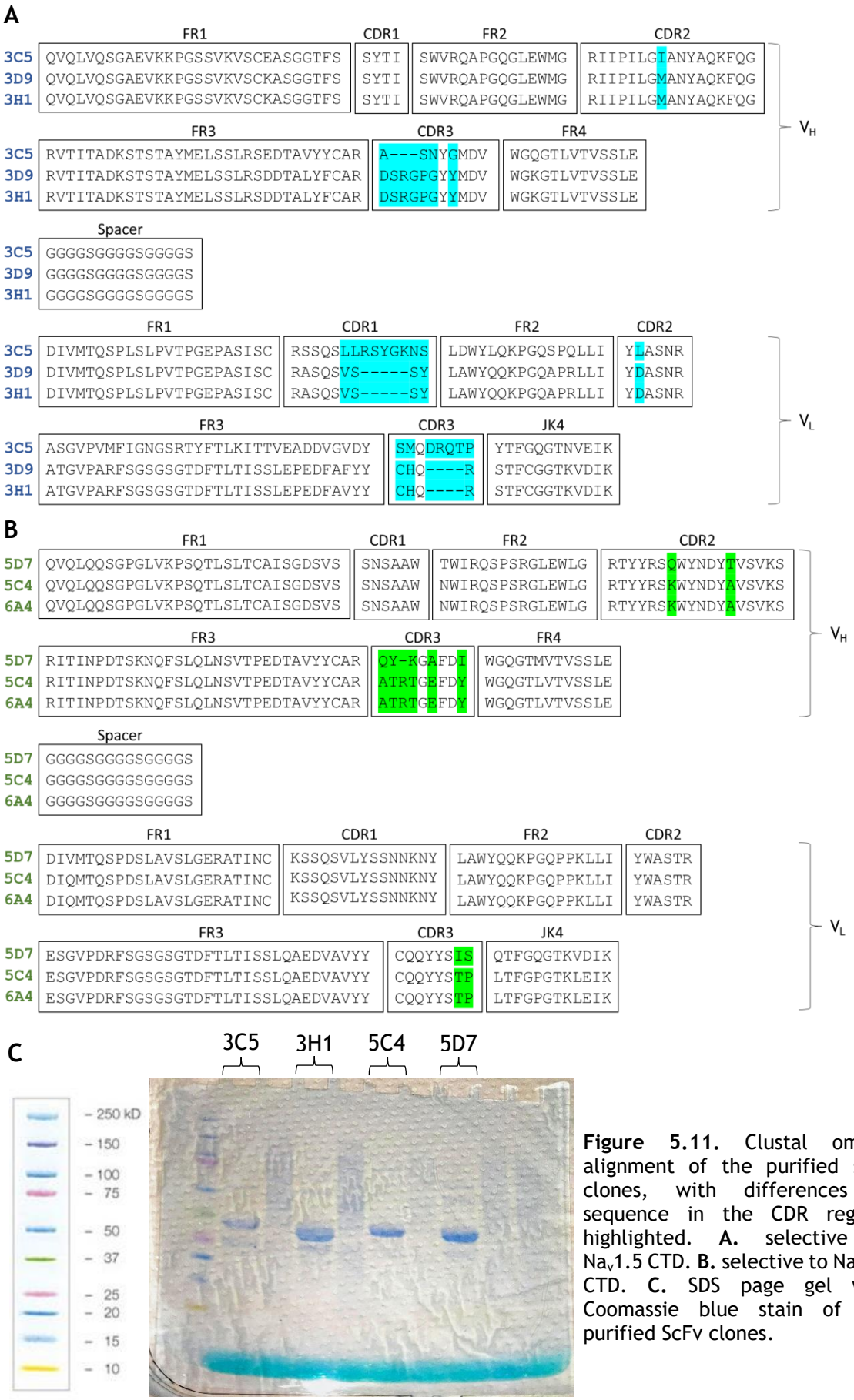

Figure 5.11. Clustal omega alignment of the purified scFv clones, with differences in sequence in the CDR regions highlighted. **A.** selective to $Na_v1.5$ CTD. **B.** selective to $Na_v1.7$ CTD. **C.** SDS page gel with Coomassie blue stain of the purified ScFv clones.

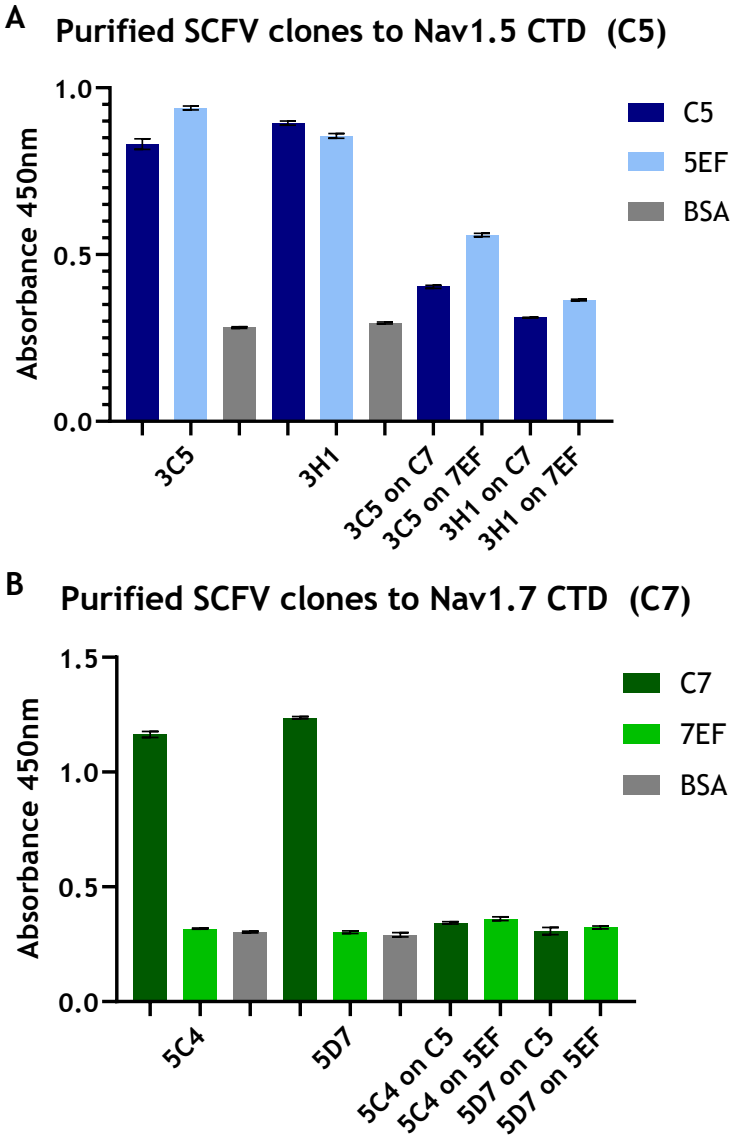

Figure 5.12. Repeat of the selection and deselection ELISA for the purified scFv clones to **A.** $Na_v1.5$ CTD and **B.** $Na_v1.7$ CTD.

5.8 ScFv clone binding in presence of Calmodulin (CaM)

It has already been shown that apoCaM interacts with both C5 and C7 and that it can be detected with ELISA (Figure 4.9). Figure 5.13 investigates whether binding of apoCaM to the Na_V CTDs has any effect on binding of the clones. For both 3C5 and 3H1 clones which recognize C5, their binding was significantly hampered by the presence of CaM, as confirmed by the higher absorbance signal recorded in the absence of CaM. For the 5C4 and 5D7 clones which recognize C7, however, presence of apoCaM showed no effect on their binding to C7.

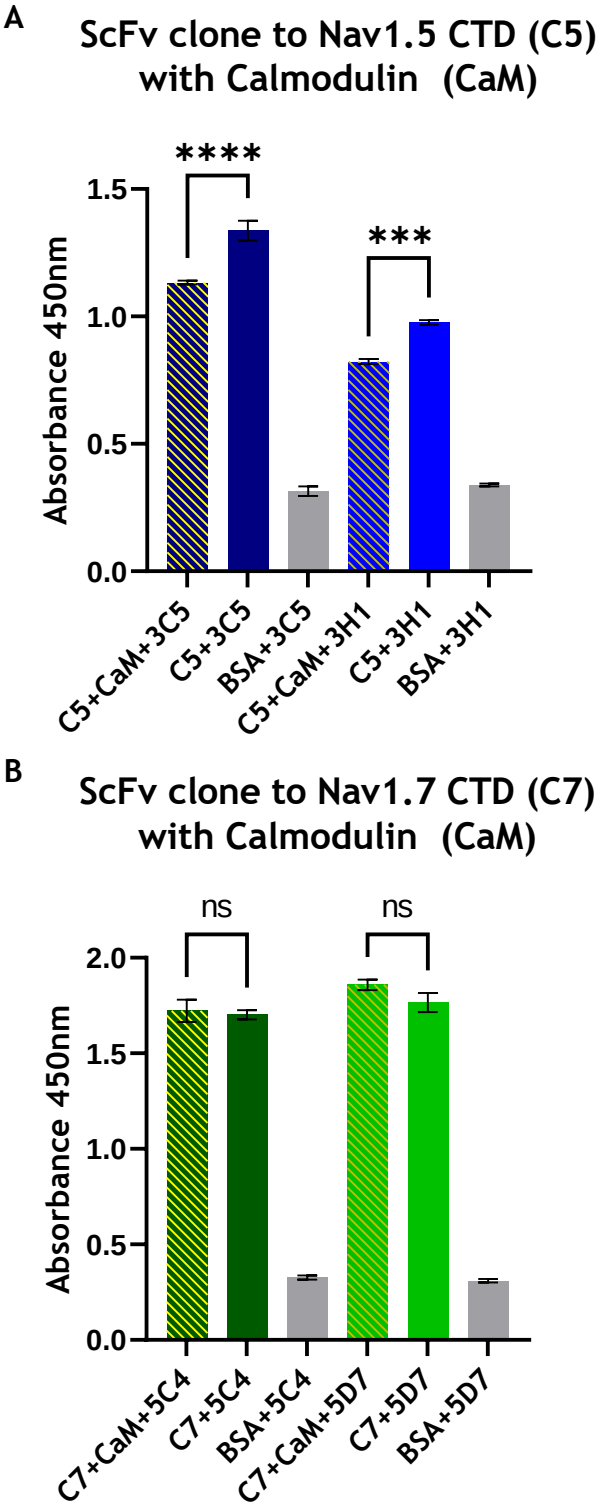

Figure 5.13. Effect of calmodulin (apo) on the binding of scFv clones to **A.** $Na_v1.5$ CTD and **B.** $Na_v1.7$ CTD.

5.9 Effect of $Na_v1.5$ CTD clone 3H1 on $Na_v1.5$ channel gating

As the selective binding of the clones to the C5 has been established, automated patch clamp was used to understand whether this binding had any effect on the steady state activation, steady state inactivation and recovery from inactivation parameters of $Na_v1.5$ channel. The results obtained for the 3H1 clone suggested that none of these parameters were affected.

A

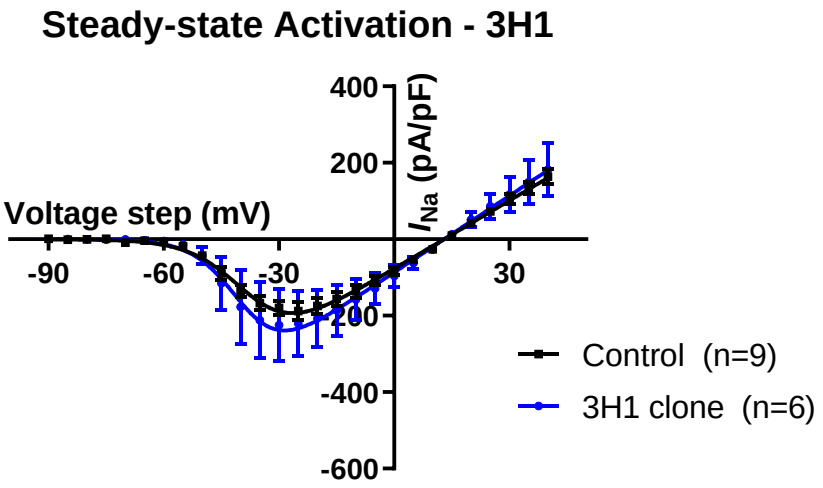

Activation – 3H1 clone

	Control	3H1 clone
Peak I_{Na}	-189.6 ± 23.94	-233.0 ± 96.46
$V_{1/2}$	-37.12 ± 1.08	-35.89 ± 1.69
k	-6.61 ± 0.42	-6.19 ± 0.47
n	9	6

B

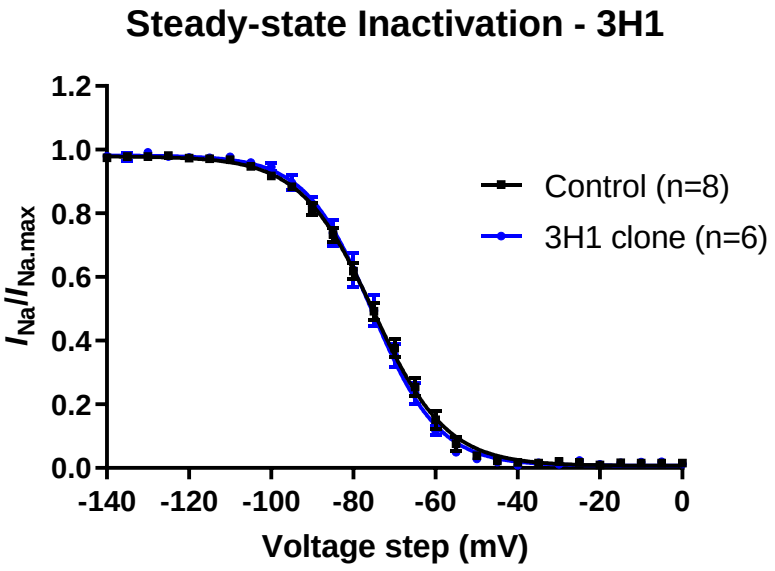

Inactivation – 3H1 clone

	Control	3H1 clone
$V_{1/2}$	-75.01 ± 1.18	-75.67 ± 1.72
k	-8.71 ± 0.39	-7.78 ± 0.41
n	8	6

C

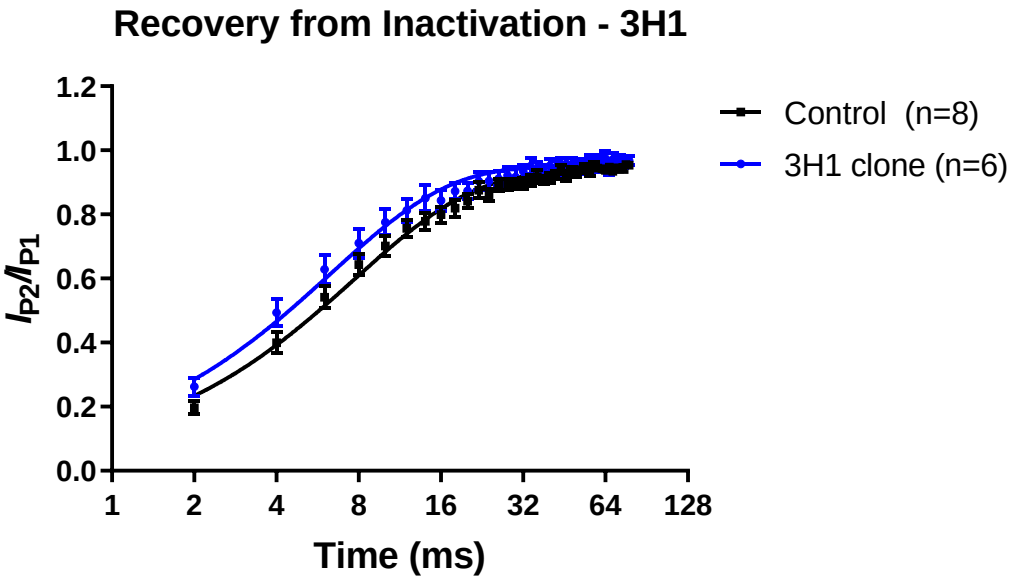

	Control	3H1 clone
k_{fast}	0.160 ± 0.014	0.211 ± 0.021
k_{slow}	0.0368 ± 0.0172	0.0444 ± 0.0105
τ_{fast} (ms)	6.64 ± 0.66	5.09 ± 0.72
τ_{slow} (ms)	25.42 ± 5.48	22.08 ± 4.03
t1/2 $_{fast}$ (ms)	4.60 ± 0.46	3.53 ± 0.50
t1/2 $_{slow}$ (ms)	17.62 ± 3.80	15.31 ± 2.79
n	8	6

Figure 5.14. ScFv clone 3H1, which selectively recognizes $Na_v1.5$ CTD, was studied under whole-cell patch clamp under various protocols using stable HEK293F cell lines expressing Nav1.5. **A.** Steady-state activation properties remained unaffected in presence of 3H1 clone at 500 nM concentration. The control consisted of the buffer that 3H1 is dissolved in minus just the clone. **B.** No effects were observed in steady-state inactivation properties. **C.** Computed parameters of recovery from inactivation protocol also showed no significant difference between 3H1 and the control.

5.10 *In silico* docking using ClusPro

ClusPro web server has been used for molecular docking of the 3H1 clone to the C5 and 5D7 clone to C7. The server generated multiple different conformations through which these proteins could interact. The best fit model was determined by their ClusPro model scores (lower the better) with the added consideration of the experimental data obtained regarding the relevant clones.

5.10.1 *In silico* docking of 3H1 clone on $Na_v1.5$ CTD

A

i. **ii.** **iii.** **iv.**

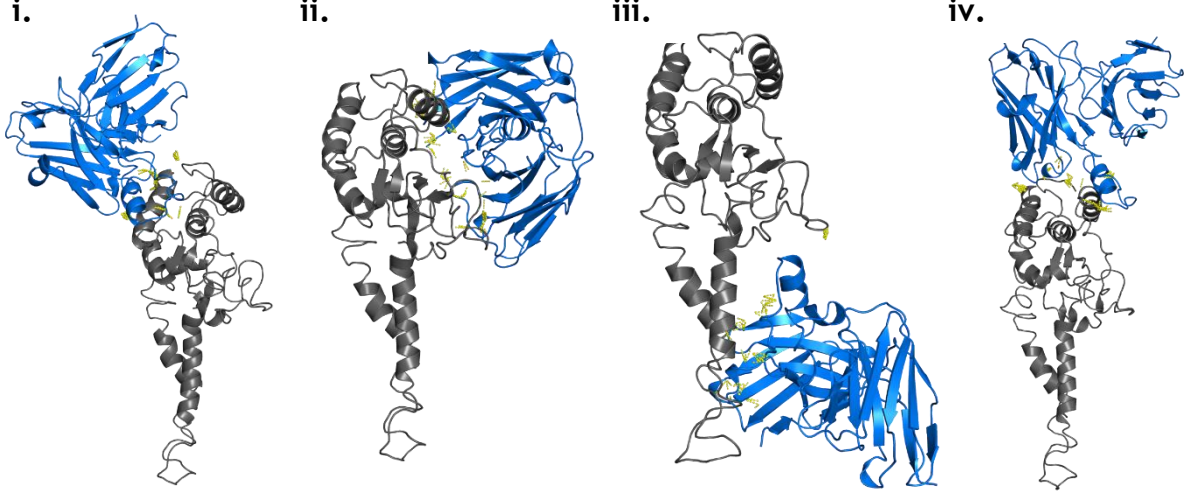

B

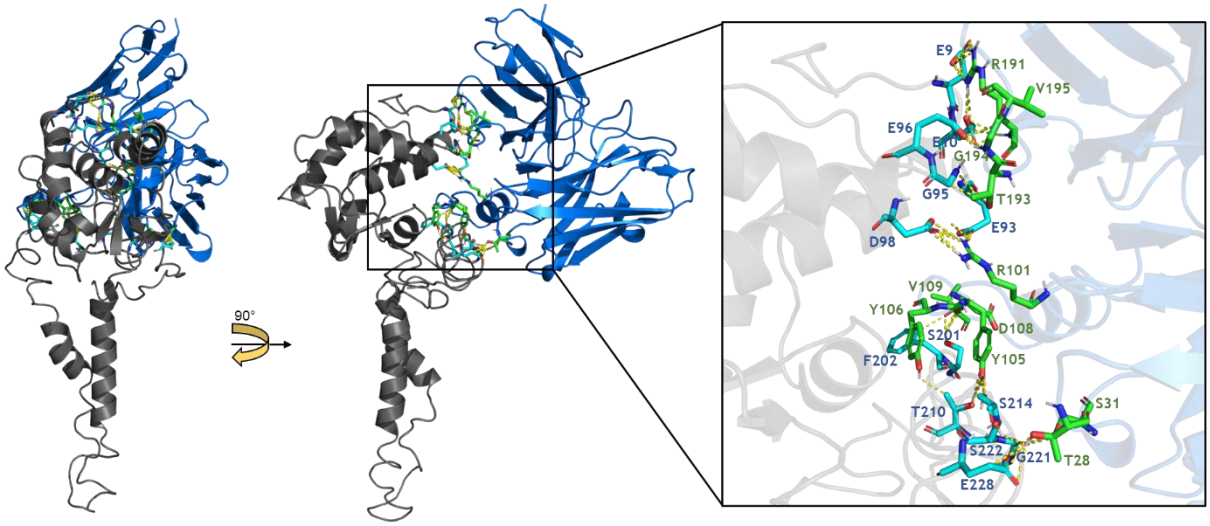

3H1 clone	Nav1.5 CTD	Bond
T28	S222	Hydrogen
	E228	Hydrogen
S31	G221	Hydrogen
R101	E93	Ionic
	D98	Ionic
Y105	S214	Hydrogen
	T210	Hydrogen
Y106	T210	Hydrogen
D108	S201	Hydrogen
	F202	Hydrogen
V109	S201	Hydrogen
R191	E9	Ionic
	E10	Ionic
T193	G95	Hydrogen
G194	E96	Hydrogen
V195	E96	Hydrogen

Figure 5.15. *In silico* docking of 3H1 clone (blue) with $Na_v1.5$ CTD (grey) performed using Cluspro. **A.** Cluspro generated models of interaction (yellow lines) between 3H1 clone and C5. **B.** The best model of interaction of 3H1 with C5. Zoomed in image shows the interaction in close-up with amino acid residues of 3H1 represented by green sticks and Nav1.5 CTD residues by blue sticks. The table lists all the interacting amino acid residues and the type of bond they form, which are within 3Å from each other.

5.10.2 *In silico* docking of 5D7 clone on $Na_v1.7$ CTD

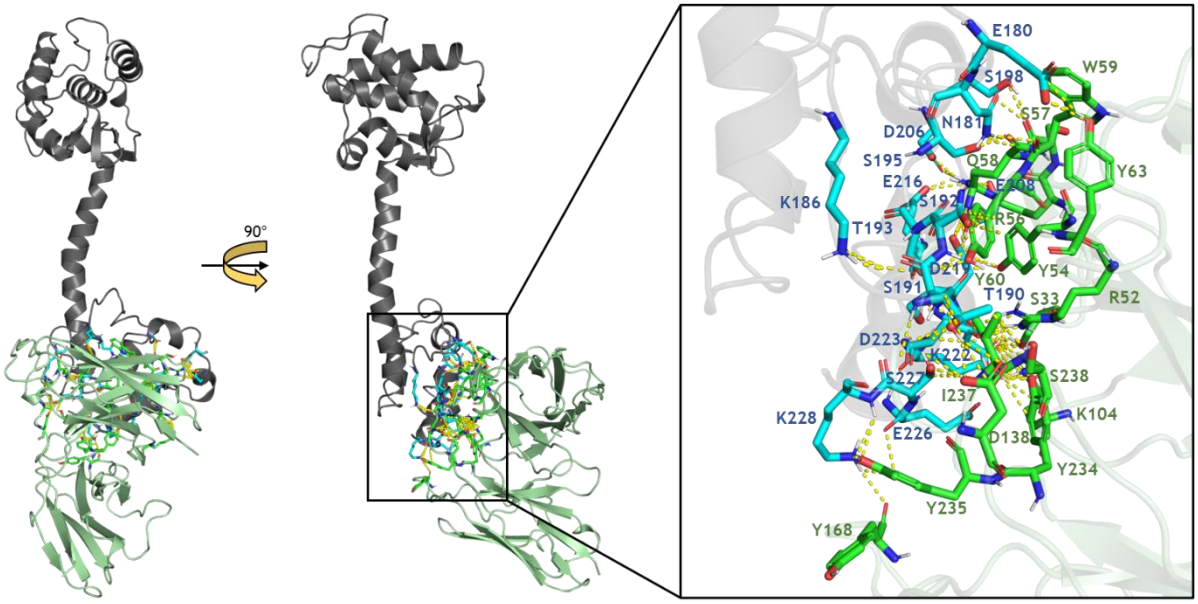

5D7 clone	Nav1.7 CTD	Bond
S33	E218	Hydrogen
R52	D223	Ionic
Y54	D219	Hydrogen
R56	D206	Ionic
	E208	Ionic
	E216	Ionic
S57	S198	Hydrogen
Q58	S195	Hydrogen
	D219	Hydrogen
W59	N181	Hydrogen
Y60	T193	Hydrogen
Y63	E180	Hydrogen
K104	E218	Ionic
D138	T190	Hydrogen
Y168	K228	Hydrogen
Y234	K222	Hydrogen
Y235	K228	Hydrogen
	E226	Hydrogen
I237	S191	Hydrogen
	S227	Hydrogen
S238	T190	Hydrogen

Figure 5.16. *In silico* docking of 5D7 clone (green) with $Na_v1.7$ CTD (grey) performed using Cluspro. The zoomed in image shows the interaction in close-up with amino acid residues of 5D7 represented by green sticks and Nav1.7 CTD residues by blue sticks. The table lists all the interacting amino acid residues and the type of bond they form, which are within 3Å from each other.

Discussion

In this study hundreds of single chain fragment variable (scFv) antibody binders were found by biopanning with 10^{11} naïve phage display library of scFvs (Figure 5.2, Figure 5.3). These scFvs were categorized into three groups, those that specifically recognize $Na_v1.5$ CTD (C5), those that specifically recognize $Na_v1.7$ CTD (C7), and those that recognized both the CTDs. Proper deselection and selection of the scFvs were determined in multiple experiments (Figure 5.7, Figure 5.8, Figure 5.9, Figure 5.10) and additionally the region of the CTDs where these scFvs were binding broadly ascertained (Figure 5.12). The clones recognizing C5 also bound to the globular 5EF, whereas the clones recognizing the C7 did not bind to the 7EF. This was further confirmed by ELISA with apoCaM (Figure 5.13) as only the binding of clones to C5 were affected by the presence apoCaM and not the clones to C7. It is well established that CaM binds to the IQ motif and EF region of the Na_v CTDs, since the clones recognizing C5 were found to also bind to 5EF region: either they are competing with the binding site of CaM and/or the already bound CaM is posing steric hindrance to the scFvs. In case of the clones to C7 which were found to bind to a region which is post-7EF, the presence of CaM does not interfere with its binding to C7.

In silico docking experiments shed more light on this phenomenon (Figure 5.15, Figure 5.16). The docking was performed using the ClusPro web server which works by simulating 70,000 rotations of the ligand, from which 1000 of them with the best scores are chosen for more rigorous clustering analysis. Ligand positions with the most neighbours within 9Å C-alpha rmsd radius are chosen as cluster centers and this function repeated numerous times to generate more than or equal to 5 protein-protein interaction models consisting of the best model scores. Figure 5.15A and B shows the 5 generated models for the interaction between 3H1 clones with C5. Figure 5.15B shows the model with the lowest score and the one that is backed by other experimental data. For instance, in the first model (Figure 5.15Ai) the 3H1 clone is modelled to bind to the EF hand region of C5 where the N-terminus of CaM binds. Although from Figure 5.13A we know that presence of apoCaM significantly reduces the binding of 3H1 to C5, if this ClusPro model was accurate it would have meant that 3H1 and apoCaM could not bind to C5 at the same time at all, which we know is not the case. In case of the second and third model (Figure 5.15Aii and iii) however, 3H1 is modelled to bind completely away from the apoCaM binding site, which is also not supported by the Figure 5.13A which confirms that binding of 3H1 is affected by

the presence of apoCaM. Figure 5.15Aiv is also not an accurate representation of 3H1 interaction with C5, since it is modelled to bind to a position which would inhibit the DIII-DIV linker to access the cleft of the C5 EF hand region and thus have a significant impact on the gating parameters, which were not observed (Figure 5.14). The best model, Figure 5.15B shows the 3H1 clones binding to the 5EF region, which is not directly at the N-lobe binding location of CaM neither in a location that will hinder DIII-DIV binding to the EF hand cleft. Also, when CaM is bound to the C5, it will not completely abolish but impede the binding of the scFv clone through steric hindrance. Similarly, although not shown, in case of the 5D7 clones, multiple protein-protein interaction models were considered to find the best model (Figure 5.16). This model shows that 5D7 binds to the very tail end of the C7, in the post-IQ motif region, confirming why 5D7 interaction with C7 was not affected when apoCaM binds to the C7 (Figure 5.13B).

In case of the 3H1 clone, binding to the C5 primarily involved multiple hydrogen bonding and ionic bonding by the CDR3 region of V_H fragment (residues R101, Y105, Y106, D108, V109). Additionally, CDR1-V_H (S31), CDR2-V_L (R191) and FR3-V_L also made contact with C5. Differences in C5 and C7 that could potentially explain the selectivity of 3H1 to C5 include the S201 in C5 to threonine in C7, F202 in C5 to serine in C7, S214 to lysine C7, E228 to glycine and G221 to arginine. Most of these aforementioned differences between C5 and C7 account for disruption in hydrogen bond formation with the 3H1 clone.

The 5D7 clones bind to C7 primarily through its CDR2-V_H (R52, R56, S57, Q58, W59, Y54, Y60, Y63) forming hydrogen and ionic bonds. Involvement of CDR1-V_H (S33), CDR3-V_H (K104), CDR3-V_L (Y234, Y235, I237, S238) and FR1-V_L (D138, Y168) are also observed. Although some similarities are observed in the amino acid residues of C7 and C5, there are some differences which most likely account for the selectivity of the 5D7 clone to C7. For example, R56 of 5D7 forms an ionic bond with D206 of C7, however the corresponding amino acid in C5 is a threonine which will not be able to take part in the ionic bond. Similarly, ionic bonds between K104 of 5D7 and E218 of C7 will not form in C5 which has a serine residue in that location. More modest differences in C5, such as the presence of aspartic acids in place of glutamic acids in the E208 and E216 position, histidine in place of D219, serine in place of T190, can overall have an additive effect which prevents the 5D7 clone from recognizing C5.

Whether the clone 3H1 had any effect on the gating parameters of $Na_V1.5$ channel was also studied using whole cell patch clamp. No significant differences, between the 3H1 clone and control, were observed in the parameters obtained from steady-state activation, inactivation and recovery from inactivation protocols. It was observed in earlier studies than the binding of 3H1 clone is significantly reduced in presence of CaM. It is plausible that endogenous CaM present in HEK293F cells are out competing 3H1 clones in binding to the C5. Further work with the other clones specific to C5 and C7 could be studied to find ones that affect gating properties and could be potentially useful in downstream research and/or therapeutic applications.

Chapter 6

Conclusion

6. Conclusion

The overall aim of this work was to explore the structural and functional roles of the voltage-gated sodium channel (Na_V), focusing on the extracellular turret region and the C-terminal domain (CTD). The role of the voltage sensing domains (VSDs), inactivation gate (IG) and the pore has traditionally been the focus of research to better understand Na_V. Literature is replete with research involving these essential regions of Na_V, however extensive focus on other regions are lacking. This is in spite of the fact that the clinical literature describes numerous examples of point mutations in these less apparent regions which are associated with major cardiac pathologies.

Initially, I investigated point mutations found on the interface between domain II and domain III of $Na_V1.5$, which were earlier shown to be involved in BrS without any structural understanding of their significance in causing this pathology. My aim was to understand the impact of these point mutations on the $Na_V1.5$ channel gating. The study revealed an intricate set of ionic and cation-π bonds holding the two domains together, disruption of which resulted in drastic effects on channel function, in most cases complete loss of Na^+ current. I also showed that even conservative changes to this region, like exchanging the positive and negatively charged side chain residues still resulted in complete loss of function of the channel. Moreover, none of these non-functioning channels could be revived by the Na_V agonist veratridine, which acts by inhibiting channel inactivation. Also, these mutations did not prevent the channel from folding appropriately to become expressed on the plasma membrane. This led to collaborative explorations to seek explanations though the use of MD simulation. The *in silico* work showed how some of these mutations caused overall as well as local instabilities in the Na_V. Also, it was demonstrated that the mutated channels that did not conduct Na^+ ion showed constricted pore regions; their selectivity filter (DEKA) residues were rearranged with the consequences that the positively charged lysine residue occluded the opening of the pore thereby inhibiting permeation of the Na^+.

The present studies examined mutated Na_V channels individually. Further work could co-transfect both mutated channel and wild-type channel in the HEK293 cells, with their effect observed using whole cell patch clamp. This will result in findings that

more closely represent the physiological effects of such mutations in vivo. Thus, in the clinical situation, all these mutations involved in pathology are heterozygous, with one copy of the gene still retaining the WT allele. Moreover, MD simulation only examined a specific smaller subset of the mutations that were characterized using electrophysiology. Further MD work could not only include all the mutations, but a longer duration of simulation could add to the understanding. Some very recent work on structure determination of $Na_v1.5$ reported open-state structure by blocking inactivation through mutation[328]. In this studyall MD simulation work were performed on the available cryoEM structure of $Na_v1.5$ which resembled the inactivated state, since taking a Na_v channel out of a ruptured membrane, i.e. rendering its surrounding to effectively 0 mV, resulted in the Na_v channel assuming its inactivated state. Running MD simulation on an open-state Na_v channel would provide further insights into these mutations. Also, as mentioned previously, these mutations in corresponding highly conserved homologous regions of other Na_v subtypes and even some Cav, are found in the literature; some of these are implicated in various pathologies. Future work on how these mutations' effect on those other channels could potentially reveal a great deal about the structure and function of the voltage gated ion channel family in general and establish with more certainty the importance of the oft neglected extracellular turret regions. Armed with the knowledge of how disruption of simple salt-bridges on the extracellular surface of the Na_v can cause such dramatic effect to the channel activity, drug target campaigns can be run focusing on these regions.

In the next study, I cloned, expressed, and purified various recombinant proteins including, the full length and truncated CTDs of $Na_v1.5$ (C5 and 5EF) and $Na_v1.7$ (C7 and 7EF) and Calmodulin (CaM). As in the case of previously reported C5 and its interaction with CaM, using ELISA, ITC and BLI, I showed that C7 also interacts with CaM, particularly apoCaM. Also, I reported the K_D values of full length CTDs, both $Na_v1.5$ and $Na_v1.7$, which have not been reported previously. Furthermore, attempt has been made to solve the structure of the full length $Na_v1.7$ CTD using x-ray crystallography. In the future other structure determination methods like cryoEM could be considered.

The final work of this project involved screening for scFvs that were selective to C5 and C7. This generated hundreds of hits, of which a few were expressed and purified and their effect on overall channel activity observed using automated whole cell patch clamp. *In silico* docking revealed that the scFvs that were selected for C5 were binding at the EF-hand region, close to its binding site for the N-lobe of CaM; as expected, the presence of CaM significantly reduced the binding of these scFvs. On the other hand the scFvs selective to C7 bound near the tail end region of the CTD, nowhere near the CaM binding sites (IQ motif and EF hand); as expected their binding was unaffected by the presence of CaM. Of the hundreds of positive hits only a handful were tested under whole cell patch clamp and these did not show very drastic effects on the channel gating. Clones that show effects could have various downstream application ranging from therapeutics, diagnostics, and research. For instance, fluorescent proteins like thermal green, mCherry etc can be added between the V_H and V_L chain without affecting its affinity and specificity[329]. These fluorescent scFvs can then be used for simple fluorescent assay to detect binding. Moreover, scFvs with therapeutic potential could be examined for use as intrabodies, using intracellular drug delivery like cell penetrating peptides (CPPs), carbon dots and nanomicelles. CPPs are small strings of amino acid sequence which when added to another molecule helps it to cross the cell membrane, with more than 1700 CPPs that exist which have been experimentally validated[330]. Most widely studied examples include the protein derived TAT peptide (GRKKRRQRRRPPQ), synthetic 8-lysines (KKKKKKKK), chimeric Pep-1 HIV-reverse transcriptase/SV40 T-antigen (KETWWETWWTEWSQPKKKRKV), synthetic MAP (KLALKLALKALKAALKLA) etc[331–334]. Many CPP-conjugated drugs are already under clinical trials currently for treatments against cancer, heart disease etc[335,336].

Nevertheless, for future work, more clones could be purified and tested. Manipulations of the CDR region of scFv, through rational protein design (site-directed mutagenesis) or directed evolution (error prone PCR) could be employed to enhance binding affinity to the CTDs. Additionally, for the C7 specific scFv clones that bound close to the tail end of the CTD, these could be used to stabilize this flexible disordered structure, which were predicted using *in silico* structure prediction, and help in structure determination using x-ray crystallography.

References

1. Beneski DA, Catterall WA. Covalent labeling of protein components of the sodium channel with a photoactivable derivative of scorpion toxin. *Proc Natl Acad Sci*. 1980;77(1):639-643. doi:10.1073/pnas.77.1.639
2. L. HA, F. HA. A quantitative description of membrane current and its application to conduction and excitation in nerve. *J Physiol*. 1952;117(4):500-544. doi:10.1113/jphysiol.1952.sp004764
3. Goldin AL. Diversity of mammalian voltage-gated sodium channels. *Ann N Y Acad Sci*. 1999;868:38-50.
4. Dib-Hajj S, Black JA, Cummins TR, Waxman SG. NaN/Nav1.9: a sodium channel with unique properties. *Trends Neurosci*. 2002;25(5):253-259.
5. Rabert DK, Koch BD, Ilnicka M, et al. A tetrodotoxin-resistant voltage-gated sodium channel from human dorsal root ganglia, hPN3/SCN10A. *Pain*. 1998;78(2):107-114.
6. Catterall WA, Goldin AL, Waxman SG. International Union of Pharmacology. XLVII. Nomenclature and structure-function relationships of voltage-gated sodium channels. *Pharmacol Rev*. 2005;57(4):397-409. doi:10.1124/pr.57.4.4
7. Watanabe E, Fujikawa A, Matsunaga H, et al. Nav2/NaG channel is involved in control of salt-intake behavior in the CNS. *J Neurosci*. 2000;20(20):7743-7751. doi:10.1523/JNEUROSCI.20-20-07743.2000
8. George ALJ, Knittle TJ, Tamkun MM. Molecular cloning of an atypical voltage-gated sodium channel expressed in human heart and uterus: evidence for a distinct gene family. *Proc Natl Acad Sci U S A*. 1992;89(11):4893-4897. doi:10.1073/pnas.89.11.4893
9. Felipe A, Knittle TJ, Doyle KL, Tamkun MM. Primary structure and differential expression during development and pregnancy of a novel voltage-gated sodium channel in the mouse. *J Biol Chem*. 1994;269(48):30125-30131.
10. Yu FH, Catterall WA. Overview of the voltage-gated sodium channel family. *Genome Biol*. 2003;4(3):207. doi:10.1186/gb-2003-4-3-207
11. Anderson PA V, Greenberg RM. Phylogeny of ion channels: clues to structure and function. *Comp Biochem Physiol Part B Biochem Mol Biol*. 2001;129(1):17-28. doi:https://doi.org/10.1016/S1096-4959(01)00376-1

12. Ren D, Navarro B, Xu H, Yue L, Shi Q, Clapham DE. A prokaryotic voltage-gated sodium channel. *Science*. 2001;294(5550):2372-2375. doi:10.1126/science.1065635
13. Yau KW. Cyclic nucleotide-gated channels: an expanding new family of ion channels. *Proc Natl Acad Sci U S A*. 1994;91(9):3481-3483. doi:10.1073/pnas.91.9.3481
14. Catterall WA. From Ionic Currents to Molecular Mechanisms: The Structure and Function of Voltage-Gated Sodium Channels. *Neuron*. 2000;26(1):13-25. doi:https://doi.org/10.1016/S0896-6273(00)81133-2
15. Goldin AL, Barchi RL, Caldwell JH, et al. Nomenclature of Voltage-Gated Sodium Channels. *Neuron*. 2000;28(2):365-368. doi:https://doi.org/10.1016/S0896-6273(00)00116-1
16. Sivilotti L, Okuse K, Akopian AN, Moss S, Wood JN. A single serine residue confers tetrodotoxin insensitivity on the rat sensory-neuron-specific sodium channel SNS. *FEBS Lett*. 1997;409(1):49-52. doi:10.1016/s0014-5793(97)00479-1
17. Payandeh J, Gamal El-Din TM, Scheuer T, Zheng N, Catterall WA. Crystal structure of a voltage-gated sodium channel in two potentially inactivated states. *Nature*. 2012;486(7401):135-139. doi:10.1038/nature11077
18. McCusker EC, Bagneris C, Naylor CE, et al. Structure of a bacterial voltage-gated sodium channel pore reveals mechanisms of opening and closing. *Nat Commun*. 2012;3:1102. doi:10.1038/ncomms2077
19. Koishi R, Xu H, Ren D, et al. A superfamily of voltage-gated sodium channels in bacteria. *J Biol Chem*. 2004;279(10):9532-9538. doi:10.1074/jbc.M313100200
20. Liebeskind BJ, Hillis DM, Zakon HH. Independent acquisition of sodium selectivity in bacterial and animal sodium channels. *Curr Biol*. 2013;23(21):R948-9. doi:10.1016/j.cub.2013.09.025
21. Gamal El-Din TM, Scheuer T, Catterall WA. Tracking S4 movement by gating pore currents in the bacterial sodium channel NaChBac. *J Gen Physiol*. 2014;144(2):147-157. doi:10.1085/jgp.201411210
22. Irie K, Kitagawa K, Nagura H, Imai T, Shimomura T, Fujiyoshi Y. Comparative study of the gating motif and C-type inactivation in prokaryotic voltage-gated sodium channels. *J Biol Chem*. 2010;285(6):3685-3694.

doi:10.1074/jbc.M109.057455

23. Shen H, Zhou Q, Pan X, Li Z, Wu J, Yan N. Structure of a eukaryotic voltage-gated sodium channel at near-atomic resolution. *Science*. 2017;355(6328). doi:10.1126/science.aal4326
24. Yan Z, Zhou Q, Wang L, et al. Structure of the Nav1.4-beta1 Complex from Electric Eel. *Cell*. 2017;170(3):470-482.e11. doi:10.1016/j.cell.2017.06.039
25. Xiaojing P, Zhangqiang L, Qiang Z, et al. Structure of the human voltage-gated sodium channel Nav1.4 in complex with ß1. *Science (80-)*. 2018;362(6412):eaau2486. doi:10.1126/science.aau2486
26. Jiang D, Tonggu L, Gamal El-Din TM, et al. Structural basis for voltage-sensor trapping of the cardiac sodium channel by a deathstalker scorpion toxin. *Nat Commun*. 2021;12(1):128. doi:10.1038/s41467-020-20078-3
27. Jiang D, Shi H, Tonggu L, et al. Structure of the Cardiac Sodium Channel. *Cell*. 2020;180(1):122-134.e10. doi:10.1016/j.cell.2019.11.041
28. Shen H, Liu D, Wu K, Lei J, Yan N. Structures of human Na(v)1.7 channel in complex with auxiliary subunits and animal toxins. *Science*. 2019;363(6433):1303-1308. doi:10.1126/science.aaw2493
29. Chiamvimonvat N, Perez-Garcia MT, Tomaselli GF, Marban E. Control of ion flux and selectivity by negatively charged residues in the outer mouth of rat sodium channels. *J Physiol*. 1996;491 (Pt 1:51-59.
30. Favre I, Moczydlowski E, Schild L. On the structural basis for ionic selectivity among Na+, K+, and Ca2+ in the voltage-gated sodium channel. *Biophys J*. 1996;71(6):3110-3125. doi:10.1016/S0006-3495(96)79505-X
31. Yarov-Yarovoy V, DeCaen PG, Westenbroek RE, et al. Structural basis for gating charge movement in the voltage sensor of a sodium channel. *Proc Natl Acad Sci U S A*. 2012;109(2):E93-102. doi:10.1073/pnas.1118434109
32. Stuhmer W, Conti F, Suzuki H, et al. Structural parts involved in activation and inactivation of the sodium channel. *Nature*. 1989;339(6226):597-603. doi:10.1038/339597a0
33. Guy HR, Seetharamulu P. Molecular model of the action potential sodium channel. *Proc Natl Acad Sci U S A*. 1986;83(2):508-512. doi:10.1073/pnas.83.2.508
34. Catterall WA. Molecular properties of voltage-sensitive sodium channels. *Annu Rev Biochem*. 1986;55:953-985. doi:10.1146/annurev.bi.55.070186.004513

35. Clairfeuille T, Xu H, Koth CM, Payandeh J. Voltage-gated sodium channels viewed through a structural biology lens. *Curr Opin Struct Biol*. 2017;45:74-84. doi:10.1016/j.sbi.2016.11.022
36. DeCaen PG, Yarov-Yarovoy V, Zhao Y, Scheuer T, Catterall WA. Disulfide locking a sodium channel voltage sensor reveals ion pair formation during activation. *Proc Natl Acad Sci*. 2008;105(39):15142 LP - 15147. doi:10.1073/pnas.0806486105
37. Payandeh J, Scheuer T, Zheng N, Catterall WA. The crystal structure of a voltage-gated sodium channel. *Nature*. 2011;475(7356):353-358. doi:10.1038/nature10238
38. Ahern CA, Payandeh J, Bosmans F, Chanda B. The hitchhiker's guide to the voltage-gated sodium channel galaxy. *J Gen Physiol*. 2016;147(1):1-24. doi:10.1085/jgp.201511492
39. Villalba-Galea CA, Sandtner W, Starace DM, Bezanilla F. S4-based voltage sensors have three major conformations. *Proc Natl Acad Sci*. 2008;105(46):17600 LP - 17607. doi:10.1073/pnas.0807387105
40. Peyser A, Nonner W. The sliding-helix voltage sensor: mesoscale views of a robust structure-function relationship. *Eur Biophys J*. 2012;41(9):705-721. doi:10.1007/s00249-012-0847-z
41. Capes DL, Goldschen-Ohm MP, Arcisio-Miranda M, Bezanilla F, Chanda B. Domain IV voltage-sensor movement is both sufficient and rate limiting for fast inactivation in sodium channels. *J Gen Physiol*. 2013;142(2):101-112. doi:10.1085/jgp.201310998
42. Vilin YY, Ruben PC. Slow inactivation in voltage-gated sodium channels: molecular substrates and contributions to channelopathies. *Cell Biochem Biophys*. 2001;35(2):171-190. doi:10.1385/CBB:35:2:171
43. Bennett ES. Isoform-specific effects of sialic acid on voltage-dependent Na+ channel gating: functional sialic acids are localized to the S5-S6 loop of domain I. *J Physiol*. 2002;538(Pt 3):675-690.
44. Bennett E, Urcan MS, Tinkle SS, Koszowski AG, Levinson SR. Contribution of sialic acid to the voltage dependence of sodium channel gating. A possible electrostatic mechanism. *J Gen Physiol*. 1997;109(3):327-343. doi:10.1085/jgp.109.3.327
45. Tyrrell L, Renganathan M, Dib-Hajj SD, Waxman SG. Glycosylation alters

steady-state inactivation of sodium channel Nav1.9/NaN in dorsal root ganglion neurons and is developmentally regulated. *J Neurosci*. 2001;21(24):9629-9637. doi:10.1523/JNEUROSCI.21-24-09629.2001

46. Namadurai S, Balasuriya D, Rajappa R, et al. Crystal structure and molecular imaging of the Nav channel beta3 subunit indicates a trimeric assembly. *J Biol Chem*. 2014;289(15):10797-10811. doi:10.1074/jbc.M113.527994
47. Malhotra JD, Thyagarajan V, Chen C, Isom LL. Tyrosine-phosphorylated and nonphosphorylated sodium channel beta1 subunits are differentially localized in cardiac myocytes. *J Biol Chem*. 2004;279(39):40748-40754. doi:10.1074/jbc.M407243200
48. Namadurai S, Yereddi NR, Cusdin FS, Huang CLH, Chirgadze DY, Jackson AP. A new look at sodium channel beta subunits. *Open Biol*. 2015;5(1):140192. doi:10.1098/rsob.140192
49. Brackenbury WJ, Isom LL. Na Channel beta Subunits: Overachievers of the Ion Channel Family. *Front Pharmacol*. 2011;2:53. doi:10.3389/fphar.2011.00053
50. Das S, Gilchrist J, Bosmans F, Van Petegem F. Binary architecture of the Nav1.2-beta2 signaling complex. *Elife*. 2016;5. doi:10.7554/eLife.10960
51. Gilchrist J, Das S, Van Petegem F, Bosmans F. Crystallographic insights into sodium-channel modulation by the beta4 subunit. *Proc Natl Acad Sci U S A*. 2013;110(51):E5016-24. doi:10.1073/pnas.1314557110
52. Makita N, Bennett PB, George Jr. AL. Molecular Determinants of ß₁ Subunit-Induced Gating Modulation in Voltage-Dependent Na⁺ Channels. *J Neurosci*. 1996;16(22):7117 LP - 7127. http://www.jneurosci.org/content/16/22/7117.abstract.
53. Clatot J, Hoshi M, Wan X, et al. Voltage-gated sodium channels assemble and gate as dimers. *Nat Commun*. 2017;8(1):2077. doi:10.1038/s41467-017-02262-0
54. Richards S, Aziz N, Bale S, et al. Standards and guidelines for the interpretation of sequence variants: a joint consensus recommendation of the American College of Medical Genetics and Genomics and the Association for Molecular Pathology. *Genet Med Off J Am Coll Med Genet*. 2015;17(5):405-424. doi:10.1038/gim.2015.30
55. Hurst DL. Epidemiology of severe myoclonic epilepsy of infancy. *Epilepsia*.

1990;31(4):397-400. doi:10.1111/j.1528-1157.1990.tb05494.x

56. Cavazzuti GB, Ferrari P, Lalla M. Follow-up study of 482 cases with convulsive disorders in the first year of life. *Dev Med Child Neurol*. 1984;26(4):425-437. doi:10.1111/j.1469-8749.1984.tb04467.x
57. Dravet C, Bureau M, Oguni H, Fukuyama Y, Cokar O. Severe myoclonic epilepsy in infancy: Dravet syndrome. *Adv Neurol*. 2005;95:71-102.
58. Wolff M, Cassé-Perrot C, Dravet C. Severe myoclonic epilepsy of infants (Dravet syndrome): natural history and neuropsychological findings. *Epilepsia*. 2006;47 Suppl 2:45-48. doi:10.1111/j.1528-1167.2006.00688.x
59. Claes L, Ceulemans B, Audenaert D, et al. De novo SCN1A mutations are a major cause of severe myoclonic epilepsy of infancy. *Hum Mutat*. 2003;21(6):615-621. doi:10.1002/humu.10217
60. Vadlamudi L, Dibbens LM, Lawrence KM, et al. Timing of de novo mutagenesis--a twin study of sodium-channel mutations. *N Engl J Med*. 2010;363(14):1335-1340. doi:10.1056/NEJMoa0910752
61. Patino GA, Claes LRF, Lopez-Santiago LF, et al. A functional null mutation of SCN1B in a patient with Dravet syndrome. *J Neurosci*. 2009;29(34):10764-10778. doi:10.1523/JNEUROSCI.2475-09.2009
62. Shi X, Yasumoto S, Nakagawa E, Fukasawa T, Uchiya S, Hirose S. Missense mutation of the sodium channel gene SCN2A causes Dravet syndrome. *Brain Dev*. 2009;31(10):758-762. doi:10.1016/j.braindev.2009.08.009
63. Syrbe S, Hedrich UBS, Riesch E, et al. De novo loss- or gain-of-function mutations in KCNA2 cause epileptic encephalopathy. *Nat Genet*. 2015;47(4):393-399. doi:10.1038/ng.3239
64. Thomas RH, Zhang LM, Carvill GL, et al. CHD2 myoclonic encephalopathy is frequently associated with self-induced seizures. *Neurology*. 2015;84(9):951-958. doi:10.1212/WNL.0000000000001305
65. Nava C, Dalle C, Rastetter A, et al. De novo mutations in HCN1 cause early infantile epileptic encephalopathy. *Nat Genet*. 2014;46(6):640-645. doi:10.1038/ng.2952
66. Carvill GL, Weckhuysen S, McMahon JM, et al. GABRA1 and STXBP1: novel genetic causes of Dravet syndrome. *Neurology*. 2014;82(14):1245-1253. doi:10.1212/WNL.0000000000000291
67. Shen D, Hernandez CC, Shen W, et al. De novo GABRG2 mutations associated

with epileptic encephalopathies. *Brain*. 2017;140(1):49-67. doi:10.1093/brain/aww272

68. Trivisano M, Pietrafusa N, Ciommo V di, et al. PCDH19-related epilepsy and Dravet Syndrome: Face-off between two early-onset epilepsies with fever sensitivity. *Epilepsy Res*. 2016;125:32-36. doi:10.1016/j.eplepsyres.2016.05.015
69. Mulley JC, Hodgson B, McMahon JM, et al. Role of the sodium channel SCN9A in genetic epilepsy with febrile seizures plus and Dravet syndrome. *Epilepsia*. 2013;54(9):e122-6. doi:10.1111/epi.12323
70. Larsen J, Carvill GL, Gardella E, et al. The phenotypic spectrum of SCN8A encephalopathy. *Neurology*. 2015;84(5):480-489. doi:10.1212/WNL.0000000000001211
71. Ohmori I, Ouchida M, Ohtsuka Y, Oka E, Shimizu K. Significant correlation of the SCN1A mutations and severe myoclonic epilepsy in infancy. *Biochem Biophys Res Commun*. 2002;295(1):17-23.
72. Yu FH, Mantegazza M, Westenbroek RE, et al. Reduced sodium current in GABAergic interneurons in a mouse model of severe myoclonic epilepsy in infancy. *Nat Neurosci*. 2006;9(9):1142-1149. doi:10.1038/nn1754
73. Han S, Tai C, Westenbroek RE, et al. Autistic-like behaviour in Scn1a+/- mice and rescue by enhanced GABA-mediated neurotransmission. *Nature*. 2012;489(7416):385-390. doi:10.1038/nature11356
74. Brugada R, Campuzano O, Sarquella-Brugada G, Brugada J, Brugada P. Brugada syndrome. *Methodist Debakey Cardiovasc J*. 2014;10(1):25-28.
75. Brugada P, Brugada J. Right bundle branch block, persistent ST segment elevation and sudden cardiac death: a distinct clinical and electrocardiographic syndrome. A multicenter report. *J Am Coll Cardiol*. 1992;20(6):1391-1396.
76. Schwartz PJ, Ackerman MJ, Antzelevitch C, et al. Inherited cardiac arrhythmias. *Nat Rev Dis Prim*. 2020;6(1):58. doi:10.1038/s41572-020-0188-7
77. Boukens BJ, Sylva M, de Gier-de Vries C, et al. Reduced sodium channel function unmasks residual embryonic slow conduction in the adult right ventricular outflow tract. *Circ Res*. 2013;113(2):137-141. doi:10.1161/CIRCRESAHA.113.301565
78. Di Diego JM, Sun ZQ, Antzelevitch C. I(to) and action potential notch are

smaller in left vs. right canine ventricular epicardium. *Am J Physiol*. 1996;271(2 Pt 2):H548-61. doi:10.1152/ajpheart.1996.271.2.H548

79. Smits JPP, Eckardt L, Probst V, et al. Genotype-phenotype relationship in Brugada syndrome: electrocardiographic features differentiate SCN5A-related patients from non-SCN5A-related patients. *J Am Coll Cardiol*. 2002;40(2):350-356. doi:10.1016/s0735-1097(02)01962-9
80. Kapplinger JD, Tester DJ, Alders M, et al. An international compendium of mutations in the SCN5A-encoded cardiac sodium channel in patients referred for Brugada syndrome genetic testing. *Hear Rhythm*. 2010;7(1):33-46. doi:10.1016/j.hrthm.2009.09.069
81. Wilde AAM, Antzelevitch C, Borggrefe M, et al. Proposed diagnostic criteria for the Brugada syndrome. *Eur Heart J*. 2002;23(21):1648-1654. doi:10.1053/euhj.2002.3382
82. Antzelevitch C, Yan G-X, Ackerman MJ, et al. J-Wave syndromes expert consensus conference report: Emerging concepts and gaps in knowledge. *Hear Rhythm*. 2016;13(10):e295-324. doi:10.1016/j.hrthm.2016.05.024
83. Barajas-Martínez HM, Hu D, Cordeiro JM, et al. Lidocaine-induced Brugada syndrome phenotype linked to a novel double mutation in the cardiac sodium channel. *Circ Res*. 2008;103(4):396-404. doi:10.1161/CIRCRESAHA.108.172619
84. Belhassen B. Management of Brugada Syndrome 2016: Should All High Risk Patients Receive an ICD? Alternatives to Implantable Cardiac Defibrillator Therapy for Brugada Syndrome. *Circ Arrhythm Electrophysiol*. 2016;9(11). doi:10.1161/CIRCEP.116.004185
85. Nademanee K, Veerakul G, Chandanamattha P, et al. Prevention of ventricular fibrillation episodes in Brugada syndrome by catheter ablation over the anterior right ventricular outflow tract epicardium. *Circulation*. 2011;123(12):1270-1279. doi:10.1161/CIRCULATIONAHA.110.972612
86. Hu D, Barajas-Martinez H, Burashnikov E, et al. A mutation in the beta 3 subunit of the cardiac sodium channel associated with Brugada ECG phenotype. *Circ Cardiovasc Genet*. 2009;2(3):270-278. doi:10.1161/CIRCGENETICS.108.829192
87. Olesen MS, Jespersen T, Nielsen JB, et al. Mutations in sodium channel beta-subunit SCN3B are associated with early-onset lone atrial fibrillation. *Cardiovasc Res*. 2011;89(4):786-793. doi:10.1093/cvr/cvq348
88. Barc J, Tadros R, Glinge C, et al. Genome-wide association analyses identify

new Brugada syndrome risk loci and highlight a new mechanism of sodium channel regulation in disease susceptibility. *Nat Genet*. 2022;54(3):232-239. doi:10.1038/s41588-021-01007-6

89. Papadatos GA, Wallerstein PMR, Head CEG, et al. Slowed conduction and ventricular tachycardia after targeted disruption of the cardiac sodium channel gene Scn5a. *Proc Natl Acad Sci U S A*. 2002;99(9):6210-6215. doi:10.1073/pnas.082121299
90. Martin CA, Zhang Y, Grace AA, Huang CL-H. In vivo studies of Scn5a+/- mice modeling Brugada syndrome demonstrate both conduction and repolarization abnormalities. *J Electrocardiol*. 2010;43(5):433-439. doi:10.1016/j.jelectrocard.2010.05.015
91. Huang CL-H. Murine Electrophysiological Models of Cardiac Arrhythmogenesis. *Physiol Rev*. 2017;97(1):283-409. doi:10.1152/physrev.00007.2016
92. Hong K, Brugada J, Oliva A, et al. Value of electrocardiographic parameters and ajmaline test in the diagnosis of Brugada syndrome caused by SCN5A mutations. *Circulation*. 2004;110(19):3023-3027. doi:10.1161/01.CIR.0000144299.17008.07
93. Fish JM, Antzelevitch C. Cellular and ionic basis for the sex-related difference in the manifestation of the Brugada syndrome and progressive conduction disease phenotypes. *J Electrocardiol*. 2003;36 Suppl:173-179. doi:10.1016/j.jelectrocard.2003.09.054
94. Davis RP, Casini S, van den Berg CW, et al. Cardiomyocytes derived from pluripotent stem cells recapitulate electrophysiological characteristics of an overlap syndrome of cardiac sodium channel disease. *Circulation*. 2012;125(25):3079-3091. doi:10.1161/CIRCULATIONAHA.111.066092
95. Selga E, Sendfeld F, Martinez-Moreno R, et al. Sodium channel current loss of function in induced pluripotent stem cell-derived cardiomyocytes from a Brugada syndrome patient. *J Mol Cell Cardiol*. 2018;114:10-19. doi:10.1016/j.yjmcc.2017.10.002
96. Ma D, Liu Z, Loh LJ, et al. Identification of an I(Na)-dependent and I(to)-mediated proarrhythmic mechanism in cardiomyocytes derived from pluripotent stem cells of a Brugada syndrome patient. *Sci Rep*. 2018;8(1):11246. doi:10.1038/s41598-018-29574-5
97. Liang P, Sallam K, Wu H, et al. Patient-Specific and Genome-Edited Induced

Pluripotent Stem Cell-Derived Cardiomyocytes Elucidate Single-Cell Phenotype of Brugada Syndrome. *J Am Coll Cardiol*. 2016;68(19):2086-2096. doi:10.1016/j.jacc.2016.07.779

98. Maury P, Moreau A, Hidden-Lucet F, et al. Novel SCN5A mutations in two families with "Brugada-like" ST elevation in the inferior leads and conduction disturbances. *J Interv Card Electrophysiol*. 2013;37(2):131-140. doi:10.1007/s10840-013-9805-7
99. Núñez L, Barana A, Amorós I, et al. p.D1690N Nav1.5 rescues p.G1748D mutation gating defects in a compound heterozygous Brugada syndrome patient. *Hear Rhythm*. 2013;10(2):264-272. doi:10.1016/j.hrthm.2012.10.025
100. Valdivia CR, Tester DJ, Rok BA, et al. A trafficking defective, Brugada syndrome-causing SCN5A mutation rescued by drugs. *Cardiovasc Res*. 2004;62(1):53-62. doi:10.1016/j.cardiores.2004.01.022
101. Abriel H, Cabo C, Wehrens XH, et al. Novel arrhythmogenic mechanism revealed by a long-QT syndrome mutation in the cardiac Na(+) channel. *Circ Res*. 2001;88(7):740-745.
102. Rivolta I, Abriel H, Tateyama M, et al. Inherited Brugada and long QT-3 syndrome mutations of a single residue of the cardiac sodium channel confer distinct channel and clinical phenotypes. *J Biol Chem*. 2001;276(33):30623-30630. doi:10.1074/jbc.M104471200
103. Priori SG, Napolitano C, Gasparini M, et al. Natural history of Brugada syndrome: insights for risk stratification and management. *Circulation*. 2002;105(11):1342-1347.
104. Musa H, Kline CF, Sturm AC, et al. SCN5A variant that blocks fibroblast growth factor homologous factor regulation causes human arrhythmia. *Proc Natl Acad Sci U S A*. 2015;112(40):12528-12533. doi:10.1073/pnas.1516430112
105. Chen Q, Kirsch GE, Zhang D, et al. Genetic basis and molecular mechanism for idiopathic ventricular fibrillation. *Nature*. 1998;392(6673):293-296. doi:10.1038/32675
106. Meregalli PG, Tan HL, Probst V, et al. Type of SCN5A mutation determines clinical severity and degree of conduction slowing in loss-of-function sodium channelopathies. *Hear Rhythm*. 2009;6(3):341-348. doi:10.1016/j.hrthm.2008.11.009
107. Wang DW, Viswanathan PC, Balser JR, George ALJ, Benson DW. Clinical,

genetic, and biophysical characterization of SCN5A mutations associated with atrioventricular conduction block. *Circulation*. 2002;105(3):341-346.

108. Saito YA, Strege PR, Tester DJ, et al. Sodium channel mutation in irritable bowel syndrome: evidence for an ion channelopathy. *Am J Physiol Gastrointest Liver Physiol*. 2009;296(2):G211-8. doi:10.1152/ajpgi.90571.2008
109. Wagnon JL, Mencacci NE, Barker BS, et al. Partial loss-of-function of sodium channel SCN8A in familial isolated myoclonus. *Hum Mutat*. 2018;39(7):965-969. doi:10.1002/humu.23547
110. Zuberi SM, Brunklaus A, Birch R, Reavey E, Duncan J, Forbes GH. Genotype-phenotype associations in SCN1A-related epilepsies. *Neurology*. 2011;76(7):594-600. doi:10.1212/WNL.0b013e31820c309b
111. Ohba C, Kato M, Takahashi S, et al. Early onset epileptic encephalopathy caused by de novo SCN8A mutations. *Epilepsia*. 2014;55(7):994-1000. doi:10.1111/epi.12668
112. Veeramah KR, O'Brien JE, Meisler MH, et al. De novo pathogenic SCN8A mutation identified by whole-genome sequencing of a family quartet affected by infantile epileptic encephalopathy and SUDEP. *Am J Hum Genet*. 2012;90(3):502-510. doi:10.1016/j.ajhg.2012.01.006
113. Cox JJ, Sheynin J, Shorer Z, et al. Congenital insensitivity to pain: novel SCN9A missense and in-frame deletion mutations. *Hum Mutat*. 2010;31(9):E1670-86. doi:10.1002/humu.21325
114. Annesi G, Gambardella A, Carrideo S, et al. Two novel SCN1A missense mutations in generalized epilepsy with febrile seizures plus. *Epilepsia*. 2003;44(9):1257-1258. doi:10.1046/j.1528-1157.2003.22503.x
115. Sun H, Zhang Y, Liang J, et al. SCN1A, SCN1B, and GABRG2 gene mutation analysis in Chinese families with generalized epilepsy with febrile seizures plus. *J Hum Genet*. 2008;53(8):769-774. doi:10.1007/s10038-008-0306-y
116. Orrico A, Galli L, Grosso S, et al. Mutational analysis of the SCN1A, SCN1B and GABRG2 genes in 150 Italian patients with idiopathic childhood epilepsies. *Clin Genet*. 2009;75(6):579-581. doi:10.1111/j.1399-0004.2009.01155.x
117. Dimova PS, Yordanova I, Bojinova V, Jordanova A, Kremenski I. Generalized epilepsy with febrile seizures plus: novel SCN1A mutation. *Pediatr Neurol*. 2010;42(2):137-140. doi:10.1016/j.pediatrneurol.2009.09.007
118. Pineda-Trujillo N, Carrizosa J, Cornejo W, et al. A novel SCN1A mutation

associated with severe GEFS+ in a large South American pedigree. *Seizure*. 2005;14(2):123-128. doi:10.1016/j.seizure.2004.12.007

119. Depienne C, Trouillard O, Saint-Martin C, et al. Spectrum of SCN1A gene mutations associated with Dravet syndrome: analysis of 333 patients. *J Med Genet*. 2009;46(3):183-191. doi:10.1136/jmg.2008.062323
120. Miyama S, Goto T, Inoue Y, Yamakawa K. Monozygotic twins with severe myoclonic epilepsy in infancy discordant for clinical features. *Pediatr Neurol*. 2008;39(2):120-122. doi:10.1016/j.pediatrneurol.2008.04.003
121. Nabbout R, Gennaro E, Dalla Bernardina B, et al. Spectrum of SCN1A mutations in severe myoclonic epilepsy of infancy. *Neurology*. 2003;60(12):1961-1967. doi:10.1212/01.wnl.0000069463.41870.2f
122. Mancardi MM, Striano P, Gennaro E, et al. Familial occurrence of febrile seizures and epilepsy in severe myoclonic epilepsy of infancy (SMEI) patients with SCN1A mutations. *Epilepsia*. 2006;47(10):1629-1635. doi:10.1111/j.1528-1167.2006.00641.x
123. Wang J, Shi X, Kurahashi H, et al. Prevalence of SCN1A mutations in children with suspected Dravet syndrome and intractable childhood epilepsy. *Epilepsy Res*. 2012;102(3):195-200. doi:10.1016/j.eplepsyres.2012.06.006
124. Lemke JR, Riesch E, Scheurenbrand T, et al. Targeted next generation sequencing as a diagnostic tool in epileptic disorders. *Epilepsia*. 2012;53(8):1387-1398. doi:10.1111/j.1528-1167.2012.03516.x
125. Marini C, Mei D, Temudo T, et al. Idiopathic epilepsies with seizures precipitated by fever and SCN1A abnormalities. *Epilepsia*. 2007;48(9):1678-1685. doi:10.1111/j.1528-1167.2007.01122.x
126. Fujiwara T, Sugawara T, Mazaki-Miyazaki E, et al. Mutations of sodium channel alpha subunit type 1 (SCN1A) in intractable childhood epilepsies with frequent generalized tonic-clonic seizures. *Brain*. 2003;126(Pt 3):531-546. doi:10.1093/brain/awg053
127. Carvill GL, Heavin SB, Yendle SC, et al. Targeted resequencing in epileptic encephalopathies identifies de novo mutations in CHD2 and SYNGAP1. *Nat Genet*. 2013;45(7):825-830. doi:10.1038/ng.2646
128. Zucca C, Redaelli F, Epifanio R, et al. Cryptogenic epileptic syndromes related to SCN1A: twelve novel mutations identified. *Arch Neurol*. 2008;65(4):489-494. doi:10.1001/archneur.65.4.489

129. Ohmori I, Kahlig KM, Rhodes TH, Wang DW, George ALJ. Nonfunctional SCN1A is common in severe myoclonic epilepsy of infancy. *Epilepsia*. 2006;47(10):1636-1642. doi:10.1111/j.1528-1167.2006.00643.x
130. Sun H, Zhang Y, Liu X, et al. Analysis of SCN1A mutation and parental origin in patients with Dravet syndrome. *J Hum Genet*. 2010;55(7):421-427. doi:10.1038/jhg.2010.39
131. Le SV, Le PHT, Le TK Van, Kieu Huynh TT, Hang Do TT. A mutation in GABRB3 associated with Dravet syndrome. *Am J Med Genet A*. 2017;173(8):2126-2131. doi:10.1002/ajmg.a.38282
132. Fukuma G, Oguni H, Shirasaka Y, et al. Mutations of neuronal voltage-gated Na+ channel alpha 1 subunit gene SCN1A in core severe myoclonic epilepsy in infancy (SMEI) and in borderline SMEI (SMEB). *Epilepsia*. 2004;45(2):140-148. doi:10.1111/j.0013-9580.2004.15103.x
133. Berkovic SF, Harkin L, McMahon JM, et al. De-novo mutations of the sodium channel gene SCN1A in alleged vaccine encephalopathy: a retrospective study. *Lancet Neurol*. 2006;5(6):488-492. doi:10.1016/S1474-4422(06)70446-X
134. Harkin LA, McMahon JM, Iona X, et al. The spectrum of SCN1A-related infantile epileptic encephalopathies. *Brain*. 2007;130(Pt 3):843-852. doi:10.1093/brain/awm002
135. Kodera H, Kato M, Nord AS, et al. Targeted capture and sequencing for detection of mutations causing early onset epileptic encephalopathy. *Epilepsia*. 2013;54(7):1262-1269. doi:10.1111/epi.12203
136. Depienne C, Trouillard O, Gourfinkel-An I, et al. Mechanisms for variable expressivity of inherited SCN1A mutations causing Dravet syndrome. *J Med Genet*. 2010;47(6):404-410. doi:10.1136/jmg.2009.074328
137. Stefanaki E, Aggelakou V, Orfanou M, Kokori E, Boutoufianakis S. Epilepsy with a de novo missense mutation in the sodium channel a1 subunit: a case report. *Acta Paediatr*. 2006;95(12):1703-1706. doi:10.1080/08035250600778628
138. Heron SE, Scheffer IE, Iona X, et al. De novo SCN1A mutations in Dravet syndrome and related epileptic encephalopathies are largely of paternal origin. *J Med Genet*. 2010;47(2):137-141. doi:10.1136/jmg.2008.065912
139. Okumura A, Uematsu M, Imataka G, et al. Acute encephalopathy in children with Dravet syndrome. *Epilepsia*. 2012;53(1):79-86. doi:10.1111/j.1528-1167.2011.03311.x

140. Herini ES, Gunadi, Harahap ISK, et al. Generalized epilepsy with febrile seizures plus (GEFS+) spectrum: clinical manifestations and SCN1A mutations in Indonesian patients. *Epilepsy Res*. 2010;90(1-2):132-139. doi:10.1016/j.eplepsyres.2010.04.003
141. Herini ES, Gunadi, van Kempen MJA, et al. Novel SCN1A mutations in Indonesian patients with severe myoclonic epilepsy in infancy. *Pediatr Int*. 2010;52(2):234-239. doi:10.1111/j.1442-200X.2009.02916.x
142. Rhodes TH, Vanoye CG, Ohmori I, Ogiwara I, Yamakawa K, George ALJ. Sodium channel dysfunction in intractable childhood epilepsy with generalized tonic-clonic seizures. *J Physiol*. 2005;569(Pt 2):433-445. doi:10.1113/jphysiol.2005.094326
143. Nicita F, Spalice A, Papetti L, et al. Genotype-phenotype correlations in a group of 15 SCN1A-mutated Italian patients with GEFS+ spectrum (seizures plus, classical and borderline severe myoclonic epilepsy of infancy). *J Child Neurol*. 2010;25(11):1369-1376. doi:10.1177/0883073810365737
144. Lauxmann S, Verbeek NE, Liu Y, et al. Relationship of electrophysiological dysfunction and clinical severity in SCN2A-related epilepsies. *Hum Mutat*. 2018;39(12):1942-1956. doi:10.1002/humu.23619
145. Nakamura K, Kato M, Osaka H, et al. Clinical spectrum of SCN2A mutations expanding to Ohtahara syndrome. *Neurology*. 2013;81(11):992-998. doi:10.1212/WNL.0b013e3182a43e57
146. Howell KB, McMahon JM, Carvill GL, et al. SCN2A encephalopathy: A major cause of epilepsy of infancy with migrating focal seizures. *Neurology*. 2015;85(11):958-966. doi:10.1212/WNL.0000000000001926
147. Ptacek LJ, Gouw L, Kwieciński H, et al. Sodium channel mutations in paramyotonia congenita and hyperkalemic periodic paralysis. *Ann Neurol*. 1993;33(3):300-307. doi:10.1002/ana.410330312
148. Matthews E, Tan S V, Fialho D, et al. What causes paramyotonia in the United Kingdom? Common and new SCN4A mutations revealed. *Neurology*. 2008;70(1):50-53. doi:10.1212/01.wnl.0000287069.21162.94
149. Tsujino A, Maertens C, Ohno K, et al. Myasthenic syndrome caused by mutation of the SCN4A sodium channel. *Proc Natl Acad Sci U S A*. 2003;100(12):7377-7382. doi:10.1073/pnas.1230273100
150. Cordeiro JM, Barajas-Martinez H, Hong K, et al. Compound heterozygous

mutations P336L and I1660V in the human cardiac sodium channel associated with the Brugada syndrome. *Circulation*. 2006;114(19):2026-2033. doi:10.1161/CIRCULATIONAHA.106.627489

151. Vatta M, Dumaine R, Antzelevitch C, et al. Novel mutations in domain I of SCN5A cause Brugada syndrome. *Mol Genet Metab*. 2002;75(4):317-324. doi:10.1016/S1096-7192(02)00006-9
152. Pfahnl AE, Viswanathan PC, Weiss R, et al. A sodium channel pore mutation causing Brugada syndrome. *Hear Rhythm*. 2007;4(1):46-53. doi:10.1016/j.hrthm.2006.09.031
153. Makiyama T, Akao M, Tsuji K, et al. High risk for bradyarrhythmic complications in patients with Brugada syndrome caused by SCN5A gene mutations. *J Am Coll Cardiol*. 2005;46(11):2100-2106. doi:10.1016/j.jacc.2005.08.043
154. Zhang Y, Wang T, Ma A, et al. Correlations between clinical and physiological consequences of the novel mutation R878C in a highly conserved pore residue in the cardiac Na+ channel. *Acta Physiol (Oxf)*. 2008;194(4):311-323. doi:10.1111/j.1748-1716.2008.01883.x
155. Liang P, Liu W, Hu D, Li C, Tao W, Li L. [Novel SCN5A gene mutations associated with Brugada syndrome: V95I, A1649V and delF1617]. *Zhonghua Xin Xue Guan Bing Za Zhi*. 2006;34(7):616-619.
156. Makita N, Shirai N, Wang DW, et al. Cardiac Na(+) channel dysfunction in Brugada syndrome is aggravated by beta(1)-subunit. *Circulation*. 2000;101(1):54-60. doi:10.1161/01.cir.101.1.54
157. Dumaine R, Towbin JA, Brugada P, et al. Ionic mechanisms responsible for the electrocardiographic phenotype of the Brugada syndrome are temperature dependent. *Circ Res*. 1999;85(9):803-809. doi:10.1161/01.res.85.9.803
158. Chakrabarti S, Wu X, Yang Z, et al. MOG1 rescues defective trafficking of Na(v)1.5 mutations in Brugada syndrome and sick sinus syndrome. *Circ Arrhythm Electrophysiol*. 2013;6(2):392-401. doi:10.1161/CIRCEP.111.000206
159. Kapplinger JD, Tester DJ, Salisbury BA, et al. Spectrum and prevalence of mutations from the first 2,500 consecutive unrelated patients referred for the FAMILION long QT syndrome genetic test. *Hear Rhythm*. 2009;6(9):1297-1303. doi:10.1016/j.hrthm.2009.05.021
160. Tester DJ, Will ML, Haglund CM, Ackerman MJ. Compendium of cardiac channel mutations in 541 consecutive unrelated patients referred for long QT syndrome

genetic testing. *Hear Rhythm*. 2005;2(5):507-517. doi:10.1016/j.hrthm.2005.01.020

161. Millat G, Chevalier P, Restier-Miron L, et al. Spectrum of pathogenic mutations and associated polymorphisms in a cohort of 44 unrelated patients with long QT syndrome. *Clin Genet*. 2006;70(3):214-227. doi:10.1111/j.1399-0004.2006.00671.x
162. Darbar D, Kannankeril PJ, Donahue BS, et al. Cardiac sodium channel (SCN5A) variants associated with atrial fibrillation. *Circulation*. 2008;117(15):1927-1935. doi:10.1161/CIRCULATIONAHA.107.757955
163. Wallace RH, Hodgson BL, Grinton BE, et al. Sodium channel alpha1-subunit mutations in severe myoclonic epilepsy of infancy and infantile spasms. *Neurology*. 2003;61(6):765-769. doi:10.1212/01.wnl.0000086379.71183.78
164. Li N, Zhang J, Guo J, Yan X, Xia K, Tang B. Novel mutation of SCN1A in familial generalized epilepsy with febrile seizures plus. *Neurosci Lett*. 2010;480(3):211-214. doi:10.1016/j.neulet.2010.06.040
165. Rusconi R, Scalmani P, Cassulini RR, et al. Modulatory proteins can rescue a trafficking defective epileptogenic Nav1.1 Na+ channel mutant. *J Neurosci*. 2007;27(41):11037-11046. doi:10.1523/JNEUROSCI.3515-07.2007
166. Nagao Y, Mazaki-Miyazaki E, Okamura N, Takagi M, Igarashi T, Yamakawa K. A family of generalized epilepsy with febrile seizures plus type 2-a new missense mutation of SCN1A found in the pedigree of several patients with complex febrile seizures. *Epilepsy Res*. 2005;63(2-3):151-156. doi:10.1016/j.eplepsyres.2004.11.005
167. Spampanato J, Kearney JA, de Haan G, et al. A novel epilepsy mutation in the sodium channel SCN1A identifies a cytoplasmic domain for beta subunit interaction. *J Neurosci*. 2004;24(44):10022-10034. doi:10.1523/JNEUROSCI.2034-04.2004
168. Hindocha N, Nashef L, Elmslie F, et al. Two cases of sudden unexpected death in epilepsy in a GEFS+ family with an SCN1A mutation. *Epilepsia*. 2008;49(2):360-365. doi:10.1111/j.1528-1167.2007.01439_2.x
169. Trump N, McTague A, Brittain H, et al. Improving diagnosis and broadening the phenotypes in early-onset seizure and severe developmental delay disorders through gene panel analysis. *J Med Genet*. 2016;53(5):310-317. doi:10.1136/jmedgenet-2015-103263

170. Martin HC, Kim GE, Pagnamenta AT, et al. Clinical whole-genome sequencing in severe early-onset epilepsy reveals new genes and improves molecular diagnosis. *Hum Mol Genet*. 2014;23(12):3200-3211. doi:10.1093/hmg/ddu030
171. Baasch A-L, Hüning I, Gilissen C, et al. Exome sequencing identifies a de novo SCN2A mutation in a patient with intractable seizures, severe intellectual disability, optic atrophy, muscular hypotonia, and brain abnormalities. *Epilepsia*. 2014;55(4):e25-9. doi:10.1111/epi.12554
172. Parrini E, Marini C, Mei D, et al. Diagnostic Targeted Resequencing in 349 Patients with Drug-Resistant Pediatric Epilepsies Identifies Causative Mutations in 30 Different Genes. *Hum Mutat*. 2017;38(2):216-225. doi:10.1002/humu.23149
173. Berecki G, Howell KB, Deerasooriya YH, et al. Dynamic action potential clamp predicts functional separation in mild familial and severe de novo forms of SCN2A epilepsy. *Proc Natl Acad Sci U S A*. 2018;115(24):E5516-E5525. doi:10.1073/pnas.1800077115
174. Haug K, Hallmann K, Rebstock J, et al. The voltage-gated sodium channel gene SCN2A and idiopathic generalized epilepsy. *Epilepsy Res*. 2001;47(3):243-246. doi:10.1016/s0920-1211(01)00312-6
175. Zaman T, Helbig I, Božović IB, et al. Mutations in SCN3A cause early infantile epileptic encephalopathy. *Ann Neurol*. 2018;83(4):703-717. doi:10.1002/ana.25188
176. Holland KD, Kearney JA, Glauser TA, et al. Mutation of sodium channel SCN3A in a patient with cryptogenic pediatric partial epilepsy. *Neurosci Lett*. 2008;433(1):65-70. doi:10.1016/j.neulet.2007.12.064
177. Rojas C V, Wang JZ, Schwartz LS, Hoffman EP, Powell BR, Brown RHJ. A Met-to-Val mutation in the skeletal muscle Na+ channel alpha-subunit in hyperkalaemic periodic paralysis. *Nature*. 1991;354(6352):387-389. doi:10.1038/354387a0
178. Xiuhai G, Weiping W, Ke Z, Hongbin W, Yiling S, MaoYanling. Mutations of sodium channel alpha-subunit genes in Chinese patients with normokalemic periodic paralysis. *Cell Mol Neurobiol*. 2008;28(5):653-661. doi:10.1007/s10571-007-9231-4
179. Kubota T, Kinoshita M, Sasaki R, et al. New mutation of the Na channel in the severe form of potassium-aggravated myotonia. *Muscle Nerve*. 2009;39(5):666-

673. doi:10.1002/mus.21155

180. Groome JR, Larsen MF, Coonts A. Differential effects of paramyotonia congenita mutations F1473S and F1705I on sodium channel gating. *Channels (Austin)*. 2008;2(1):39-50. doi:10.4161/chan.2.1.6051

181. Bezzina CR, Rook MB, Groenewegen WA, et al. Compound heterozygosity for mutations (W156X and R225W) in SCN5A associated with severe cardiac conduction disturbances and degenerative changes in the conduction system. *Circ Res*. 2003;92(2):159-168.

182. Huang W, Liu M, Yan SF, Yan N. Structure-based assessment of disease-related mutations in human voltage-gated sodium channels. *Protein Cell*. 2017;8(6):401-438. doi:10.1007/s13238-017-0372-z

183. Kapplinger JD, Giudicessi JR, Ye D, et al. Enhanced Classification of Brugada Syndrome–Associated and Long-QT Syndrome–Associated Genetic Variants in the SCN5A-Encoded Nav1.5 Cardiac Sodium Channel. *Circ Cardiovasc Genet*. 2015;8(4):582-595. doi:10.1161/CIRCGENETICS.114.000831

184. Petitprez S, Jespersen T, Pruvot E, et al. Analyses of a novel SCN5A mutation (C1850S): conduction vs. repolarization disorder hypotheses in the Brugada syndrome. *Cardiovasc Res*. 2008;78(3):494-504. doi:10.1093/cvr/cvn023

185. Rook MB, Bezzina Alshinawi C, Groenewegen WA, et al. Human SCN5A gene mutations alter cardiac sodium channel kinetics and are associated with the Brugada syndrome*. *Cardiovasc Res*. 1999;44(3):507-517. doi:10.1016/S0008-6363(99)00350-8

186. Frustaci A, Priori SG, Pieroni M, et al. Cardiac Histological Substrate in Patients With Clinical Phenotype of Brugada Syndrome. *Circulation*. 2005;112(24):3680-3687. doi:10.1161/CIRCULATIONAHA.105.520999

187. Bébarová M, O'Hara T, Geelen JLMC, et al. Subepicardial phase 0 block and discontinuous transmural conduction underlie right precordial ST-segment elevation by a SCN5A loss-of-function mutation. *Am J Physiol Circ Physiol*. 2008;295(1):H48-H58. doi:10.1152/ajpheart.91495.2007

188. Wei J, Wang DW, Alings M, et al. Congenital long-QT syndrome caused by a novel mutation in a conserved acidic domain of the cardiac Na+ channel. *Circulation*. 1999;99(24):3165-3171. doi:10.1161/01.cir.99.24.3165

189. Makita N, Behr E, Shimizu W, et al. The E1784K mutation in SCN5A is associated with mixed clinical phenotype of type 3 long QT syndrome. *J Clin Invest*.

2008;118(6):2219-2229. doi:10.1172/JCI34057

190. An RH, Wang XL, Kerem B, et al. Novel LQT-3 mutation affects Na+ channel activity through interactions between alpha- and beta1-subunits. *Circ Res*. 1998;83(2):141-146. doi:10.1161/01.res.83.2.141
191. Napolitano C, Priori SG, Schwartz PJ, et al. Genetic testing in the long QT syndrome: development and validation of an efficient approach to genotyping in clinical practice. *JAMA*. 2005;294(23):2975-2980. doi:10.1001/jama.294.23.2975
192. Benito B, Brugada R, Perich RM, et al. A mutation in the sodium channel is responsible for the association of long QT syndrome and familial atrial fibrillation. *Hear Rhythm*. 2008;5(10):1434-1440. doi:10.1016/j.hrthm.2008.07.013
193. Makita N, Horie M, Nakamura T, et al. Drug-induced long-QT syndrome associated with a subclinical SCN5A mutation. *Circulation*. 2002;106(10):1269-1274. doi:10.1161/01.cir.0000027139.42087.b6
194. Ackerman MJ, Siu BL, Sturner WQ, et al. Postmortem molecular analysis of SCN5A defects in sudden infant death syndrome. *JAMA*. 2001;286(18):2264-2269. doi:10.1001/jama.286.18.2264
195. Benhorin J, Goldmit M, MacCluer JW, et al. Identification of a new SCN5A mutation, D1840G, associated with the long QT syndrome. Mutations in brief no. 153. Online. *Hum Mutat*. 1998;12(1):72. doi:10.1002/(SICI)1098-1004(1998)12:1<72::AID-HUMU19>3.0.CO;2-T
196. Bankston JR, Sampson KJ, Kateriya S, et al. A novel LQT-3 mutation disrupts an inactivation gate complex with distinct rate-dependent phenotypic consequences. *Channels (Austin)*. 2007;1(4):273-280. doi:10.4161/chan.4956
197. Shinlapawittayatorn K, Du XX, Liu H, Ficker E, Kaufman ES, Deschênes I. A common SCN5A polymorphism modulates the biophysical defects of SCN5A mutations. *Hear Rhythm*. 2011;8(3):455-462. doi:10.1016/j.hrthm.2010.11.034
198. Ellinor PT, Nam EG, Shea MA, Milan DJ, Ruskin JN, MacRae CA. Cardiac sodium channel mutation in atrial fibrillation. *Hear Rhythm*. 2008;5(1):99-105. doi:https://doi.org/10.1016/j.hrthm.2007.09.015
199. Selly J-B, Boumahni B, Edmar A, et al. [Cardiac sinus node dysfunction due to a new mutation of the SCN5A gene]. *Arch Pediatr*. 2012;19(8):837-841.

doi:10.1016/j.arcped.2012.04.017

200. Wagnon JL, Barker BS, Hounshell JA, et al. Pathogenic mechanism of recurrent mutations of SCN8A in epileptic encephalopathy. *Ann Clin Transl Neurol*. 2016;3(2):114-123. doi:10.1002/acn3.276
201. Wang J, Gao H, Bao X, et al. SCN8A mutations in Chinese patients with early onset epileptic encephalopathy and benign infantile seizures. *BMC Med Genet*. 2017;18(1):104. doi:10.1186/s12881-017-0460-1
202. Anand G, Collett-White F, Orsini A, et al. Autosomal dominant SCN8A mutation with an unusually mild phenotype. *Eur J Paediatr Neurol EJPN Off J Eur Paediatr Neurol Soc*. 2016;20(5):761-765. doi:10.1016/j.ejpn.2016.04.015
203. Grimes JA, Fraser SP, Stephens GJ, et al. Differential expression of voltage-activated Na+ currents in two prostatic tumour cell lines: contribution to invasiveness in vitro. *FEBS Lett*. 1995;369(2-3):290-294. doi:10.1016/0014-5793(95)00772-2
204. Laniado ME, Lalani EN, Fraser SP, et al. Expression and functional analysis of voltage-activated Na+ channels in human prostate cancer cell lines and their contribution to invasion in vitro. *Am J Pathol*. 1997;150(4):1213-1221.
205. Hernandez-Plata E, Ortiz CS, Marquina-Castillo B, et al. Overexpression of NaV 1.6 channels is associated with the invasion capacity of human cervical cancer. *Int J cancer*. 2012;130(9):2013-2023. doi:10.1002/ijc.26210
206. Fraser SP, Diss JKJ, Chioni A-M, et al. Voltage-gated sodium channel expression and potentiation of human breast cancer metastasis. *Clin cancer Res an Off J Am Assoc Cancer Res*. 2005;11(15):5381-5389. doi:10.1158/1078-0432.CCR-05-0327
207. Brisson L, Gillet L, Calaghan S, et al. Na(V)1.5 enhances breast cancer cell invasiveness by increasing NHE1-dependent H(+) efflux in caveolae. *Oncogene*. 2011;30(17):2070-2076. doi:10.1038/onc.2010.574
208. Gillet L, Roger S, Besson P, et al. Voltage-gated Sodium Channel Activity Promotes Cysteine Cathepsin-dependent Invasiveness and Colony Growth of Human Cancer Cells. *J Biol Chem*. 2009;284(13):8680-8691. doi:10.1074/jbc.M806891200
209. Yang M, Kozminski DJ, Wold LA, et al. Therapeutic potential for phenytoin: targeting Na(v)1.5 sodium channels to reduce migration and invasion in metastatic breast cancer. *Breast Cancer Res Treat*. 2012;134(2):603-615.

doi:10.1007/s10549-012-2102-9

210. Nelson M, Yang M, Millican-Slater R, Brackenbury WJ. Nav1.5 regulates breast tumor growth and metastatic dissemination in vivo. *Oncotarget*. 2015;6(32):32914-32929. doi:10.18632/oncotarget.5441
211. Chioni A-M, Shao D, Grose R, Djamgoz MBA. Protein kinase A and regulation of neonatal Nav1.5 expression in human breast cancer cells: activity-dependent positive feedback and cellular migration. *Int J Biochem Cell Biol*. 2010;42(2):346-358. doi:10.1016/j.biocel.2009.11.021
212. Nelson M, Millican-Slater R, Forrest LC, Brackenbury WJ. The sodium channel ß1 subunit mediates outgrowth of neurite-like processes on breast cancer cells and promotes tumour growth and metastasis. *Int J cancer*. 2014;135(10):2338-2351. doi:10.1002/ijc.28890
213. House CD, Vaske CJ, Schwartz AM, et al. Voltage-gated Na+ channel SCN5A is a key regulator of a gene transcriptional network that controls colon cancer invasion. *Cancer Res*. 2010;70(17):6957-6967. doi:10.1158/0008-5472.CAN-10-1169
214. Gao R, Shen Y, Cai J, Lei M, Wang Z. Expression of voltage-gated sodium channel alpha subunit in human ovarian cancer. *Oncol Rep*. 2010;23(5):1293-1299. doi:10.3892/or_00000763
215. Carrithers MD, Dib-Hajj S, Carrithers LM, et al. Expression of the voltage-gated sodium channel NaV1.5 in the macrophage late endosome regulates endosomal acidification. *J Immunol*. 2007;178(12):7822-7832. doi:10.4049/jimmunol.178.12.7822
216. Xu H, Ren D. Lysosomal physiology. *Annu Rev Physiol*. 2015;77:57-80. doi:10.1146/annurev-physiol-021014-071649
217. White CR, Dungan M, Carrithers MD. Activation of human macrophage sodium channels regulates RNA processing to increase expression of the DNA repair protein PPP1R10. *Immunobiology*. 2019;224(1):80-93. doi:10.1016/j.imbio.2018.10.005
218. Bevan S, Chiu SY, Gray PT, Ritchie JM. The presence of voltage-gated sodium, potassium and chloride channels in rat cultured astrocytes. *Proc R Soc London Ser B, Biol Sci*. 1985;225(1240):299-313. doi:10.1098/rspb.1985.0063
219. Chiu SY, Schrager P, Ritchie JM. Neuronal-type Na+ and K+ channels in rabbit cultured Schwann cells. *Nature*. 1984;311(5982):156-157.

doi:10.1038/311156a0

220. Black JA, Newcombe J, Waxman SG. Astrocytes within multiple sclerosis lesions upregulate sodium channel Nav1.5. *Brain*. 2010;133(Pt 3):835-846. doi:10.1093/brain/awq003
221. Hoffman JF, Dodson A, Wickrema A, Dib-Hajj SD. Tetrodotoxin-sensitive Na⁺ channels and muscarinic and purinergic receptors identified in human erythroid progenitor cells and red blood cell ghosts. *Proc Natl Acad Sci U S A*. 2004;101(33):12370 LP - 12374. doi:10.1073/pnas.0404228101
222. Xiao Y, Blumenthal K, Jackson JO 2nd, Liang S, Cummins TR. The tarantula toxins ProTx-II and huwentoxin-IV differentially interact with human Nav1.7 voltage sensors to inhibit channel activation and inactivation. *Mol Pharmacol*. 2010;78(6):1124-1134. doi:10.1124/mol.110.066332
223. Revell JD, Lund P-E, Linley JE, et al. Potency optimization of Huwentoxin-IV on hNav1.7: a neurotoxin TTX-S sodium-channel antagonist from the venom of the Chinese bird-eating spider Selenocosmia huwena. *Peptides*. 2013;44:40-46. doi:10.1016/j.peptides.2013.03.011
224. Heinemann SH, Terlau H, Stühmer W, Imoto K, Numa S. Calcium channel characteristics conferred on the sodium channel by single mutations. *Nature*. 1992;356(6368):441-443. doi:10.1038/356441a0
225. Noda M, Suzuki H, Numa S, Stühmer W. A single point mutation confers tetrodotoxin and saxitoxin insensitivity on the sodium channel II. *FEBS Lett*. 1989;259(1):213-216. doi:https://doi.org/10.1016/0014-5793(89)81531-5
226. Shcherbatko A, Rossi A, Foletti D, et al. Engineering Highly Potent and Selective Microproteins against Nav1.7 Sodium Channel for Treatment of Pain. *J Biol Chem*. 2016;291(27):13974-13986. doi:10.1074/jbc.M116.725978
227. Xu S-Z, Zeng F, Lei M, et al. Generation of functional ion-channel tools by E3 targeting. *Nat Biotechnol*. 2005;23(10):1289-1293. doi:10.1038/nbt1148
228. Liu D, Tseng M, Epstein LF, et al. Evaluation of recombinant monoclonal antibody SVmab1 binding to Na (V)1.7 target sequences and block of human Na (V)1.7 currents. *F1000Research*. 2016;5:2764. doi:10.12688/f1000research.9918.1
229. Muroi Y, Ru F, Kollarik M, et al. Selective silencing of Na(V)1.7 decreases excitability and conduction in vagal sensory neurons. *J Physiol*. 2011;589(Pt

23):5663-5676. doi:10.1113/jphysiol.2011.215384

230. Shao J, Cao J, Wang J, et al. MicroRNA-30b regulates expression of the sodium channel Nav1.7 in nerve injury-induced neuropathic pain in the rat. *Mol Pain*. 2016;12. doi:10.1177/1744806916671523
231. Spencer NJ. Switching off pain at the source: is this the end for opioid pain relief? *Pain Manag*. 2016;6(1):39-47. doi:10.2217/pmt.15.52
232. Yang J, Yan R, Roy A, Xu D, Poisson J, Zhang Y. The I-TASSER Suite: protein structure and function prediction. *Nat Methods*. 2015;12(1):7-8. doi:10.1038/nmeth.3213
233. Wang C, Chung BC, Yan H, Lee S-Y, Pitt GS. Crystal structure of the ternary complex of a NaV C-terminal domain, a fibroblast growth factor homologous factor, and calmodulin. *Structure*. 2012;20(7):1167-1176. doi:10.1016/j.str.2012.05.001
234. Wingo TL, Shah VN, Anderson ME, Lybrand TP, Chazin WJ, Balser JR. An EF-hand in the sodium channel couples intracellular calcium to cardiac excitability. *Nat Struct Mol Biol*. 2004;11(3):219-225. doi:10.1038/nsmb737
235. Salvage SC, Habib ZF, Matthews HR, Jackson AP, Huang CL-H. Ca2+-dependent modulation of voltage-gated myocyte sodium channels. *Biochem Soc Trans*. October 2021. doi:10.1042/BST20200604
236. Nathan S, Gabelli SB, Yoder JB, et al. Structural basis of cytoplasmic NaV1.5 and NaV1.4 regulation. *J Gen Physiol*. 2020;153(1). doi:10.1085/jgp.202012722
237. Pitt GS, Lee S-Y. Current view on regulation of voltage-gated sodium channels by calcium and auxiliary proteins. *Protein Sci*. 2016;25(9):1573-1584. doi:https://doi.org/10.1002/pro.2960
238. Shah VN, Wingo TL, Weiss KL, Williams CK, Balser JR, Chazin WJ. Calcium-dependent regulation of the voltage-gated sodium channel hH1: Intrinsic and extrinsic sensors use a common molecular switch. *Proc Natl Acad Sci U S A*. 2006;103(10):3592 LP - 3597. doi:10.1073/pnas.0507397103
239. Rhoads AR, Friedberg F. Sequence motifs for calmodulin recognition. *FASEB J*. 1997;11(5):331-340. doi:https://doi.org/10.1096/fasebj.11.5.9141499
240. Tan HL, Kupershmidt S, Zhang R, et al. A calcium sensor in the sodium channel modulates cardiac excitability. *Nature*. 2002;415(6870):442-447. doi:10.1038/415442a
241. E. MW, R. MA, A. QF. Target Enzyme Recognition by Calmodulin: 2.4 Å

Structure of a Calmodulin-Peptide Complex . *Science (80-)*. 1992;257(5074):1251-1255. doi:10.1126/science.1519061

242. Sarhan MF, Tung C-C, Van Petegem F, Ahern CA. Crystallographic basis for calcium regulation of sodium channels. *Proc Natl Acad Sci*. 2012;109(9):3558 LP - 3563. doi:10.1073/pnas.1114748109
243. Johnson CN, Potet F, Thompson MK, et al. A Mechanism of Calmodulin Modulation of the Human Cardiac Sodium Channel. *Structure*. 2018;26(5):683-694.e3. doi:https://doi.org/10.1016/j.str.2018.03.005
244. Chagot B, Chazin WJ. Solution NMR Structure of Apo-Calmodulin in Complex with the IQ Motif of Human Cardiac Sodium Channel NaV1.5. *J Mol Biol*. 2011;406(1):106-119. doi:https://doi.org/10.1016/j.jmb.2010.11.046
245. Gardill BR, Rivera-Acevedo RE, Tung C-C, Van Petegem F. Crystal structures of Ca2+–calmodulin bound to NaV C-terminal regions suggest role for EF-hand domain in binding and inactivation. *Proc Natl Acad Sci*. 2019;116(22):10763 LP - 10772. doi:10.1073/pnas.1818618116
246. Luo L, Ning F, Du Y, et al. Calcium-dependent Nedd4-2 upregulation mediates degradation of the cardiac sodium channel Nav1.5: implications for heart failure. *Acta Physiol (Oxf)*. 2017;221(1):44-58. doi:10.1111/apha.12872
247. Wang Z, Vermij SH, Sottas V, et al. Calmodulin binds to the N-terminal domain of the cardiac sodium channel Na(v)1.5. *Channels (Austin)*. 2020;14(1):268-286. doi:10.1080/19336950.2020.1805999
248. Laedermann CJ, Syam N, Pertin M, Decosterd I, Abriel H. beta1- and beta3-voltage-gated sodium channel subunits modulate cell surface expression and glycosylation of Nav1.7 in HEK293 cells. *Front Cell Neurosci*. 2013;7:137. doi:10.3389/fncel.2013.00137
249. Salvage SC, Zhu W, Habib ZF, et al. Gating control of the cardiac sodium channel Nav1.5 by its β3-subunit involves distinct roles for a transmembrane glutamic acid and the extracellular domain. *J Biol Chem*. 2019;294(51). doi:10.1074/jbc.RA119.010283
250. Guo D, Jenkinson S. Simultaneous assessment of compound activity on cardiac Nav1.5 peak and late currents in an automated patch clamp platform. *J Pharmacol Toxicol Methods*. 2019;99:106575. doi:10.1016/j.vascn.2019.04.001
251. Phillips JC, Braun R, Wang W, et al. Scalable molecular dynamics with NAMD.

J Comput Chem. 2005;26(16):1781-1802. doi:10.1002/jcc.20289

252. Feller SE, MacKerell AD. An Improved Empirical Potential Energy Function for Molecular Simulations of Phospholipids. *J Phys Chem B*. 2000;104(31):7510-7515. doi:10.1021/jp0007843
253. Humphrey W, Dalke A, Schulten K. VMD: visual molecular dynamics. *J Mol Graph*. 1996;14(1):27-28,33-38. doi:10.1016/0263-7855(96)00018-5
254. Joung IS, Persil Cetinkol O, Hud N V, Cheatham TE 3rd. Molecular dynamics simulations and coupled nucleotide substitution experiments indicate the nature of A{middle dot}A base pairing and a putative structure of the coralyne-induced homo-adenine duplex. *Nucleic Acids Res*. 2009;37(22):7715-7727. doi:10.1093/nar/gkp730
255. Noskov SY, Bernèche S, Roux B. Control of ion selectivity in potassium channels by electrostatic and dynamic properties of carbonyl ligands. *Nature*. 2004;431(7010):830-834. doi:10.1038/nature02943
256. Masood T Bin, Sandhya S, Chandra N, Natarajan V. CHEXVIS: a tool for molecular channel extraction and visualization. *BMC Bioinformatics*. 2015;16:119. doi:10.1186/s12859-015-0545-9
257. Boratyn GM, Camacho C, Cooper PS, et al. BLAST: a more efficient report with usability improvements. *Nucleic Acids Res*. 2013;41(Web Server issue):W29-33. doi:10.1093/nar/gkt282
258. Wiederstein M, Sippl MJ. TopMatch-web: pairwise matching of large assemblies of protein and nucleic acid chains in 3D. *Nucleic Acids Res*. 2020;48(W1):W31-W35. doi:10.1093/nar/gkaa366
259. Martin CD, Rojas G, Mitchell JN, et al. A simple vector system to improve performance and utilisation of recombinant antibodies. *BMC Biotechnol*. 2006;6:46. doi:10.1186/1472-6750-6-46
260. Schofield DJ, Pope AR, Clementel V, et al. Application of phage display to high throughput antibody generation and characterization. *Genome Biol*. 2007;8(11):R254. doi:10.1186/gb-2007-8-11-r254
261. Kozakov D, Hall DR, Xia B, et al. The ClusPro web server for protein-protein docking. *Nat Protoc*. 2017;12(2):255-278. doi:10.1038/nprot.2016.169
262. Brenke R, Hall DR, Chuang G-Y, et al. Application of asymmetric statistical potentials to antibody-protein docking. *Bioinformatics*. 2012;28(20):2608-2614. doi:10.1093/bioinformatics/bts493

263. Abriel H, Zaklyazminskaya E V. Cardiac channelopathies: genetic and molecular mechanisms. *Gene*. 2013;517(1):1-11. doi:10.1016/j.gene.2012.12.061
264. Zhang Y, Guzadhur L, Jeevaratnam K, et al. Arrhythmic substrate, slowed propagation and increased dispersion in conduction direction in the right ventricular outflow tract of murine Scn5a+/- hearts. *Acta Physiol (Oxf)*. 2014;211(4):559-573. doi:10.1111/apha.12324
265. Baroudi G, Napolitano C, Priori SG, Del Bufalo A, Chahine M. Loss of function associated with novel mutations of the SCN5A gene in patients with Brugada syndrome. *Can J Cardiol*. 2004;20(4):425-430.
266. Veerman CC, Wilde AAM, Lodder EM. The cardiac sodium channel gene SCN5A and its gene product NaV1.5: Role in physiology and pathophysiology. *Gene*. 2015;573(2):177-187. doi:10.1016/j.gene.2015.08.062
267. Musafia B, Buchner V, Arad D. Complex salt bridges in proteins: statistical analysis of structure and function. *J Mol Biol*. 1995;254(4):761-770. doi:10.1006/jmbi.1995.0653
268. Barlow DJ, Thornton JM. Ion-pairs in proteins. *J Mol Biol*. 1983;168(4):867-885.
269. Gallivan JP, Dougherty DA. Cation-pi interactions in structural biology. *Proc Natl Acad Sci U S A*. 1999;96(17):9459-9464. doi:10.1073/pnas.96.17.9459
270. Yarov-Yarovoy V, Baker D, Catterall WA. Voltage sensor conformations in the open and closed states in ROSETTA structural models of K(+) channels. *Proc Natl Acad Sci U S A*. 2006;103(19):7292-7297. doi:10.1073/pnas.0602350103
271. Catterall WA. Structure and function of voltage-gated sodium channels at atomic resolution. *Exp Physiol*. 2014;99(1):35-51. doi:10.1113/expphysiol.2013.071969
272. Tarradas A, Selga E, Beltran-Alvarez P, et al. A novel missense mutation, I890T, in the pore region of cardiac sodium channel causes Brugada syndrome. *PLoS One*. 2013;8(1):e53220. doi:10.1371/journal.pone.0053220
273. Riuró H, Beltran-Alvarez P, Tarradas A, et al. A missense mutation in the sodium channel β2 subunit reveals SCN2B as a new candidate gene for Brugada syndrome. *Hum Mutat*. 2013;34(7):961-966. doi:10.1002/humu.22328
274. Gando I, Morganstein J, Jana K, McDonald T V, Tang Y, Coetzee WA. Infant sudden death: Mutations responsible for impaired Nav1.5 channel trafficking and function. *Pacing Clin Electrophysiol*. 2017;40(6):703-712.

doi:10.1111/pace.13087

275. Jiang R, Martz A, Gonin S, Taly A, de Carvalho LP, Grutter T. A putative extracellular salt bridge at the subunit interface contributes to the ion channel function of the ATP-gated P2X2 receptor. *J Biol Chem*. 2010;285(21):15805-15815. doi:10.1074/jbc.M110.101980
276. Venkatachalan SP, Czajkowski C. A conserved salt bridge critical for GABAA receptor function and loop C dynamics. *Proc Natl Acad Sci*. 2008;105(36):13604 LP - 13609. doi:10.1073/pnas.0801854105
277. Barnes S, Hille B. Veratridine modifies open sodium channels. *J Gen Physiol*. 1988;91(3):421-443. doi:10.1085/jgp.91.3.421
278. Denac H, Mevissen M, Scholtysik G. Structure, function and pharmacology of voltage-gated sodium channels. *Naunyn Schmiedebergs Arch Pharmacol*. 2000;362(6):453-479. doi:10.1007/s002100000319
279. Spencer CI. Actions of ATX-II and other gating-modifiers on Na(+) currents in HEK-293 cells expressing WT and DeltaKPQ hNa(V) 1.5 Na(+) channels. *Toxicon*. 2009;53(1):78-89. doi:10.1016/j.toxicon.2008.10.015
280. Zhao W-S, Sun M-Y, Sun L-F, et al. A Highly Conserved Salt Bridge Stabilizes the Kinked Conformation of ß2,3-Sheet Essential for Channel Function of P2X4 Receptors. *J Biol Chem*. 2016;291(15):7990-8003. doi:10.1074/jbc.M115.711127
281. Beu TA. Molecular dynamics simulations of ion transport through carbon nanotubes. III. Influence of the nanotube radius, solute concentration, and applied electric fields on the transport properties. *J Chem Phys*. 2011;135(4):44516. doi:10.1063/1.3615728
282. Ahmed M, Jalily Hasani H, Ganesan A, Houghton M, Barakat K. Modeling the human Na(v)1.5 sodium channel: structural and mechanistic insights of ion permeation and drug blockade. *Drug Des Devel Ther*. 2017;11:2301-2324. doi:10.2147/DDDT.S133944
283. Li Z, Jin X, Wu T, et al. Structure of human Na_v1.5 reveals the fast inactivation-related segments as a mutational hotspot for the long QT syndrome. *Proc Natl Acad Sci*. 2021;118(11):e2100069118. doi:10.1073/pnas.2100069118
284. DeMarco KR, Bekker S, Vorobyov I. Challenges and advances in atomistic simulations of potassium and sodium ion channel gating and permeation. *J*

Physiol. 2019;597(3):679-698. doi:https://doi.org/10.1113/JP277088

285. Abdul Samad F, Suliman BA, Basha SH, Manivasagam T, Essa MM. A Comprehensive In Silico Analysis on the Structural and Functional Impact of SNPs in the Congenital Heart Defects Associated with NKX2-5 Gene—A Molecular Dynamic Simulation Approach. *PLoS One*. 2016;11(5):e0153999. https://doi.org/10.1371/journal.pone.0153999.
286. Kar T, Narsaria U, Basak S, et al. A candidate multi-epitope vaccine against SARS-CoV-2. *Sci Rep*. 2020;10(1):10895. doi:10.1038/s41598-020-67749-1
287. Radwan A, Mahrous GM. Docking studies and molecular dynamics simulations of the binding characteristics of waldiomycin and its methyl ester analog to Staphylococcus aureus histidine kinase. *PLoS One*. 2020;15(6):e0234215. https://doi.org/10.1371/journal.pone.0234215.
288. Donald JE, Kulp DW, DeGrado WF. Salt bridges: geometrically specific, designable interactions. *Proteins*. 2011;79(3):898-915. doi:10.1002/prot.22927
289. Sehnal D, Svobodová Vařeková R, Berka K, et al. MOLE 2.0: advanced approach for analysis of biomacromolecular channels. *J Cheminform*. 2013;5(1):39. doi:10.1186/1758-2946-5-39
290. Phillips BP, Gomez-Navarro N, Miller EA. Protein quality control in the endoplasmic reticulum. *Curr Opin Cell Biol*. 2020;65:96-102. doi:10.1016/j.ceb.2020.04.002
291. Gvritishvili AG, Gribenko A V, Makhatadze GI. Cooperativity of complex salt bridges. *Protein Sci*. 2008;17(7):1285-1290. doi:10.1110/ps.034975.108
292. Ing C, Pomès R. Simulation Studies of Ion Permeation and Selectivity in Voltage-Gated Sodium Channels. *Curr Top Membr*. 2016;78:215-260. doi:10.1016/bs.ctm.2016.07.005
293. Sun YM, Favre I, Schild L, Moczydlowski E. On the structural basis for size-selective permeation of organic cations through the voltage-gated sodium channel. Effect of alanine mutations at the DEKA locus on selectivity, inhibition by Ca2+ and H+, and molecular sieving. *J Gen Physiol*. 1997;110(6):693-715. doi:10.1085/jgp.110.6.693
294. Shen H, Li Z, Jiang Y, et al. Structural basis for the modulation of voltage-gated sodium channels by animal toxins. *Science*. 2018;362(6412). doi:10.1126/science.aau2596

295. Xia M, Liu H, Li Y, Yan N, Gong H. The mechanism of Na^+/K^+ selectivity in mammalian voltage-gated sodium channels based on molecular dynamics simulation. *Biophys J*. 2013;104(11):2401-2409. doi:10.1016/j.bpj.2013.04.035
296. Hilber K, Sandtner W, Zarrabi T, et al. Selectivity Filter Residues Contribute Unequally to Pore Stabilization in Voltage-Gated Sodium Channels. *Biochemistry*. 2005;44(42):13874-13882. doi:10.1021/bi0511944
297. Salvage SC, Rees JS, McStea A, et al. Supramolecular clustering of the cardiac sodium channel Nav1.5 in HEK293F cells, with and without the auxiliary ß3-subunit. *FASEB J Off Publ Fed Am Soc Exp Biol*. 2020;34(3):3537-3553. doi:10.1096/fj.201701473RR
298. Adrian RH. Charge movement in the membrane of striated muscle. *Annu Rev Biophys Bioeng*. 1978;7:85-112. doi:10.1146/annurev.bb.07.060178.000505
299. Zhu W, Voelker TL, Varga Z, Schubert AR, Nerbonne JM, Silva JR. Mechanisms of noncovalent ß subunit regulation of Na(V) channel gating. *J Gen Physiol*. 2017;149(8):813-831. doi:10.1085/jgp.201711802
300. Piontkivska H, Hughes AL. Evolution of vertebrate voltage-gated ion channel alpha chains by sequential gene duplication. *J Mol Evol*. 2003;56(3):277-285. doi:10.1007/s00239-002-2399-9
301. Wu J, Yan Z, Li Z, et al. Structure of the voltage-gated calcium channel Cav1.1 complex. *Science*. 2015;350(6267):aad2395. doi:10.1126/science.aad2395
302. Mantegazza M, Yu FH, Catterall WA, Scheuer T. Role of the C-terminal domain in inactivation of brain and cardiac sodium channels. *Proc Natl Acad Sci U S A*. 2001;98(26):15348-15353. doi:10.1073/pnas.211563298
303. Babu YS, Bugg CE, Cook WJ. Structure of calmodulin refined at 2.2 A resolution. *J Mol Biol*. 1988;204(1):191-204. doi:10.1016/0022-2836(88)90608-0
304. Friedberg F, Rhoads AR. Evolutionary aspects of calmodulin. *IUBMB Life*. 2001;51(4):215-221. doi:10.1080/152165401753311753
305. Kim J, Ghosh S, Liu H, Tateyama M, Kass RS, Pitt GS. Calmodulin mediates Ca2+ sensitivity of sodium channels. *J Biol Chem*. 2004;279(43):45004-45012. doi:10.1074/jbc.M407286200
306. Yan H, Wang C, Marx SO, Pitt GS. Calmodulin limits pathogenic Na+ channel persistent current. *J Gen Physiol*. 2017;149(2):277-293. doi:10.1085/jgp.201611721
307. Kang PW, Chakouri N, Diaz J, Tomaselli GF, Yue DT, Ben-Johny M. Elementary

mechanisms of calmodulin regulation of Na_V1.5 producing divergent arrhythmogenic phenotypes. *Proc Natl Acad Sci*. 2021;118(21):e2025085118. doi:10.1073/pnas.2025085118

308. Crotti L, Johnson CN, Graf E, et al. Calmodulin mutations associated with recurrent cardiac arrest in infants. *Circulation*. 2013;127(9):1009-1017. doi:10.1161/CIRCULATIONAHA.112.001216
309. Gabelli SB, Boto A, Kuhns VH, et al. Regulation of the NaV1.5 cytoplasmic domain by calmodulin. *Nat Commun*. 2014;5:5126. doi:10.1038/ncomms6126
310. Wang C, Chung BC, Yan H, Wang H-G, Lee S-Y, Pitt GS. Structural analyses of Ca2+/CaM interaction with NaV channel C-termini reveal mechanisms of calcium-dependent regulation. *Nat Commun*. 2014;5(1):4896. doi:10.1038/ncomms5896
311. Yang L, Dong F, Yang Q, et al. FGF13 Selectively Regulates Heat Nociception by Interacting with Nav1.7. *Neuron*. 2017;93(4):806-821.e9. doi:https://doi.org/10.1016/j.neuron.2017.01.009
312. Hennessey JA, Marcou CA, Wang C, et al. FGF12 is a candidate Brugada syndrome locus. *Hear Rhythm*. 2013;10(12):1886-1894. doi:10.1016/j.hrthm.2013.09.064
313. Haghighatian M, Mofid MR, Nekouei MK, Yaghmaei P, Tafreshi AH. Isomalt production by cloning, purifying and expressing of the MDH gene from Pseudomonas fluorescens DSM 50106 in different strains of E. coli. *Pakistan J Biol Sci PJBS*. 2009;11(16):2001-2006. https://www.unboundmedicine.com/medline/citation/19266906/Isomalt_production_by_cloning_purifying_and_expressing_of_the_MDH_gene_from_Pseudomonas_fluorescens_DSM_50106_in_different_strains_of_E__coli_.
314. Luo H, Cao M, Newell K, et al. Double-peak elution profile of a monoclonal antibody in cation exchange chromatography is caused by histidine-protonation-based charge variants. *J Chromatogr A*. 2015;1424:92-101. doi:https://doi.org/10.1016/j.chroma.2015.11.008
315. Lu R-M, Hwang Y-C, Liu I-J, et al. Development of therapeutic antibodies for the treatment of diseases. *J Biomed Sci*. 2020;27(1):1. doi:10.1186/s12929-019-0592-z
316. Kesik-Brodacka M. Progress in biopharmaceutical development. *Biotechnol Appl Biochem*. 2018;65(3):306-322. doi:10.1002/bab.1617

317. Mullard A. FDA approves 100th monoclonal antibody product. *Nat Rev drug Discov*. 2021. https://www.nature.com/articles/d41573-021-00079-7.
318. Alfaleh MA, Alsaab HO, Mahmoud AB, et al. Phage Display Derived Monoclonal Antibodies: From Bench to Bedside . *Front Immunol* . 2020;11:1986. https://www.frontiersin.org/article/10.3389/fimmu.2020.01986.
319. Leavy O. The birth of monoclonal antibodies. *Nat Immunol*. 2016;17(1):S13-S13. doi:10.1038/ni.3608
320. Zhang B, Li H, Hu Z, et al. Generation of mouse–human chimeric embryos. *Nat Protoc*. 2021;16(8):3954-3980. doi:10.1038/s41596-021-00565-7
321. Ledsgaard L, Kilstrup M, Karatt-Vellatt A, McCafferty J, Laustsen AH. Basics of Antibody Phage Display Technology. *Toxins (Basel)*. 2018;10(6). doi:10.3390/toxins10060236
322. O'Connell D, Becerril B, Roy-Burman A, Daws M, Marks JD. Phage versus phagemid libraries for generation of human monoclonal antibodies. *J Mol Biol*. 2002;321(1):49-56. doi:10.1016/s0022-2836(02)00561-2
323. Smith GP. Filamentous fusion phage: novel expression vectors that display cloned antigens on the virion surface. *Science*. 1985;228(4705):1315-1317. doi:10.1126/science.4001944
324. McCafferty J, Griffiths AD, Winter G, Chiswell DJ. Phage antibodies: filamentous phage displaying antibody variable domains. *Nature*. 1990;348(6301):552-554. doi:10.1038/348552a0
325. Sela-Culang I, Alon S, Ofran Y. A systematic comparison of free and bound antibodies reveals binding-related conformational changes. *J Immunol*. 2012;189(10):4890-4899. doi:10.4049/jimmunol.1201493
326. Tsuchiya Y, Mizuguchi K. The diversity of H3 loops determines the antigen-binding tendencies of antibody CDR loops. *Protein Sci*. 2016;25(4):815-825. doi:10.1002/pro.2874
327. McDonnell A, Collins S, Ali Z, et al. Efficacy of the Nav1.7 blocker PF-05089771 in a randomised, placebo-controlled, double-blind clinical study in subjects with painful diabetic peripheral neuropathy. *Pain*. 2018;159(8):1465-1476. doi:10.1097/j.pain.0000000000001227
328. Jiang D, Banh R, Gamal El-Din TM, et al. Open-state structure and pore gating mechanism of the cardiac sodium channel. *Cell*. 2021;184(20):5151-5162.e11. doi:10.1016/j.cell.2021.08.021

329. Velappan N, Close D, Hung L-W, et al. Construction, characterization and crystal structure of a fluorescent single-chain Fv chimera. *Protein Eng Des Sel*. 2021;34:gzaa029. doi:10.1093/protein/gzaa029
330. Agrawal P, Bhalla S, Usmani SS, et al. CPPsite 2.0: a repository of experimentally validated cell-penetrating peptides. *Nucleic Acids Res*. 2016;44(D1):D1098-103. doi:10.1093/nar/gkv1266
331. Green M, Loewenstein PM. Autonomous functional domains of chemically synthesized human immunodeficiency virus tat trans-activator protein. *Cell*. 1988;55(6):1179-1188. doi:https://doi.org/10.1016/0092-8674(88)90262-0
332. Ragin AD, Morgan RA, Chmielewski J. Cellular Import Mediated by Nuclear Localization Signal Peptide Sequences. *Chem Biol*. 2002;9(8):943-948. doi:https://doi.org/10.1016/S1074-5521(02)00189-8
333. Morris MC, Vidal P, Chaloin L, Heitz F, Divita G. A new peptide vector for efficient delivery of oligonucleotides into mammalian cells. *Nucleic Acids Res*. 1997;25(14):2730-2736. doi:10.1093/nar/25.14.2730
334. Wender PA, Mitchell DJ, Pattabiraman K, Pelkey ET, Steinman L, Rothbard JB. The design, synthesis, and evaluation of molecules that enable or enhance cellular uptake: peptoid molecular transporters. *Proc Natl Acad Sci U S A*. 2000;97(24):13003-13008. doi:10.1073/pnas.97.24.13003
335. Jia L, Gorman GS, Coward LU, et al. Preclinical pharmacokinetics, metabolism, and toxicity of azurin-p28 (NSC745104) a peptide inhibitor of p53 ubiquitination. *Cancer Chemother Pharmacol*. 2011;68(2):513-524. doi:10.1007/s00280-010-1518-3
336. Gurbel PA, Bliden KP, Turner SE, et al. Cell-Penetrating Pepducin Therapy Targeting PAR1 in Subjects With Coronary Artery Disease. *Arterioscler Thromb Vasc Biol*. 2016;36(1):189-197. doi:10.1161/ATVBAHA.115.306777